

CONTINUOUS LIQUID INTERFACE PRODUCTION OF MICRONEEDLES FOR TRANSDERMAL DRUG  
DELIVERY

Ashley Rachelle Johnson

A dissertation submitted to the faculty of the University of North Carolina at Chapel Hill  
in partial fulfillment of the requirements for the degree of Doctor of Philosophy  
in the Department of Biomedical Engineering.

Chapel Hill  
2016

Approved by:

Joseph M. DeSimone

Michael Jay

Leaf Huang

Samuel Lai

Amy Oldenburg

© 2016  
Ashley Rachelle Johnson  
ALL RIGHTS RESERVED

## **ABSTRACT**

Ashley Rachelle Johnson: Continuous Liquid Interface Production of Microneedles for Transdermal Drug Delivery  
(Under the direction of Joseph M. DeSimone)

The past two decades of microneedle research has demonstrated the benefits of microneedle technology in transdermal drug delivery. Microneedles are arrays of sub-millimeter sized projections that physically pierce the outer layer of the skin to allow a therapeutic to pass into the body. Using microneedles to create physical channels within the skin has enabled transdermal delivery of many medications that would otherwise need be delivered by hypodermic injection. Because microneedles are so small that they evade nerve endings buried deep within the skin, they have enabled pain free delivery of medications, providing an opportunity for improved patient compliance. Biocompatible microneedles are of particular interest because they are thermodynamically stable at room temperature, safe for patients and enable controlled release of medication out of the patch. The micro-manufacturing processes used to manufacture such biocompatible microneedles, however, do not allow for control over critical microneedle design parameters, such as size, shape, aspect ratio and spacing.

Herein, we utilize a novel additive manufacturing technique called Continuous Liquid Interface Production (CLIP) to manufacture microneedles for transdermal drug delivery. This technique is that fastest microneedle fabrication technique in the world, to date, and enables unprecedented control over patch design parameters. We show that CLIP microneedles can be produced in under 2 minutes per patch and demonstrate capability to produce microneedle designs that cannot be fabricated using other mold-based techniques, such as arrowhead

microneedles. CLIP microneedles were produced from more than four different compositions, including photopolymerizable derivatives of biocompatible materials designed to dissolve, degrade, or swell within the skin to release a cargo. These CLIP microneedles effectively pierced murine skin *ex vivo* and released the fluorescent drug surrogate rhodamine.

Further, the mechanical properties of these microneedle devices are investigated using polyethylene glycol (PEG) with varying crosslink densities. We demonstrate that the elastic modulus of these hydrogels is a critical design parameter that influences microneedle insertion into the skin. Stiff microneedles are shown to effectively penetrate porcine skin *ex vivo* with lower application forces, whereas more rubbery microneedles require a greater force to effectively insert into the skin.

## ACKNOWLEDGEMENTS

But he said to me, “My grace is sufficient for you, for my power is made perfect in weakness.” Therefore I will boast all the more gladly of my weaknesses, so that the power of Christ may rest upon me.” 2 Corinthians 12:9

I am more grateful for graduate school than I ever thought possible. I’ve learned so much about science, even more about life, and become a stronger person more capable of handling the challenges of my future. I have been so blessed to share it with loving and inspiring people, inside and outside of the lab. I quite literally could not have done this without you.

**To my colleagues at the University of North Carolina at Chapel Hill:** I’d like to thank my advisor Dr. Joseph DeSimone for being a constant source of inspiration. Thanks for demanding my best work and trusting me enough to work on problems that really matter. Thank you for the insight, resources, and connections that have allowed me to grow as a young scientist. I’d like to thank Dr. Chris Luft for helping me navigate the many challenges of graduate school. Thank you for seeing me at my worst and yet continuing to believe in me. Many thanks to Dr. Sue Mecham for being my polymer guru and for editing this dissertation.

I would also like to thank my committee members and the many people who contributed to this work, particularly my collaborators at Carbon 3D, including Dr. Alexander Ermoshkin, Dr. David Shirvanyants, and Dr. John Tumbleston, and Ariel Herrman as well as my collaborators at UNC, including Dr. Amy Oldenburg and Dr. Richard Blackmon. Your expertise has been invaluable.

Lastly, thank you to DeSimone members past and present, especially Katie Moga, Cassie Caudill, Erin Wilson, Tammy Shen, James Byrne, Luke Roode, Jason Coffman, Cathy Fromen, Cameron Bloomquist and Ali Nebipasagil. It's an honor to persevere and to laugh beside you.

**To my Chapel Hill family:** You have shown me a depth of love and community that's more than I could have ever hoped for. Ashley Walker, Chelsea Clark, Rebecca Yau, Michelle Huckleberry, Sabrina and Adam Gardner, Betsy and Andrew Satterlee, Emily and William Commander, Tommy Sheppard, Daniel Huang, Alan Tubbs, Karl Shieh, Josh Hartzog, and anyone else I may have forgotten- thank you for making life so much fun and for being a constant source of insight and wisdom. I've cherished all of the time that we've shared together and forward to keeping in touch as I enter this next phase of my life. My phone, heart, and home are always open to you.

**To my biological family:** I performed my first science experiments in our kitchen at home as a little girl. I swore I would NEVER become an engineer, but I suppose it's not altogether surprising to anyone. Mom, thank you for doing everything you could to encourage my love for science. From taking time off of work to do science demonstrations in my elementary school class to picking up pig hearts at the grocery store, you've truly done everything you possible could to support me. Dad, so many of the little phrases you used to say to us as kids have echoed through my head throughout graduate school. "If it were easy, anyone could do it" and "If you don't have time to do it right the first time, when are you going to have time to do it a second time" are just as applicable now as they were then. Taylor, I promise I won't make you call me doctor. And I'm sure that life will provide us with many more moments for you to laugh about the things that "PhD School" hasn't taught me. Thank you for always being a short phone call away.

## TABLE OF CONTENTS

LIST OF FIGURES.....	xii
LIST OF TABLES.....	xix
LIST OF ABBREVIATIONS AND SYMBOLS.....	xx
CHAPTER 1 Microneedle Technology for Transdermal Drug Delivery .....	1
1.1 Transdermal Drug Delivery .....	1
1.1.1 Drug Delivery Market.....	1
1.1.2 First Generation Transdermal Drug Delivery.....	2
1.1.3 Structure of the Skin .....	4
1.1.4 Advancements in Transdermal Drug Delivery .....	6
1.2 Microneedle Technology.....	8
1.2.1 Microneedle Configurations .....	11
1.2.2 Microneedle Fabrication Techniques.....	14
1.2.3 Fabrication of Biocompatible Microneedles.....	18
1.2.4 Overarching Challenges in the Fabrication of Biocompatible Microneedles.....	22
1.2.5 Role of Microneedle Design Parameters on Device Efficacy .....	22
1.3 Additive Manufacturing Overview .....	27

1.3.1	Stereolithography .....	29
1.3.2	Layer-by-Layer Approaches to Additive Manufacturing of Microneedles .....	32
1.3.3	Continuous Liquid Interface Production (CLIP) .....	34
1.4	Summary and Hypothesis.....	36
CHAPTER 2 .....		46
2.1	Introduction .....	46
2.1.1	Step 1- Generation and Slicing of CAD File .....	47
2.1.2	Step 2- Projection of the Image .....	48
2.1.3	Step 3- Photopolymerization of the Part.....	55
2.1.4	Chapter Objective .....	57
2.2	Results and Discussion.....	58
2.2.1	CLIP File Path.....	58
2.2.2	Role of Light Intensity and Build Speed on Microneedle Production Using an Early Prototype .....	59
2.2.3	Effect of System Optics on a Resolution Test Pattern.....	62
2.2.4	Role of Light Intensity on Microneedle Dimensions Using Updated CLIP7 .....	66
2.2.5	Visualization of Individual Pixels Causes Stairstepping .....	69
2.2.6	Application of Antialiasing to CLIP .....	71
2.2.7	Application of Antialiasing to Microneedle Production.....	78
2.2.8	Selection of Appropriate Build Parameters .....	79
2.2.9	Control Over Microneedle Geometry .....	81

2.3	Conclusions .....	85
2.4	Experimental .....	86
2.4.1	Materials .....	86
2.4.2	TPO Absorption Spectrum.....	86
2.4.3	CLIP Instrument Specifications .....	86
2.4.4	TMPTA Part Fabrication .....	88
2.4.5	Analysis of Antialiasing Algorithms .....	90
CHAPTER 3	Controlled Release of Therapeutics from CLIP Microneedles .....	93
3.1	Introduction .....	93
3.2	Results and Discussion.....	97
3.2.1	Selection of Biocompatible Materials.....	97
3.2.2	Stereolithographic Working Curves .....	100
3.2.3	Derivation of the Working Curve from Beer-Lambert Law.....	101
3.2.4	Application of Working Curves to CLIP .....	102
3.2.5	Adaptation of Working Curves to Microneedle Fabrication .....	106
3.2.6	Production of Biocompatible CLIP Microneedles.....	110
3.2.7	Microneedle Skin Insertion Tests .....	111
3.2.8	Loading and Release of Fluorescent Drug Surrogate .....	113
3.2.9	Dissolvable PAA Microneedles Release Cargo in Skin .....	115
3.2.10	Production and Skin Testing of Tip-Loaded Microneedles .....	117

3.2.11	Biocompatibility Testing .....	119
3.3	Conclusions .....	128
3.4	Experimental .....	130
3.4.1	Synthesis of Polycaprolactone Trimethacrylate.....	130
3.4.2	Determination of Critical Exposure .....	130
3.4.3	Fabrication of Biocompatible Microneedles.....	131
3.4.4	Microneedle Dissolution and Rhodamine Release Studies in Solution.....	132
3.4.5	Skin Penetration Studies .....	132
3.4.6	Characterization of Extractable Fractions.....	134
3.4.7	Cytotoxicity of Photoreactive Monomer and Microneedle Arrays.....	134
CHAPTER 4	Microneedle Mechanical Properties and Skin Penetration .....	138
4.1	Introduction .....	138
4.2	Results and Discussion.....	141
4.2.1	Skin Penetration of Biocompatible Microneedles on Murine Skin .....	141
4.2.2	Fabrication of PEG Microneedles with Varying Crosslink Density.....	142
4.2.3	Mechanical Properties of PEG Blends.....	145
4.2.4	Quantification of Microneedle Insertion Forces .....	148
4.2.5	Percent Insertion as a Function of Composition and Applied Force .....	150
4.2.6	Depth of Penetration vs. Force.....	157
4.3	Conclusion.....	163

4.4	Experimental .....	163
4.4.1	Identification of PEG Microneedle Build Parameters .....	163
4.4.2	Fabrication of PEG Microneedles.....	164
4.4.3	Mechanical Testing of PEG Blends .....	164
4.4.4	Gel Fraction and Solvent Uptake.....	165
4.4.5	Quantification of Force of Thumb .....	165
4.4.6	Skin Insertion Tests.....	166
4.4.7	Optical Coherence Tomography (OCT) .....	166
CHAPTER 5	Conclusions and future directions .....	171
5.1	Continuous Liquid Interface Production on the Micron Scale.....	171
5.2	Continuous Liquid Interface Production of Materials for Release of Therapeutics ....	173
5.3	Development of Biocompatible CLIP Matrices.....	175
5.3.1	Biocompatibility of (Meth)acrylate Based Chemistry .....	175
5.3.2	Alternatives to Meth(acrylate) Based Chemistry.....	178
5.3.3	Role of Photoinitiators .....	178
5.3.4	Characterization of Products and Degradation Products .....	179
5.4	Incorporation of Therapeutic Cargo .....	180
5.5	Microneedle Mechanics .....	180
5.6	CLIP Microneedles for the Advancement of Transdermal Drug Delivery .....	181

APPENDIX A	Continuous Lua Script.....	171
APPENDIX B	Modeling of Small Scale CLIP Parts.....	172

## LIST OF FIGURES

Figure 1.1 Structure of the skin A) Structure of full thickness skin B) Structure of the Epidermis. Reproduced with permission from reference 19.....	5
Figure 1.2 Growth and therapeutic targets of microneedle technology. A) Number of publications involving microneedle technology annually. B) Number of publications delivering a therapeutic to treat various indications between 1998 and 2014. Data compiled from Thomson Reuters Web of Science™ .....	9
Figure 1.3 Microneedle configurations. The method of application and drug release for each of four different microneedle configurations. Figure adapted from reference 19.....	11
Figure 1.4 Distribution of microneedle compositions in literature from 1998-2014. Data compiled from Thompson Reuters Web of Science™ .....	12
Figure 1.5 Frequency of microneedle fabrication techniques and microneedle compositions A. Fabrication techniques utilized in microneedle publications released between 1998 and 2014 B. Frequency of each microneedle configuration over the same time period. Data compiled from Thompson Reuters Web of Science™ .....	14
Figure 1.6 Advantages and disadvantages of each microneedle configuration .....	15
Figure 1.7 Percentage of each microneedle configuration in literature over time. Data is presented as the number of publications released of a particular composition divided by the total number of microneedle publications in that year. Data prior to 2003 is not presented due to the small number of microneedle publications over this time period. Data compiled from Thompson Reuters Web of Science™ .....	16
Figure 1.8 Microneedle masters produced using traditional techniques. Microneedle masters have been produced using A) Cryogenic deep reactive ion etching of silicon <sup>29</sup> B) Wet etching of silicon <sup>93</sup> C) Laser ablation <sup>34</sup> and D) Tilted UV photolithography .....	19
Figure 1.9 Relationship between microneedle design parameters and therapeutic efficacy .....	22

Figure 1.10 Overview of the additive manufacturing process. A computer model is computationally sliced into individual layers. Each two dimensional (2D) layer is stacked on top of the previous layer to create the desired three-dimensional part (3D) .....	26
Figure 1.11 Types of additive manufacturing. A) Fused deposition modeling, B) laser sintering, C) polyjet, and D) stereolithography are different types of additive manufacturing that form solid parts via either a thermal or photochemical phase transition. Images reproduced with permission from references 121-124.....	27
Figure 1.12 Digital light processing (DLP) chip. A) Scanning electron micrograph (SEM) of a DLP chip showing the array of micromirrors B) Schematic showing mechanism for turning each “pixel” or micromirror on and off. Images reproduced with permission from reference 120 and 150, respectively .....	29
Figure 1.13 Layer by layer results in tradeoff between fabrication time and resolution .....	30
Figure 1.14 Microneedles produced via additive manufacturing A-C) Microneedle produced by Lu et. al. D-G) Microneedles produced by Narayan and coworkers. Images reproduced with permission from references 133 and 135 .....	33
Figure 1.15 Differences between stereolithography and CLIP.....	34
Figure 2.1 CLIP schematic A) The continuous CLIP process eliminates the tradeoff between slice thickness and fabrication time to enable rapid production of high resolution parts B) Diagram showing the essential components of a CLIP system .....	46
Figure 2.2 Representative image of a computationally sliced microneedle patch. Several microneedle array cross-sections moving from the A) microneedle patch backing, through B-F) the base and tip of the microneedles within the array. Note that only a small number of the thin cross-sections are displayed.....	48
Figure 2.3 Ray diagram of an object imaged by a double convex lens .....	50
Figure 2.4 Airy Disk. An airy disk is the point spread function of a diffraction-limited lens.....	52
Figure 2.5 Beam width is minimized at the focal plane but is wider than the point predicted by ray optics .....	53

Figure 2.6 Mechanism of free radical photopolymerization of acrylates. Figure reproduced with permission from reference 6. ....	56
Figure 2.7 CLIP file path .....	58
Figure 2.8 Structure and absorbance of resin components A) Structure of TMPTA B) Structure of TPO and C) Absorption spectrum of TPO over wavelengths of 260 to 450nm .....	59
Figure 2.9 Microneedle CAD file. A CAD File of an 8x8 array of 1000 $\mu$ m tall microneedles measuring 333 $\mu$ m in width spaced at 333 $\mu$ m on a 1mm thick backing was used throughout chapter 2 .....	60
Figure 2.10 Impact of light intensity and build speed on microneedle morphology. Top row is produced using 1 mW/cm <sup>2</sup> of light at build speeds of A) 25mm/hr, B) 100 mm/hr, and C) 200 mm/hr. Bottom row is produced using 4 mW/cm <sup>2</sup> of light at build speeds of D) 25 mm/hr E) 100 mm/hr and F) 200 mm/hr .....	61
Figure 2.11 Effect of lens focal length on resolution. The top row is fabricated using an initial, low resolution lens setup with focal lengths of 50 and 75mm at A) 50 mm/hr B) 100mm/hr and C) 150 mm/hr. The bottom row is fabricated using a high resolution lens setup with focal lengths of 75 and 100mm at D) 50 mm/hr E) 100 mm/hr and F) 150 mm/hr G) CAD file used to print the RTP. ....	62
Figure 2.12 Circularity calculation and validation A) Method for calculating circularity. Circularity of 500 $\mu$ m squares printed with B) 2 mW/cm <sup>2</sup> , C) 4 mW/cm <sup>2</sup> , D) 6 mW/cm <sup>2</sup> and E) 8 mW/cm <sup>2</sup> of light. Minimizing circularity results in improvements in the quality of the 500 $\mu$ m square .....	65
Figure 2.13 Circularity improves with improved printer optics A) Method for calculating circularity. Circularity of 500 $\mu$ m squares printed with B) 2 mW/cm <sup>2</sup> , C) 4 mW/cm <sup>2</sup> , D) 6 mW/cm <sup>2</sup> and E) 8 mW/cm <sup>2</sup> of light. Minimizing circularity results in improvements in the quality of the 500 $\mu$ m square .....	64
Figure 2.14 TMPTA Microneedles produced using different light intensities. Microneedles were produced using A) 2mW/cm <sup>2</sup> , B) 5mW/cm <sup>2</sup> , C) 8mW/cm <sup>2</sup> , D) 11mW/cm <sup>2</sup> , and E) 14mW/cm <sup>2</sup> of UV light. Build speed was held constant at 100mm/hr. Scale bars measure 500 $\mu$ m .....	67

Figure 2.15 Dimensions of TMPTA microneedles produced with varying light intensity. The dotted red line represents the height of the CAD file. The dotted blue line represents the width of the CAD file. Error bars represent the mean $\pm$ SD (n=3).....	68
Figure 2.16 Discrete pixels may produce stairstepping .....	69
Figure 2.17 Height of stair step vs. aspect ratio A) SEM image of microneedles of aspect ratios 2, 3, and 4, where each horizontal line is an undesirable “stair-step”. B) Comparison of the experimental step height between horizontal lines as compared to the theoretical step height calculated using Equation 1. Error bars represent the mean $\pm$ SD (n=3). Scale bar measures 500 $\mu$ m. ....	71
Figure 2.18 Visible effects of spatial imagealiasing. The desired image is distorted by spatial sampling at each pixel, causing the display to contain an alias, or distortion of the original signal. Reproduced with permission from reference 2. ....	71
Figure 2.19 Effect of system focus on microneedle structure. Microneedles of three different aspect ratios are fabricated A) In focus, with the lens at its focal point B) with the lens 2mm below its focal point and C) with the lens 4 mm below its focal point. Scale bars measure 500 $\mu$ m. ....	73
Figure 2.20 Supersampling of typeface letter A. A) An aliased version of typeface letter A has jagged edges B) Supersampling the typeface letter visibly improves resolution. Reproduced with permission from reference 10. ....	73
Figure 2.21 Comparison of GDI and GDI+ Grayscale Assignments .....	75
Figure 2.22 Grayscale Assignments for a 2x2 Pixel Object Shifted by One Half Micromirror. A) Grayscale value resulting from use of the GDI+ Interface B) Grayscale value resulting from use of the GDI Interface. An outline of the original object is provided in red. ....	77
Figure 2.23 Difference Between Windows GDI+ and Windows GDI Projections of Microneedle Crosssections.....	77
Figure 2.24 TMPTA Microneedles produced using Windows GDI. Microneedles were produced using A) 2mW/cm <sup>2</sup> , B) 5mW/cm <sup>2</sup> , C) 8mW/cm <sup>2</sup> , D) 11mW/cm <sup>2</sup> , and E) 14mW/cm <sup>2</sup> of UV light. Build speed was held constant at 100mm/hr. Scale bars measure 500 $\mu$ m. ....	78

Figure 2.25 Microneedle Dimensions vs. Light Intensity Using Windows GDI. Error bars represent the mean $\pm$ SD (n=3). .....	79
Figure 2.26 1000 $\mu$ m tall TMPTA Microneedles Produced Using CLIP. A) Image of CLIP Microneedles showing sharp tip radius B) Dimensions and fabrication time for microneedles in Figure A. Data are represented as mean $\pm$ SD .....	80
Figure 2.27 CLIP MNs of Different Heights MNs produced from a CAD file measuring A) 1000 $\mu$ m tall and 333 $\mu$ m wide, B) 700 $\mu$ m tall and 233 $\mu$ m wide, and C) 400 $\mu$ m tall and 133 $\mu$ m wide. D) Dimensions of all MNs show truncation in z direction, but minimal shrinkage in the x-y direction. Data are presented as mean $\pm$ SD (n=9). Scale bars measure 500 $\mu$ m. ....	82
Figure 2.28 TMPTA Microneedles of Different Shapes A) TMPTA microneedles of aspect ratio 2, 3, and 4 (left to right). 1000 $\mu$ m tall TMPTA microneedles with spacing of B) 0.5 base widths and C) 1.5 base widths. Complex microneedle geometries such as D) Arrowhead microneedles E) Tiered microneedles and F) Turret microneedles may improve mechanics of insertion into the skin. Scale bars measure 500 $\mu$ m .....	84
Figure 3.1 Advantage of Controlled Release Systems. Controlled release systems reduce fluctuations in drug concentrations to keep drug concentrations within the therapeutic window. Reproduced with permission from reference 8. ....	94
Figure 3.2 Structure of Monomers Utilized for Microneedle Fabrication A) Polyethylene glycol 550 dimethacrylate, n=9 B) Polycaprolactone trimethacrylate, n=2 C) Acrylic acid.....	100
Figure 3.3 Traditional working curve used in stereolithography. Reproduced with permission from reference 20. ....	101
Figure 3.4 Traditional working curve used in stereolithography. Reproduced with permission from reference 1. ....	101
Figure 3.5 CLIP working curves enable part production A) Method for producing working curve. B) Working curve generated on a CLIP system. Figures are reproduced with permission from reference 3. ....	103

Figure 3.6 Appropriate Build Parameters are Size Dependent on Small Scale. TMPTA test parts fabricated with A) 1mW/cm <sup>2</sup> of light at 50mm/hr B) 2mW/cm <sup>2</sup> of light at 100mm/hr and C) 4mW/cm <sup>2</sup> of light at 200mm/hr. D) CAD file of the test part with 1mm tall microneedles with base widths ranging from 100µm to 500 µm and a large square measuring 4mmx1mmx1mm. E) Percent reduction (percent error) in height of all structures in A-C .....	105
Figure 3.7 Stereolithographic Working Curve and Resin Properties. A) The cure depth of microneedle resins as a function of applied dosage B) Absorption coefficient and critical exposure of microneedle resins determined from the working curves in figure A .....	107
Figure 3.8 Dimensions of Biocompatible MNs Produced Using Parameters from Working Curve. Height and width of TMPTA, PEG, PCL, and PAA microneedles. Intended dimensions are marked with a dotted line. PAA microneedle height and width were determined to be significantly different from all other compositions at a p<0.0001 significance level. Data are presented as mean ± SD .....	109
Figure 3.9 Biocompatible microneedles. ESEM images of A) Polyethylene glycol B) Polycaprolactone and C) Polyacrylic acid microneedles measuring approximately 1000µm in height and 333µm in width D) Dimensions, print times, and tip radii of biodegradable microneedles (n=9) shown in Figure 3. Scale bars measure 500µm. All data are represented as mean ± SD .....	110
Figure 3.10 Skin insertion tests. Sites of skin penetration from CLIP Microneedle arrays made of A) PCL B) TMPTA C) PEG and D) PAA on murine skin can be visualized using a tissue marking dye. E) No insertion sites are visualized on a piece of control skin to which no microneedles were applied. Scale bars measure 1mm. ....	111
Figure 3.11 Rhodamine loaded CLIP MNs. Incorporation of rhodamine does not alter structure of A) PEG, B) PCL or C) PAA MNs characterized by ESEM. Rhodamine distributes throughout D) PEG, E) PCL, and F) PAA MNs needles visualized via confocal microscopy. The rhodamine channel is displayed in purple. Scale bars measure 500µm. ....	113
Figure 3.12 Rhodamine release rates Rates of rhodamine release from A) PEG, PCL and B) PAA MNs loaded with 0.1wt% rhodamine.....	114
Figure 3.13 Dissolution of Rhodamine Containing PAA Microneedles .....	115

Figure 3.14 Ex-vivo skin penetration and dye release. H&E stained skin sections show A) epidermal breach upon application of PAA microneedles but B) no epidermal breach in untreated control. C) The application of rhodamine containing polyacrylic acid microneedles releases rhodamine into the skin. D) No fluorescence is visualized in sections to which no microneedles were applied. All scale bars measure 100 $\mu$ m. ....	116
Figure 3.15 Tip loaded CLIP microneedles. The base of the microneedle is composed of PCL and rhodamine. The tip of the microneedle is composed of polyacrylic acid encapsulating fluorescein as a fluorescent drug surrogate. Scale bar measures 500 $\mu$ m. ....	117
Figure 3.16 Tip-loaded CLIP microneedles release entire payload in skin. Scale bars measure 1mm. ....	119
Figure 3.17 Microneedle transwell study. A) Diagram of experimental design, which shows the microneedle containing porous transwell incubating in a cell culture plate B) MTT Assay for A549 cells incubating with one PEG, PCL, or PAA microneedle patch over 24 to 72 hr.....	121
Figure 3.18 Cell viability of A549 and HuVEC cells incubated with A) PEG and B) PCL MNs over 24, 48, and 72 h. Data are presented as mean $\pm$ SD with n=3 wells per timepoint.....	122
Figure 3.19 Oligomer toxicity and IC <sub>50</sub> values. A) Toxicity of monomers on A549 cells B) Toxicity of monomers on HuVEC cells C) IC <sub>50</sub> values of monomers on A549 and HuVEC cells. Concentrations are given as volume of monomer divided by total solution volume.....	123
Figure 3.20 Soluble and low molecular weight fraction of PEG, PCL, and PAA MNs.....	125
Figure 3.21 Cytotoxicity of Purified and Unpurified PAA MNs. Unpurified MNs were tested directly after printing plus a brief acetone wash. Purified MNs were tested after the brief acetone wash plus post cure plus 48 hours of heating at 120°C for 48 hr.....	126

Figure 3.22 Reaction scheme for PCL-trimethacrylate synthesis. PCL was functionalized by reacting hydroxyl groups from a PCL-triol with methacryloyl chloride. <sup>1</sup> H NMR spectrum confirms methacrylate functionalization with peaks at 6.08 (c), 5.54 (b) and 1.93 ppm (d). Degree of functionalization was determined to be 89% by comparing the peak areas corresponding to the vinyl protons (c and b, 6.08 and 5.54 ppm) to the protons of the methyl group in the PCL backbone (a, 0.89 ppm).....	130
Figure 4.1 Typical Stress-Strain Curve.....	139
Figure 4.2 Skin Penetration on Murine and Porcine Skin A) PAA, B) TMPTA, C) PCL, and D) PEG CLIP microneedles effectively pierce murine skin, but the E) negative control shows no sites of penetration. F) PAA and G) TMPTA microneedles effectively pierce porcine skin, but H) PCL microneedles, I) PEG microneedles and J) the negative control show no sites of penetration. Scale bars measure 1mm. ....	141
Figure 4.3 Stereolithographic Working Curve and Resin Properties for PEG Blends. A) The cure depth of microneedle resins as a function of applied dosage B) Absorption coefficient and critical exposure of microneedle resins determined from the working curves in figure A. The build parameters for each resin were calculated as described in Chapter 4 and are also listed. ....	143
Figure 4.4. CLIP Microneedles Fabricated from PEG Blends. CLIP Microneedles are fabricated from A) Neat PEG550-dMa and B)50-50, C)67-33, D) 59-41, and E)50-50ratios of PEG550-dMa to EG-dMa. All formulations are mixed with 2.5wt% TPO as a photoinitiator. Scale bars measure 500μm.....	144
Figure 4.5 Mechanical Properties of PEG Blends. A) Young’s moduli, B) Failure stress and C) Strain at failure for all PEG blends. Failure stress and strain at failure were determined using a zero slope method. Data are presented as mean ±SD (n=3).....	146
Figure 4.6 Gel Fraction and Solvent Uptake of PEG Networks. Cylindrical test samples and microneedle patches were found to have similar A) gel fractions and B) solvent uptakes. Data are presented as mean ± SD (n=3). ....	147
Figure 4.7 Study Design for Quantifying Force of Thumb .....	148

Figure 4.8. Quantification of Force of Thumb. A) Force vs. time curves for ten participants applying microneedle patches to porcine skin B) Quantification of the force applied by each of ten participants directly to the microneedle patch and to the compression plates. These forces correspond to the diagram in Figure 5.7 B and C, respectively C) Rate at which the force is applied and released from the microneedle patch for each of the ten participants ..... 149

Figure 4.9 PEG Microneedle Arrays After Application with 75N Force. Microneedles composed of A) PEG550dMa, B)PEG550dMa-EGdMa 75-25, C) PEG550dMa-EGdMa 67-33, D) PEG550dMa-EGdMa 5941, E) PEGdMa-EGdMa 50-50, and F) PEG550dMa-EGdMa 75-25 remain intact after application. Scale bars measure 500 $\mu$ m. .... 151

Figure 4.10 Assessment of Percent Insertion Using Tissue Marking Dye. Some microneedles arrays A) do not insert into the skin, B) partially insert into the skin or C) completely insert into the skin. Percent penetration is taken by dividing the number of penetration sites visualized by the total number of microneedles in an array (64 microneedles). Scale bars measure 1mm. .... 152

Figure 4.11 Percent of needles that puncture skin as a function of insertion force. Arrays of 64 microneedles composed of a variety of PEG blends were applied to porcine skin ex vivo with A) 6N, B) 12.5N, C) 25N, or D) 75N of force. Data is presented as mean  $\pm$ SD (n=6) of the percent of microneedles inserting into skin, calculated by dividing the number of insertion sites by the total number of microneedles in the array. The dotted line represents 90% of microneedles inserting into the skin. .... 154

Figure 4.12 OCT Experimental Setup and Images. A) Images were obtained by pointing the laser through the backing of the applied microneedle patch into skin. B) HH image of blank microneedle array in porcine skin. C) HV-HH overlay of microneedle array containing GNRs ..... 158

Figure 4.13 Depth of Penetration of PEG Blends. A) Depth of penetration of microneedle arrays as determined by OCT. B) The same data is given numerically. Data are presented as mean $\pm$ SD between arrays (n=3 arrays), where the average penetration depth for each array is calculated from n=32 needles on that array. .... 159

Figure 4.14 Process of microneedle penetration into the skin. Adapted from reference 34. .... 162

Figure 5.1 Methacrylate monomers and oligomers used commercially ..... 176

Figure 5.2 Methacrylate monomers and oligomers utilized in commercial products..... 176

## LIST OF TABLES

Table 1.1 Generations of Transdermal Drug Delivery .....	2
Table 1.2 List of medications FDA approved for systemic delivery using a transdermal patch. Table adapted from reference 11.....	3
Table 1.3 Advantages of Transdermal Drug Delivery .....	4
Table 1.4 Force Required for Microneedle Insertion as a function of spacing between needles, the total number of microneedles per array, and the velocity of insertion. Forces are given as both Newtons per array and Newtons per microneedle on that array. Table adapted from reference 112. ....	25
Table 2.1 Comparison of GDI and GDI+ Pixel Grayscale Assignments .....	75
Table 2.2 MNs of Different Heights Truncate without Z Scale Factor. Dimensions of all MNs show truncation in z direction, but minimal shrinkage in the x-y direction. Data are presented as mean±SD, n=9.....	82
Table 2.3 CLIP 3 Specifications .....	87
Table 2.4 CLIP 7 Specifications .....	88
Table 3.1 Build Parameters for Biocompatible CLIP Microneedles .....	110
Table 3.2 Comparison of Extractable Fractions and Monomer IC50 values. When complete release of the extractable fraction produces concentrations (row 1) that are higher than the IC50 value, the IC50 value is shown in red. When complete release of the extractable fraction produces concentrations (row 1) that are lower than the IC50 value, the IC50 value is shown in green. ....	127
Table 4.1 Composition of PEG Blends Utilized in Chapter 5 .....	142
Table 4.2 Dimensions of CLIP Microneedles Fabricated with PEG Blends. Data are presented as mean ±SD (n=9). No statistically significant difference in microneedle dimensions were found. Statistics were performed via one way ANOVA with Tukey’s honestly significantly different (HSD) post-test .....	145

## LIST OF ABBREVIATIONS AND SYMBOLS

3D	three dimensional
A	area
$\alpha$	absorption coefficient
AA	acrylic acid
ABS	acrylonitrile butadiene styrene
API	active pharmaceutical ingredient
AR	aspect ratio
ASTM	American Society of the International Association for Testing and Materials
Bis-GMA	2,2-bis[4-(2-hydroxy-3-methacryloyloxypropyl)phenyl]propane
BSA	bovine serum albumin
c	speed of light
$C_T$	cured thickness
CAD	computer aided design
CLIP	Continuous Liquid Interface Production
cm	centimeter
CMC	carboxymethylcellulose
CQ	camphorquinone
D	lens aperature
d	distance
$d_i$	distance to an image
$d_o$	distance to an object

DCM	dichloromethane
DLP	digital light processing
dMa	dimethacrylate
DNA	deoxyribonucleic acid
DPI	dots per inch
DSC	differential scanning calorimetry
E	strain (Chapter 4)
E	exposure (all other chapters and appendices)
$E_c$	critical exposure
EDHA	electrohydrodynamic atomization
Erf	error function
ESEM	environmental scanning electron microscopy
DRIE	deep reactive ion etching
F	force
f	focal point
FDA	Food and Drug Administration
FDM	fused deposition modeling
FEI	Field Electron and Ion Co.
G	grayscale value
GA	glycolic acid
GDI	graphic device interface
GNR	gold nanorod
GPa	gigapascal

GPC	gel permeation chromatography
GRAS	generally recognized as safe
h	height
h <sub>o</sub>	height of an object
h <sub>i</sub>	height of an image
<sup>1</sup> H NMR	proton nuclear magnetic resonance
HCl	hydrochloric acid
HEMA	hydroxyethyl methacrylate
HH	horizontal, horizontal polarization
HIV	human immunodeficiency virus
HP	Hewlett-Packard
hr	hour
HuVEC	human umbilical vein endothelial cells
HV	horizontal, vertical polarization
hν	light
Hz	Hertz
I	initiator species (Chapter 2)
I	light intensity (all other chapters and appendices)
IACUC	Institutional Animal Care and Use Committee
IC <sub>50</sub>	half maximal inhibitory concentration
Inc.	Incorporated
ISO	International Organization for Standardization
k <sub>d</sub>	rate constant for initiator dissociation

$k_p$	rate constant for polymerization
kPa	kilopascal
KOH	potassium hydroxide
LA	lactic acid
LED	light emitting diode
ln	natural logarithm
M	magnification (Chapter 2)
M·	monomer containing free radical
[M]	concentration of monomer
MA	maleic anhydride
MAcCl	methacryloyl chloride
MED	minimum effective dose
MeOH	methanol
min	minute
mJ	millijoule
mL	milliliter
mm	millimeter
MMA	methyl methacrylate
mN	millinewton
MN	microneedle
mol	mole
MPa	megapascal
MTD	maximum tolerated dose

mW	milliwatt
MW	molecular weight
N	Newton
n	number
NaOH	sodium hydroxide
nm	nanometer
NMR	nuclear magnetic resonance
NSAIDs	nonsteroidal anti-inflammatory drugs
OCT	optical coherence tomography
PAA	polyacrylic acid
PBS	phosphate buffered saline
PC	polycarbonate
PCL	polycaprolactone
PCL1110-tMa	polycaprolactone 1110 trimethacrylate
PDMS	polydimethylsiloxane
PEG	polyethylene glycol
PEG550-dMa	polyethylene glycol 550 dimethacrylate
PEG-dMa	polyethylene glycol dimethacrylate
PLA	polylactic acid
PLGA	poly(lactide-co-glycolide)
ppm	parts per million
PSF	point spread function
PS-SD-OCT	polarization sensitive spectral domain optical coherence tomography

PVA	polyvinyl alcohol
PVME	polymethylvinyl ether
PVP	polyvinylpyrrolidone
r	radius
R·	free radical
R <sub>i</sub>	rate of initiation
R <sub>p</sub>	rate of polymerization
R&D	research and development
RGB	red green blue
RPMI	Roswell Park Memorial Institute medium
r.t.	room temperature
RTP	resolution test pattern
s	second
SD	standard deviation
SEM	scanning electron micrograph
SLA	stereolithography
SLS	selective laser sintering
STL	standard tessellation language
SVG	scalable vector graphics
t	time
TEA	triethanolamine
TEGMA	triethyleneglycoldimethacrylate
TMAH	tetramethylammonium hydroxide

TMPTA	trimethylolpropane triacrylate
TPO	diphenyl (2,4,6- trimethylbenzoyl) phosphine oxide
u	scalar function of a wave
UDMA	1,6-bis-[2-methacryloxyethoxycarbonylamino]-2,4,4-trimethyl hexane
UNC	University of North Carolina
UV	ultraviolet
v	volume
W	width
$W_i$	initial weight
$W_s$	weight after solvent uptake
$w_0$	radius of a Gaussian light distribution
wt	weight
X	unspecified chemical compound
z	distance or coordinate along the z axis
$z_R$	Raleigh length
°C	degrees Celsius
%	percent
®	registered
$\lambda$	wavelength
$\mu\text{L}$	microliter
$\mu\text{m}$	micrometer
$\sigma$	stress
$\phi$	initiator efficiency

## **CHAPTER 1 MICRONEEDLE TECHNOLOGY FOR TRANSDERMAL DRUG DELIVERY**

### **1.1 Transdermal Drug Delivery**

#### **1.1.1 Drug Delivery Market**

The discovery and development of new therapeutics is a massive effort, both in the United States and abroad. Major pharmaceutical companies in the United States spend approximately \$50 billion dollars in collective annual R&D spending, with an average cost to market of a new molecular entity averaging \$1.8 billion dollars.<sup>1</sup> Pharmaceutical sales in the United States account for approximately 40% of global sales, which are estimated at a formidable \$1.1 trillion dollars.<sup>2</sup> The ability to deliver these valuable active pharmaceutical agents (APIs) to their site of action within the body is critical to their therapeutic efficacy, but drug delivery remains a substantial challenge.<sup>3</sup> Although oral delivery is the most widely utilized route of administration, many drugs suffer from poor oral bioavailability<sup>1</sup> due to a variety of factors including poor solubility, degradation within the gastrointestinal tract, poor absorption through the stomach wall, and first pass metabolism in the liver and spleen<sup>4</sup>. These challenges are particularly significant for the delivery of protein and nucleic acid based therapeutics, which accounted for 71% of revenue for the top ten selling pharmaceutical products in 2012.<sup>5</sup> Many strategies have been utilized to increase bioavailability, including computational approaches designed to improve drug properties (solubility, potency, toxicity, etc.),<sup>6,7</sup> chemical modifications such as pro-drugs,<sup>8</sup> and more sophisticated formulations, such as nanoparticles and polymer-drug conjugates.<sup>9</sup> Despite advancements in these areas, many drugs can still only be delivered via intravenous, subcutaneous, or intramuscular injections with a hypodermic needle.

### 1.1.2 First Generation Transdermal Drug Delivery

One alternative to hypodermic injections is transdermal drug delivery, wherein a therapeutic of interest is delivered through the skin. Transdermal drug delivery has the potential to improve bioavailability by enabling drugs to traffic directly through the skin and into the blood stream, bypassing the stomach, liver, and spleen.<sup>10-13</sup> The transdermal drug delivery market is estimated at \$30 billion dollars globally, making up over 12% of the total drug delivery market.<sup>11</sup>

The advancement of transdermal drug delivery technologies has been described as having three evolutionary “generations”,<sup>10</sup> as shown in Table 1.1. First generation transdermal drug delivery refers to any transdermal drug delivery technology that introduces an API to systemic circulation via passive diffusion through the skin. It should be noted that ointments and creams used for the treatment of local skin conditions, such as sunscreen, antibiotics used to treat acne and other skin-laden bacterial infections, and corticosteroids used for psoriasis, eczema, and dermatitis are topical treatments, not transdermal delivery systems because they do not seek to deliver the API into systemic circulation. In 1979, the first transdermal patch was FDA approved for the delivery of scopolamine to treat motion sickness.<sup>11</sup> Transdermal patches are drug-containing matrices (solid, liquid, or gel) attached to an adhesive backing. Since this time, 19 different drugs have

**Table 1.1 Generations of transdermal drug delivery**

Generation	Definition	Examples
First	Relies on passive diffusion of the therapeutic into the skin	<ul style="list-style-type: none"><li>• Traditional transdermal patches</li></ul>
Second	Alters chemical or electrical gradient to aid diffusion into the skin	<ul style="list-style-type: none"><li>• Chemical enhancers</li><li>• Iontophoresis</li></ul>
Third	Physically disrupts the stratum corneum to allow a wider range of therapeutics to pass into the skin	<ul style="list-style-type: none"><li>• Cavitation ultrasound</li><li>• Jet injection</li><li>• Microdermabrasion</li><li>• Microneedles</li></ul>

**Table 1.2 List of medications FDA approved for systemic delivery using a transdermal patch.** Table adapted from reference 11.

Year	Drug	Indication
1979	Scopolamine	Motion sickness
1984	Clonidine	Hypertension
1986	Estradiol	Menopausal symptoms
1990	Fentanyl	Chronic pain
1991	Nicotine	Smoking cessation
1993	Testosterone	Testosterone deficiency
1998	Nitroglycerin	Angina pectoris
1999	Lidocaine	Pain
2001	Ethinyl estradiol/norelgestromin	Contraception
2003	Estradiol/levonorgestrel	Menopause
2003	Oxybutynin	Overactive bladder
2006	Methylphenidate	ADHD
2006	Selegiline	Depression
2007	Diclofenac epolamine	Pain
2007	Rivastigmine	Dementia
2008	Granisetron	Chemo-induced emesis
2009	Capsaicin	Pain
2010	Buprenorphine	Pain
2012	Rotigotine	Parkinson's disease

been FDA approved for systemic delivery using transdermal patches; a list of these medications is provided in Table 1.2.<sup>11</sup> Transdermal patches delivering nicotine for smoking cessation and ethinyl estradiol/norelgestromin for contraception have been particularly successful commercial products that are now commonly used.<sup>11</sup> Over one billion transdermal patches are now manufactured annually.<sup>10</sup>

Delivery of medication using transdermal patches has several inherent benefits (Table 1.3). Unlike typical hypodermic injections, transdermal patches allow for pain-free drug delivery and can be self-administered without trained medical personnel.<sup>11</sup> Most transdermal patches

**Table 1.4 Advantages of transdermal drug delivery**

<b>Advantages of Transdermal Drug Delivery</b>
Avoids first pass metabolism
Pain free
Potential for self-administration
Improved patient compliance
Eliminates sharp, biohazardous waste
No risk of needle re-use

enable sustained release of the drug out of the patch to reduce required dosing frequency; one patch application can be equivalent to days or weeks of daily oral medication.<sup>13</sup> For these reasons, delivery of medication using transdermal patches typically results in increased patient compliance when compared to other routes of administration. For example, a recent study of elderly patients with hypertension demonstrated that patients correctly applied a single transdermal patch 96% of the time, whereas daily oral medication was taken as directed only 50% of the time.<sup>14</sup> Similar improvements have been reported for contraceptives<sup>15</sup> and for medications used to treat dementia of Alzheimer's type.<sup>16</sup> Moreover, transdermal patches prevent accidental needle injuries by avoiding the generation of sharp, biohazardous wastes.<sup>10</sup>

Despite these clear advantages, the use of first generation transdermal drug delivery technologies has been severely limited by the structure of the skin,<sup>10-13</sup> described in more detail below.

### **1.1.3 Structure of the Skin**

The skin, shown in Figure 1.1A, is composed of three distinct layers: the epidermis, dermis, and adipose tissue<sup>1,2</sup>. The epidermis is the outermost layer of the skin, measuring anywhere from 50-1500µm in thickness,<sup>17</sup> depending on genetic and environmental factors<sup>18</sup> and the area of the body, with the eyelids being the thinnest and the palms and soles of the feet being

the thickest. Depending on the region of the body, the epidermis is composed of up to 5 layers<sup>19-</sup>  
<sup>20-</sup> the stratum basale, stratum spinosum, stratum granulosum, stratum lucidum (only present in  
some regions), and stratum corneum, moving from the inside outward (Figure 1.1B).

The epidermis is constantly replenished through cellular proliferation followed by  
sequential differentiation to generate each stratified layer.<sup>19-21</sup> This differentiation process is  
important because it is the mechanism by which the tough, impermeable outer layer of the skin is  
eventually produced. Differentiation begins with keratinocyte cells in the stratum basale, the  
innermost layer of the epidermis. This layer also contains melanocytes, which are responsible for  
producing pigment, Langerhans cells which are involved in immunity,<sup>22</sup> and Merkel cells which  
are involved in the sensation of touch.<sup>19</sup> In the stratum spinosum, the keratinocytes begin to  
adhere to one another through the formation of desmosomes and to produce polar lipids,  
contained within lamellar vesicles within the Golgi body.<sup>19,21</sup> The stratum spinosum also  
contains a high concentration of Langerhans cells. In the stratum granulosum, keratinocytes lose  
their nuclei and begin to excrete the lipid containing lamellar vesicles into the extracellular

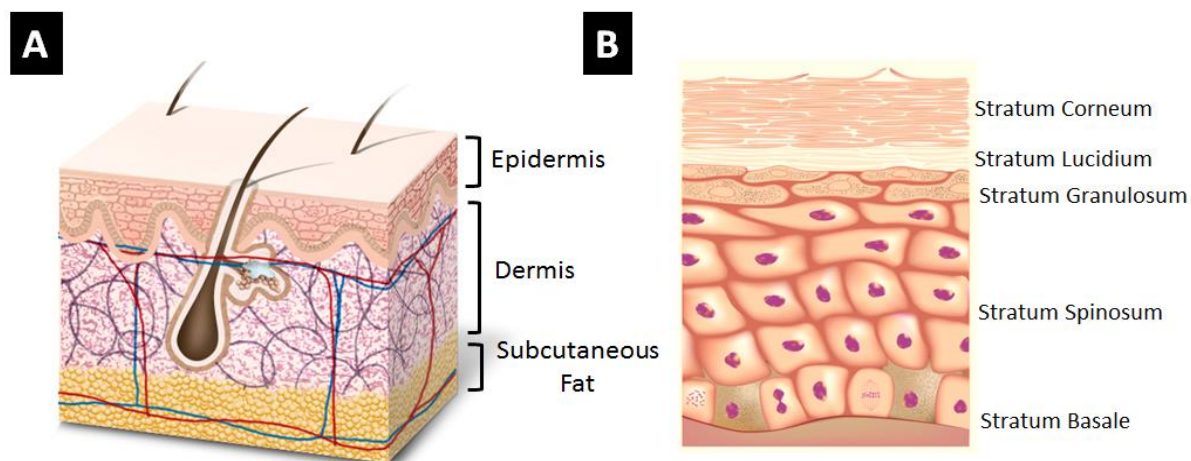


**Figure 1.1 Structure of the skin** A) Structure of full thickness skin B) Structure of the Epidermis. Reproduced with permission from reference 19.

space, where they are converted into nonpolar lipids that prevent water loss into the surrounding environment.<sup>21</sup> Completion of the differentiation process results in the formation of the corneocytes that make up the outermost layer of the skin, called the stratum corneum. The stratum corneum is a densely packed 10-15 $\mu$ m thick layer of dead corneocytes surrounded by the nonpolar fatty acids ceramide and cholesterol.<sup>21</sup> Together, these anucleated cells and extracellular lipids make up a “brick-and-mortar structure” that acts as a formidable barrier against foreign substances only permeated by small, lipophilic substances.<sup>21</sup> For this reason, transdermal drug delivery has traditionally been limited to the delivery of hydrophobic compounds measuring less than 500 Daltons in size.<sup>10-13</sup>

Beneath the epidermis lies the dermis (1-2mm thick), a network of collagen fibers that retains the structural and mechanical integrity of the skin. Unlike the epidermis, which is composed of 95% keratinocytes and a high concentration of T cells,<sup>23</sup> the dermis also contains a network of capillaries, lymphatics, sweat glands, and a high concentration of macrophages, mast cells and resident dermal dendritic cells.<sup>19-21</sup> Below the dermis lies the adipose tissue, laden with fat, blood vessels, and the nerve endings responsible for perception of pain.<sup>19-21</sup>

#### **1.1.4 Advancements in Transdermal Drug Delivery**

Many approaches have been developed to improve the skin’s permeability to therapeutic agents in an effort to enable a wider range of therapeutics to be delivered through the skin.

Langer and Prausnitz have classified these more advanced, technological approaches as second and third generation transdermal drug delivery technologies (see Table 1.1).<sup>10</sup>

Second generation techniques seek to increase the skin’s permeability to a therapeutic by increasing the driving force that enables small molecule therapeutics to pass into the skin. These second generation techniques include chemical enhancers and iontophoresis. Chemical enhancers

are typically amphiphilic molecules utilized to temporarily disrupt the physical structure of the extracellular lipids within the stratum corneum to enable small molecule drugs to more easily pass into the skin.<sup>10-11</sup> Although many chemical enhancers have been utilized, disruption of the skin has a tendency to cause skin irritation; the development of non-irritating enhancers is an ongoing effort.<sup>10-11,24</sup> Iontophoresis, a technique that utilizes an electrical charge gradient to drive small molecules into the skin, has also been successfully utilized,<sup>25</sup> but requires complex medical devices to enable successful delivery.<sup>10</sup>

Third generation technologies seek to physically disrupt the structure of the skin to create pores that allow the therapeutic to more easily enter the body.<sup>10</sup> Although these techniques are reviewed comprehensively elsewhere,<sup>10-11,26-28</sup> some techniques which physically disrupt the skin include cavitation ultrasound, jet injectors, microdermabrasion, and microneedles.<sup>10</sup> Briefly, cavitation ultrasound uses ultrasound, or high frequency sound waves, to generate bubbles in a solution containing a therapeutic. When these bubbles grow to an unstable size, they collapse and create a strong pressure gradient that pushes the solution into skin.<sup>26</sup> This highly pressurized fluid erodes the outer layer of the skin to enable the therapeutic to pass into the body.<sup>26</sup> Similarly, jet injectors create a high velocity fluid stream (>100m/s) using compressed air or a compression stream; this high velocity stream creates pores in the skin measuring between 75µm and 360µm wide to enable the therapeutic to enter the body.<sup>27</sup> Despite over 50 years of development and their ability to enhance bioavailability, jet injectors are not commonly used due to lack of injection reproducibility and their tendency to cause bruising of the skin.<sup>27</sup> Microdermabrasion increases skin permeability by physically sanding away the dead cells that make up the stratum corneum to enable therapeutics to more easily pass into the body.<sup>10,28</sup>

The remainder of this dissertation focuses on transdermal drug delivery using microneedle arrays, which are described in more detail below.

## 1.2 Microneedle Technology

Microneedle technology was developed in the 1990s as a novel way to penetrate the skin for transdermal drug delivery.<sup>29</sup> Microneedles are arrays of sharp, sub-millimeter sized needles (~100-1000 $\mu$ m in length) that physically pierce the stratum corneum to deliver therapeutics into the body.<sup>30</sup> Because these needles create perforations within the skin, they eliminate the need for passive diffusion of the therapeutic through the stratum corneum, thereby allowing therapeutics of any size, ranging from small molecules<sup>31-33</sup> to nanoparticles,<sup>34-35</sup> to enter the body. Because of their small size, microneedles avoid the nerve endings responsible for pain, which are buried deep within the adipose layer, to enable pain free drug delivery.<sup>36-38</sup>

The first report of microneedles was a 1998 publication by the Prausnitz lab which utilized silicon microneedles measuring 150 $\mu$ m in length to increase the permeability of the fluorescent drug surrogate calcein by three to five orders of magnitude.<sup>29</sup> Since this point in time, the microneedle field has expanded rapidly, with 80 microneedle publications in 2014 alone (Figure 1.2A). Microneedles have been utilized to deliver a wide variety of therapeutics, including proteins,<sup>39-40</sup> nucleic acids,<sup>41-42</sup> small molecules,<sup>31-33</sup> and nanoparticles<sup>34</sup> in pre-clinical and clinical studies. Microneedle technology has been applied to the treatment of a number of different indications (Figure 1.2B), including delivery of insulin for the treatment of diabetes,<sup>36,39,43,44</sup> the delivery of nonsteroidal anti-inflammatory drugs (NSAIDs) for the treatment of pain<sup>33, 45-46</sup> and the delivery of chemotherapeutics for the treatment of cancer,<sup>47-48</sup> but the most common application of microneedles has been in vaccine delivery.<sup>49</sup>

Vaccine delivery is an ideal target for microneedle technology for a number of different reasons. Firstly, intradermal vaccination has been associated with improved protection as compared to intramuscular injection.<sup>50-55</sup> The vast majority of literature indicates that vaccine delivery using microneedles induces a dose-sparing response, wherein a lower concentration of antigen delivered with microneedles produces equivalent antibody titers to higher concentrations

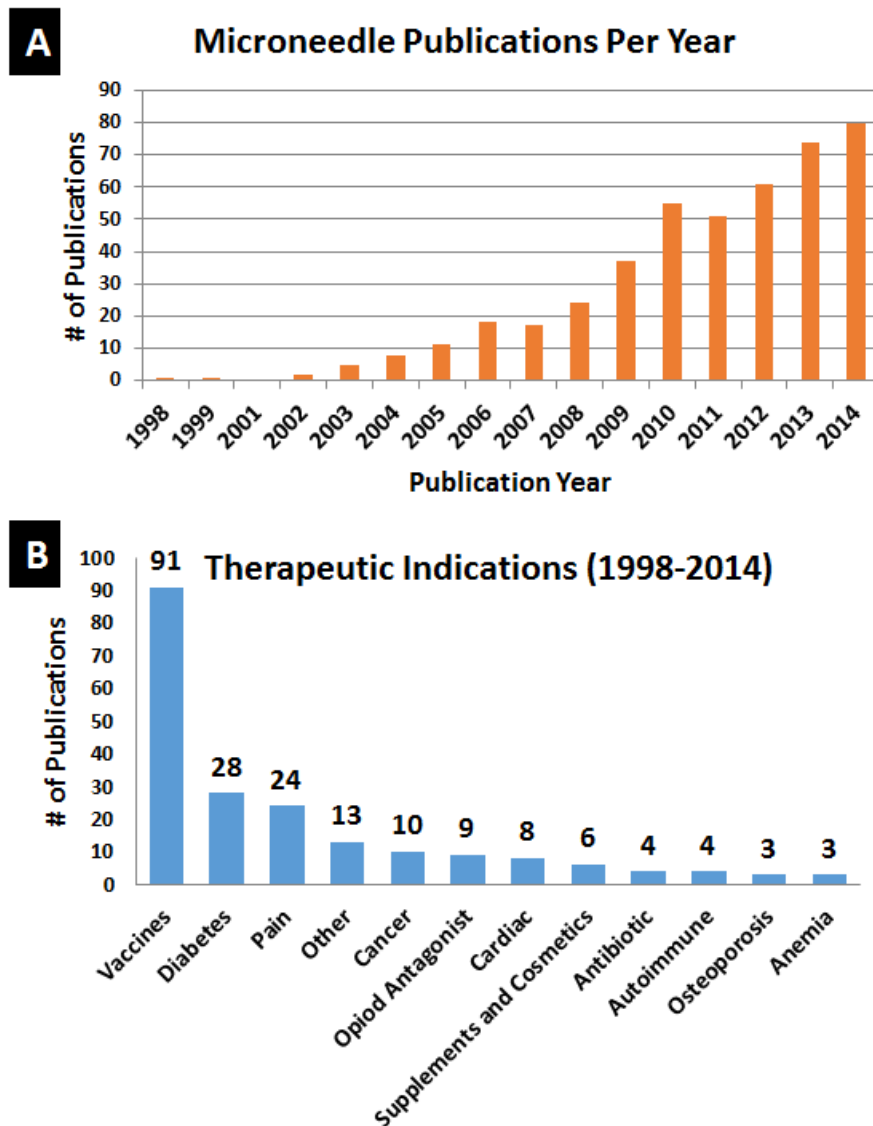


**Figure 1.2 Growth and therapeutic targets of microneedle technology.** A) Number of publications involving microneedle technology annually. B) Number of publications delivering a therapeutic to treat various indications between 1998 and 2014. Data compiled from Thomson Reuters Web of Science™

of intramuscularly administered antigen.<sup>50-53</sup> A limited number of reports indicate higher antibody titers than intramuscular and subcutaneous controls.<sup>54-55</sup>

These improvements in immune response are thought to be due to the convergence of a number of different factors. As mentioned previously, the skin contains a high concentration of immune cells, such as the Langerhans cells and dendritic T cells located in the epidermis.<sup>10-13,??</sup> The ability to specifically target these immune cells using microneedle technology is thought to improve total immune responses.<sup>49</sup> The skin also provides excellent access to the draining lymph node, where activation of dendritic cells, B cells, and T cells occurs.<sup>21,56</sup> This improved lymph node access is thought to be a combination of direct migration of antigen through the skin's extensive network of capillaries and lymphatics and efficient migration of innate immune cells (such as dendritic cells, macrophages, and mast cells) resulting from chemokine signaling in the skin.<sup>21,56,57</sup> Although a number of different investigators have suggested that improved immune responses are also the result of unique properties of Langerhans dendritic cells located into the skin, the role of Langerhans dendritic cells is largely unproven and is a subject of continuing investigations.<sup>56-58</sup>

In addition to these improvements in immune response, many microneedle formulations are stable at room temperature over months at a time.<sup>49,59-60</sup> This enhanced stability has the potential to eliminate the need for refrigeration in each step of the global vaccine distribution supply chain to improve vaccine access in remote or under-resourced locations.<sup>49,59-60</sup> To this end, microneedles have been investigated as a promising approach for vaccination against seasonal<sup>61</sup> and pandemic influenza,<sup>62</sup> measles,<sup>63</sup> polio,<sup>46</sup> diphtheria,<sup>64</sup> human immunodeficiency virus (HIV),<sup>41</sup> rotavirus,<sup>65</sup> and malaria,<sup>66</sup> among others. The small, microgram doses required for vaccination are also well-suited to microneedle based delivery.<sup>10</sup>

### 1.2.1 Microneedle Configurations

Microneedles can be classified into four distinct configurations- hollow microneedles, solid uncoated microneedles, solid microneedles coated with a powdered therapeutic, and polymeric microneedles, each of which differs in its method of application (Figure 1.3).<sup>19,30,67</sup> Hollow microneedles are typically made of metal or silicon containing a cylindrical bore; they are utilized for the delivery of liquid formulations which are pumped through the patch into the skin.<sup>19,30,67</sup> Solid microneedles, which are also typically made of metal or silicon, are temporarily applied to generate holes in the skin before removal.<sup>19,30,67</sup> A topical therapeutic liquid or cream agent can then be applied and allowed to diffuse through the channels created by the microneedle patch.<sup>19,30,67</sup> When microneedles are coated with a dry therapeutic coating, the microneedles are left in the skin to allow the coating to dissolve before removal of the patch.<sup>19,30,67</sup> In addition to these metal and silicon designs, microneedles have also been fabricated

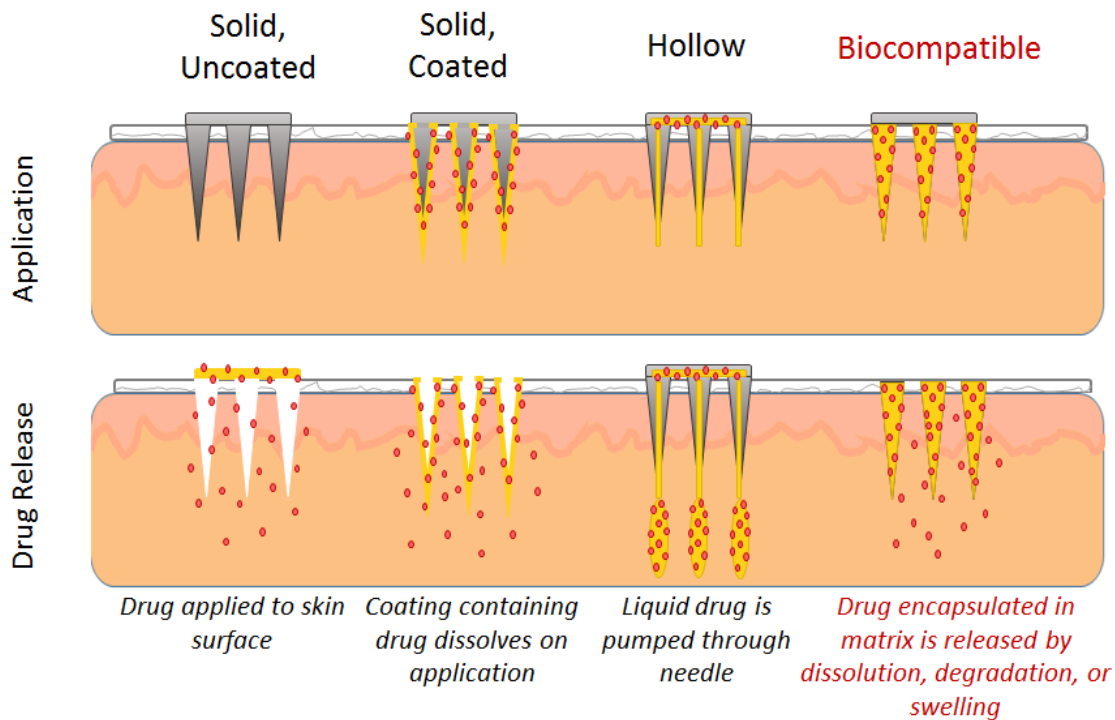


**Figure 1.3 Microneedle configurations.** The method of application and drug release for each of four different microneedle configurations. Figure adapted from reference 19.

from biocompatible materials, such as natural and synthetic polymers.<sup>68</sup> In this case, drug is typically directly incorporated into the microneedle matrix, which swells,<sup>69</sup> degrades,<sup>68</sup> or dissolves<sup>68</sup> to release the therapeutic into the skin. A pie chart showing the relative distribution of materials used in publications describing microneedle technology between 1998 and 2014 is given in Figure 1.4. Microneedles have been made of metal, silicon, and polymers (including natural and synthetic) with approximately equivalent frequency.

It is worth noting that the distinctions between these different categories are approximate. For the purpose of this dissertation, microneedles are classified based on their drug release mechanism, not their composition. For example, in a few cases, biocompatible or polymeric materials have been utilized to make coated<sup>41</sup> or hollow<sup>70</sup> microneedle configurations. However, because a PLGA microneedle coated with a therapeutic releases the therapeutic into the body via dissolution of the coating, we would consider a coated PLGA microneedle to be a solid, coated microneedle for the purposes of this dissertation. Conversely, non-polymeric materials such as

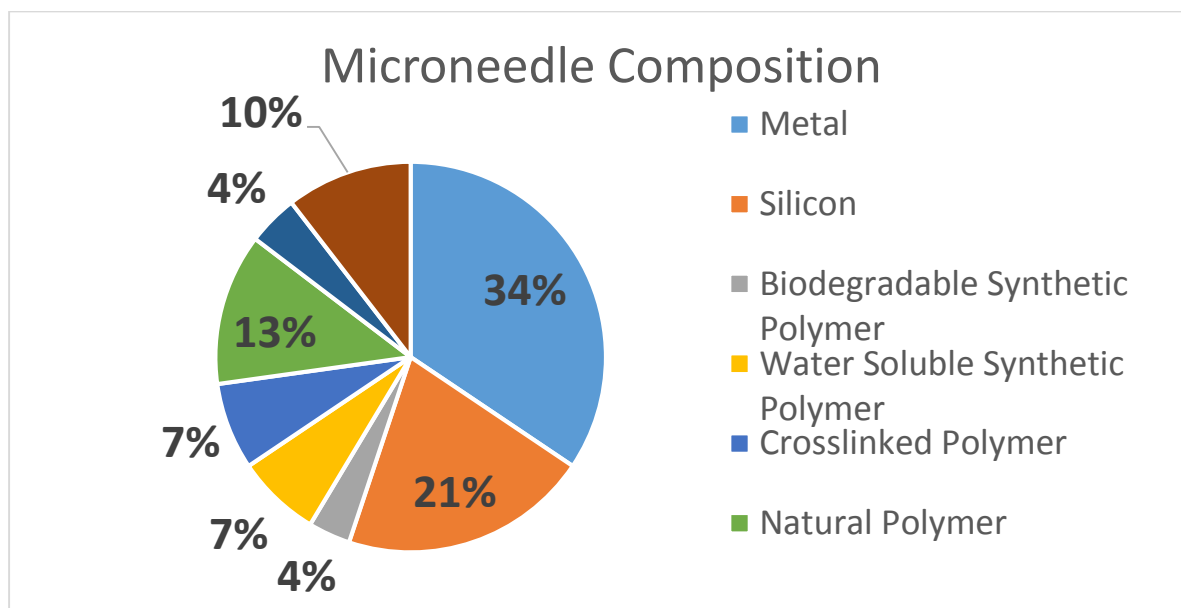


**Figure 1.4 Distribution of microneedle compositions in literature from 1998-2014.** Data compiled from Thompson Reuters Web of Science™

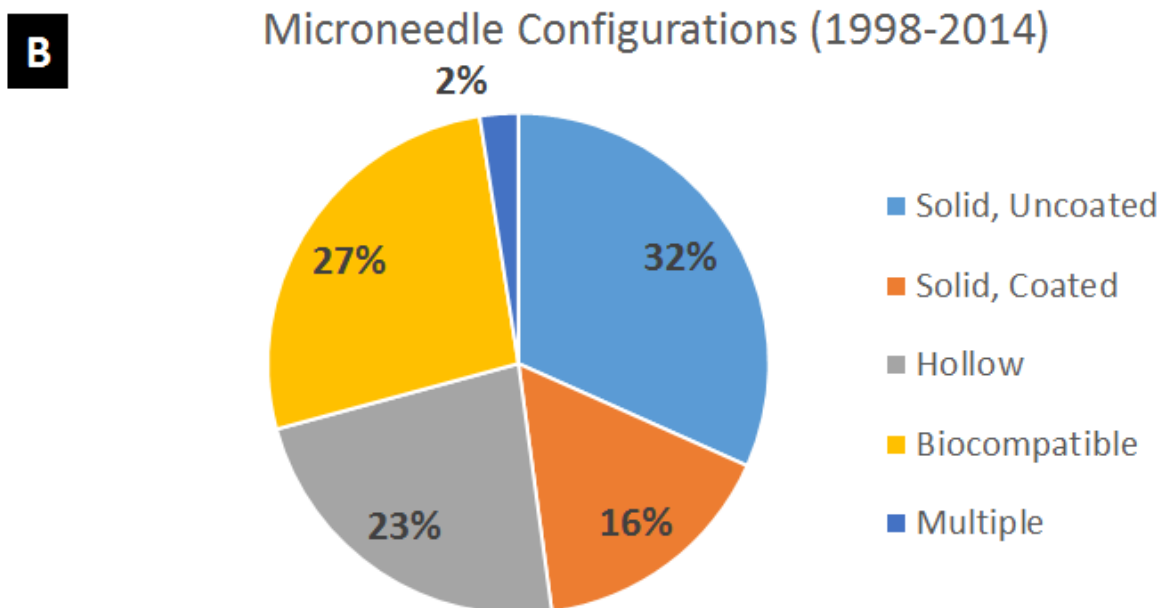
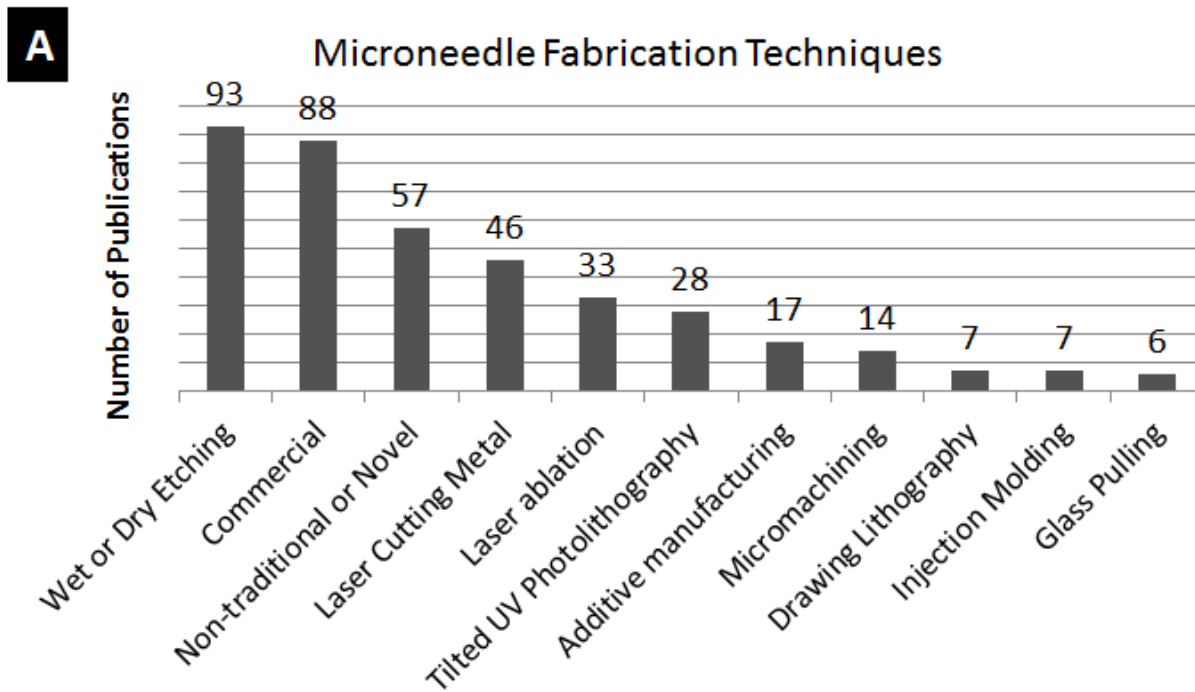


**Figure 1.5 Frequency of microneedle fabrication techniques and microneedle compositions** A. Fabrication techniques utilized in microneedle publications released between 1998 and 2014 B. Frequency of each microneedle configuration over the same time period. Data compiled from Thompson Reuters Web of Science™

stainless steel are considered to be biocompatible because they have no adverse reaction with cells in the body.<sup>71</sup> However, because drug release from a stainless steel needle would be achieved via a surface coating or through a hollow bore, we would consider a stainless steel needle to be either solid or hollow for the purposes of this dissertation, keeping with convention from microneedle literature. Therefore, throughout this dissertation the term “biocompatible microneedle” is used to refer to a microneedle loaded with cargo which is intended to swell, dissolve, or degrade to release said cargo.

### **1.2.2 Microneedle Fabrication Techniques**

The device type, material, desired geometry, and intended therapeutic payload influences which specific fabrication technology may be selected for device assembly, but the most commonly used microneedle fabrication techniques are given in Figure 1.5A.

These four different configurations (solid and uncoated, solid and coated, hollow, and biocompatible) have been represented with approximately equivalent frequency in microneedle literature (Figure 1.5B). Solid, uncoated microneedles are slightly more common than solid, coated formulations, presumably due to the large portion of microneedle publications that do not involve the incorporation of a therapeutic. This roughly equivalent prevalence of all microneedle configurations is indicative of the fact that each configuration has its distinct advantages and disadvantages (Table 1.4), making the choice of an optimal microneedle configuration highly situationally dependent. Important factors to consider when selecting the appropriate microneedle configuration are described here. In general, there is a tradeoff between the difficulty of device fabrication and the overall utility of the device (Figure 1.6). For example, solid, uncoated microneedles are typically very easy to fabricate by laser cutting metal,<sup>72-73</sup> which can be polished to remove burrs and then used directly (in-plane),<sup>72</sup> or bent 90° and then

Microneedle Configuration	Advantages	Disadvantages
Solid, Uncoated	<ul style="list-style-type: none"> <li>• Simple</li> </ul>	<ul style="list-style-type: none"> <li>• Poor dose control</li> </ul>
Hollow	<ul style="list-style-type: none"> <li>• Simple</li> </ul>	<ul style="list-style-type: none"> <li>• Bulky pumps are required</li> <li>• Administration may be painful</li> </ul>
Solid, Coated	<ul style="list-style-type: none"> <li>• Stabilizes proteins at room temperature</li> <li>• Improved dose consistency</li> </ul>	<ul style="list-style-type: none"> <li>• Small volume for cargo loading</li> <li>• Development of appropriate coating techniques</li> </ul>
Biocompatible	<ul style="list-style-type: none"> <li>• Stabilizes proteins at room temperature</li> <li>• Improved dose consistency</li> <li>• Larger volume for cargo loading</li> <li>• Ability to control release</li> <li>• Potential to eliminate sharp biohazardous wastes</li> <li>• Eliminates safety risk associated with needle fragmentation in skin</li> </ul>	<ul style="list-style-type: none"> <li>• Long and difficult fabrication techniques</li> <li>• Softer materials may not effectively insert into the skin</li> </ul>

**Figure 1.7 Advantages and disadvantages of each microneedle configuration**

used (out-of-plane).<sup>73</sup> Out-of-plane microneedles have the advantage of having multiple rows of microneedles that form an array, whereas in-plane techniques typically only have a single row.<sup>72-73</sup> Solid metal microneedles are also available from commercial sources.<sup>74-75</sup> These simple fabrication techniques enable researchers to investigate how physically breaching the skin affects the skin's permeability to an existing, topically-applied therapeutic without substantial fabrication efforts. Unfortunately, this topical administration severely limits control over applied dose.<sup>76</sup> For this reason, solid, uncoated microneedles can only be used for the delivery of medications with a large therapeutic window.<sup>76</sup>

The use of hollow microneedles similarly requires little fabrication effort. Hollow microneedles can be obtained from industrial partners and attached to a standard syringe to administer existing liquid formulations.<sup>77</sup> The administration of large volumes of therapeutics is challenging, however, because pumping fluid through micron-sized needles can introduce pressure buildup within the skin.<sup>78-81</sup> Some clinical trials have shown that this pressure buildup is

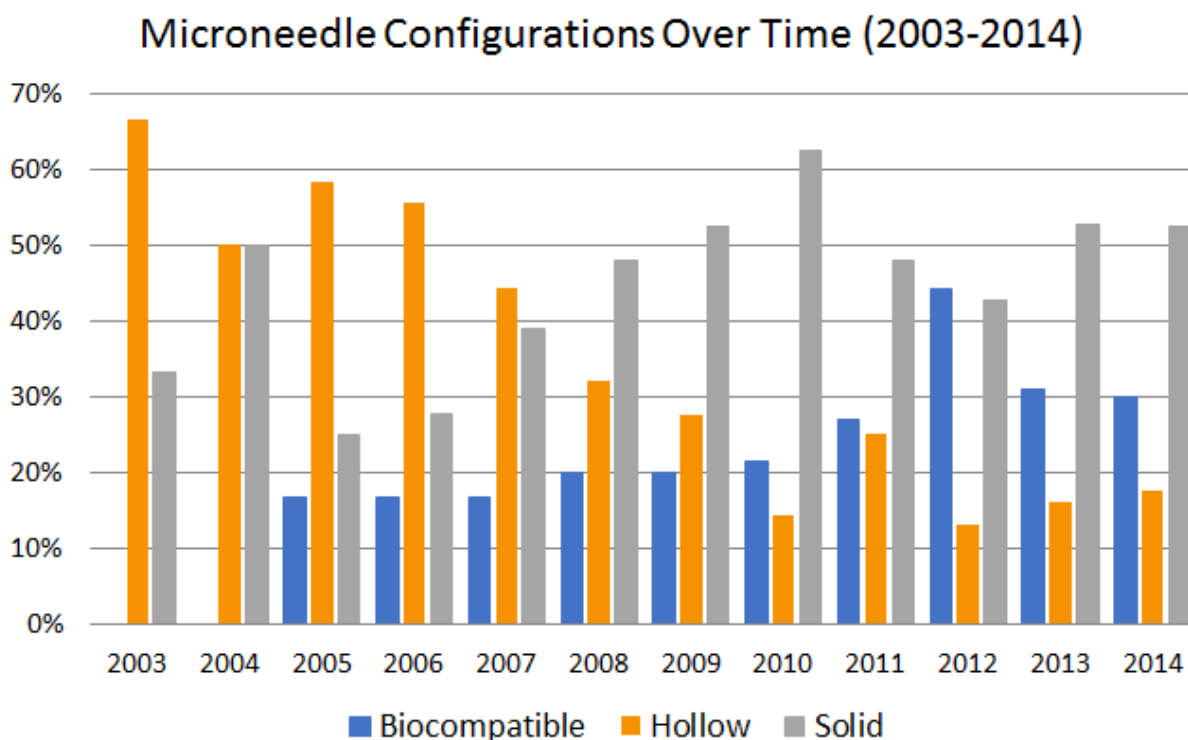


**Figure 1.8 Percentage of each microneedle configuration in literature over time.** Data is presented as the number of publications released of a particular composition divided by the total number of microneedle publications in that year. Data prior to 2003 is not presented due to the small number of microneedle publications over this time period. Data compiled from Thompson Reuters Web of Science™

painful to patients, thereby negating the advantage of having a pain-free microneedle based drug delivery system. One source of this pressure buildup is skin tissue at the microneedle tip, which can act as a physical “plug” that prevents fluid flow out of the needle.<sup>80</sup> Some investigators have designed hollow formulations with side-openings to circumvent this issue,<sup>82-83</sup> but the total volume that can be introduced is a practical limitation. Bulky devices are also sometimes necessary to control the flow of viscous fluids, thereby increasing the cost and complexity of hollow microneedle devices.<sup>84</sup> Together, these disadvantages have led to an overall decrease in the utilization of hollow microneedle configurations over time (Figure 1.7).

More advanced microneedle configurations- solid, coated microneedles and water-soluble or biodegradable microneedles- provide several advantages. Because these microneedle

configurations incorporate the therapeutic directly into the patch, they exhibit improved dose consistency relative to solid, uncoated needles, which rely on topical administration of the therapeutic. Successful administration of medications with smaller therapeutic windows is possible with these improvements in dose consistency. Unlike solid, uncoated and hollow microneedles, more advanced configurations also stabilize therapeutic proteins through dehydration to enable safe storage at room temperature for several months at a time.<sup>49,59-60</sup> This long term stability provides an opportunity to simplify the global supply chain for all protein based therapeutics by eliminating the need for refrigeration.<sup>49,59-60</sup> The global distribution of protein-based vaccines to remote locations with little access to electricity is a particularly promising application for this technology.<sup>49</sup> Together, these advantages have provided an incentive to develop solid, coated microneedles and biocompatible microneedles, despite the increased complexity of fabrication processes for these configurations.

Some important distinctions in the utility of solid, coated microneedles and biocompatible microneedle configurations can be made. Coated microneedles are arguably more straightforward to fabricate than biocompatible configurations.<sup>73</sup> Typically, a two dimensional metal sheet is cut to the desired shape using a laser cutter and electropolished to remove burrs.<sup>73</sup> This metal microneedle array is then coated using one of many different techniques, which include dip coating, gas-jet drying, spray drying, electrohydrodynamic atomization (EDHA), or ink jet printing, as reviewed elsewhere.<sup>85</sup> However, establishing coating techniques that reproducibly and uniformly deposit the therapeutic on the microneedle tips without coating the base of the array<sup>73</sup> requires extensive optimization. The relatively small amount of cargo that can be deposited on the surface of the microneedles<sup>86</sup> prohibits anything but the most potent therapeutic cargos from being administered in the matter. Further, small, metal or silicon

microneedle fragments accidentally deposited within the skin may trigger an immune response against the microneedle device.<sup>67</sup>

Biocompatible microneedles are often considered the gold standard for patient safety.<sup>68,87</sup> The use of biocompatible materials eliminates immunological risks associated with needles accidentally fragmenting in the skin.<sup>67</sup> Biocompatible microneedles that are dissolvable or biodegradable also eliminate the production of sharp, biohazardous wastes to prevent accidental needle-stick injuries and reduce disease transmission caused by needle re-use.<sup>67-68, 88-89</sup> Careful material selection also provides an opportunity to have rapid or sustained release of a therapeutic into the skin to optimize drug release profiles and maximize therapeutic efficacy.<sup>67-68, 88-89</sup> Altogether, these benefits have led to an increase in the prevalence of biocompatible microneedles over time in preclinical literature (Figure 1.7). Despite these many advantages and the clear potential of biocompatible microneedle formulations, only one biocompatible microneedle system, developed by Corium International Inc. has been utilized in clinical trials.<sup>90</sup> The goal of this dissertation is to improve the ease and adaptability of biocompatible microneedle fabrication so that the many advantages of biocompatible configurations (Figure 1.7) can be harnessed in a clinical environment.

### **1.2.3 Fabrication of Biocompatible Microneedles**

Biocompatible microneedles are usually fabricated in three distinct steps: master template fabrication, mold casting, and mold filling.<sup>40,68,91</sup> Even though these processes have enabled progress in the microneedle field, they all present challenges which hinder further advancements.

#### **1.2.3.1 Master Fabrication Techniques**

In a typical process, a master template is created using traditional microfabrication techniques, such as deep reactive ion etching,<sup>92</sup> wet etching,<sup>93</sup> laser ablation,<sup>41</sup> or tilted ultraviolet

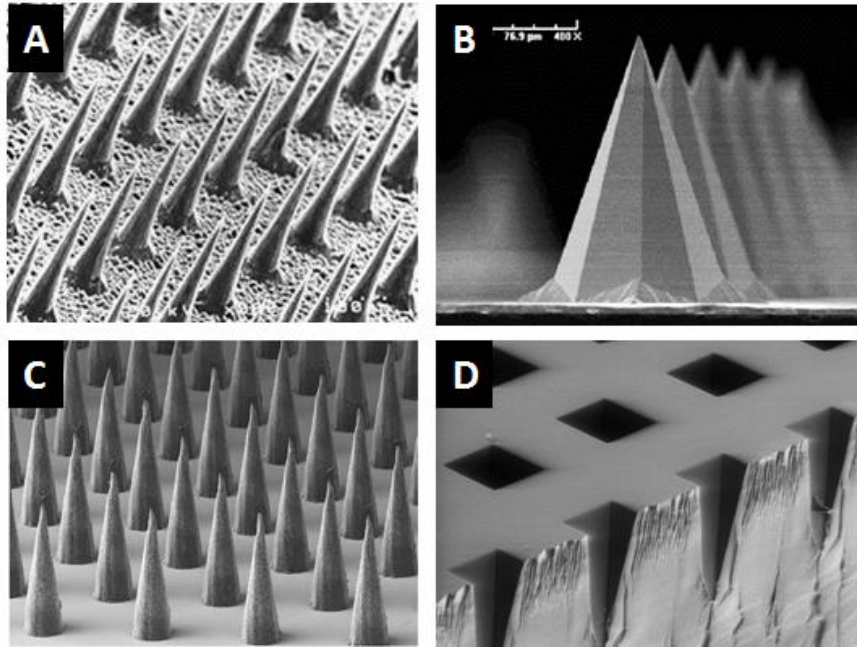


**Figure 1.12 Microneedle masters produced using traditional techniques.** Microneedle masters have been produced using A) Cryogenic deep reactive ion etching of silicon<sup>29</sup> B) Wet etching of silicon<sup>93</sup> C) Laser ablation<sup>34</sup> and D) Tilted UV photolithography

photolithography.<sup>68</sup> Some examples of microneedles fabricated using each of these techniques are provided in Figure 1.8.

Tilted UV photolithography is a common approach to master fabrication.<sup>68,87-88</sup> A silicon wafer is first coated with a thick layer of photoresist, typically SU8, and placed in contact with a patterned mask containing an array of transparent squares.<sup>68,88,94</sup> The complex is then exposed to UV light at an incident angle that defines the resulting microneedle height.<sup>68,88,94</sup> The substrate is rotated and re-exposed a total of four times to produce a negative master containing square pyramidal cavities in photoresist.<sup>68,88,94</sup> More information regarding this process can be found in Han et. al.<sup>94</sup> This technique has been successfully and extensively used by Prausnitz<sup>68,88,95</sup> to generate square pyramidal microneedles of different sizes. Although this technique is robust, process optimization is time consuming and diffraction of the incident UV light at the tip of the SU8 master has been known to limit the sharpness achievable by this approach.<sup>94</sup> It is also

limited to the production of square pyramidal microneedles; more complex geometries have not been produced.

When utilizing deep reactive ion etching (DRIE) for the production of microneedle masters, a silicon wafer is patterned with an etch mask (metal or photoresist) using standard photolithography based techniques.<sup>96-97</sup> This patterned wafer is then bombarded with high energy plasma, etching away unprotected regions to create a microneedle structure.<sup>96-97</sup> This technique has been utilized to produce ultrasharp microneedles up to 150 $\mu\text{m}$  in height<sup>29</sup> with etch rates on the order of 1-5 $\mu\text{m}$  per minute.<sup>98</sup> The height and aspect ratio of generated structures can theoretically be controlled by altering the chemical composition of the plasma (such as the ratio of  $\text{SF}_6$  and  $\text{O}_2$ ), the plasma density, and total etch times.<sup>96,98</sup> This process, however, requires excruciatingly difficult process control to prevent undercutting of the desired structure and to prevent undesired structures from being created from debris in the reactor.<sup>96,98</sup> Any change in microneedle size, shape, aspect ratio, or spacing requires a new etch recipe to be generated,<sup>98</sup> resulting in long lead times (on the order of months) for new microneedle designs.

Wet etching uses a liquid solution (rather than a dry gas) to chemically etch a metal or silicon substrate. When utilized for the production of microneedles, an anisotropic etch solution, such as potassium hydroxide (KOH) or tetramethylammonium hydroxide (TMAH), is used to selectively etch the silicon along a specific crystal plane.<sup>37,93</sup> This approach has been used by Wilke et. al. and others to produce microneedles ranging in size from 10 to 300 $\mu\text{m}$  with an aspect ratio of 1.5.<sup>37,93</sup> Although this approach is capable of producing microneedles of atomic level sharpness, this technique is also slow (on the order of 1 $\mu\text{m}$  per minute) and the aspect ratio of the resulting microneedles is predetermined by the selectivity ratio of the etchant (related to the etch

rate in a particular direction) along silicon's crystal planes.<sup>37,93</sup> For this reason, this approach provides little to no ability to adjust microneedle aspect ratio.<sup>37,99</sup>

Laser ablation provides the most control over microneedle geometry of current master fabrication processes.<sup>34,41, 99</sup> A silicone substrate is exposed to a laser beam which rasters across the surface of the substrate in a pattern defined by a computer aided design file.<sup>99</sup> This laser beam etches away the silicon to produce a mold that can be filled using a material of interest.<sup>34,41,99</sup> Although this technique provides substantial control over microneedle geometry, the resolution of the technique is limited to about 10 $\mu$ m;<sup>100</sup> mold filling processes are still required after master fabrication.

### **1.2.3.2 Mold Casting and Filling**

Following master fabrication, a mold is then cast in polydimethylsiloxane (PDMS)<sup>15,24-25</sup> and filled with a formulation of interest.<sup>34,68,87</sup> Mold casting is typically the least troublesome of the three fabrication steps (master template generation, mold casting, mold filling), but still has two significant challenges. Mold casting adds an additional time consuming step<sup>34,68,87</sup> and in some cases has also been known to decrease the fidelity of very small features,<sup>101</sup> which limits the achievable sharpness of microneedle structures.<sup>102</sup>

After this mold is cast, it is filled with the material of interest, typically a natural or synthetic polymer such as hyaluronic acid,<sup>103</sup> carboxymethylcellulose (CMC),<sup>68</sup> maltose,<sup>104</sup> chitosan,<sup>105</sup> Gantrez,<sup>48</sup> polyvinylpyrrolidone (PVP),<sup>106</sup> or poly(lactic-co-glycolic acid) (PLGA),<sup>107</sup> combined with the therapeutic. Many products are efficiently and cost-effectively fabricated using injection molding, where final material is heated and injected into the mold before it is allowed to cool into the final part.<sup>108</sup> However, the sensitive nature of target

therapeutics delivered via microneedle technology, such as proteins and nucleic acids, prohibits heating to high temperatures.<sup>68,109</sup> For this reason, most microneedles are fabricated by mixing a polymer with a solvent (typically water), casting this solution over the mold, applying a centrifugal force to fill the mold, and then allowing the solvent to evaporate over time under vacuum.<sup>68,109</sup> This process is sometimes repeated many times to fill the mold.<sup>87</sup> The batch-to-batch nature of these techniques combined with long evaporation times (on the order of days) make the mold filling process a laborious endeavor that encumbers microneedle research.<sup>87</sup>

#### **1.2.4 Overarching Challenges in the Fabrication of Biocompatible Microneedles**

Taken as a whole, current microneedle fabrication processes provide little to no opportunity to easily alter microneedle design. Prototyping new microneedle designs is often impractical because of the poorly controlled nature of micromanufacturing techniques and because microneedle fabrication is time consuming, with total fabrication times ranging from 14 to 142 hours per patch.<sup>68,110</sup> Because of the expensive equipment and substantial expertise required, fabrication is typically performed at advanced, centralized facilities where lead time for new microneedle patch designs can be greater than a month long. The need for extensive process optimization causes microneedle composition and geometry to be dictated by the feasibility of fabrication rather than ideal design,<sup>99,111</sup> despite substantial evidence that microneedle design parameters play a critical role in device efficacy, as discussed in the following section.

#### **1.2.5 Role of Microneedle Design Parameters on Device Efficacy**

There is an increasing interest in how microneedle design parameters, such as composition and geometry, influence device efficacy.<sup>99,111</sup> A diagram which lists several input design parameters and their potential therapeutic effects is given in Figure 1.9. The relationship between

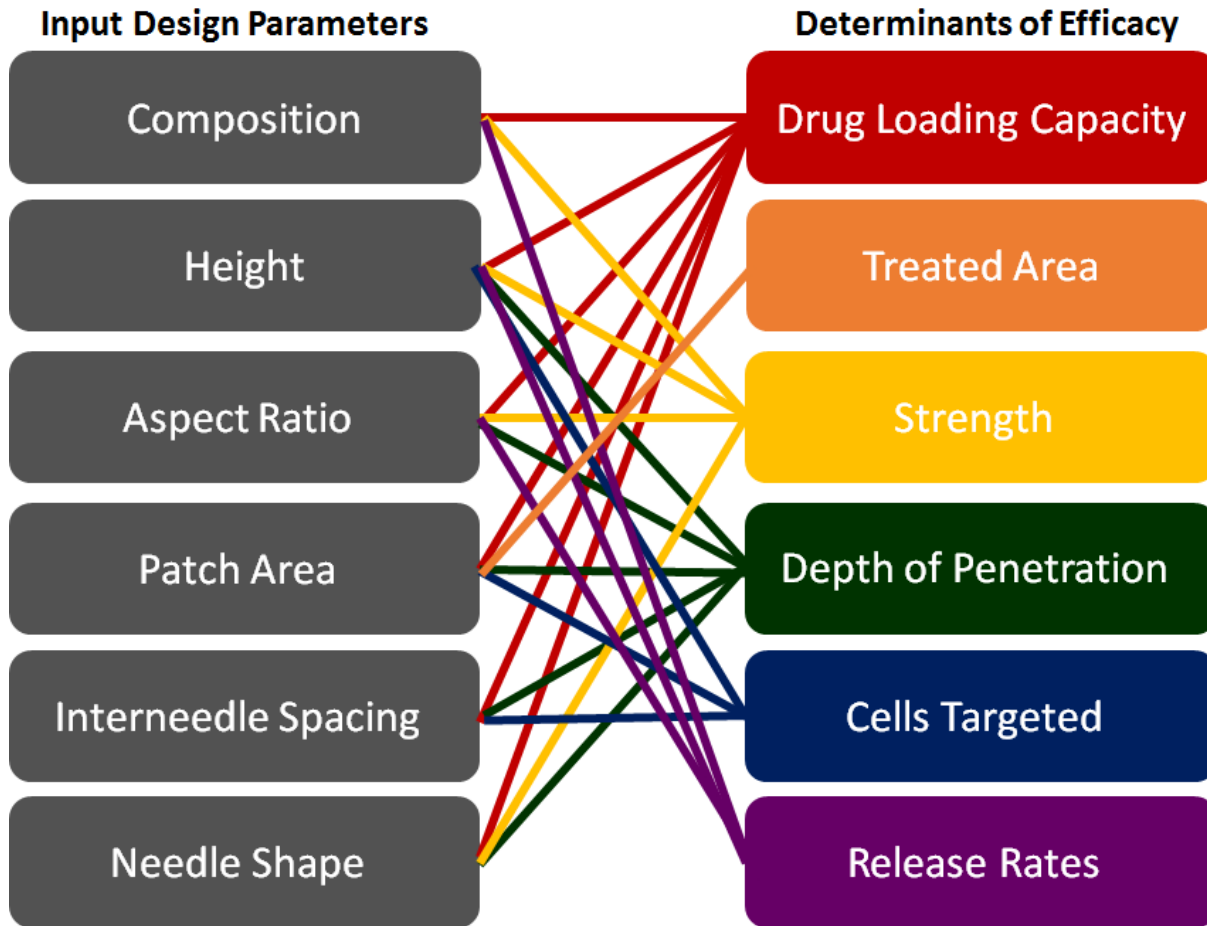


**Figure 1.14 Relationship between microneedle design parameters and therapeutic efficacy**  
 the input design parameters and determinants of efficacy is a complex web, where each design parameter affects multiple outcomes associated with device efficacy.

Studies investigating the role of microneedle design parameters, particularly microneedle geometry (including needle height, aspect ratio, spacing, and shape) on device efficacy have been limited. Poor control of existing fabrication techniques,<sup>99</sup> combined with their long fabrication times,<sup>87</sup> prohibits efficient and cost effective modulation of microneedle design parameters. Nevertheless, some existing studies underscore the importance of deliberate microneedle design.

For example, a 2012 study by Olantunji et al investigated how the total number of microneedles in an array influences the force required to insert that array into the skin.<sup>112</sup> Microneedle insertion is affected by a phenomenon called the “bed-of-nails” effect where the total application force applied to an array of needles is divided amongst all of the needles in the array.<sup>112</sup> Because a given microneedle array may have a multitude of needles, this effect can substantially increase the total force required to insert a microneedle array into the skin. The bed of nails effect is described quantitatively in equation 1, below, where N is the total number of microneedles in the array.

$$F_{single\ needle} = \frac{F_{total}}{N} \quad (1)$$

Olantunji et. al. investigated the force required to enable microneedles made out of a poly methyl vinyl ether- maleic anhydride copolymer to successfully insert into the skin.<sup>112</sup> Array interspacing was varied between 30 and 600 $\mu$ m, thereby altering the total number of microneedles present on an array of constant area.<sup>112</sup> Note that regardless of interspacing between needles, the required insertion force per microneedle remains constant (Table 1.4), providing empirical evidence to support the “bed-of-nails” effect.<sup>112</sup> Reducing the total number of microneedles on an array decreases the total force required to insert the array.<sup>112</sup> Work by Kochhar et. al. corroborates these findings.<sup>113</sup> Therefore, minimizing the number of needles per array presents a viable approach ensuring that each needle properly inserts into the skin with a reasonable application force. An obvious compromise is that this reduction in the number of needles reduces total drug loading volume. Approaches to combat this optimization problem are further discussed in Chapter 2, Section 2.2.9.

**Table 1.5 Force required for microneedle insertion** as a function of spacing between needles, the total number of microneedles per array, and the velocity of insertion. Forces are given as both Newtons per array and Newtons per microneedle on that array. Table adapted from reference 112.

MN Interspacing ( $\mu\text{m}$ )	MN Per Array	0.5 mm/s Insertion Velocity		1 mm/s Insertion Velocity	
		N/MN Array	N/MN	N/MN Array	N/MN
30	12	$0.4800 \pm 0.0017$	$0.0300 \pm 0.0001$	$0.3456 \pm 0.0002$	$0.0216 \pm 0.0001$
50	16	$0.4648 \pm 0.0023$	$0.0291 \pm 0.0001$	$0.3442 \pm 0.0003$	$0.0215 \pm 0.0001$
150	9	$0.2524 \pm 0.0017$	$0.0280 \pm 0.0002$	$0.1926 \pm 0.0001$	$0.0214 \pm 0.0001$
300	9	$0.2524 \pm 0.0019$	$0.0280 \pm 0.0002$	$0.1926 \pm 0.0002$	$0.0214 \pm 0.0001$
600	4	$0.1122 \pm 0.0014$	$0.0280 \pm 0.0003$	$0.0856 \pm 0.0001$	$0.0214 \pm 0.0001$

Another interesting study by Park et. al. investigated microneedle failure force (the force required to break the needle) as a function of aspect ratio.<sup>107</sup> The failure force of PLGA microneedles measuring  $200\mu\text{m}$  across the base with aspect ratios ranging from approximately 3 to 20 was determined using a force-displacement test station.<sup>107</sup> This study found that the short microneedles were approximately three times stronger than the high aspect ratio microneedles.<sup>107</sup> It is important that microneedle insertion force be substantially less than failure force to provide a high safety margin;<sup>30</sup> tailoring microneedle aspect ratio is therefore an important aspect of the design of safe and efficacious microneedle devices.

Another study by Lee et. al. investigated the role of microneedle composition on strength and efficacy of insertion.<sup>68</sup> The authors fabricated microneedles from polylactic acid (PLA), amylopectin, carboxymethylcellulose (CMC), and bovine serum albumin (BSA). The Young's modulus of each microneedle composition was assessed and found to range from 1 to 5GPa (for CMC and PLA, respectively).<sup>68</sup> The solubility of each polymer in the solution used to fill microneedle molds was also found to play an important role in the mechanical properties of the resulting microneedle devices.<sup>68</sup> The authors suggest, using mathematical modeling, that these differences in Young's moduli will affect microneedle failure force, but no empirical validation

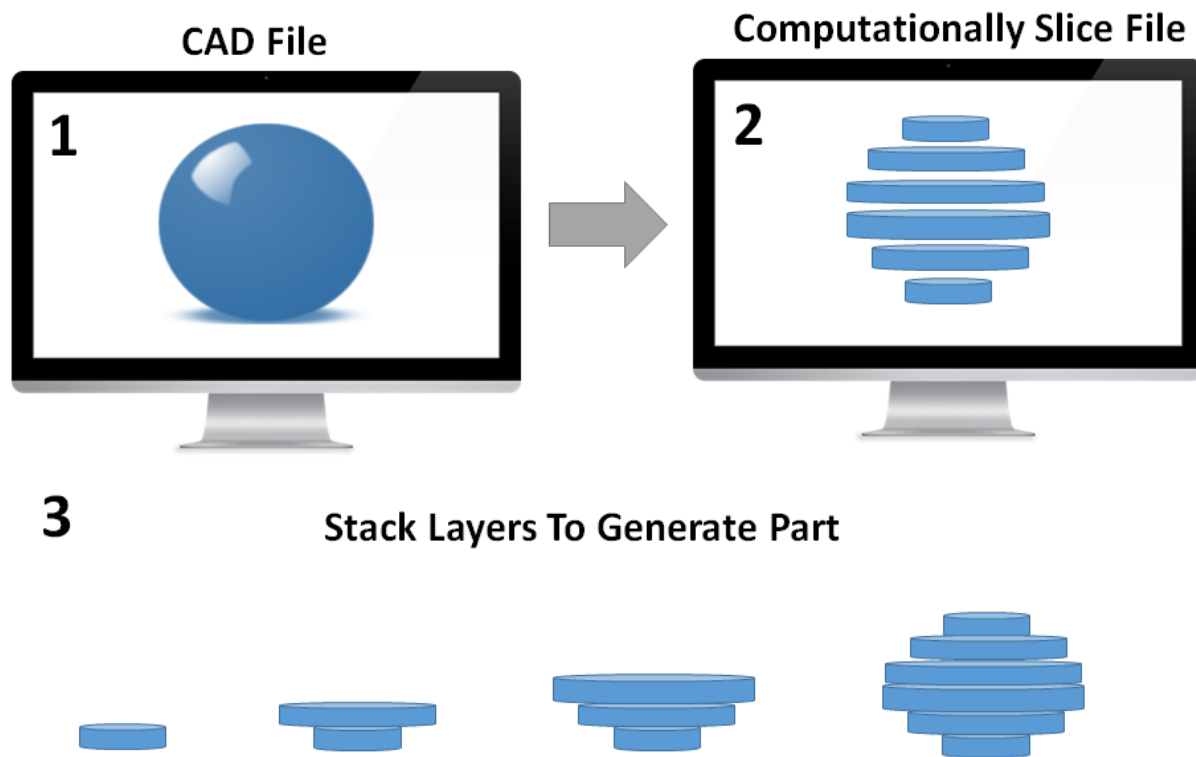


**Figure 1.15 Overview of the additive manufacturing process.** A computer model is computationally sliced into individual layers. Each two dimensional (2D) layer is stacked on top of the previous layer to create the desired three-dimensional part (3D)

is provided.<sup>68</sup> Nevertheless, this work suggests that microneedle composition is also a critical factor influencing microneedle insertion into the skin.<sup>68</sup>

Other publications have also investigated the role of aspect ratio on failure forces,<sup>114</sup> the influence of microneedle height on skin permeability *in vitro*,<sup>115</sup> the role of microneedle sharpness on insertion forces,<sup>116,117</sup> and the role of microneedle application force on depth of penetration.<sup>111</sup> Altogether, these results underscore the importance of investigating microneedle design parameters in a high throughput fashion, but the time intensive and poorly controlled nature of current fabrication techniques hinders such investigations. Therefore, this dissertation seeks to develop a rapid, robust and tunable method of fabricating microneedle devices for transdermal drug delivery. We seek to use recent advancements in additive manufacturing to

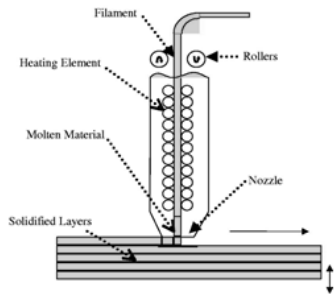
bring an unlimited design space to microneedle manufacturing in order to facilitate a better understanding of how a multitude of different design parameters influence device efficacy.

### **1.3 Additive Manufacturing Overview**

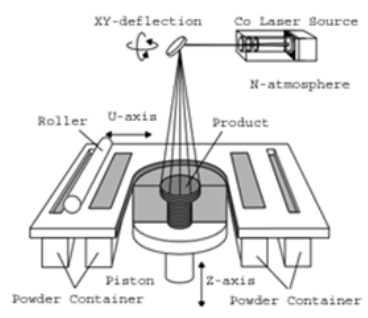
Additive manufacturing, more colloquially known as “3D Printing”, may provide an opportunity to rapidly alter many of the design parameters associated with microneedle fabrication with little to no lead time. These factors include microneedle composition, height, aspect ratio, interneedle spacing, patch size, and microneedle shape, among others. Additive manufacturing, developed in the 1980s, is defined by ASTM F2792-12a as “a process of joining materials to make objects from 3D model data, usually layer upon layer, as opposed to subtractive manufacturing methodologies” where a bulk material is machined down to produce the desired part.<sup>118</sup> Although many different types of 3D Printing have been developed, the vast majority of 3D printing technologies follow the overall process shown in Figure 1.10.<sup>119-120</sup> First, a computer aided design (CAD) file of the desired part is created using 3D modeling software such as Solidworks or AutoCAD. This digital part is then computationally sliced along the z axis to produce many layers.<sup>119-120</sup> Each of these layers is then sequentially stacked on top of the previous layer to form the desired part.<sup>119-120</sup> Typically, each layer is either added as a liquid or powder which is solidified via either a thermal or photochemical phase transition to form a solid part.<sup>119</sup>

The most common types of 3D Printing are fused deposition modeling (FDM), selective laser sintering (SLS), polyjet technology, and stereolithography (SLA), shown in Figure 1.11.<sup>119</sup><sup>121</sup> These techniques are reviewed comprehensively elsewhere,<sup>119-121</sup> but a short summary of each method is also included here. Fused deposition modeling and selective laser sintering both form parts utilizing a thermal phase transition, where the final part is generated through heating and

**A** *Fused Deposition Modeling*

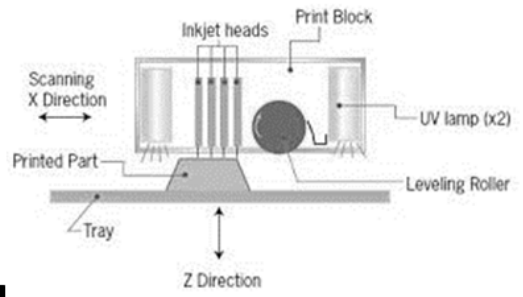


**B** *Laser Sintering*

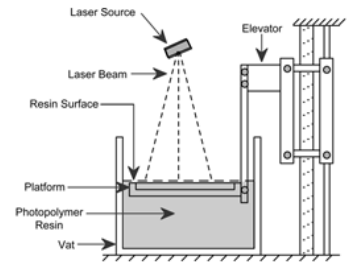


**Thermal Phase Transition**

**C** *Polyjet*



**D** *Stereolithography*



**Photochemical Phase Transition**

**Figure 1.18 Types of additive manufacturing.** A) Fused deposition modeling, B) laser sintering, C) polyjet, and D) stereolithography are different types of additive manufacturing that form solid parts via either a thermal or photochemical phase transition. Images reproduced with permission from references 121-124.

cooling of the material.<sup>119-121</sup> Fused deposition modeling (FDM) can be thought of as a robotic hot glue gun, where a plastic filament, commonly acrylonitrile butadiene styrene (ABS), Nylon 12, or polycarbonate (PC),<sup>126</sup> is heated above its melting temperature and squeezed through a pressurized nozzle. This nozzle moves to cover a shape defined by the CAD file to produce each layer of the part; the nozzle then moves upward to generate the next layer, stacking sequential layers to produce a 3D part.<sup>119-121</sup> Major manufacturers of FDM based systems include MakerBot and Stratasys.<sup>126-127</sup> Selective laser sintering is a technique in which a layer of powder, typically made of metals (such as steel, titanium, and alloys), ceramic, polyamide (nylon), or glass, is heated at a specified location using a laser beam.<sup>119</sup> This laser beam rasters over the part in a

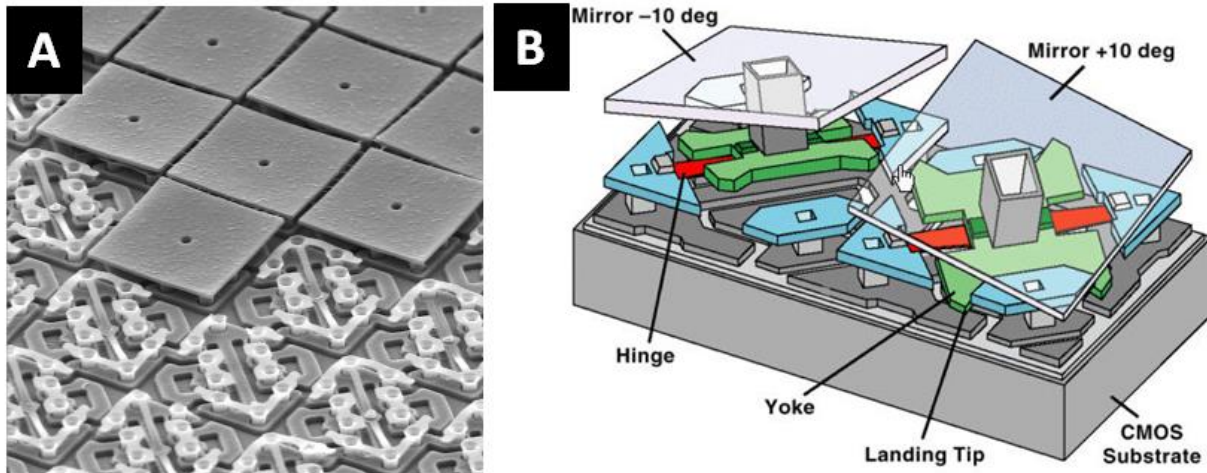


**Figure 1.19 Digital light processing (DLP) chip.** A) Scanning electron micrograph (SEM) of a DLP chip showing the array of micromirrors B) Schematic showing mechanism for turning each “pixel” or micromirror on and off. Images reproduced with permission from reference 120 and 150, respectively

shape defined by a computer aided design file, melting the powder together to form a solid mass.

After every layer, a new layer of powder is rolled over the part, and the laser traces the next layer. This process is repeated in a layer-by-layer fashion to produce the final part.<sup>119-121</sup>

Unlike FDM and SLS, polyjet and stereolithography based systems rely on a photochemical reaction to form the solid part. A liquid resin containing a photoreactive monomer, such as an acrylate or epoxy, is mixed with a photoinitiator. This photoinitiator absorbs light to form a free radical which reacts with monomer via free radical polymerization to form a solid part.<sup>126</sup> Polyjet technologies, such as the Stratasys PolyJet 3D and Hewlett-Packard (HP) Multi Jet Fusion, utilize arrays of small nozzles (similar to inkjet printers) to dispense photosensitive liquid droplets at a particular location.<sup>126</sup> Each of these liquid droplets is exposed to light in a layer-by-layer fashion to form a solid part via photopolymerization.<sup>126</sup>

### 1.3.1 Stereolithography

Stereolithography (SLA) is most similar to Continuous Liquid Interface Production (CLIP), which is used throughout the remainder of this thesis. SLA was first developed in 1986

by 3D Systems,<sup>127</sup> but a number of other manufacturers including Envisiontech and Formlabs have manufactured SLA based additive manufacturing systems since this point in time.<sup>126</sup> Like polyjet techniques, stereolithography produces parts via photopolymerization of a liquid resin.<sup>126</sup> However, rather than depositing resin onto a substrate using inkjet nozzles, the SLA process produces parts via spatially localized polymerization of a vat of resin.<sup>126,127</sup> The location of photopolymerization is controlled via either a rastering laser or via light reflected off of a Digital Light Processing (DLP) chip.<sup>127</sup> DLP chips, which have been utilized in projectors and big screen televisions, computationally control the shape of a light projection using an array of micromirrors,<sup>127</sup> such as those shown in Figure 1.12. Each of these micromirrors, which typically range in size from ~7 to 14 $\mu\text{m}$  in width,<sup>128</sup> can be turned on and off by adjusting the tilt angle of the mirror, as shown in Figure 1.12B. When the micromirror tilts to face the incoming light source, it is in the “ON” position; when it faces away from incoming light it is “OFF”. Therefore,

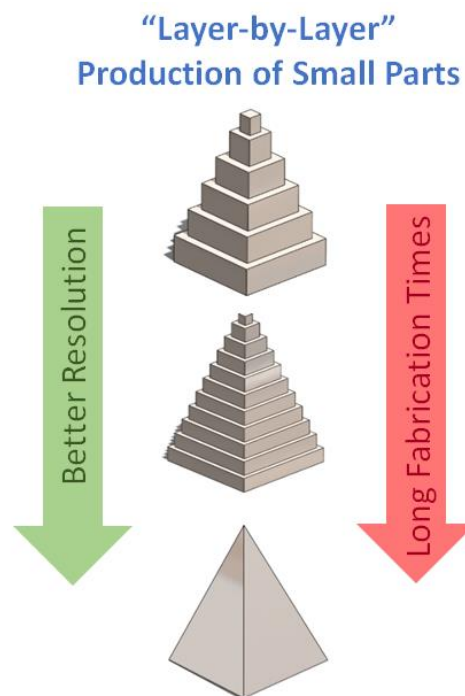


**Figure 1.20 Layer by layer results in tradeoff between fabrication time and resolution**

the specific pattern of mirrors that are turned on and off defines the shape of the light that projects onto the liquid resin.

DLP based systems typically provide faster fabrication speeds because the entire layer is cured simultaneously, whereas systems that rely on laser rastering typically have slower fabrication times due to the time required to trace the desired object with a thin laser beam.<sup>127</sup> Laser-based stereolithography typically has higher resolution, however, because the laser beam provides extremely localized photopolymerization.<sup>127</sup>

In addition to classifying stereolithography systems based on the nature of the light source, stereolithography systems can also be classified as either “bottom-up” or “top-down”.<sup>126,127</sup> In a “top-down” system, the light illuminates the resin vat from the top, as shown in Figure 1.11D. After each sequential light exposure, the part is then dipped further into the bath; the top of the structure is then re-coated with resin before the next exposure. “Bottom-up” systems, in which light illuminates the bath from the bottom, are becoming increasingly common. In this case, the light typically illuminates through the bottom of a UV transparent vat. After each successive exposure, the part is mechanically separated from the bottom of the bath, pulled upward and repositioned prior to the next exposure. This approach provides several advantages when compared to the “top-down” approach, particularly that renewing the build area with fresh resin is simpler because gravity pushes new resin to the bottom of the vat.<sup>127</sup> However, the mechanical force required to physically separate the part from the bottom of the vat after it cures can be up to 60N.<sup>131</sup> These high forces often damage parts, especially delicate high resolution parts, during production.<sup>131</sup> **The process of separating and realigning the part is the rate-limiting step in this process, limiting production speeds to millimeters per hour in the z direction.**<sup>132</sup> A new approach to overcoming some of these challenges will be discussed in

section 1.5, but first we will overview approaches to use existing additive manufacturing technologies to fabricate microneedles for transdermal drug delivery.

### **1.3.2 Layer-by-Layer Approaches to Additive Manufacturing of Microneedles**

All existing approaches are inherently “layer-by-layer” approaches to manufacturing, where a 3D part is fabricated by stacking two dimensional cross sections on top of one another. The fabrication of small parts, such as microneedles, requires high resolution systems. For layer-by-layer additive manufacturing techniques, the z resolution is defined by the thickness of each layer; this thickness impacts the quality of the overall part, as shown in Figure 1.13. Although traditional stereolithography systems are not amenable to the production of microneedles because each layer is too thick (approximately 25-100 $\mu\text{m}$  thick each),<sup>127</sup> some investigators have utilized custom additive manufacturing devices to fabricate microneedles, as discussed in more detail below.<sup>133-136</sup> In general, these approaches decrease the thickness of each layer, resulting in lengthened fabrication times due to the need to realign between each layer.<sup>127, 133-136</sup>

One report of additive manufacturing of microneedles was published by Lu et. al. at The University of Akron. A custom microstereolithography apparatus was designed to produce the 2x2 mm array of poly(propylene fumarate) microneedles shown in Figure 1.14A-C.<sup>133</sup> The custom apparatus is made up of a mercury lamp, lightgate prism, an achromatic doublet lens, and a DLP chip from Texas Instruments with individual micromirrors measuring 13.68 $\mu\text{m}$  square.<sup>133</sup> Each slice measures 20  $\mu\text{m}$  thick in the z direction. These microneedles produced using this custom apparatus measure approximately 1000 $\mu\text{m}$  in length and 200  $\mu\text{m}$  in width.<sup>133</sup> Overall fabrication times for these microneedle arrays are on the order of hours.<sup>133</sup> Similar findings have been presented by Yun et. al.<sup>134</sup>

Roger Narayan and coworkers have also impressively utilized an additive manufacturing technique called two photon polymerization for the production of microneedles (Figure 1.14D-G).<sup>135</sup> This process utilizes a rastering laser pulse to initiate photopolymerization based on two photons with nano-scale accuracy; photopolymerization only occurs in a small volume located at the tip of the laser.<sup>135</sup> Although this technique has been able to produce delicate microneedle structures from a variety of different materials, including Ormocer® ceramic materials and eShell 200,<sup>136</sup> master fabrication times are still long (on the order of days).<sup>135</sup> For this reason, two photon polymerization is typically used to create microneedle master templates, which are subsequently replicated via the micromolding processes previously described.

This previous work in additive manufacturing of microneedles demonstrates proof of concept that additive manufacturing can be used to provide additional flexibility in microneedle device design. However, due to the long fabrication times that are still associated with these additive manufacturing techniques, they have only been utilized to produce master templates for

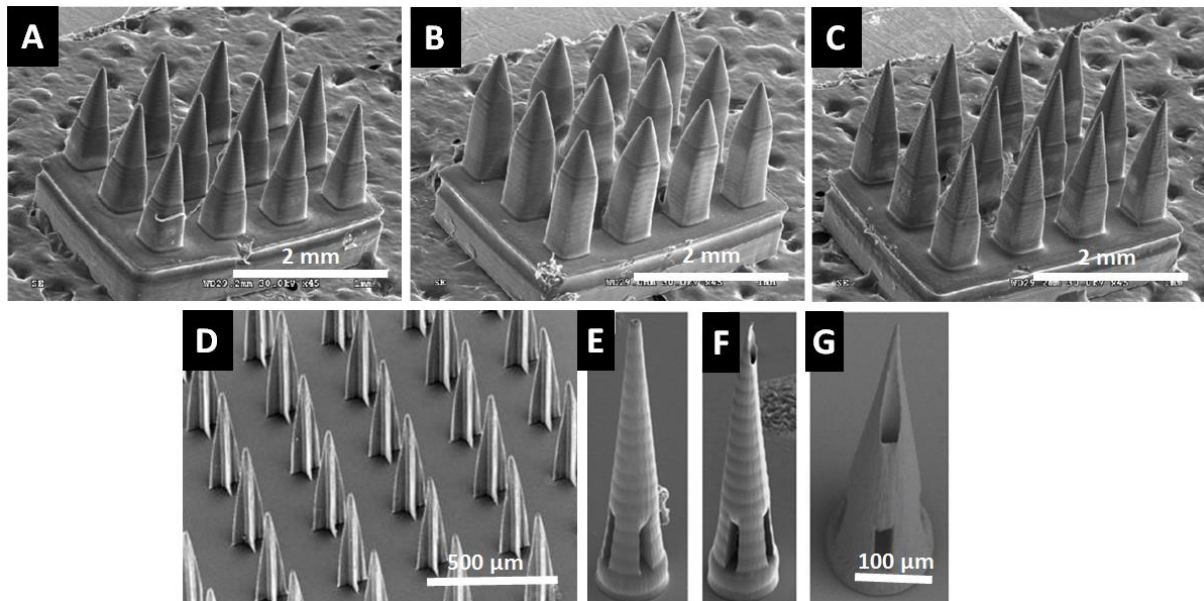


**Figure 1.23 Microneedles produced via additive manufacturing** A-C) Microneedle produced by Lu et. al. D-G) Microneedles produced by Narayan and coworkers. Images reproduced with permission from references 133 and 135

subsequent micromolding. Time-consuming mold casting and mold-filling processes are still required. The work presented in this dissertation can be differentiated from these previous approaches by 1) the reduction in fabrication time relative to other additive manufacturing techniques and 2) the ability to directly fabricate microneedle arrays in a single, mold-independent step using potentially biocompatible materials.

### **1.3.3 Continuous Liquid Interface Production (CLIP)**

In an effort to bring a virtually unlimited design space into microneedle fabrication and enable rapid prototyping of such designs, this thesis seeks to apply a new additive manufacturing technique called Continuous Liquid Interface Production (CLIP), invented by the startup company Carbon3D, to the fabrication of biocompatible microneedles for transdermal drug delivery.

Of the additive manufacturing systems discussed in this chapter, CLIP is most similar to bottom-up stereolithography with a DLP light source. The difference between CLIP and bottom-up stereolithography is shown in Figure 1.15. As mentioned previously (see Section 1.41.), bottom-up stereolithography works by photopolymerizing within a vat of liquid resin in a layer-by-layer fashion to produce a solid part. This process involves several steps. First, the photosensitive resin is exposed to light projected through a UV transparent window under the vat of resin. This light cures the resin under the build elevator, shown in dark blue, to the glass window shown in green. Because this curing step adheres the part to the glass window, the part must be mechanically separated from the glass window to allow resin to flow into the build area. The part must then be realigned before exposing the next layer. The process of moving the part up and down to rip it off of the window and realign takes several seconds, limiting build speeds

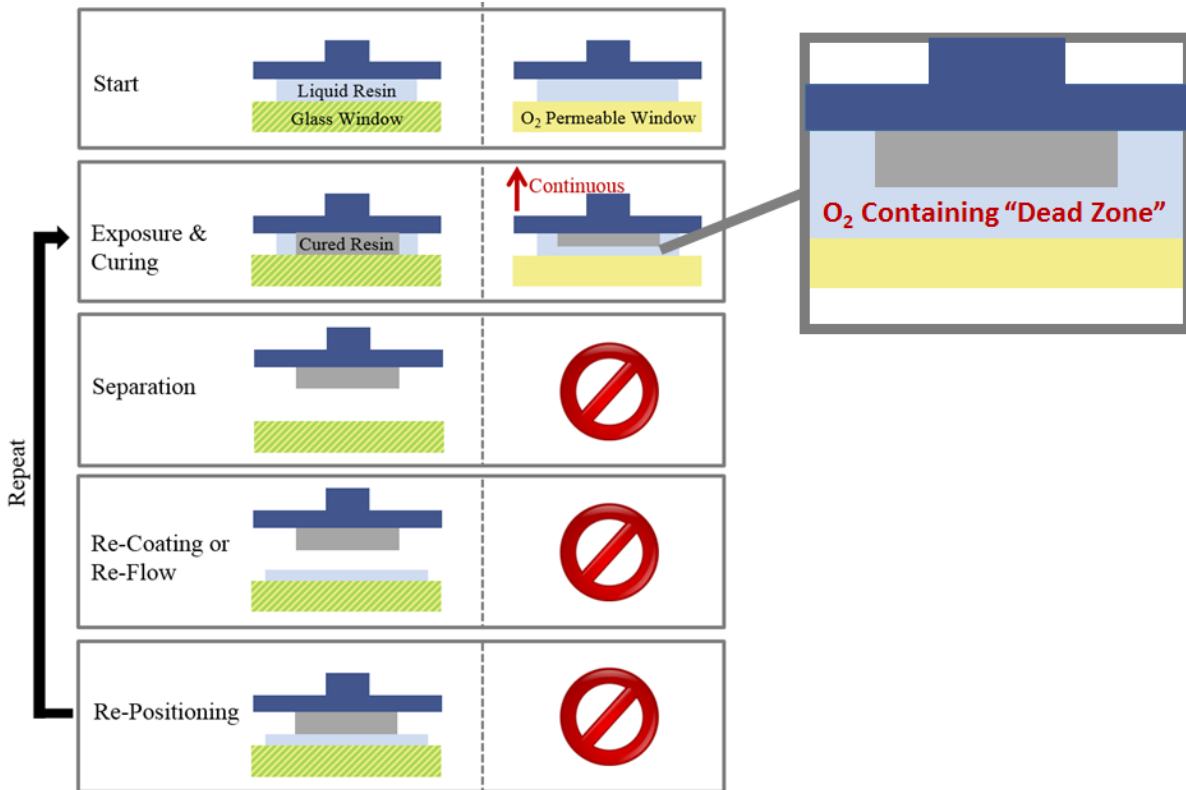


**Figure 1.25 Differences between stereolithography and CLIP**

to millimeters per hour. Mechanical strain on the part limits the size and delicacy of parts that can be created.

In contrast, CLIP systems have a UV transparent, oxygen permeable window beneath the vat of resin. This special window enables oxygen to diffuse into the resin. Because oxygen is a well-known inhibitor to photopolymerization, this special window creates a “dead-zone” in which no photopolymerization occurs. This physical gap between the building part and the window prevents the part from adhering to the window, thereby eliminating the need for mechanical separation and realignment. This enables the build elevator to move upward continuously, allowing continuous rather than “layer-by-layer” production of the part. Continuous production affords several advantages, including 1) the potential to produce small, delicate, and intricate parts without fear of damaging those parts during processing and 2) the

ability to fabricate parts from infinitesimally thin slices without slowing down production. These advantages make this an ideal method for additive manufacturing of microneedles for transdermal drug delivery.

#### **1.4 Summary and Hypothesis**

Microneedles are simple devices that show promise for painlessly delivering a wide variety of different therapeutics into the body through the skin. However, current approaches to manufacturing microneedles are costly, complicated, and time consuming, and provide little ability to alter critical microneedle design parameters such as microneedle height, aspect ratio, spacing, and geometry, which can influence efficacy. This thesis seeks to utilize a new additive manufacturing technique called CLIP to fabricate biocompatible microneedles for transdermal drug delivery to enable complete and rapid control over microneedle design, as proposed in US Patent 9,211,678.<sup>137</sup>

## REFERENCES

- (1) Paul, S. M.; Mytelka, D. S.; Dunwiddie, C. T.; Persinger, C. C., Munos, B. H.; Lindborg, S. R.; Schacht, A. L. *Nat Rev Drug Discov.* **2010**, *9*, 202-214.
- (2) International Federation of Pharmaceutical Manufacturing. The Pharmaceutical Industry and Global Health: Facts and Figures 2014. [http://www.ifpma.org/fileadmin/content/Publication/2014/IFPMA\\_-\\_Facts\\_And\\_Figures\\_2014.pdf](http://www.ifpma.org/fileadmin/content/Publication/2014/IFPMA_-_Facts_And_Figures_2014.pdf) (Accessed January 27<sup>th</sup>, 2016)
- (3) Langer, R. *Nature.* **1998**, *392*, 5-10.
- (4) Pathak, K.; Raghuvanshi, S. *Clin Pharmacokinet.* **2015**, *54*, 325-357.
- (5) Mitragotri, S.; Burke, P. A.; Langer R. *Nat Rev Drug Discov.* **2014**, *13*, 655-672.
- (6) Van de Waterbeemd, H.; Gifford, D. *Nat Rev Drug Discov.* **2003**, *2*, 192-204.
- (7) Ou-Yang, S. S.; Lu J. Y; Kong, X. Q.; Liang, Z. J.; Luo, C.; Jiang, H. *Acta Pharmacol Sin.* **2012**, *33*, 1131-1140.
- (8) Jana, S.; Mandlekar, S.; Marathe, P. *Curr Med Chem.* **2010**, *17*, 3874-3908.
- (9) Farokhzad, O. C.; Langer R. *ACS Nano.* **2009**, *3*, 16-20.
- (10) Prausnitz, M. R.; Langer, R. *Nat Biotechnol.* **2008**, *26*, 1261-1268.
- (11) Paudel, K. S.; Milewski, M.; Swadley, C. L.; Brogden, N. K.; Ghosh, P.; Stinchcomb, A. L. *Ther Deliv.* **2010**, *1*, 109-131.
- (12) Heather, A.; Benson, E.; Watkinson A.C. *Topical and Transdermal Drug Delivery: Principles and Practice*; John Wiley & Sons. 2012
- (13) Naik, A; Kalia, Y. N.; Guy, R. H. *Pharm Sci Tech Today.* **2000**, *3*, 318-326.
- (14) Burris, J. F.; Papademetriou, V.; Wallin J. D.; Cook, M. E; Weidler, D. J. *Am J Med.* **2016**, *91*, S22-S28.
- (15) Lopez, L. M.; Grimes, G. A.; Gallo, M. F.; Stockton, L. L.; Schultz, K. F. *The Cochrane Collaboration.* **2013**, *4*, 1-139.
- (16) Molinuevo, J. L.; Arranz, F. J. *Expert Rev Neurother.* **2012**, *12*, 31-37.
- (17) MedScape. Skin Anatomy. <http://emedicine.medscape.com/article/1294744-overview> (accessed January 27<sup>th</sup>, 2016)

- (18) Moller, S. J.; Poulsen, T.; Wulf, H.C. *Acta Derm Venereol.* **2003**, *83*, 410-413.
- (19) Donnelly, R. F.; Singh, T. R. R.; Morrow, D. I. J.; Woolfson, A. D. *Microneedle-mediated Transdermal and Intra-dermal Drug Delivery*; John Wiley & Sons, Ltd. 2012.
- (20) Menon, G. K. *Adv Drug Deliv Rev.* **2002**, *54*, S3-S17.
- (21) Prausnitz, M. R.; Elias, P. M.; Franz, T. J.; Schmuth, M.; Tsai, J. C.; Menon, G. K.; Holleran, W. M.; Feingold, K. R. *Medical Therapy: Skin Barrier and Transdermal Drug Delivery*; Elsevier Saunders 2012
- (22) Pasparakis, M.; Haase, I., Nestle, F. O. *Nat Rev Immunology.* **2014**, *14*, 289-301.
- (23) Carneiro, J. R. M.; Fuzii, H. T.; Kayser, C.; Alberto, F. L.; Soares, F. A.; Sato, E. I.; Andrade, L. E. C. *Clinics.* **2011**, *66*, 77-82.
- (24) Pathan, I. B.; Setty, C. K. *Trop J Pharm Res.* **2009**, *8*, 173-179.
- (25) Rawat, S.; Vengurlekar, S.; Rakesh, B.; Jain, S.; Srikarti G. *Indian J Pharm Sci.* **2008**, *70*, 1-5.
- (26) Smith, N. B. *Int J Nanomedicine.* **2007**, *2*, 4.
- (27) Schramm, J.; Mitragotri, S. *Pharm Res.* **2002**, *19*, 1673-1679.
- (28) Brown, M. B.; Traynor, M. J.; Martin, G. P.; Akomeah, F. K.; *Drug Deliv Syst.*; Humana Press. 2008; pp. 119-139.
- (29) Henry, S.; McAllister, D. V.; Allen, M. G.; Prausnitz, M. R.; *J Pharm Sci.* **1998**, *87*, 922-925.
- (30) Prausnitz, M. R. *Adv Drug Deliv Rev.* **2004**, *56*, 581-587.
- (31) Wermeling, D. P.; Banks, S. L.; Hudson, D. A.; Gill, H. S.; Gupta, J.; Prausnitz, M. R.; Stinchcomb, A. L. *Proc Natl Acad Sci USA.* **2008**, *105*, 2058-2063.
- (32) Banks, S. L.; Pinninti, R. R.; Gill, H. S.; Crooks, P. A.; Prausnitz, M. R.; Stinchcomb, A. L. *Pharm Res.* **2008**, *25*, 1677-1685.
- (33) Kochhar, J. S.; Lim, W. X. S.; Zou, S.; Foo, W. Y.; Pan, J.; Kang, L. *Mol Pharm.* **2013**, *10*, 4272-4280.
- (34) DeMuth, P. C.; Su, X.; Samuel, R. E.; Hammond, P. T.; Irvine, D. J. *Adv Mater.* **2010**, *22*, 4851-4856.

- (35) Zaric, M.; Lyubomska, O.; Touzelet, O.; Poux, C.; Al-Zahrani, S.; Fay, F.; Wallace, L.; Terhorst, D.; Malissen, B.; Henri, S.; Power, U. F. Scott, C. J.; Donnelly, R. F.; Kissenpfennig, A. *ACS Nano*. **2013**, *7*, 2042-2055.
- (36) Norman, J. J.; Brown, M. R.; Raviele, N. A.; Prausnitz, M. R.; Felner, E. I. *Pediatr Diabetes*. **2013**, *14*, 459-465.
- (37) Haq, M. I.; Smith, E.; John, D. N.; Kalavala, M.; Edwards, C.; Anstey, A.; Morrissey, A.; Birchall, J. C. *Biomed Microdevices*. **2009**, *11*, 35-47.
- (38) Gill, H. S.; Denson, D. D.; Burris, B. A.; Prausnitz, M. R. *Clin J Pain*. **2008**, *24*, 585-594.
- (39) Davis, S. P.; Marnanto W.; Allen, M. G.; Prausnitz, M. R. *IEEE Trans Biomed Eng*. **2005**, *52*, 909-915.
- (40) Sullivan, S. P.; Murthy, N.; Prausnitz, M. R. *Adv Mater* **2008**, *20*, 933-938.
- (41) DeMuth, P. C.; Min, Y.; Huang, B.; Kramer, J. A.; Miller, A. D.; Barouch, D. H.; Hammond, P. T.; Irvine, D. J. *Nat Mater*. **2013**, *12*, 367-376.
- (42) Yin, D.; Liang, W.; Xing, S.; Gao, Z.; Zhang, W.; Guo, Z.; Gao, S. *Biol Pharm Bull*. **2013**, *36*, 1283-1291.
- (43) Pettis, R. J.; Hirsch, L.; Kapitza, C.; Nosek, L.; Hovelmann, U.; Kurth, H. J.; Sutter, D. E.; Harvey, N. G.; Heinemann, L. *Diabetes Technol Ther*. **2011**, *13*, 443-450.
- (44) Martano, W.; Davis, S. P.; Holiday, N. R.; Wang, J.; Gill, H. S.; Prausnitz, M. R. *Pharm Res*. **2004**, *21*, 947-952.
- (45) Ito, Y.; Ohta, J.; Imada, K.; Akamatsu, S.; Tsuchida, N.; Inoue, G.; Inoue, N.; Takada, K. *J Drug Target*. **2013**, *8*, 770-775.
- (46) Gupta, J.; Denson, D. D.; Felner, E.I, Prausnitz, M. R. *Clin J Pain*. **2012**, *28*, 129-135.
- (47) Qiu, Y.; Gao, Y.; Hu, K.; Li, F. *J Control Release*. **2008**, *129*, 144-150.
- (48) Donnelly, R. F.; Morrow, D. I.; McCrudden, M. T.; Alkilani, A. Z.; Vincente-Perez, E. M.; O'Mahony, C.; Gonzalez-Vazquez, P.; McCarron, P. A.; Woolfson, A. D. *Photochem Photobiol*. **2014**, *90*, 641-647.
- (49) Prausnitz, M. R.; Mikszta, J. A.; Cormier, M.; Andrianov, A. K. *Curr Top Microbiol Immunol*. **2009**, *333*, 369-393.

- (50) Van Damme, P.; Oosterhuis-Kafeja, F.; Van der Wielen, M.; Almagor, Y.; Sharon, O.; Levin, Y. *Vaccine*. **2009**, *27*, 454-459.
- (51) Widera, G.; Johnson, J.; Kim, L.; Libiran, L.; Nyam, K.; Daddona, P. E.; Cormier, M. *Vaccine*. **2006**, *24*, 1653-1664.
- (52) Fernando, G. J.; Chen, X.; Prow, T. W.; Crichton, M. L.; Fairmaid, E. J.; Roberts, M. S.; Frazer, I. H.; Brown, L. E.; Kendall, M. A. *PLoS One*. **2010**, *5*, e10266.
- (53) Andrianov, A. K.; Decollibus, D. P.; Gillis, H. A.; Kha, H. H.; Marin, A.; Prausnitz, M. R.; Babiuk, L. A.; Townsend, H.; Mutwiri, G. *Proc Natl Acad Sci USA*. **2009**, *106*, 18936-18941.
- (54) Weldon, W. C.; Martin, M. P.; Zarnitsyn, V.; Wang, B.; Koutsouanos, D.; Skountzou, I.; Prausnitz, M. R.; Compans, R. W. *Clin Vaccine Immunol*. **2011**, *18*, 647-654.
- (55) Quan, F. S.; Kim, Y. C.; Vunnava, A.; Yoo, D. G.; Song, J. M.; Prausnitz, M. R.; Compans, R. W.; Kang, S. W. *J Virol*. **2010**, *84*, 7760-7769.
- (56) Nicolas, J. F.; Guy, B. *Expert Rev. Vaccines*. **2008**, *7*, 1201-1214.
- (57) Heath, W. R.; Carbone, F. R. *Nat Immunol*. **2013**, *10*, 978-985.
- (58) Villadangos, J. A.; Schnorrer, P. *Nat Rev Immunology*. **2007**, *7*, 543-555.
- (59) Mistilis, M. J.; Bommarius, A. S.; Prausnitz, M. R. *J Pharm Sci*. **2014**, *2*, 740-749.
- (60) Kommareddy, S.; Baudner, B. C.; Bonificio, A.; Gallorini, S.; Palladino, G.; Determan, A.S.; Dohmeier, D. M.; Kroells, K. D.; Sternjohn, J. R.; Singh, M.; Dormitzer, P. R.; Hansen, K. J.; O'Hagan, D. T. *Vaccine*. **2013**, *31*, 3435-3441.
- (61) Levin, Y.; Kochba, E.; Kenney, R. *Vaccine*. **2014**, *32*, 4249-4252.
- (62) Troy, S. B.; Kouliavskaia, J.; Siik, E.; Kochba, H.; Beydoun, O.; Mirochnitchenko, Y.; Levin, Y.; Khardori, N.; Chumakov, Y.; Maldano, Y. *J Infect Dis*. **2015**, *211*, 12.
- (63) Edens, C.; Collins, M. L.; Goodson, J. L.; Rota, P. A.; Prausnitz, M. R. *Vaccine*. **2015**, *33*, 4712-4718.
- (64) Ding, Z.; Bal, S. M.; Romeijn, S.; Kersten, G. F.; Jiskoot, W.; Bouwstra, J. A. *Pharm Res*. **2011**, *28*, 145-158.
- (65) Moon, S.; Wang, Y.; Edens, C.; Gentsch, J. R.; Prausnitz, M. R.; Jiang, B. *Vaccine*. **2013**, *31*, 3396-2402.

- (66) Pearson, F. E.; O'Mahony, C.; Moore, A. C.; Hill, A. V. *Vaccine*. **2015**, *33*, 3248-3255.
- (67) Escobar-Chavez, J. J.; Bonilla-Martinez, D.; Villegas-Gonzalez, M. A.; Molina-Trinidad, E.; Casas-Alanaster, N.; Revilla-Vazquez, A. L. *J. Clin. Pharmacol.* **2011**, *51*, 964-977.
- (68) Lee, J. W.; Park, J. H.; Prausnitz, M. R. *Biomaterials*. **2008**, *29*, 2113-2124.
- (69) Donnelly, R. F.; McCrudden, M. T.; Zaid-Alkilani, A.; Larraneta, E.; McAlister, E.; Courtenay, A. J.; Kearney, M. C.; Singh, T. R.; McCarthy, H. O.; Kett, V. L. Caffarel, S. E., Al-Zahrani, S.; Woolfson, A. D. *PloS One*. **2014**, *9*, e111547.
- (70) Gonzalez-Gonzalez, E.; Speaker, T. J.; Hickerson, R. P.; Spitler, R.; Flores, M. A.; Leake, D.; Contag, C. H.; Kaspar, R. L. *Mol Ther.* **2010**, *18*, 1667-1674.
- (71) Disegi, J. A.; Eschbach, L. *Injury*. **2000**, *S4*, 2-6.
- (72) Banks, S. L.; Pinninti, R. R.; Gill, H. S.; Paudel, K. S.; Crooks, P. A.; Brogden, N. K.; Prausnitz, M. R. *J Pharm Sci.* **2010**, *99*, 3072-3080.
- (73) Gill, H. S.; Prausnitz, M. R. *J Control Release*. **2007**, *117*, 227-237.
- (74) Zhang, D.; Das, D. B.; Rielly, C. D. *J Pharm Sci.* **2013**, *102*, 3632-3644.
- (75) Bhowmik, T.; Souza, B.; Shashidharamurthy, R.; Oettinger, C.; Selvaraj, P.; D'Souza, M. *J. Microencapsul.* **2011**, *28*, 294-300.
- (76) Barry, B.W. *Eur J Pharm Sci.* **2001**, *14*, 101-114.
- (77) 3M. Hollow Microneedle Technology. [http://solutions.3m.com/wps/portal/3M/en\\_WW/3M-DDSD/Drug-Delivery-Systems/Technologies/Microneedle/hollow/](http://solutions.3m.com/wps/portal/3M/en_WW/3M-DDSD/Drug-Delivery-Systems/Technologies/Microneedle/hollow/) (accessed Jan 28 2016)
- (78) Martanto, W.; Moore, J. S.; Kashlan, O.; Kamath, R.; Wang, P. M.; O'Neal, J. M.; Prausnitz, M. R. *Pharm Res.* **2006**, *23*, 1.
- (79) Martanto, W.; Moore, J. S.; Couse, R.; Prausnitz. *J Control Release*. **2006**, *112*, 3.
- (80) Wang, P. M.; Cornwell, M.; Hill, J.; Prausnitz, M. R. *J Invest Dermatol.* **2006**, *126*, 5.
- (81) Norman, J. J.; Arya, J. M.; McClain, M. A.; Frew, P. M.; Meltzer, M. I.; Prausnitz, M. R. *Vaccine*. **2014**, *32*, 16.
- (82) Roxhed, N.; Gasser, T. C.; Griss, G. A.; Holzapfel, A.; Stemme, G. *J of Microelectromech Syst.* **2007**, *16*, 6.

- (83) Gardeniers, H. J. G. E.; Luttge, R.; Berenschot, E. J. W.; DeBoer, M. J.; Yeshurun, S. Y.; Hefetz, M.; Vant' Oever, R.; van Den Berg, A. *Microelectromech Syst.* **2003**, *12*, 6.
- (84) Ma, B.; Liu, S.; Gan, G.; Liu, X.; Cai, H.; Zhang, Z.; Yang, Z. *Microfluidics and Nanofluidics.* **2006**, *2*, 5.
- (85) Haj-Ahmad, R.; Khan, H.; Arshad, M. S.; Rasekh, M.; Hussain, A.; Walsh, S.; Li, X.; Chang, M. W.; Ahmad, Z. *Pharmaceutics.* **2015**, *7*, 486-502.
- (86) Banga, A. K. *Transdermal and Intradermal Delivery of Therapeutic Agents: Application of Physical Technologies.* Taylor and Francis Group. 2011
- (87) Moga, K. A.; Bickford, L. R.; Geil, R. D.; Dunn, S. S.; Pandya, A. A.; Wang, Y.; Fain, J. H.; Archuleta, C. F.; O'Neill, A. T.; DeSimone, J. M. *Adv. Mater.* **2013**, *25*, 5060-5066.
- (88) Park, J. H.; Allen, M. G.; Prausnitz, M. R. *Pharm Res.* **2006**, *23*, 1008-1019.
- (89) Lee, J. W.; Choi, S. O.; Felner, E.; Prausnitz, M. R. *Small.* **2011**, *7*, 4.
- (90) Corium International. Corium Initiates Phase 1 Clinical Trial of Corplex™ Donezipil Transdermal System for the Treatment of Alzheimer's Disease. <http://ir.coriumgroup.com/releasedetail.cfm?releaseid=928725> (Accessed Jan 28 2016)
- (91) Park, J. H.; Allen, M. G.; Prausnitz, M. R. *J Control Release.* **2005**, *104*, 51-66.
- (92) Mukerjee, E. V.; Collins, S. D.; Isseroff, R. R.; Smith, R. L. *Sens Actuators A Phys.* **2004**, *114*, 267-275.
- (93) Wilke, N.; Mulcahy, A.; Ye, S. R.; Morrissey, A. *Microelectronics J.* **2005**, *36*, 650-656.
- (94) Han, M.; Lee, W.; Lee, S. K.; Lee, S. S. *Sens Actuators A Phys.* **2004**, *111*, 14-20.
- (95) Sullivan, S. P.; Koutsonanos, D. G.; Martin, M. P.; Lee, J. W.; Zarnitsyn, V.; Choi, S. O.; Murthy, N.; Compans, R. W.; Skountzou, I.; Prausnitz, M. R. *Nature Med.* **2010**, *16*, 915-920.
- (96) Addae-Mensah, K.; Retterer, S.; Opalenik, S. R.; Thomas, D.; Lavrik, N. V.; Wikswa, J. P. *J Microelectromech Syst.* **2010**, *19*, 64-74.
- (97) Jansen, H. V.; de Boer, M. J.; Unnikrishnan, S.; Louwense, M. C.; Elwenspoek, M. C. *J Micromech Microeng.* **2009**, *19*, 033001.
- (98) Jansen, H. V.; de Boer, M. J.; Legtenberg, R.; Elwenspoek, M. *J Micromech Microeng.* **1995**, *5*, 115-120.

- (99) Donnelly, R. F.; Majithiya, R.; Singh, T. R. R.; Morrow, D. I. J.; Garland, M. J.; Demir, Y. K.; Migalska, K.; Ryan, E.; Gillen, D.; Scott, C. J.; Woolfson, D. A. *Pharm Res.* **2011**, *28*, 41-47.
- (100) Fogarassy, E.; Goehagan, D.; Stuke, M. *Laser Ablation*; Newness. 2012; pp. 515.
- (101) Lipomi, D. J.; Martinez, R. V.; Cademartiri, L.; Whitesides, G. M. *Polymer Science: A Comprehensive Reference*; Elsevier. 2012; pp. 211-231.
- (102) Perennes, F.; Marmiroli, B.; Matteucci, M.; Tormen, M.; Vaccari, L.; Di Fabrizio. *J Micromech Microeng.* **2006**, *16*, 473-479.
- (103) Liu, S.; Jin, M. N.; Quan, Y. S.; Kamiyama, F.; Katsumi, H.; Sakane, T., Yamamoto, A. *J Control Release.* **2012**, *10*, 933-941.
- (104) Kolli, C. S.; Banga, A. K. *Pharm Res.* **2012**, *25*, 104-113.
- (105) Chen, M. C.; Ling, M. H.; Lai, K. Y.; Pramudityo, E. *Biomacromolecules.* **2012**, *13*, 4022-4031.
- (106) Guo, L.; Chen, J.; Qiu, Y.; Zhang, S.; Xu, B.; Gao, Y. *Int J Pharm.* **2013**, *447*, 22-30.
- (107) Park, J. H.; Prausnitz, M. R. *J Korean Phys Soc.* **2010**, *56*, 1223-1227.
- (108) Rosato, D. V., Rosato, M. G. *Injection Molding Handbook*; Springer Science & Business Media. 2012; pp. 1-27.
- (109) Kim, Y. C.; Park, J. H.; Prausnitz, M. R. *Adv Drug Deliv Rev.* **2012**, *64*, 1547-1568.
- (110) Demuth, P. C.; Min, Y.; Irvine, D. J.; Hammond, P. T. *Adv Healthc Mater.* **2014**, *3*, 47-58.
- (111) Donnelly, R. F.; Garland, M. J.; Morrow, D. I.; Migalska, K.; Singh, T. R.; Majithiya, R.; Woolfson, A. D. *J Control Release.* **2010**, *147*, 333-341.
- (112) Olatunji, O.; Das, D. B.; Garland, M. J.; Belaid, L.; Donnelly, R. F. *J Pharm Sci.* **2013**, *102*, 1209-1021.
- (113) Kochhar, J. S.; Quek, T. C.; Soon, W. J.; Choi, J.; Zou, S.; Kang, L. *J Pharm Sci.* **2013**, *11*, 4100-4108.
- (114) Ji, J.; Tay, F. E. H.; Miao, J.; Iliescu, C. *J Micromech Microeng.* **2006**, *16*, 958.
- (115) Badran, M. M.; Kuntsche, J.; Fahr, A. *Eur J Pharm.* **2009**, *36*, 511-523.

- (116) Davis, S. P.; Landis, B. J.; Adams, Z. H.; Allen, M. G.; Prausnitz, M. R. *J Biomech.* **2004**, *37*, 1155-1163.
- (117) Romgens, A. M.; Bader, D. L.; Bouwstra, J. A.; Baaijens, F. P.; Oomens, C. W. *J Mech Behav Biomed Mater.* **2014**, *40*, 397-405.
- (118) F42 Committee. *Terminology for Additive Manufacturing Technologies*; ASTM International: West Conshohocken, PA, 2012; pp 1–3.
- (119) Kruth, J. P.; Leu, M. C.; Nakagawa, T. *CIRP Annals- Manufact Tech.* **1998**, *47*, 525-540.
- (120) Gibson, I.; Rosen, D.; Stucker, B. *Additive Manufacturing Technologies*; 2<sup>nd</sup> ed.; Springer. 2015
- (121) Ahmad Martin. Rapid prototyping- 3Dimensional Printing. <http://martin-engineer.blogspot.com/2012/03/rapid-prototyping-3-dimensional.html> (Accessed Jan 29 2016)
- (122) Rapid Prototyping Center: Selective Laser sintering. [http://www.rpc.msos.edu/machines\\_slis.php](http://www.rpc.msos.edu/machines_slis.php) (Accessed Jan 29 2016)
- (123) Polyjet matrix 3D Printing Services Process. <http://proto3000.com/polyjet-matrix-3d-printing-services-process.php> (Accessed Mar 3 2016)
- (124) Solidsmack. Stereolithography down to 1/10 of a micron. <http://www.solidsmack.com/fabrication/stereolithography-110-micron-old-world-laboratories-nano-3d-printer/> (Accessed Jan 29 2016)
- (125) Mecham, S. J.; Januszewicz, R.; Fox, C.; Chen, S.; Rolland, J.; Hopkinson, N.; DeSimone, J. M. *Nature Rev Mat.* **2016**, under review.
- (126) Johnson, W. M.; Rowell, M.; Deason, B.; Eubanks, M. In *Proceeding of the 22<sup>nd</sup> Annual International Solid Freeform Fabrication Symposium.* **2011**, 197-211.
- (127) Melchels, F. P. W.; Feijen, J.; Grijpma, D. W. *Biomaterials.* **2010**, *31*, 6121-6130.
- (128) Texas Instruments. DLP Products & MEMS. <http://www.ti.com/lscs/ti/dlp/advanced-light-control/microarray-greater-than-1million-products.page?paramCriteria=no> (Accessed Jan 31 2016)

- (129) Rothbot's Microscopy. <http://rothbot.blogspot.com/2009/06/dlp-mirrors.html> (Accessed Jan 31 2016)
- (130) Bothun, G. The Evolution of Display Technologies Continued. <http://home-work-uoregon.edu/pub/class/155/out155/dt2.html> (Accessed Jan 31 2016)
- (131) Zhou, C.; Chen, Y.; Zhigang, Y.; Khoshnevis, B. *J Rapid Prototyping*. **2013**, *19*, 153-165.
- (132) Tumbleston, J. R.; Ermoshkin, A.; Shirvanyants, D.; Ermoshkin, N.; Januszewicz, R.; Johnson, A. R.; Kelly, D.; Chen, K.; Pinschmidt, R.; Rolland, J. P.; Samulski, E. T.; DeSimone, J. M. *Science*. **2015**, *347*, 1349-1352.
- (133) Lu, Y.; Mantha, S. N.; Crowder, D. C.; Chinchilla, S.; Shah, K. N.; Yun, Y. H.; Wicker, R. B.; Choi, J. W. *Biofabrication*. **2015**, *7*, 045001.
- (134) Yun, H.; Kim, H. *J Mech Sci Tech*. **2013**, *10*, 2973-2978.
- (135) Gittard, S. D.; Ovsianikov, A.; Chichkov, B. N.; Doraiswamy, A.; Narayan, R. J. *Expert Opin Drug Deliv*. **2011**, *7*, 513-533.
- (136) Gittard, S. D.; Ovsianiov, A.; Monteiro-Riviere, N. A.; Lusk, J.; Morel, P.; Minghetti, P.; Lenardi, C.; Chichkov, B. N.; Narayan, R. J. *J Diabetes Sci Technol*. **2009**, *3*, 304.
- (137) DeSimone, J. M.; Ermoshkin, Alexander.; Samulski, E. T. *US Patent 9211678B2*. Washington, D. C.; US Trademark and Patent Office

## CHAPTER 2 FABRICATION OF MICRONEEDLES USING A MODEL RESIN

### 2.1 Introduction

The aim of this research is to fabricate microneedles using a new additive manufacturing technique called Continuous Liquid Interface Production (CLIP). As described in Chapter 1, CLIP provides unique potential to rapidly generate high resolution structures because it enables continuous, rather than “layer-by-layer” production of a part. Continuous production eliminates the mechanical separation steps that can damage small structures and enables very thin slicing of the part without increasing fabrication times (Figure 2.1A). A schematic diagram of a CLIP system is shown in Figure 2.1B.

As described in Chapter 1, CLIP systems contain a light source that illuminates a DLP chip. A DLP chip is an array of computationally controlled micromirrors that generates a UV

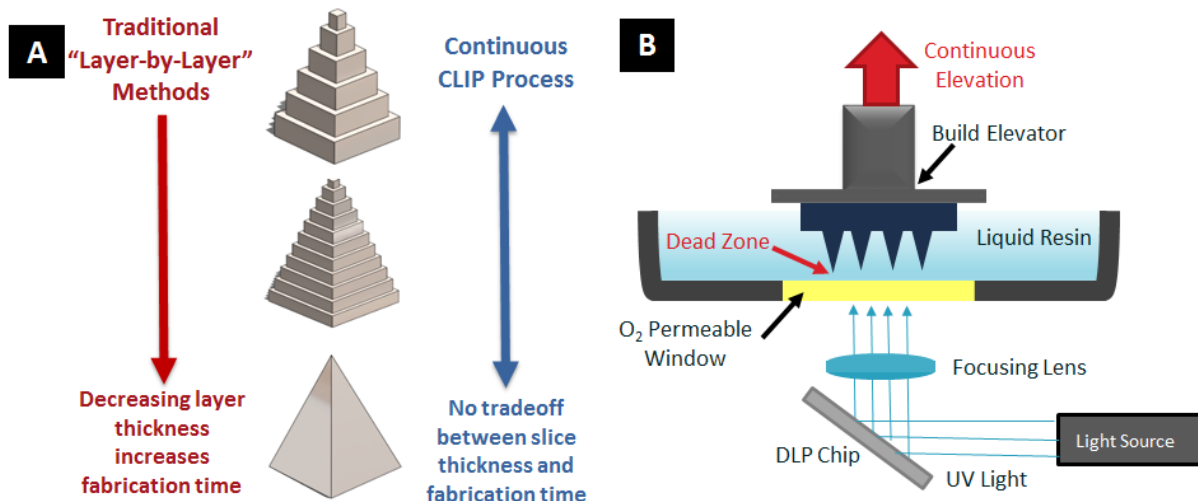


**Figure 2.1 CLIP schematic** A) The continuous CLIP process eliminates the tradeoff between slice thickness and fabrication time to enable rapid production of high resolution parts B) Diagram showing the essential components of a CLIP system

light movie in the shape of a Computer Aided Design (CAD) file. This UV movie illuminates through a series of lenses that focus the light on an oxygen permeable window in the bottom of a vat of photoreactive resin. A build elevator moves continually upward as the UV movie plays, allowing the desired part to grow on the build elevator via photopolymerization of the resin. A detailed description of the steps required for successful Continuous Liquid Interface Production and some theoretical considerations involved with each step are provided here.

### **2.1.1 Step 1- Generation and Slicing of CAD File**

As mentioned in Chapter 1, additive manufacturing processes start with a computer aided design (CAD) file of the desired part. This part is then computationally sliced into cross-sections along the z axis. In a typical “layer-by-layer” stereolithography process, a single cross-section is projected onto the window for a specified length of time to cure the first layer onto the build platform by photopolymerization (Figure 1.15).<sup>1</sup> This layer is then mechanically separated from the window and realigned prior to exposing the resin to the projection that forms the next layer. The process of curing the resin and mechanically separating and realigning the part is repeated to form the final part in a “layer-by-layer” fashion.

CLIP’s deadzone eliminates the need for mechanical separation and realignment of the part, enabling part production to proceed continuously, rather than in a “layer-by-layer” fashion (Figure 1.15). Because the mechanical separation and realignment steps are rate-limiting in traditional processes, CLIP’s continuous movement reduces fabrication times for high resolution objects by enabling infinitely thin slicing of the computer aided design file without concomitant increases in fabrication times. Such infinitely thin cross-sectional slices are projected off of a DLP chip in rapid succession (as opposed to long, discrete frames) to form a UV movie. An example of such cross-sectional slices is shown in Figure 2.2. Of note, the DLP chips used

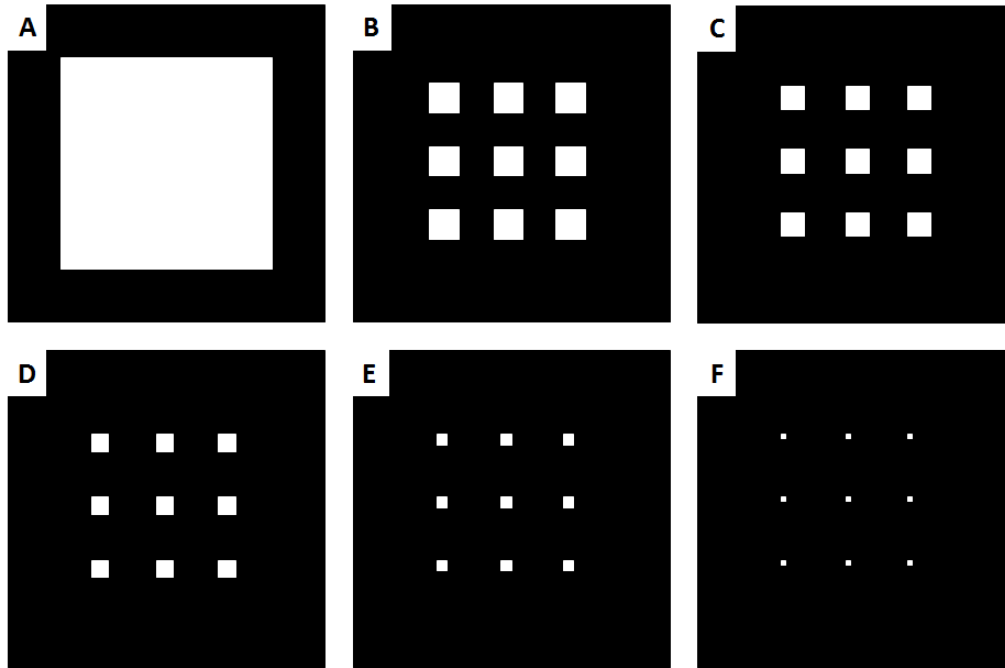


**Figure 2.2 Representative image of a computationally sliced microneedle patch.** Several microneedle array cross-sections moving from the A) microneedle patch backing, through B-F) the base and tip of the microneedles within the array. Note that only a small number of the thin cross-sections are displayed.

throughout this dissertation have refresh rates on the order of 4,000 to over 32,000 Hz.<sup>2-3</sup>

Therefore, DLP refresh rate is not a rate limiting step to CLIP. For example, the maximum build speed for an object sliced at one micron spacing would be over 4 millimeters per second, or 14.4 meters per hour, for these DLP chips if build speed were limited by DLP refresh rate alone. The fastest build speeds utilized in this dissertation are on the order of hundreds of millimeters per hour. Other factors, namely the rate of the polymerization reaction, have been shown to play a more important role in maximizing build speed.

This UV projection induces the photopolymerization that produces the final part. Image projection is described in further detail in the following section.

### 2.1.2 Step 2- Projection of the Image

As shown in Figure 2.1, a light source (UV LED,  $\lambda=370\text{nm}$ ) is projected onto a DLP chip. This DLP chip is a series of micromirrors, which typically range in size from  $\sim 7 \times 7$  to

~13x13 $\mu\text{m}$  in width.<sup>2-3</sup> Each mirror can be turned on or off by adjusting the tilt angle of the micromirror relative to the incoming light. When the micromirror tilts to face the incoming light source (the “ON” position), the light is reflected off of the micromirror towards the build window. Conversely, when the micromirror faces away from the incoming light source (the “OFF” position), light is not reflected off of the micromirror towards the build window. Computationally controlling the micromirror array creates a patterned light projection in the shape of the CAD file; micromirrors within the specified object are turned “ON”, whereas micromirrors outside of the specified object are turned “OFF”.

The light intensity distribution at the window surface influences the maximum resolution of the additive manufacturing system and the size and shape of the resulting part. Importantly, the light intensity distribution at the window surface is different from the light intensity distribution reflecting directly off of the micromirror array because of the way that the system’s lenses focus incoming light onto the build window. The differences between the light projecting off of the DLP chip (input) and the light distribution at the window surface (output) are described here, first according to the basic theory of ray optics followed by a more nuanced discussion of Gaussian optics. The fundamental difference between these two models is that the first assumes that light propagates in straight lines along a single direction, whereas the second model also considers the periodic nature of propagating electromagnetic wavefronts.

### **2.1.2.1 Image Magnification as Predicted by Ray Optics**

The magnification of an image,  $M$ , can be calculated using traditional geometric optics using a ray diagram, such as the one shown in Figure 2.3. Such a ray diagram is based off of the basic postulates that light is propagated in straight lines in homogenous medium, but refracts

according to Snell's law as it passes through distinct media. The magnification of the imaged object is defined by

$$M = -\frac{h_o}{h_i} \quad (2.1)$$

where  $h_i$  is defined as size of the image and  $h_o$  is the size of the original object. Using basic trigonometry, it can be shown that the magnification at the focal point can be equivalently represented by the equation

$$M = \frac{d_o}{d_i} \quad (2.2)$$

where  $d_o$  is the distance between the object and the lens and  $d_i$  is the distance between the object and the lens. Substituting Equation 2 into the thin lens equation (Equation 2.3)

$$\frac{1}{f} = \frac{1}{d_o} + \frac{1}{d_i} \quad (2.3)$$

yields an alternate solution for the magnification, as a function of the focal length of the lens and the distance between the object and the lens relative to its focal point.

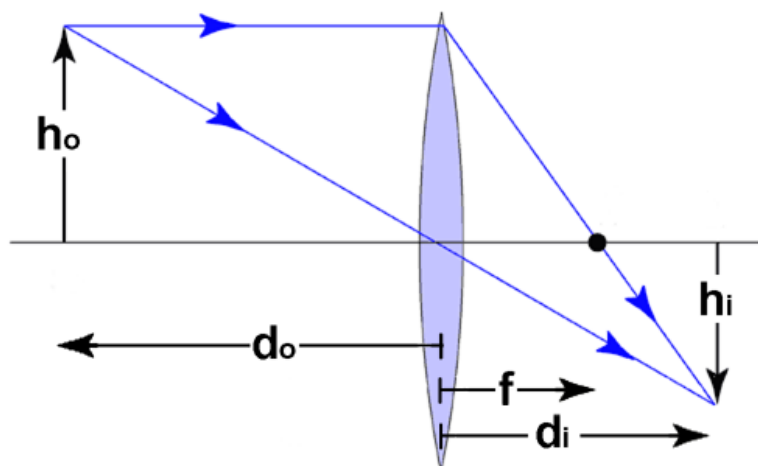


Figure 2.3 Ray diagram of an object imaged by a double convex lens

$$M = \frac{f}{f-d_o} \quad (2.4)$$

Therefore, the size of an individual pixel (e.g. pixel magnification) at the build area can be altered by changing a lens's focal length and the distance between the lens and the DLP chip. This pixel size is an important determinant of optical resolution. The minimum size of an object that can be produced, and the minimum spacing between such objects, is theoretically equal to this pixel size. Pixel size can also be utilized (in combination with the spacing between pixels) to calculate how many pixels per square inch (PPI), equivalently called dots per square inch (DPI) are used in this projection. DPI is another commonly used metric for resolution.

It is important to note that while the magnification of an individual pixel is an important, tunable variable in the design of a CLIP system, the total object magnification is typically held constant at one in our studies because we seek to fabricate an object that matches a CAD file. The total number of pixels used to project an object increases as pixel size decreases to maintain constant object magnification.

### 2.1.2.2 Image Projections Predicted by Gaussian Optics

Light propagates in waves, with each wave satisfying the wave equation (Equation 2.5)

$$\frac{d^2u}{dt^2} - c^2\nabla^2u = 0 \quad (2.5)$$

where  $c$  is the velocity of light,  $t$  is time, and  $u$  is a scalar function for positions as a function of time. This linear wave function is subject to the principle of superposition, in which the total wave form is formed by addition of the individual waves. This interference between waves complicates the simplistic representation of light intensity distributions represented using ray optics. Further, although ray optics assumes that light travels in a line wave fronts actually travel

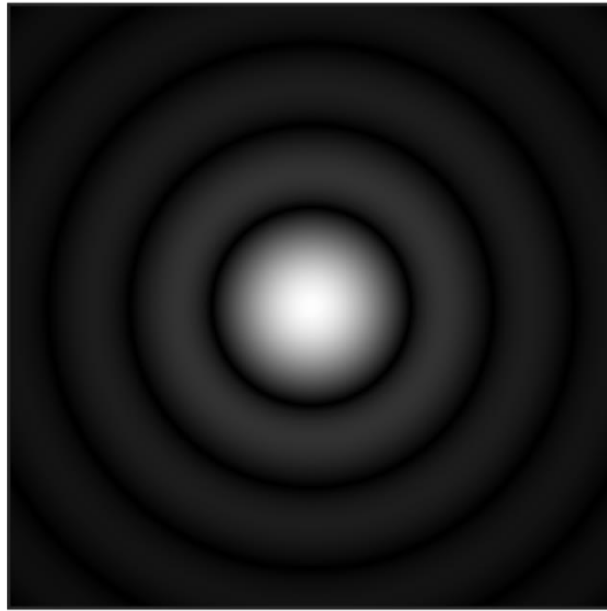


**Figure 2.4 Airy Disk. An airy disk is the point spread function of a diffraction-limited lens**

in all directions. Due to the highly complex nature of summing electromagnetic radiation in all directions, a paraxial (or Fresnel) approximation is often used, where only light making small angles with the direction of propagation is considered.<sup>4</sup> This assumption can be considered valid when the imaging plane is close to the lens (typically at the focal length or closer). It allows propagating waves to be summed to determine the total light intensity distribution that results from a focusing lens.

While ray optics predict that the lens simply magnifies or de-magnifies the image, real lenses are subject to diffraction and various aberrations. Some aberrations include spherical aberrations, caused by the fact that most lenses are spherical rather than a more ideal partial ellipsoid and achromatic aberrations introduced by differences in the wavelengths of incoming light rays, among others. Even in the absence of such aberrations, however, all lenses are limited by diffraction. For a perfect, diffraction-limited lens, a perfect point source is projected as an Airy disc (Figure 2.4), which results from interference of interacting wave forms. The Airy disk is

called the system's point spread function (PSF), defined as the focused response (output) of a system when the input is a perfect point source.<sup>4</sup> This PSF can also be more generally termed an impulse response for a system that is not in perfect focus. The first null of this Airy disc is often approximated as a Gaussian function with a radius (or "spot size") given by Equation 2.6

$$2w_0 = \frac{1.22f\lambda}{D} \quad (2.6)$$

where  $w_0$  is the radius of the spot,  $f$  is the focal length of the lens,  $\lambda$  is the wavelength of the input light, and  $D$  is the aperture of the lens.<sup>4</sup> If a lens produces a spot size that is close to the predicted size  $w_0$ , the lens is said to be "diffraction-limited". If the spot size produced by the lens is much larger than  $w_0$ , the lens is said to be "instrument-limited".

In addition to diffraction and aberrations, many optical systems are subject to imperfect focus, which also affects the system's response to a given input. As shown in Figure 2.5, the width of a beam of light is the smallest at the "beam waist", which is located at the focal point of the lens.<sup>4</sup> Therefore, a diffraction-limited lens projecting a point source in perfect focus would have a beam waist with a radius defined by Equation 2.6, as previously established. However, as

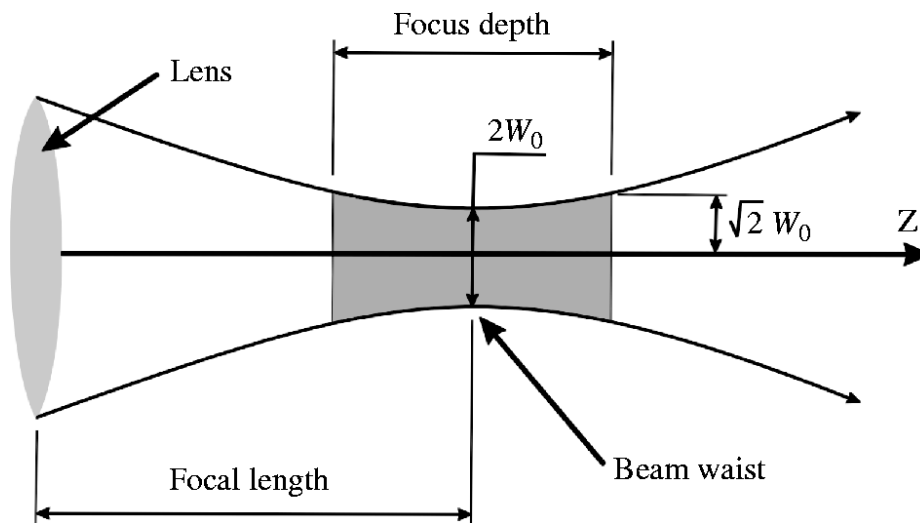


**Figure 2.5** Beam width is minimized at the focal plane but is wider than the point predicted by ray optics

the image plane moves further and further from the focal point, the width of the beam increases, thereby decreasing the resolution of the system. The increase in the radius at the imaging plane as it moves away from the focal point can be described by Equation 2.7. <sup>4</sup>

$$w(z) = w_0 \sqrt{1 + \left(\frac{z}{z_R}\right)^2} \quad (2.7)$$

where  $w_0$  is, again, the radius of the spot at the focal plane,  $z$  is the distance of the imaging plane from the focal plane, and  $z_R$  is the Raleigh length given by Equation 2.8.

$$z_R = \frac{\pi w_0^2}{\lambda} \quad (2.8)$$

The Raleigh length is defined as the distance from the focal point to the point at which the spot size doubles (measured along the axis of light propagation). Therefore, accurately focusing at the focal length is important to ensuring optimal performance of the optical system.

Together, these effects (magnification, wave interference, lens diffraction, and accuracy of focus) provide a theoretical basis for differences in light distributions before and after interaction with a focusing lens. These mathematical calculations assume that the light input is a perfect point radiator. However, no such point source exists in nature; this point source is simply a mathematical construct used to model and understand optical imaging systems. When modeling a real system, the image produced by the lens is actually represented by the convolution of the input light distribution and the lens's impulse response at the imaging plane. Although complete modeling of the optical system used in CLIP additive manufacturing systems is outside of the scope of this dissertation, these fundamental relationships will be useful to understanding the experimental results presented in this chapter.

### 2.1.3 Step 3- Photopolymerization of the Part

#### 2.1.3.1 Photopolymerization Kinetics

The shape and intensity of the resulting light projection directly affects the structure of the photopolymerized part. Photopolymerization is known to proceed in three different steps: initiation, propagation, and termination, which are described by the chemical equations below.<sup>5</sup>

Initiation occurs when an initiator I is irradiated to produce an excited state by absorption of light photons, which subsequently undergoes hemolysis to produce two free radicals R.



This free radical can then attack a double bond within a photoreactive monomer, using one of the electrons within the double bond to form a single bond between the initiator and monomer. This complete process (Equations 2.9-2.11) is termed “initiation”. The other electron from the double bond returns to the second atom, which forms another free radical that continues to propagate the chain. Subsequent addition of monomer to the growing chain is termed “propagation” (Equation 2.12). The mechanism of free radical polymerization of acrylate monomer is shown in Figure 2.6.



Termination of the polymer chain can occur via one of three different mechanisms: combination, disproportionation, or chain transfer. Combination occurs when two active chain ends join together to form one long chain (Equation 2.13), as shown below.



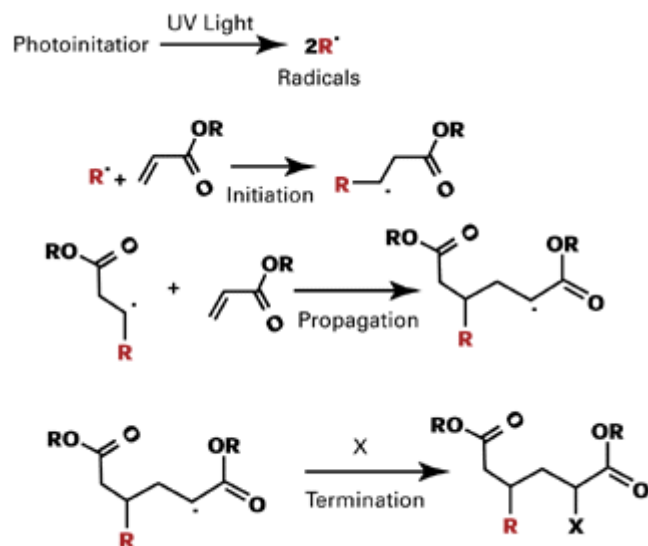


**Figure 2.6 Mechanism of free radical photopolymerization of acrylates.** Figure reproduced with permission from reference 6.

Disproportionation occurs when a hydrogen is abstracted from one chain end to produce one polymer with a terminal saturated group and another polymer with a terminal unsaturated group (Equation 2.14), as shown below.



Lastly, chain transfer occurs when the free radical on the growing polymer chain is abstracted by another molecule ( $XR'$ ), which begins to propagate a new chain (Equation 2.15).



Basic combination of the rate equations for each of these steps yields Equation 2.16 for the total rate of radical photopolymerization, as described elsewhere.<sup>5</sup>

$$R_p = k_p[M] \left( \frac{R_i}{k_t} \right)^{\frac{1}{2}} \quad (2.16)$$

where  $k_p$  is the polymerization rate constant,  $[M]$  is the monomer concentration,  $k_t$  is the termination rate constant, and  $R_i$  is the rate of initiation given by Equation 2.17

$$R_i = 2\phi k_d [I] \quad 2.17)$$

where  $\phi$  is initiator efficiency,  $[I]$  is the concentration of initiator, and  $k_d$  is the rate constant for dissociation of photoinitiator. Therefore, polymerization rates are dependent on the amount of initiator and the efficiency of its dissociation as well of the amount of monomer and the efficiency of monomer combination. The rate limiting step of such photopolymerization reactions, however, is typically the rate of initiation, because the rate constant for hemolysis is typically much smaller than the rate constant for propagation of the polymer chain. The quantitative relationship between light intensity distributions and the size and shape of the resulting part will be discussed both in Chapter 3 and Appendix B. Here, it is sufficient to state that the amount of light required to initiate photopolymerization must be above a certain threshold. Above this threshold, photopolymerization of the part occurs whereas below this minimum amount of light, no photopolymerization forms and the part is not formed. In this way, polymerized parts can provide insight into the light distributions projected by additive manufacturing systems.

#### **2.1.4 Chapter Objective**

Using early prototypes of CLIP systems, this chapter presents investigations into the role of four important variables on the morphology and dimensions of CLIP microneedle arrays. These variables are 1) the intensity of the light source, given in  $\text{mW}/\text{cm}^2$ , 2) the build speed given in  $\text{mm}/\text{hr}$ , 3) the optical system responsible for focusing the image from the DLP chip onto the build window, and 4) the software system that converts a CAD file into instructions for the

DLP chip. The theory presented in this introduction will serve as a useful platform for interpreting experimental results.

We demonstrate that proper optimization of these four variables enables production of microneedle arrays via CLIP. This additive manufacturing based approach can be utilized to rapidly alter microneedle design parameters, including microneedle size, shape, spacing and aspect ratio with the potential to improve therapeutic outcomes.

## 2.2 Results and Discussion

### 2.2.1 CLIP File Path

In order to generate parts using CLIP, a series of steps were taken. First, a CAD file of a desired microneedle array was designed using Solidworks 2014 3D modeling software and saved in standard tessellation language (.STL) format. This file format defines the surface topology of the part as a series of triangles. It eliminates unnecessary information typically associated with



**Figure 2.7 CLIP file path**

the CAD file, such as color, lighting and surface texture. The .STL file was then sliced in  $1\mu\text{m}$  sections along the z axis using the opensource software Slic3r to generate a Scaleable Vector Graphics (.SVG) file containing the object's coordinates on each slice. This .SVG file is referenced by a component of Carbon3D's custom software called a graphic device interface (GDI), which converts the .SVG file to a bitmap sent to the DLP chip. This bitmap controls which micromirrors are turned on and off at each point during production of the part. The

components of the CLIP system, including the light source and build elevator, are controlled by a LUA script written by the user. More information regarding .LUA scripts is provided in Appendix A. A graphic outlining the file path used in the CLIP process is given in Figure 2.7

### 2.2.2 Role of Light Intensity and Build Speed on Microneedle Production Using an Early Prototype

We first sought to determine the impact that light intensity and build speed have on the fabrication of microneedles using CLIP. Of note, throughout this dissertation, the terms “build parameters” or “print parameters” will be used to refer to a particular combination of light intensity and build speed. In this chapter, we utilize a model resin composed of trimethylolpropane triacrylate (TMPTA) mixed with 2.5 wt% diphenyl (2,4,6-trimethylbenzoyl) phosphine oxide (TPO) as a photoinitiator. TMPTA was chosen because it is a fast-reacting, low viscosity material that has previously been used in stereolithography.<sup>6</sup> TPO is a type 1 photoinitiator selected based on its solubility, high efficiency, and absorbance at 365-370nm. The structure and absorption spectrum of TPO and the structure of TMPTA are given in Figure 2.8.

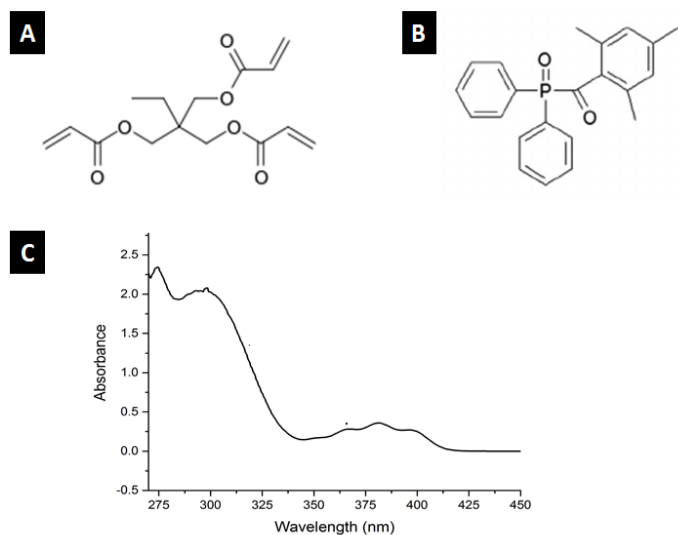


**Figure 2.8 Structure and absorbance of resin components A) Structure of TMPTA B) Structure of TPO and C) Absorption spectrum of TPO over wavelengths of 260 to 450nm**

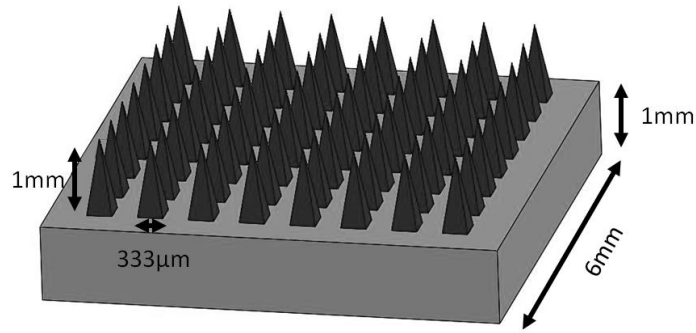


**Figure 2.9 Microneedle CAD file.** A CAD File of an 8x8 array of 1000 $\mu\text{m}$  tall microneedles measuring 333 $\mu\text{m}$  in width spaced at 333 $\mu\text{m}$  on a 1mm thick backing was used throughout chapter 2

In order to determine the effect light intensity and build speed on microneedle morphology, a computer aided design file containing microneedles measuring 1000  $\mu\text{m}$  tall and 333 $\mu\text{m}$  wide was generated (Figure 2.9) and sliced along the z axis. CLIP3, an additive manufacturing system prototype, was then utilized to produce microneedles with a range of light intensities and build speeds. Scanning electron micrographs (SEMs) of microneedles produced using 1 to 4  $\text{mW}/\text{cm}^2$  of light at build speeds ranging from 25mm/hr to 200mm/hr are shown in Figure 2.10.

Several important observations regarding the effect of light intensity and build speed were made. Microneedles produced with 1  $\text{mW}/\text{cm}^2$  of light (Figure 2.10 A-C) generally looked “under-exposed”, meaning that the microneedles are shorter and thinner than the input CAD file shown in Figure 2.4. In some cases (Figure 2.10C), the base of the microneedle array even failed to cure, leaving large holes in the substrate. Increasing speed (moving from left to right in Figure 2.5) while holding light intensity constant further reduced the cured volume; both the size of the microneedles and the amount of curing between needles decreased with increasing speeds. This reduction in the cured volume occurred because the total exposure time per slice decreased with increasing speed, thereby reducing the total amount of light utilized to produce the part. The specific mechanisms that dictate cured volume will be further discussed in Chapter 3. When a

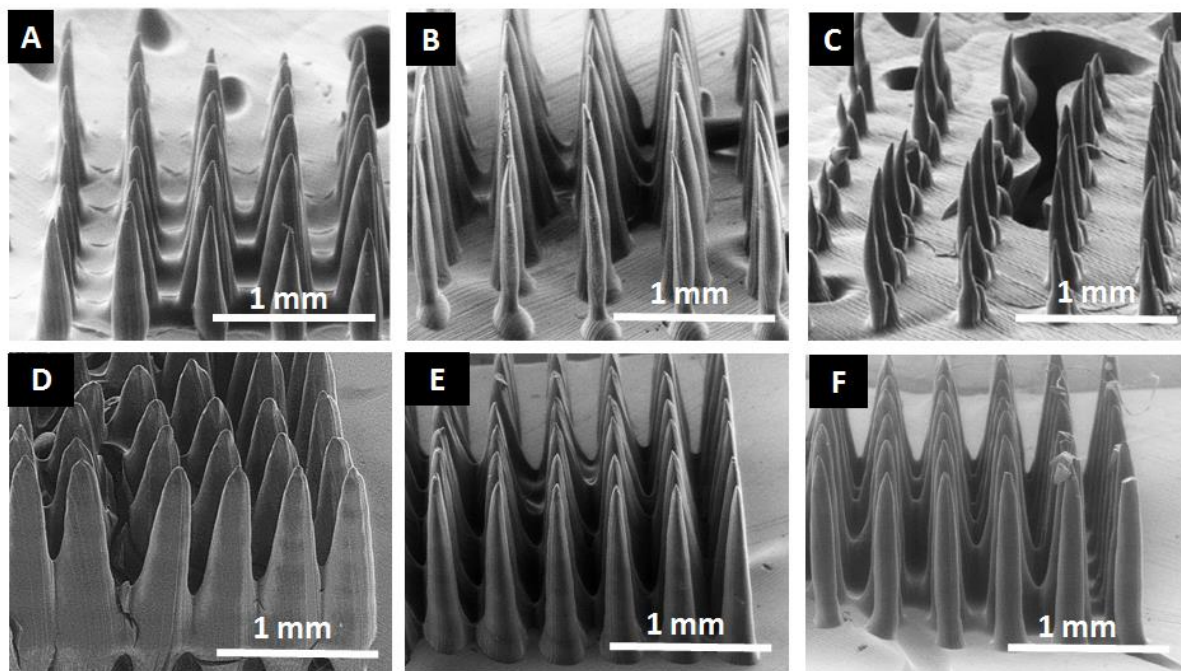


**Figure 2.11 Impact of light intensity and build speed on microneedle morphology.** Top row is produced using 1 mW/cm<sup>2</sup> of light at build speeds of A) 25mm/hr, B) 100 mm/hr, and C) 200 mm/hr. Bottom row is produced using 4 mW/cm<sup>2</sup> of light at build speeds of D) 25 mm/hr E) 100 mm/hr and F) 200 mm/hr

higher light intensity is used (4 mW/cm<sup>2</sup>, Figure 2.10 D-F), microneedles became much larger.

Although some structures looked more similar to the desired CAD file (Figure 2.10E) than others, much of the material between needles cured at this higher light intensity. Similarly to the series produced with 1 mW/cm<sup>2</sup> of light, increasing build speed reduced the dimensions of structures produced with 4 mW/cm<sup>2</sup> of light. Together, these results suggest that light intensity and build speed have opposite effects on part dimensions. Increasing light intensity increased part dimensions, whereas increasing build speed decreased part dimensions. **Importantly, however, these results demonstrate that no combination of light intensity and build speed produced high quality microneedles. Therefore, we sought to make improvements to this initial printer prototype to enable microneedle fabrication.**

### 2.2.3 Effect of System Optics on a Resolution Test Pattern

The poor microneedle morphology exhibited in Figure 2.5 established a need to improve the performance of CLIP prototypes for microneedle production. In order to more easily compare the performance of each new prototype, a test part called a resolution test pattern (RTP) was designed. This RTP, shown in Figure 2.11G, contains sets of four squares measuring  $500\mu\text{m} \times 500\mu\text{m}$ ,  $250\mu\text{m} \times 250\mu\text{m}$ , and  $125\mu\text{m} \times 125\mu\text{m}$ , moving from bottom to top right, respectively. All squares are spaced at one width apart. Because each of these sets of squares represents the cross section of microneedle arrays of different sizes, this RTP provides an easy way to determine the dimensions of the smallest microneedles that could be produced using a given CLIP system.

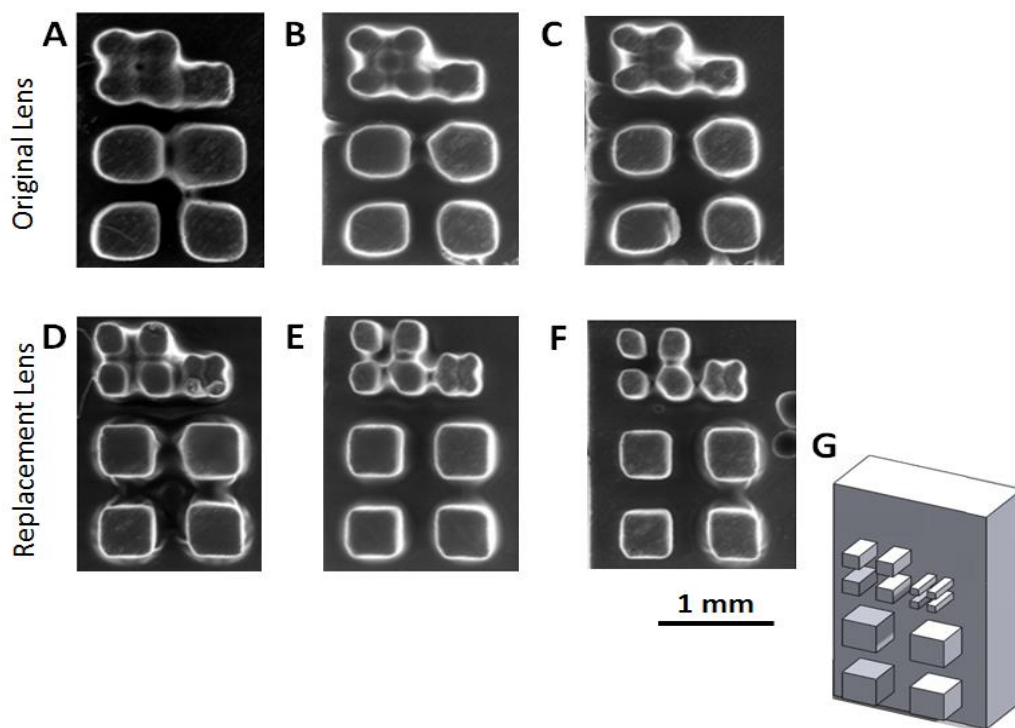


**Figure 2.13 Effect of lens focal length on resolution.** The top row is fabricated using an initial, low resolution lens setup with focal lengths of 50 and 75mm at A) 50 mm/hr B) 100mm/hr and C) 150 mm/hr. The bottom row is fabricated using a high resolution lens setup with focal lengths of 75 and 100mm at D) 50 mm/hr E) 100 mm/hr and F) 150 mm/hr G) CAD file used to print the RTP.

An experiment was designed to determine whether improvements to the prototype's optical system could improve microneedle morphology. The RTP shown in Figure 2.11G was printed using two different lens setups. The first lens, containing two achromatic doublets with focal lengths of 50 and 75mm, was replaced with a different lens, containing two achromatic doublets with focal lengths of 75 and 100mm. Lenses were spaced at 25.4 cm apart for both systems. The distance between the lens and the window surface was adjusted until the image appeared to be in focus. The combined focal length of each system was determined to be 14.8 mm and 21.2 mm for the original and replacement lenses, respectively. As described in Equation 2.4, increasing the focal length de-magnifies each pixel, thereby reducing the size of each projected pixel from  $16\mu\text{m} \times 16\mu\text{m}$  to  $8\mu\text{m} \times 8\mu\text{m}$  (convolved with the unknown impulse response of the system). Decreasing pixel size increases the number of dots per inch (DPI) to improve the theoretical resolution of the system.

SEMs of of the RTP fabricated using the two different lens setups are given in Figure 2.11. Figure 2.11A-C are produced using the low resolution lens setup at 50mm/hr, 100mm/hr and 150mm/hr, respectively. Figure 2.11D-F are produced using the high resolution lens setup with equivalent build speeds. Reducing the pixel size by changing the lens was observed to dramatically increase the quality of the produced part. Notably, the  $250 \times 250\mu\text{m}$  features that are not resolved with the low resolution lens setup in Figures 2.11A-C, begin to separate into distinct squares in Figure 2.11F. The quality of the larger,  $500 \times 500\mu\text{m}$  squares, which are fairly circular when printed with the low resolution lens setup, also substantially improves when using the high resolution lens setup (Figure 2.11D-G). **Therefore, we concluded that although light intensity and build speed have an effect on part dimensions and quality, the printer's optical system is the primary driver of the quality of parts produced on a small scale.** This can be expected

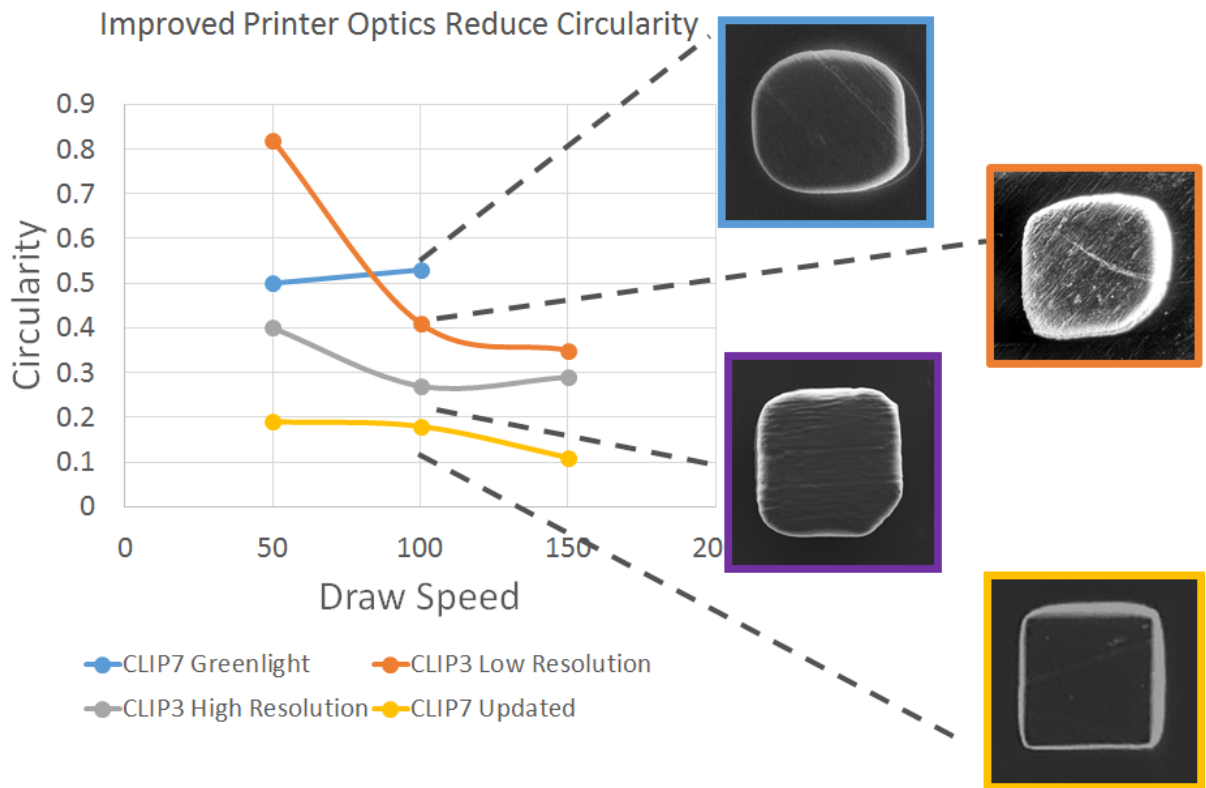


**Figure 2.15 Circularity improves with improved printer optics** A) Method for calculating circularity. Circularity of  $500\mu\text{m}$  squares printed with B)  $2\text{ mW}/\text{cm}^2$ , C)  $4\text{ mW}/\text{cm}^2$ , D)  $6\text{ mW}/\text{cm}^2$  and E)  $8\text{ mW}/\text{cm}^2$  of light. Minimizing circularity results in improvements in the quality of the  $500\mu\text{m}$  because the input light distribution coming off of each individual pixel is smaller. Even though the impulse response of the system is unknown, it could be expected that the output light distribution would be smaller if the input light distribution is smaller, even after convolution with the impulse response. It is worth noting that the optical system produced using the replacement lenses was very non-ideal. Using Equation 2.6 to calculate the radius of the spot size for a diffraction limited 4F system containing a 75mm and 100mm doublets produces a diffraction limited spot size of less than 1nm. Therefore, our system is clearly instrument limited rather than diffraction limited. Further optimization of the optical system should lead to improved resolution. We consequently chose to focus on continuing to improve printer optics using the

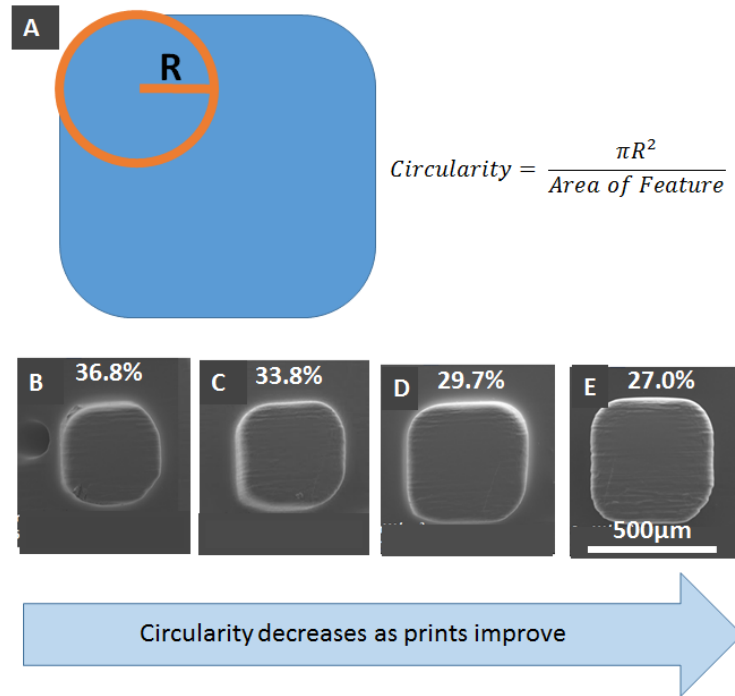


**Figure 2.16 Circularity calculation and validation** A) Method for calculating circularity. Circularity of 500 $\mu$ m squares printed with B) 2 mW/cm<sup>2</sup>, C) 4 mW/cm<sup>2</sup>, D) 6 mW/cm<sup>2</sup> and E) 8 mW/cm<sup>2</sup> of light. Minimizing circularity results in improvements in the quality of the 500 $\mu$ m square

square resolution test pattern. In total, four different optical systems were investigated over a range of different light intensities and build speeds.

To compare the quality of the RTP resulting from each optical system and build parameter combination, a quantitative measure of the quality of the squares produced was developed. This measure, termed “circularity”, quantifies how rounded the corners of each fabricated square are (Figure 2.12). Briefly, circularity is calculated by taking the area of a circle whose radius is the radius of curvature of the corner of the square and dividing it by the total area of the square (Figure 2.12A). For a round circle, this function is one. For a perfect square with infinitely sharp corners, this function is zero. Therefore, we sought to minimize circularity by improving the printer’s optical system.

In order to establish that circularity is a valid approach for assessing the quality of a 3D printed square, RTPs were produced using light intensities ranging from 2 mW/cm<sup>2</sup> to 8mW/cm<sup>2</sup> at a build speed of 100 mm/hr. The circularity of a 500 μm x 500μm square from each array was calculated as shown in Figure 2.12.

Therefore, we compared the circularity of 500μm squares printed using four different optical setups and a range of different print parameters in an effort to identify the best optical system. The specifications for each CLIP system are provided in Table 1 and Table 2 for the CLIP7 and CLIP3 respectively (see materials and methods). An ideal system would minimize the circularity of each square. The results of this study are shown in Figure 2.13. Of the four different optical systems tested (CLIP3 low resolution, CLIP3 high resolution, CLIP7 Greenlight, CLIP7 updated), the updated CLIP7 optical system was most effective, producing the sharp 500μm square shown in yellow. With these improvements to the optical system, we moved forward with the production of microneedles for transdermal drug delivery in Section 2.2.4. It should be noted that a more thorough, mathematical analysis of the impulse response of the optical system could provide further improvements in optical performance. However, because the ultimate goal of this work was to fabricate microneedles for transdermal drug delivery, we moved forward with microneedle production.

#### **2.2.4 Role of Light Intensity on Microneedle Dimensions Using Updated CLIP7**

After improving the optical system, which was shown to play a dominant role in part quality (section 2.2.2), we revisited the effect of light intensity on microneedle production. Because light intensity and build speed were found to have opposite effects on microneedle dimensions (Figure 2.10), we chose to isolate the effect of light intensity by holding build speeds constant at 100 mm/hr throughout this experiment. This constant 100mm/hr build speed provides

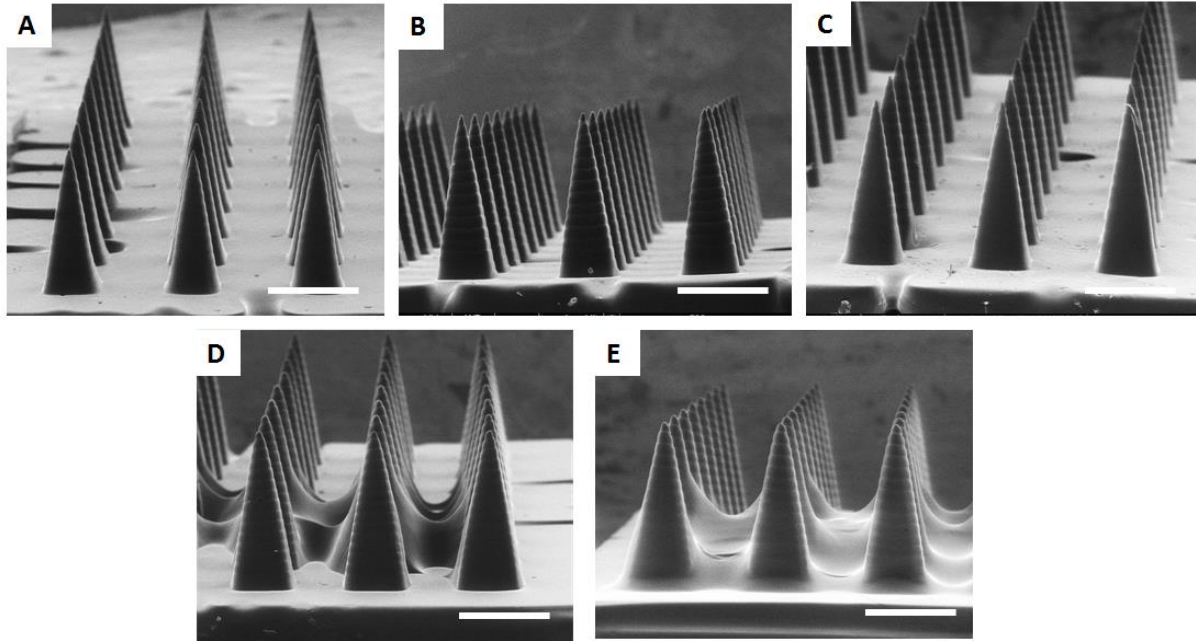


**Figure 2.19 TMPTA Microneedles produced using different light intensities.** Microneedles were produced using A) 2mW/cm<sup>2</sup>, B) 5mW/cm<sup>2</sup>, C) 8mW/cm<sup>2</sup>, D) 11mW/cm<sup>2</sup>, and E) 14mW/cm<sup>2</sup> of UV light. Build speed was held constant at 100mm/hr. Scale bars measure 500μm

fast build times (less than two minutes per patch), but is slow enough to reduce any potential defects due to incomplete resin flow into the build area.

CLIP microneedles were generated using light intensities ranging from 2mW/cm<sup>2</sup> to 14mW/cm<sup>2</sup> (Figure 2.14). In general, these microneedles exhibited more desirable structures than compared to the first CLIP3 microneedles in Figure 2.10, confirming that the improvements to the system's optics improved microneedle structure. Some observations regarding the effect of light intensity were made. Similarly to the CLIP3 studies shown in Figure 2.4, as the light intensity of the CLIP7 increased, more curing was observed, resulting in both an increase in the height and the width of an individual microneedle with increasing light intensity (Figure 2.15). This increase in curing was especially evident when printing with 11mW/cm<sup>2</sup> or 14mW/cm<sup>2</sup> of light, which also produces unwanted curing between microneedles. However, although we hoped to identify the appropriate light intensity for the production of dimensionally accurate

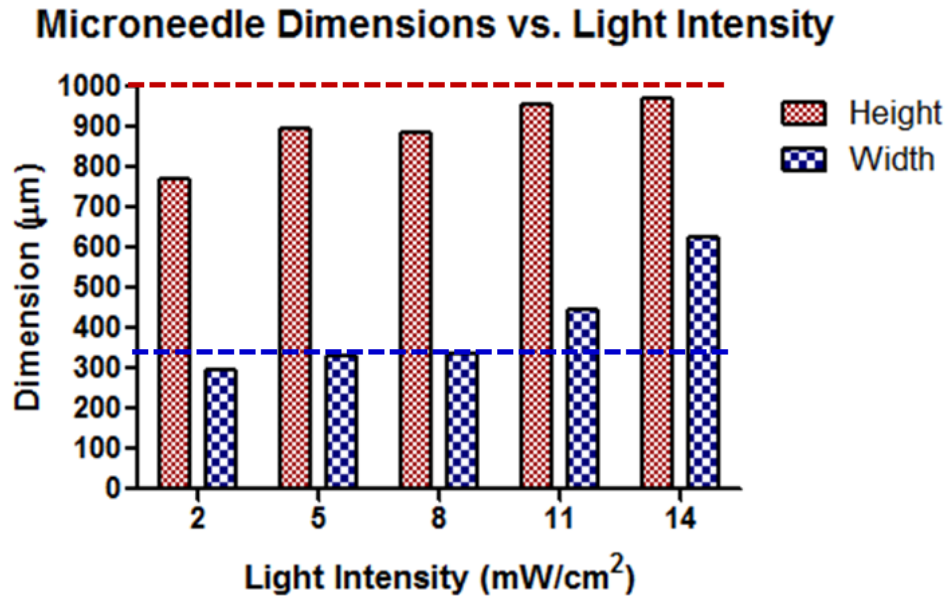


**Figure 2.21 Dimensions of TMPTA microneedles produced with varying light intensity.** The dotted red line represents the height of the CAD file. The dotted blue line represents the width of the CAD file. Error bars represent the mean  $\pm$  SD (n=3)

microneedles, all microneedles were truncated in the z direction relative to the 1000 $\mu$ m CAD file (Figure 2.15). **Together, these observations suggest that print parameters such as light intensity are as important to determining the size and shape of the resulting part as the CAD file utilized to produce the part.** While this experiment suggests that further increases in light intensity may produce tall enough microneedles, the microneedles are already wider than the desired width; increases in light intensity would exacerbate this issue. Therefore, an alternate strategy is necessary to enable production of dimensionally accurate needles.

Furthermore, the microneedles produced here (Figure 2.14) have a stair-stepping surface texture that is present regardless of the light intensity used. The stair-stepping is visually undesirable and may prevent smooth insertion into the skin. Furthermore, the reason for this unexpected stair-stepping pattern is unknown. Therefore, the next section seeks to determine the

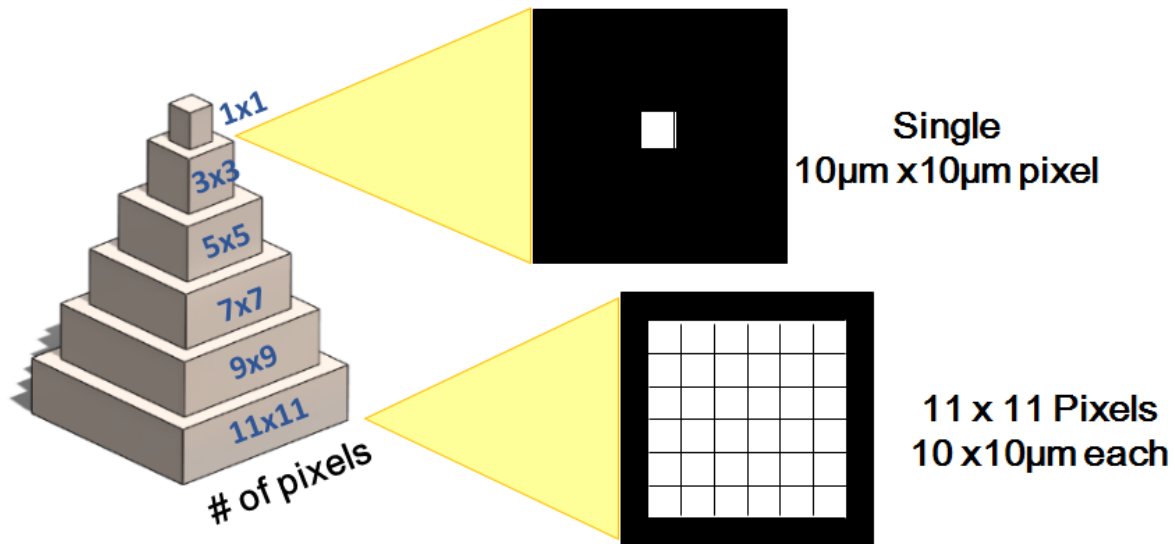


**Figure 2.23 Discrete pixels may produce stairstepping**

underlying cause of the stair-stepping and develop methods to eliminate stair-stepping to produce microneedles with smooth sidewalls.

### **2.2.5 Visualization of Individual Pixels Causes Stairstepping**

It was hypothesized that the undesirable stair-stepping texture present in Figure 2.14 could be the result of either Hypothesis A- uneven movement of the build elevator during part production or Hypothesis B- the visualization of individual pixels within the micromirror array. Hypothesis A is that if the build elevator vibrates or catches as it moves upward, some ridges may be created due to uneven movement during photopolymerization. Hypothesis B is further explained in Figure 2.16. One could imagine that a microneedle measuring 110µm X 110µm at the base would be projected as a 11x11 pixel image, where each of the instrument's micromirrors is a 10µm X 10µm pixel at the build area. As the width of the microneedle decreases moving towards the microneedle tip, fewer and fewer pixels are illuminated. However, because each

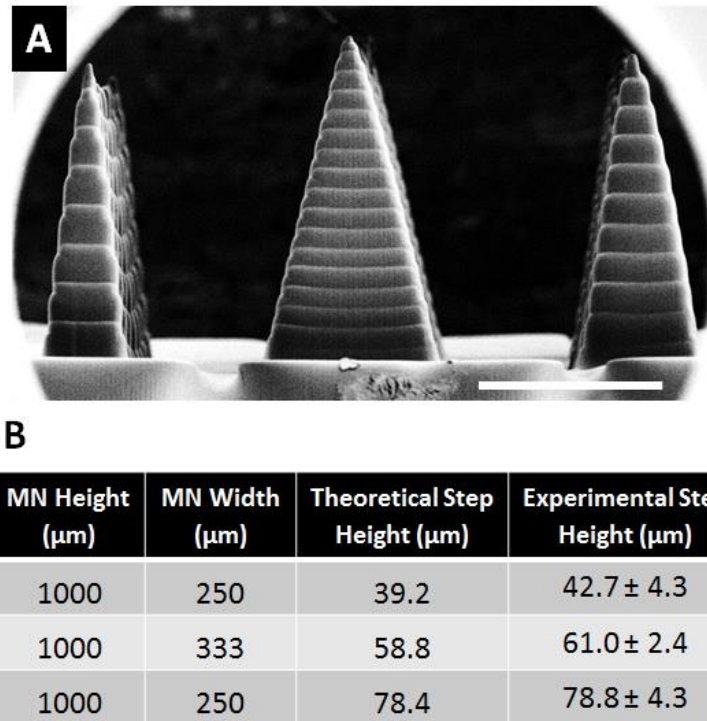


**Figure 2.25 Height of stair step vs. aspect ratio** A) SEM image of microneedles of aspect ratios 2, 3, and 4, where each horizontal line is an undesirable “stair-step”. B) Comparison of the experimental step height between horizontal lines as compared to the theoretical step height calculated using Equation 1. Error bars represent the mean ± SD (n=3). Scale bar measures 500μm.

pixel is a discrete unit that can be turned on or off, the resolution of the system is limited to a 10μm step size, creating a stair-stepping pattern along the side of the microneedle array.

In order to differentiate between these two alternate hypotheses, microneedles of three different aspect ratios were printed on a single array. If Hypothesis A is true and the elevator movement is the cause of the stair-stepping surface texture, all three aspect ratios should have the same step size, which is dictated by the elevator’s movement. If Hypothesis B is true and the stair-stepping is the visualization of individual pixels, microneedles of different aspect ratios should have different step heights due to the differences in the sidewall slopes. The theoretical step height for each aspect ratio can be calculated according to Equation 2.18, below, if stair-stepping is the result of visualizing individual pixels.

$$H_{Step} = \frac{H_{MN}}{\# \text{ of steps}} = \frac{H_{MN}}{W_{MN}/(2 \cdot W_{pixel})} \quad (2.18)$$

where  $H_{Step}$  is the height of each step,  $H_{MN}$  is the height of each microneedle,  $W_{MN}$  is the width of each microneedle and  $W_{pixel}$  is the width of each pixel. Using Equation 2.18 and the heights and widths of microneedle CAD files, the expected step height of each microneedle could be calculated, as shown in Figure 2.17B.

An ESEM image of microneedles of three different aspect ratios produced using CLIP is shown in Figure 2.17. The height of each step in the stair-stepping surface texture is different for each of the three aspect ratios, suggesting that the stair-stepping pattern is due to the visualization of individual pixels. A comparison of the theoretical and experimental step heights is provided in Figure 2.17B. All experimental step heights fall within one standard deviation of the theoretical step heights, indicating that this surface topology is indeed due to the visualization of individual pixels within the printed part.

### 2.2.6 Application of Antialiasing to CLIP

Stated in another way, the stair-stepping pattern is caused by discrete spatial sampling of a continuous line once every  $10\mu\text{m}$  at the location of an individual micromirror on the DLP chip. This sampling creates an “alias”, or distortion of the signal, which results in the production of jagged sidewalls. An example of aliasing is provided in Figure 2.18, below, where a desired continuous line (Figure 2.18A) is displayed as a jagged line (Figure 2.18B) composed of discrete pixels.<sup>7</sup> Aliasing is a common issue affecting the resolution of graphics projected onto pixel-based screens, such as computer screens and TV monitors. It primarily affects the representation of small objects, areas containing complicated details, and the edges of an object.<sup>8</sup> Figures 2.14 and 2.17 demonstrate that aliasing also affects 3D printing of parts on a small scale.

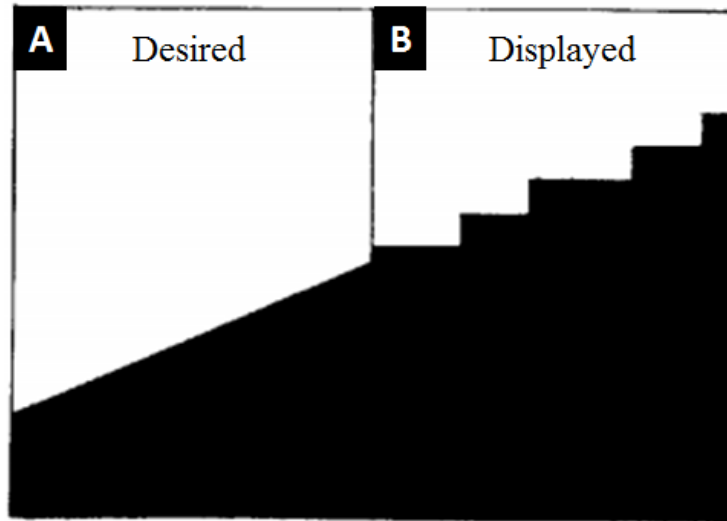


**Figure 2.28 Visible effects of spatial image aliasing.** The desired image is distorted by spatial sampling at each pixel, causing the display to contain an alias, or distortion of the original signal. Reproduced with permission from reference 2.

When graphics are displayed on computer monitors, televisions, or on gaming systems, a process called antialiasing is used to correct for distortions. A number of different antialiasing algorithms have been developed; their mechanisms are comprehensively reviewed elsewhere.<sup>7-9</sup> Here, we considered three different approaches to antialiasing and their application to the CLIP 3D printing process. These three approaches are 1) reducing the size of each pixel 2) defocusing the image and 3) applying an antialiasing algorithm called supersampling.

The first, and most obvious, antialiasing approach is to increase the resolution of the system's hardware by adding additional pixels to resolve finer details.<sup>8</sup> This approach has been widely utilized to improve the resolution of DLP based television screens, but typically substantially increases the cost of the system. When applied to 3D printing of microneedle arrays, this approach necessitates decreasing the pixel size by either 1) increasing the number of micromirrors on the DLP chip or 2) shrinking the UV image projection to reduce pixel size at the cost of total available build area. However, because utilizing a larger DLP chip would require

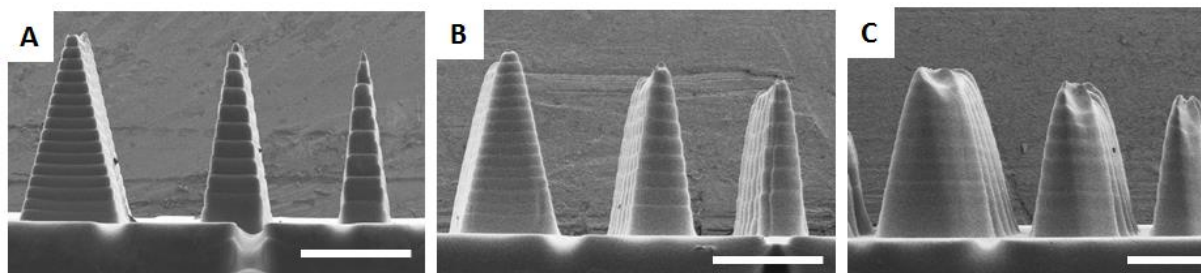


**Figure 2.30 Effect of system focus on microneedle structure.** Microneedles of three different aspect ratios are fabricated A) In focus, with the lens at its focal point B) with the lens 2mm below its focal point and C) with the lens 4 mm below its focal point. Scale bars measure 500 $\mu$ m.

redesigning the printer's optical system and reducing the build area is undesirable, the remaining two approaches were considered.

A second approach to antialiasing is defocusing the image so that jagged sidewall profiles are less noticeable. Although this approach is simple, the image loses sharpness that is retained using other antialiasing methods. However, we decided to assess the role of system focus on microneedle antialiasing due to the simplicity of this approach and its potential to generate microneedles with smooth sidewalls. Defocusing was achieved by moving the lens setup away from the window platform, further from the focal point of the lens. TMPTA microneedles were printed at different focal distances including at the focal point of the lens (Figure 2.19A), 2 mm away from the focal point (Figure 2.19B) and 4 mm away from the focal point of the lens (Figure 2.19C). Poor focus results in the production of wider, shorter microneedles than those produced using an in-focus system, demonstrating that microneedle dimensions are also dictated by the focus of the system as well as the CAD file used and the print parameters. Although defocusing had visible effects on microneedle morphology, the stair-stepping pattern was still evident at all focus levels. The system reached an unacceptable level of sharpness (Figure 2.19C), but still exhibited aliasing effects visible as horizontal lines across each microneedle. Therefore, defocusing is not a suitable method to eliminate stair-stepping.

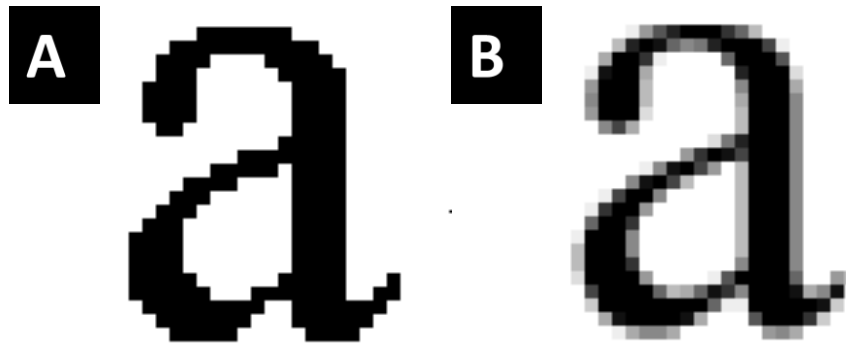


**Figure 2.31 Supersampling of typeface letter A.** A) An aliased version of typeface letter A has jagged edges B) Supersampling the typeface letter visibly improves resolution. Reproduced with permission from Reference 10.

The third and most attractive approach to antialiasing is introducing grayscale using an antialiasing technique called supersampling.<sup>8</sup> Object edges can be blended to create the illusion of a continuous line by using gray pixels, rather than only relying on pixels that are either black (“OFF”) or white (“ON”). Figure 2.15 is an example of supersampling the typeface lowercase letter “a”. When using black and white pixels only, this system appears to have poor resolution, with individual pixels very clearly visible (Figure 2.20A). However, the use of grayscale values along the object’s edges (Figure 2.20B) visibly improves resolution. This supersampling approach shown here is very similar to methods currently used for commercial projection systems and DLP televisions.<sup>8</sup>

More specifically, when a supersampling antialiasing algorithm is applied, the pixel’s grayscale value is calculated by averaging light intensity of all of the objects falling within a single pixel, according to Equation 2.19, below.  $G$  is grayscale value,  $A$  is the area occupied by a particular object within a single pixel, and  $i$  is the number of objects that fall within that pixel.

$$G_{pixel} = \frac{\sum_1^i G_i A_i}{\sum_1^i A_i} \quad (2.19)$$

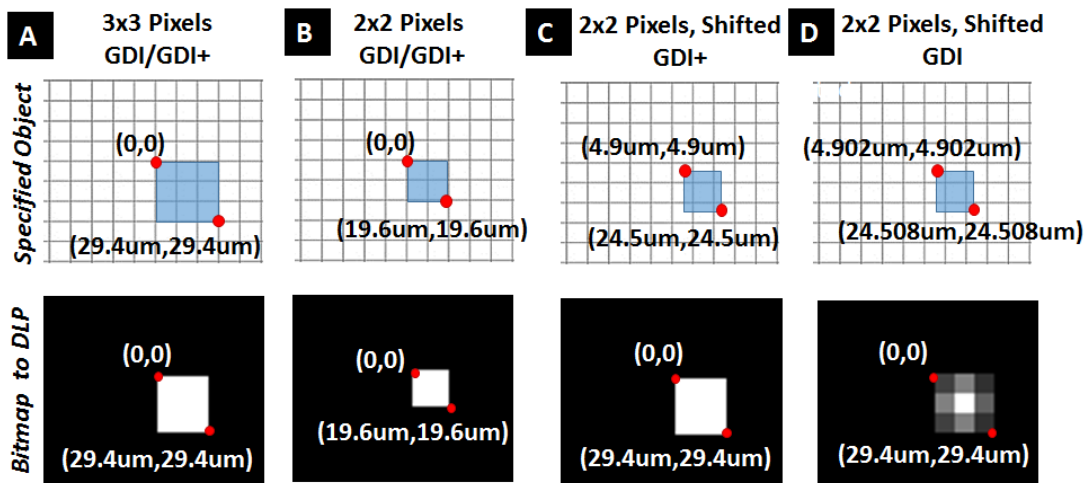


Figure 2.32 Comparison of GDI and GDI+ Grayscale Assignments

Typically, this grayscale value is a number between 0 (black) and 255 (white), based on a linear red, green, blue (RGB) color scale. In some cases, it is also given as percent of maximum light intensity.

In order to apply supersampling to 3D printing, a method of assigning a grayscale value to each micromirror had to be developed. DLP chips are inherently discrete systems, in which each micromirror is either “ON” or “OFF” at a given moment in time, but high frequency dithering, or oscillation, of each micromirror can be utilized to create the illusion of grayscale. For example, if a micromirror is in the “ON” position for 50% of the duration of the frame and in the “OFF” position for the remaining 50% of the frame, the pixel appears to project 50% of the

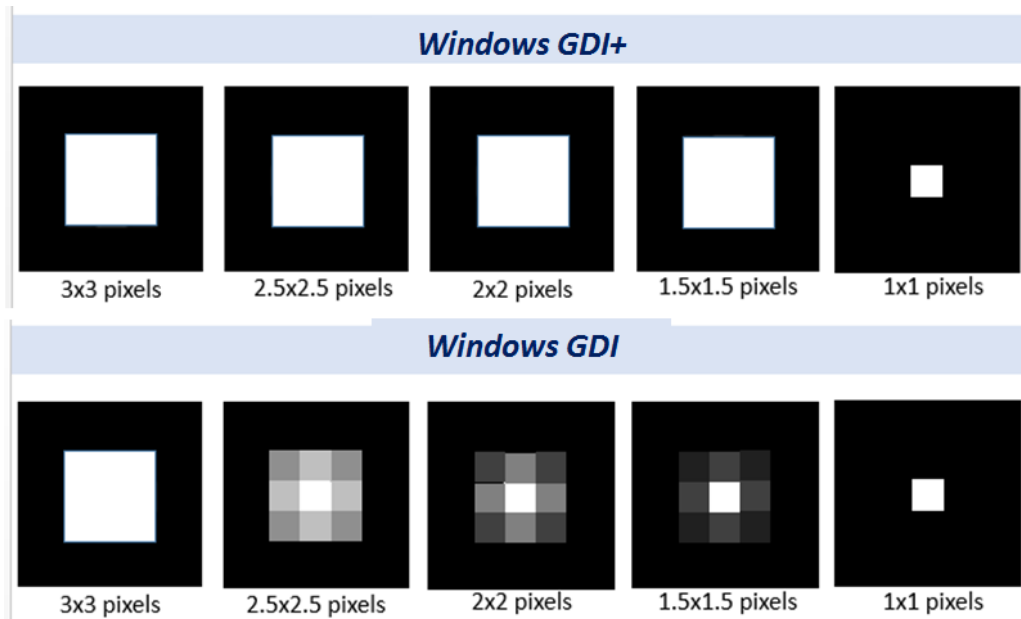
Table 2.1 Comparison of GDI and GDI+ Pixel Grayscale Assignments

Fig.	Square Input Image	Upper Left Corner Coordinate	Software Interface	Bitmap Image	Bitmap Light Intensity	Antialiasing
2.16A	3x3 pixels	(0μm, 0μm)	GDI+	3x3 pixel object	Maximum	No
2.16A	3x3 pixels	(0μm, 0μm)	GDI	3x3 pixel object	Maximum	No
2.16B	2x2 pixels	(0μm, 0μm)	GDI+	2x2 pixel object	Maximum	No
2.16B	2x2 pixels	(0μm, 0μm)	GDI	2x2 pixel object	Maximum	No
2.16C	2x2 pixels	(4.902μm, 4.902 μm)	GDI+	3x3 pixel object	Maximum	No
2.16D	2x2 pixels	(4.902μm, 4.902 μm)	GDI	3x3 pixel object	Various	Yes

maximum light intensity. Likewise, a pixel assigned to 75% of the maximum light intensity would be in the “ON” position for 75% of the duration of the frame and in the “OFF” position for the remaining 25% of the frame. Visualizing the bitmap used to control the DLP chip enables us to identify whether any antialiasing algorithm is being applied during projection of the image.

The grayscale value of each pixel is controlled by a component of the system’s software called the graphic device interface (GDI). Two different graphic device interfaces- Windows GDI+, which used for the production of stairstep microneedles, and Windows GDI, an alternate version, were compared to determine how each version assigns grayscale values to an image. Grayscale assignment was determined by capturing a screenshot of the bitmap image that controls the DLP chip for several different test images. Input test images were simple squares of a specific sizes at a particular location on the build area (Table 2.1). The results of the experiment are given in Figure 2.21 and described in detail in the next paragraph.

The GDI and GDI+ interfaces differ in the way that they assign an input image to a bitmap that controls grayscale values on the DLP chip. When the input image exactly align’s with the DLP’s micromirrors, no approximation is required. For example, when a 3x3 pixel square is located at the origin (Figure 2.21A), the entire 3x3 pixel square is projected at maximum light intensity, shown in white, regardless of the graphic device interface that is used. Similar results are seen when a 2x2 pixel square is located at the origin; a 2x2 pixel square is projected at maximum light intensity (Figure 2.21B). However, when this 2x2 pixel square is translated such that it does not directly align with the DLP’s micromirrors, the system must approximate the specified image when it is projected to account for each partial pixel. The GDI and GDI+ interfaces perform this approximation in different ways. Windows GDI+ rounds each partial pixel up to the next largest pixel, projecting a 3x3 pixel image at maximum light intensity



**Figure 2.35** Difference Between Windows GDI+ and Windows GDI Projections of Microneedle Cross-sections (Figure 2.21C). Windows GDI performs the desired supersampling procedure and approximates each partial pixel in grayscale (Figure 2.21D)

In order to better understand the antialiasing algorithm and appreciate how it may affect microneedle fabrication as well as the fabrication of other small objects, the grayscale values for each pixel in Figure 2.21C-D were calculated. These grayscale values are shown in Figure 2.22. As expected, the GDI+ interface “rounds-up” to the next largest pixel, projecting the entire object at the maximum light intensity (Figure 2.22). The grayscale values resulting from use of the GDI interface are calculated using equation 1, where each grayscale value is proportional to the percentage of that pixel that is covered by the original object. For example, because 25% of the each corner pixel is covered by the original object, the corners are projected at 25% of the maximum light intensity.

To represent the potential effects of these antialiasing algorithms on the production of microneedles using CLIP, squares of decreasing size were projected. These squares represent the

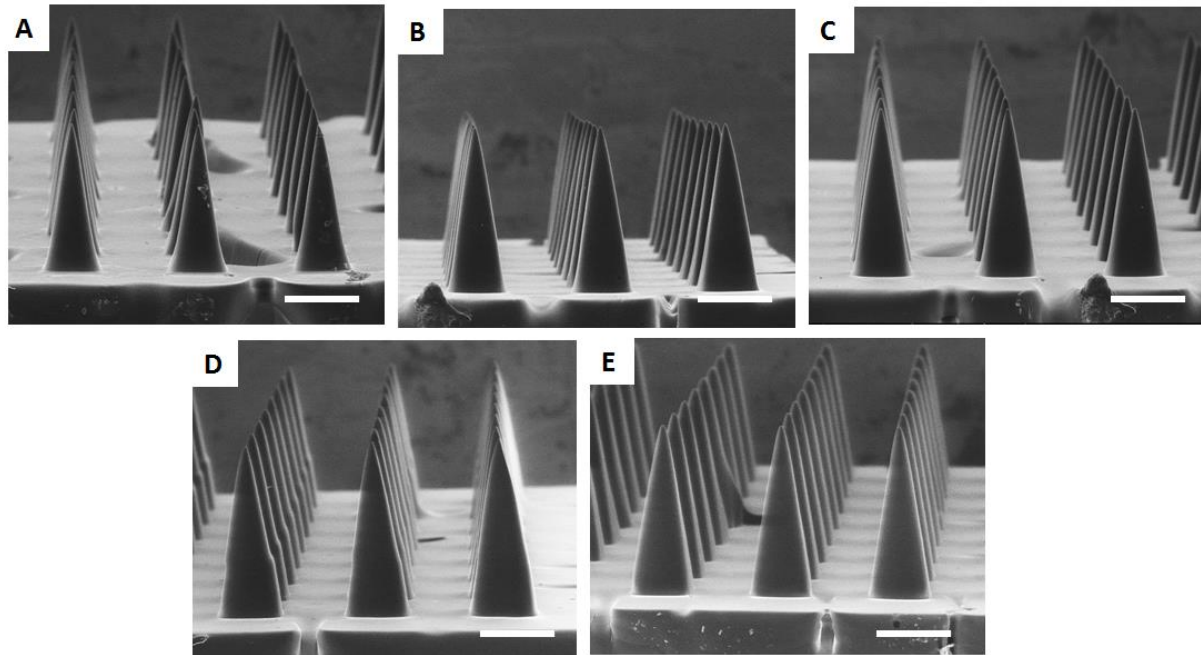


**Figure 2.36 TMPTA Microneedles produced using Windows GDI.** Microneedles were produced using A) 2mW/cm<sup>2</sup>, B) 5mW/cm<sup>2</sup>, C) 8mW/cm<sup>2</sup>, D) 11mW/cm<sup>2</sup>, and E) 14mW/cm<sup>2</sup> of UV light. Build speed was held constant at 100mm/hr. Scale bars measure 500µm.

cross-section of an individual microneedle in the array, moving from the microneedle's base to the tip of the needle. A printscreen of the bitmap sent to the DLP was visualized to determine the grayscale value assigned to each individual pixel. As shown in Figure 2.23, Windows GDI+ produces an abrupt transition between pixels, whereas Windows GDI utilizes grayscale to create a smooth transition moving from microneedle base to tip. Therefore, we moved forward with applying supersampling to microneedle production using Windows GDI in hopes that this approach would generate smooth microneedle sidewalls.

### 2.2.7 Application of Antialiasing to Microneedle Production

In order to determine whether this antialiasing algorithm effectively eliminates stair-stepping along microneedle sidewalls, microneedles were fabricated using the GDI version of the digital graphics interface according to previously established methods. A range of different light intensities, from 2mW/cm<sup>2</sup> to 14mW/cm<sup>2</sup> was investigated with build speed held constant at

100mm/hr. The ESEMs of these microneedles shown in Figure 2.24 demonstrate that the addition of an antialiasing algorithm eliminates the stair-stepping effect at all light intensity values. Therefore, we concluded that a supersampling antialiasing algorithm can be used to eliminate the visualization of individual pixels (“stair-stepping”) on the small scale to enable the production of parts with smooth sidewalls.

### 2.2.8 Selection of Appropriate Build Parameters

After successfully eliminating stair-stepping to produce microneedles with smooth sidewalls, we revisited the role of light intensity on microneedle dimensions. The microneedles printed using a range of light intensities in Figure 2.24 were measured to assess dimensional accuracy, with results given in Figure 2.25.

Overcuring between needles at high light intensity ( $11\text{mW/cm}^2$  and  $14\text{mW/cm}^2$ ) is somewhat reduced when using the GDI interface as opposed to the GDI+ interface, presumably

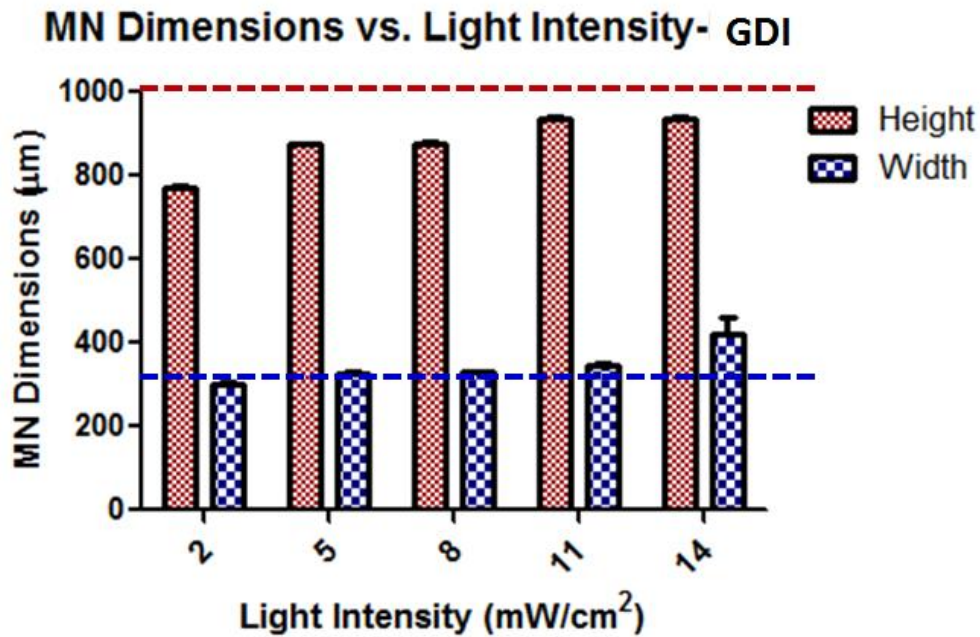
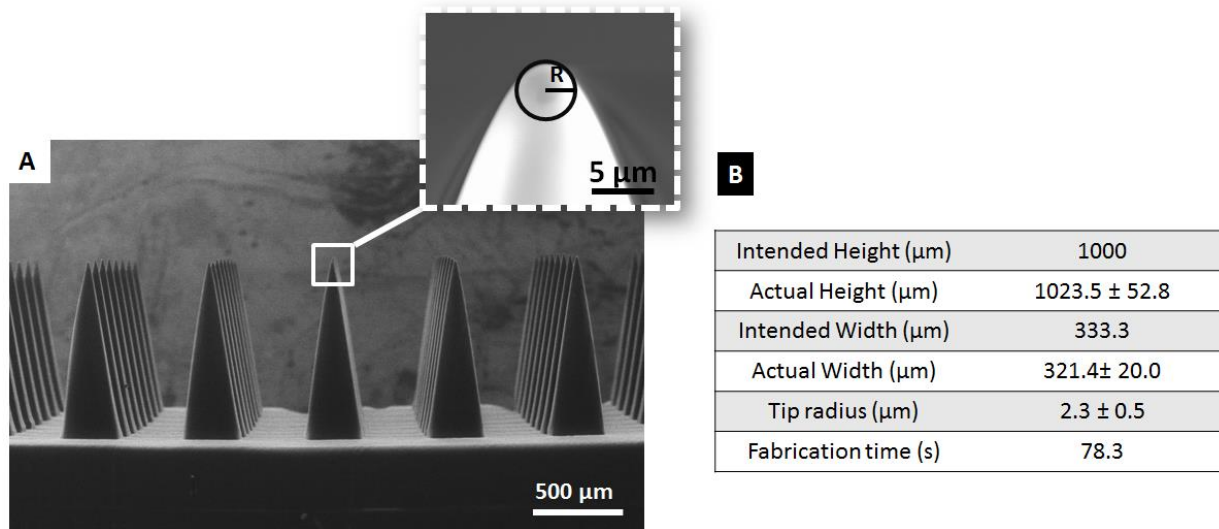


Figure 2.38 Microneedle Dimensions vs. Light Intensity Using Windows GDI. Error bars represent the mean  $\pm$  SD (n=3).



**Figure 2.39 1000 $\mu\text{m}$  tall TMPTA Microneedles Produced Using CLIP.** A) Image of CLIP Microneedles showing sharp tip radius B) Dimensions and fabrication time for microneedles in Figure A. Data are represented as mean  $\pm$  SD

due to decrease in the light intensity (introduction of grayscale) of each microneedle's exterior pixel. However, although we hoped to identify the appropriate light intensity for the production of dimensionally accurate microneedles using the new GDI interface, all microneedles were truncated in the z direction relative to the 1000 $\mu\text{m}$  CAD file (Figure 2.9). A hypothesis to explain this truncation is provided in Appendix B. While further increases in light intensity may produce tall enough microneedles, the microneedles are already wider than the desired width; increases in light intensity would exacerbate this issue. Therefore, microneedles were produced using the light intensity that resulted in an appropriate width ( $8\text{mW}/\text{cm}^2$ ) and scaled in the z direction (z scale factor=1.175, e.g. the initial CAD file was scaled to a height of 1175 $\mu\text{m}$ ) to produce microneedles measuring approximately 1000 $\mu\text{m}$  tall (Figure 2.26). At 100mm/hr, the total print time for this microneedle array is 78.3 seconds, which is the fastest fabrication time for a microneedle array presented in literature, to our knowledge. We estimate that these production speeds are approximately 400-1600X faster than traditional etching techniques used to fabricate microneedles, which are typically accomplished at 1-5 $\mu\text{m}$  per minute.<sup>11-13</sup> The

average tip radius of each microneedle in the array is  $2.3\mu\text{m}$ , which is approximately three times sharper than the sharpest polymeric microneedles in literature.<sup>14</sup>

## 2.2.9 Control Over Microneedle Geometry

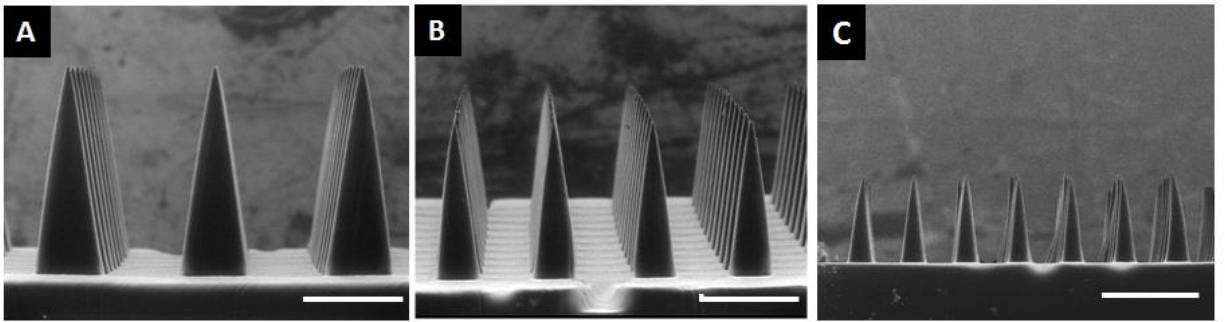
As previously mentioned, utilizing additive manufacturing to fabricate microneedles may provide unprecedented control over microneedle design parameters, such as microneedle size, shape, spacing, and aspect ratio. Design alterations should be achievable by simply exchanging the input CAD file with little to no additional process optimization for new designs. In order to test this hypothesis, a number of different microneedle designs were fabricated using the model resin TMPTA.

### 2.2.9.1 Fabrication of Microneedles of Different Heights

Microneedles of different heights are useful for controlling depth of penetration in the skin and to alter the volume available for cargo loading. Controlled depth of penetration may enable targeting of specific cell types within the skin, such as targeting the basal layer for basal cell carcinomas. Controlling microneedle penetration depth may also alter the rate and/or degree of therapeutic exposure to systemic circulation. CAD files of microneedles of different heights, measuring  $1000\mu\text{m}$ ,  $700\mu\text{m}$ , and  $400\mu\text{m}$  tall, were generated with aspect ratio held constant (AR=3). Using the light intensity and build speed previously identified for production of 1000

**Table 2.2 MNs of Different Heights Truncate without Z Scale Factor.** Dimensions of all MNs show truncation in z direction, but minimal shrinkage in the x-y direction. Data are presented as mean $\pm$ SD, n=9

Dimensional Accuracy Assessment- MNs of Different Heights					
Intended Height (um)	Actual Height (um)	% Difference	Intended Width (um)	Actual Width (um)	% Difference
1000	911.7 $\pm$ 27.2	-8.83%	333.3	334.0 $\pm$ 12.0	0.23%
700	557.2 $\pm$ 9.5	-20.4%	233.3	226.3 $\pm$ 11.5	-3.0%
400	296.8 $\pm$ 4.9	-25.8%	133.3	127.1 $\pm$ 4.7	-4.6%



Z Scale Factor	Microneedle Dimensions					
	Intended Height (um)	Actual Height (um)	% Difference	Intended Width (um)	Actual Width (um)	% Difference
1.175	1000	1023.5 ± 52.8	2.4%	333.3	321.4± 20.0	-3.5%
1.4	700	712.6 ± 13.7	1.8%	233.3	236.3± 8.7	1.3%
1.6	400	383.7 ± 8.6	-4.1%	133.3	135.4± 8.3	1.6%

**Figure 2.42 CLIP MNs of Different Heights** MNs produced from a CAD file measuring A) 1000 $\mu\text{m}$  tall and 333 $\mu\text{m}$  wide, B) 700 $\mu\text{m}$  tall and 233 $\mu\text{m}$  wide, and C) 400 $\mu\text{m}$  tall and 133 $\mu\text{m}$  wide. D) Dimensions of all MNs show truncation in z direction, but minimal shrinkage in the x-y direction. Data are presented as mean $\pm$ SD (n=9). Scale bars measure 500 $\mu\text{m}$ .

$\mu\text{m}$  tall microneedles (8mW/cm<sup>2</sup>, 100mm/hr), microneedles of different heights were fabricated (z scale factor=1) and measured to assess dimensional accuracy (Table 2.2). Microneedle width was initially found to be within 5% of the intended dimensions, indicating that these build parameters were appropriate for setting the width of the needles. Microneedle heights, however, were approximately 100 $\mu\text{m}$  too short, regardless of the initial height. This 100 $\mu\text{m}$  difference accounts for a larger and larger portion of the total height as the microneedles become smaller (Table 2.2). Therefore, a z scale factor was added to scale the microneedles to an appropriate height, shown in Figure 2.27. After scaling, all microneedle heights and widths were found to be within 5% of intended dimensions.

### 2.2.9.2 Fabrication of Microneedles of Different Geometries

The geometry of a microneedle array is known to affect its cargo loading volume, failure force,<sup>15</sup> and ability to effectively insert into the skin.<sup>15-18</sup> In order to determine whether CLIP can

be utilized to rapidly adjust patch geometry, we fabricated CLIP microneedles with different shapes, aspect ratios and spacings.

In order to adjust microneedle aspect ratio, CAD files of microneedles having ARs ranging from 2 to 4 were generated. Microneedles were then fabricated using the light intensity and build speed previously optimized for TMPTA microneedles ( $8\text{mW}/\text{cm}^2$ ,  $100\text{mm}/\text{hr}$ ), as shown in Figure 2.28A. Similar adjustments in microneedle aspect ratio have been previously shown to impact microneedle strength;<sup>15</sup> aspect ratio is therefore an important determinant of efficacy. Similarly, CAD files of microneedles spaced at 0.5 and 1.5 base widths apart were readily generated and utilized to produce CLIP microneedle patches with adjustable inter-needle spacing (Figure 2.24B-C). Microneedle height was held constant at approximately  $1000\mu\text{m}$ . More closely spaced microneedles have more volume available for cargo loading per unit patch

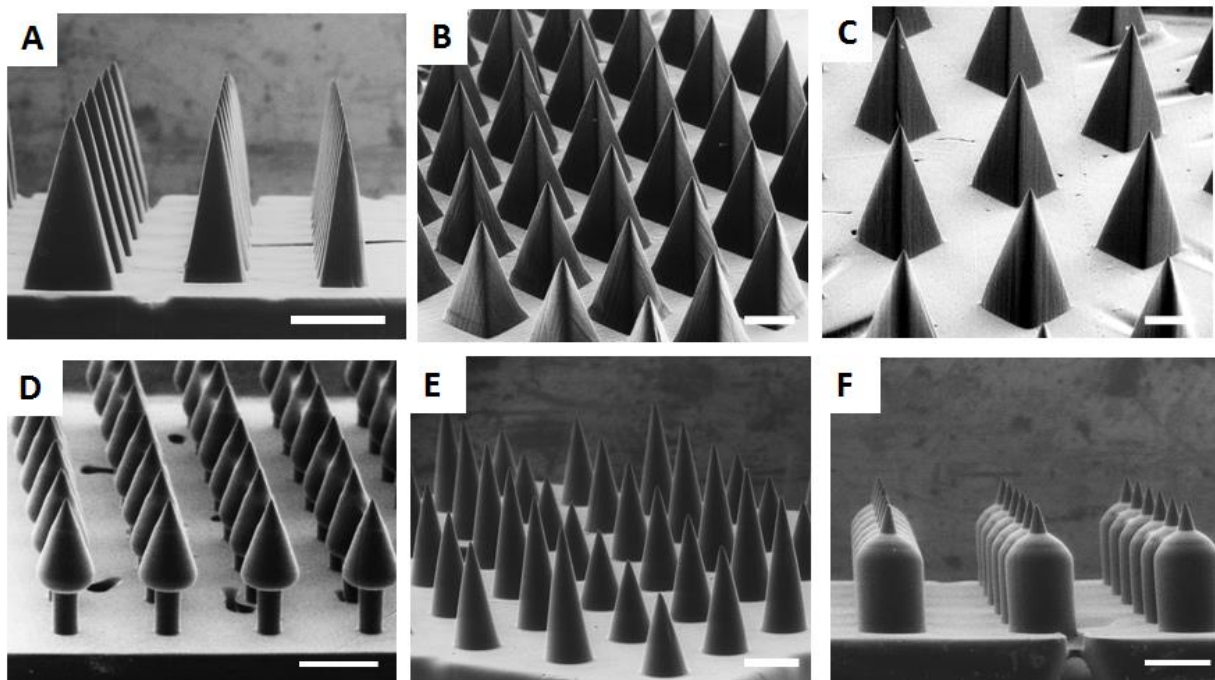


**Figure 2.44 TMPTA Microneedles of Different Shapes** A) TMPTA microneedles of aspect ratio 2, 3, and 4 (left to right).  $1000\mu\text{m}$  tall TMPTA microneedles with spacing of B) 0.5 base widths and C) 1.5 base widths. Complex microneedle geometries such as D) Arrowhead microneedles E) Tiered microneedles and F) Turret microneedles may improve mechanics of insertion into the skin. Scale bars measure  $500\mu\text{m}$

area. Unfortunately, increasing the total number of needles also increases the total force required to insert microneedles into the skin due to the “bed-of-nails” effect discussed in Chapter 1. Therefore, inter-needle spacing is another important design parameter that can be optimized using the CLIP platform.

Although conical and square pyramidal microneedles have been the mainstay of microneedle technology, more complex geometries may afford improved penetration into the skin. Therefore, we aimed to use CLIP to fabricate microneedle geometries that would be difficult to impossible to fabricate using other microfabrication techniques. For example, arrowhead microneedles may improve the consistency of needle penetration by resisting the elastic nature of the skin to remain embedded at their maximum penetration depth.<sup>19-20</sup> Successful microneedle penetration into the skin is also known to be inhibited by the “bed-of-nails” effect, wherein the total insertion force is divided evenly amongst every microneedle in an array, increasing the total force required for insertion.<sup>15</sup> The design of “tiered” microneedles, which contain microneedles of different heights on a single array, may reduce required insertion forces by concentrating the force on fewer needles at a given moment in time. Lastly, traditional square pyramidal microneedles of different aspect ratios are thought to present a trade-off between ease of insertion and microneedle strength wherein wider needles provide mechanical stability, but thinner needles more easily insert into the skin.<sup>14</sup> “Turret” microneedles containing sharp tips with a wide base may easily puncture the skin, but also afford improved mechanical strength.

CLIP was utilized to fabricate arrowhead microneedles, “tiered” microneedles, and “turret” microneedles, shown in 2.23D-F, respectively. This work demonstrates proof of concept that CLIP can be utilized to rapidly generate an almost infinite library of computationally defined

microneedle geometries, which can be used to systematically investigate how microneedle geometry influences efficacy.

### **2.3 Conclusions**

Herein, we have demonstrated that microneedle structures composed of the model resin TMTPA can be produced via CLIP in less than 90 seconds per patch. This process is the fastest microneedle production technique in the world, producing the sharpest polymeric microneedles in literature. Therefore, CLIP shows promise as a microneedle fabrication technique due its speed and unprecedented control over microneedle geometry. Further, CLIP enables novel microneedle geometries, such as arrowhead microneedles, to be produced, with the potential to improve microneedle insertion into the skin. Such geometries are difficult to impossible to fabricate using other techniques. CLIP microneedles will be further discussed in Chapter 4, which focuses on the development of CLIP microneedles designed to encapsulate and release a therapeutic cargo.

The data presented in this chapter also demonstrates important fundamental information about the CLIP process, which provides useful guidelines for the fabrication of any small part via CLIP. First, the characteristics of the optical system that focuses the image from the DLP chip onto the build window were found to be of paramount importance to the structure of small objects. Second, in order to produce small parts with smooth surfaces, a technique called antialiasing must be applied during production. A specific type of antialiasing called supersampling was employed, blurring distinctions between pixels with grayscale to produce small objects. Third, microneedle build parameters, particularly speed and light intensity, were shown to play as big of a role in part dimensions as the dimensions of the input CAD file. More specifically, increasing light intensity was shown to increase part dimensions, whereas increasing

build speeds was shown to decrease part dimensions. Therefore, judicious control over speed and light intensity are of paramount importance to effective use of CLIP. Chapter 3 will continue to explore the role of printer optics, light intensity and build speed on part dimensions, with the ultimate goal of applying a predictive mathematical model to CLIP that could automate selection of CLIP build parameters.

Altogether, these findings establish proof of concept that CLIP can be utilized to fabricate microneedles and provide a foundation for utilizing CLIP for the production of micron-scale parts for a variety of different applications.

## **2.4 Experimental**

### **2.4.1 Materials**

Diphenyl (2,4,6- trimethylbenzoyl) phosphine oxide (TPO) and trimethylolpropane triacrylate (TMPTA) were obtained from Sigma Aldrich and used as received. DLP chips were obtained from Texas Instruments, with specifications given in Tables 2 and 3 for the CLIP3 and CLIP7, respectively. Lenses were purchased from Edmund Optics, with specifications given in Tables 2 and 3 for the CLIP3 and CLIP7, respectively.

### **2.4.2 TPO Absorption Spectrum**

2mL of TPO at 10ppm in dimethylacetamide (DMAC) was added to a quartz cuvette with a path length of 1mm. The absorption spectrum was taken over 260 to 450nm using a UV Vis system.

### **2.4.3 CLIP Instrument Specifications**

The parts produced in this chapter were made using either the CLIP3 or CLIP7 additive manufacturing systems provided by Carbon 3D, Redwood City. Specifications for each system are given in Table 2.2 and Table 2.3 for the CLIP3 and CLIP7, respectively.

**Table 2.5 CLIP 3 Specifications**

<b>CLIP 3 Specifications</b>	
<b>Light Source</b>	Mercury Lamp
<b>Maximum Light Intensity</b>	77 mW/cm <sup>2</sup>
<b>DLP Chip</b>	Texas Instruments DLP3000
<b>DLP Specifications</b>	608x684 micromirrors, 7.6µm each
<b>Pixel Size</b>	Initial- 16µm Replacement- 8 µm
<b>Lenses</b>	Low resolution- Two achromatic doublets, 50 and 75 mm focal lengths High resolution- Two achromatic doublets, 75 and 100 mm focal lengths
<b>Build Area</b>	Low resolution lens- 11.1mm x 9.8mm High resolution lens- 5.4mm x 4.8mm

The CLIP3 system is composed of a mercury lamp and a DLP 3000 DLP chip containing a 608x684 array of micromirrors measuring 7.6µm x 7.6µm each. Light reflects off of the DLP chip through a lens composed of two achromatic doublets, off of a mirror, and onto the build window. Depending on the focal length of the lenses (Edmund Optics), each of these micromirrors was projected at a 1:2.1 or 1:1.05 ratio on the build window such that each micromirror forms a 16µx16µm or an 8µx8µm pixel, convolved with the impulse response of the system, on the build surface

The CLIP7 system is composed of an ultraviolet light emitting diode (UV LED) emitting light at a wavelength of 370nm. Light emitted from the LED is reflected off of a DLP7000 DLP

**Table 2.6 CLIP 7 Specifications**

<b>CLIP 7 Specifications</b>	
<b>Light Source</b>	UV LED (λ=370nm)
<b>DLP Chip</b>	Texas Instruments DLP7000
<b>DLP Specifications</b>	1024x768 micromirrors, 13µm each
<b>Pixel Size</b>	9.803 µm
<b>Lenses</b>	Initial- Greenlight® Optics Updated- Two achromatic Doublets, 75mm focal lengths
<b>Build Area</b>	10.3mm x 7.7 mm

chip containing a 1024x768 array of micromirrors measuring 13 $\mu\text{m}$  x 13 $\mu\text{m}$  each. This light then travels through two achromatic doublet lenses and is focused on the build window at a 1:0.754 magnification to produce a maximum image size of 10.3mm x 7.7mm. Each micromirror, therefore, produces a single pixel of light measuring 9.803 $\mu\text{m}$  x 9.803 $\mu\text{m}$  at the window surface.

#### **2.4.4 TMPTA Part Fabrication**

TMPTA and 2.5 wt% TPO were mixed in an amber bottle on a magnetic stirplate with a stirbar at 60°C until TPO solubilized. Parts were designed using Solidworks 2014 3D modeling software and saved as .STL files. The .STL file was then sliced in 1 $\mu\text{m}$  sections along the z axis using the opensource software Slic3r to generate a .SVG file containing the object's coordinates on each slice. This .SVG file is referenced by a .LUA script which controls the CLIP system's light source and build elevator. More information regarding .LUA scripts is provided in Appendix A. Parts were then fabricated using a CLIP3 system with a high resolution or low resolution lens setup or a CLIP7 system with Greenlight® or updated lenses from Edmund Optics. All of the parts in this dissertation are produced in continuous mode, where the light illuminates throughout the entire build and the build elevator moves upwards continuously.

To produce microneedles of different heights, CAD files of square pyramidal microneedles measuring 1000, 700, and 400  $\mu\text{m}$  tall with an aspect ratio of 3 (aspect ratio= height/width) were generated using Solidworks 2014. All microneedles were spaced at one base width apart on a base measuring 6x6x1mm. CAD files were then sliced at 1 $\mu\text{m}$  slice thickness using the open source software Slic3r. Microneedles were then produced using a CLIP additive manufacturing system (Carbon 3D, Redwood City, CA) in a mixture of trimethylolpropane triacrylate (Sigma Aldrich) and 2.5wt% Diphenyl(2,4,6-trimethylbenzoyl)phosphine oxide

(Sigma Aldrich) with  $5.4\text{mW}/\text{cm}^2$  of UV light ( $\lambda=370\text{nm}$  LED) as measured by the Dymax AccuCal™50 (Dymax Corporation) or  $8\text{mW}/\text{cm}^2$  as measured using an in-house photometer. at 100mm/hr Z scale factors of 1.175, 1.175, and 1.6 were added during scaling to counteract z-axis truncation visualized without scaling. All microneedles were visualized using an environmental scanning electron microscope (FEI Quanta 200) in low vacuum mode.

To demonstrate ability to alter microneedle size and shape, CAD files were created and sliced as previously described. The CAD file used to generate microneedles of varying aspect ratios contained microneedles measuring  $1000\mu\text{m}$  in height and  $500\mu\text{m}$ ,  $333\mu\text{m}$ , and  $250\mu\text{m}$  in width for aspect ratios of 2, 3, and 4, respectively. These microneedles were spaced at  $333\mu\text{m}$  apart. CAD files for microneedles of varying spacing measured  $1000\mu\text{m}$  in height and  $500\mu\text{m}$  in width with spacing at  $250\mu\text{m}$  or  $500\mu\text{m}$  apart.

Arrowhead microneedles measuring  $1000\mu\text{m}$  tall and  $500\mu\text{m}$  wide were fabricated from TMPTA + 2.5wt% TPO and 0.1wt% 2-(3'-tert-butyl-2'-hydroxy-5'-methylphenyl)-5-chlorobenzotriazole (Sigma Aldrich) at 41mm/hr with  $5.4\text{mW}/\text{cm}^2$  of UV light (Dymax). Tiered microneedles, measuring  $1000\mu\text{m}$ ,  $800\mu\text{m}$ , and  $600\mu\text{m}$  tall and  $400\mu\text{m}$  wide, and turret microneedles measuring  $1000\mu\text{m}$  tall and  $500\mu\text{m}$  wide were fabricated at 25mm/hr with  $1.35\text{mW}/\text{cm}^2$  of UV light (Dymax).

All part images were obtained using electron microscopy. Figures 2.5-2.9 were obtained using the FEI Quanta 200 in low vacuum mode. Figures 2.12 and 2.14 were sputter coated with 3nm of gold and imaged using an FEI Helios and Hitachi S-4700, respectively. All image measurements were obtained using ImageJ.

#### **2.4.5 Analysis of Antialiasing Algorithms**

The effect of antialiasing algorithms on CLIP microneedles was determined using custom software provided by Carbon3D equipped with either Windows Graphic Device Interface or Windows Graphic Device Interface Plus. Bitmap images were obtained by taking a screenshot of the image sent to the printer. Grayscale values of these bitmap images were obtained using the eyedropper tool in Windows Paint.

## REFERENCES

- (1) Tumbleston, J. R.; Ermoshkin, A.; Shirvanyants, D.; Ermoshkin, N.; Janusiewicz, R.; Johnson, A. R.; Kelly, D.; Chen, K.; Pinschmidt, R.; Rolland, J. P.; Samulski, E. T.; DeSimone, J. M. *Science*. **2015**, *347*, 1349-1352.
- (2) Texas Instruments. DLP3000. <http://www.ti.com/product/DLP3000> (Accessed Apr 8 2016)
- (3) Texas Instruments. DLP7000. <http://www.ti.com/product/DLP7000> (Accessed Apr 8 2016)
- (4) Saleh, B. E.; Teich, M. C. *Fundamentals of Photonics*; John Wiley & Sons, Inc. 1991.
- (5) Odian, G. *Principles of Polymerization*; John Wiley & Sons, Inc. 2004.
- (6) Jariwela A.S.; Ding, F.; Boddapati, A.; Breeveld, V.; Grover, M. A. *Rapid Prototyping Journal*. **2011**, *17*,168-175.
- (7) Fahad, M.; Hopkinson, N. *ICPMAE 2012*. **2012**, 234-238.
- (8) Leler, WJ. Human vision, anti-aliasing, and the cheap 4000 line display. *Association for Computing Machinery* 1980; *14*(3):308-313.
- (9) Crow, FC. The aliasing problem in computer-generated shaded images. *Communications of the ACM* 1977; *20*(11):799-805.
- (10) Sdltutorials.com. SDL TTF Fonts and How to Use Them. <http://www.sdltutorials.com/sdl-ttf> (Accessed Feb 4 2016)
- (11) Wilke, N.; Mulcahy, A.; Ye, S. R.; Morrissey, A. *Microelectronics J*. **2005**, *36*, 650-656.
- (12) Jansen, H. V.; de Boer, M. J.; Legtenberg, R.; Elswenspoek, M. *J Micromech Microeng*. **1995**, *5*, 115-120.
- (13) Chaudhuri, B. P.; Ceysens, F.; VanHoof, C.; Puers, R. *Conf Proc IEEE Eng Med Biol Soc*. **2013**, 156-159.
- (14) Park, J. H.; Prausnitz, M. R. *J Korean Phys Soc*. **2010**, *56*, 1223-1227.
- (15) Olatunji, O.; Das, D. B.; Garland, M. J.; Belaid, L; Donnelly, R. F. *J Pharm Sci*. **2013**, *102*, 1209-1021.
- (16) Davis, S. P.; Landis, B. J.; Adams, Z. H.; Allen, M. G.; Prausnitz, M. R. *J Biomech*. **2004**, *37*, 1155-1163.
- (17) Badran, M. M.; Kuntsche, J.; Fahr, A. *Eur J Pharm*. **2009**, *36*, 511-523.

- (18) Donnelly, R. F.; Garland, M. J; Morrow, D. I.; Migalska, K.; Singh, T. R.; Majithiya, R.; Woolfson, A. D. *J Control Release*. **2010**, *147*, 333-341.
- (19) Mahvash, M.; Dupont, P. E. *IEEE Transact on Biomed Eng*. **2010**, *57*, 934-943.
- (20) Chu, L. Y.; Prausnitz, M. R. *J Control Release*. **2011**, *149*, 242-249.

## CHAPTER 3 CONTROLLED RELEASE OF THERAPEUTICS FROM CLIP MICRONEEDLES

### 3.1 Introduction

As outlined in Chapter 1, numerous different types of microneedles have been fabricated for transdermal drug delivery. These microneedles are typically classified into four different configurations- 1) solid, uncoated microneedles, 2) solid, coated microneedles, 3) hollow microneedles and 4) biocompatible microneedles.<sup>1-2</sup> Each of these configurations differs in its mechanism of drug release (Figure 1.3).<sup>1-2</sup> Biocompatible microneedles are typically made of natural or synthetic polymer that swells,<sup>3</sup> dissolves,<sup>4</sup> or degrades<sup>5</sup> to release a therapeutic into the skin. Biocompatible microneedles are particularly promising because they eliminate the risk of accidentally depositing hazardous materials into the skin during microneedle use.<sup>1,6</sup> Biocompatible microneedles have a large volume available for encapsulation of the therapeutic and provide more control over the applied dose than other microneedle configurations.<sup>1</sup> Biodegradable or water soluble microneedles also eliminate sharp, biohazardous wastes thereby preventing needle stick injuries and disease transmission due to needle re-use. Importantly, biocompatible microneedles also present a unique opportunity to control drug release rates into the skin through careful matrix selection.

All controlled release systems aim to improve the effectiveness of therapeutics by altering drug concentration versus time profiles within the body.<sup>7-8</sup> Medications should be delivered at concentrations that are within a therapeutic window, i.e. higher than the minimum effective dose (MED) required to have a therapeutic effect, but well below the maximum tolerated dose (MTD)

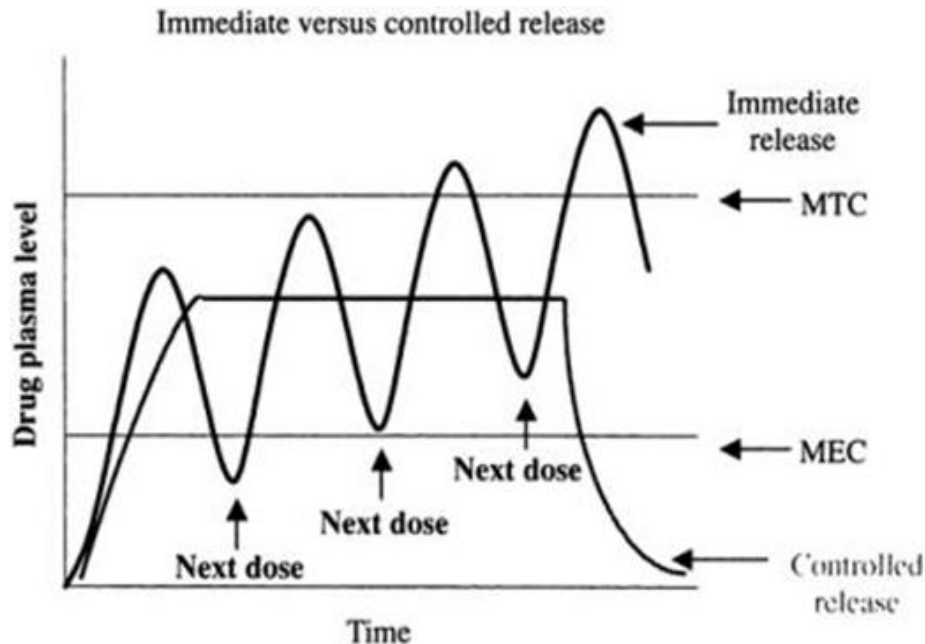


**Figure 3.1 Advantage of Controlled Release Systems.** Controlled release systems reduce fluctuations in drug concentrations to keep drug concentrations within the therapeutic window. Reproduced with permission from reference 8.

where toxic side effects begin to occur.<sup>7-8</sup> For agents intended to have a long duration of action, maintaining therapeutic concentrations often requires frequent dosing (Figure 3.1). The use of controlled release systems can reduce undesired fluctuations in drug concentration to maximize therapeutic effects while minimizing side effects (Figure 3.1).<sup>7-8</sup> These controlled release systems also provide an opportunity to minimize dosing frequency to improve patient compliance.<sup>7-8</sup> Microneedles may provide an ideal platform for a controlled release device because they can be deposited in the skin without a need for injection or surgical implantation.

In Chapter 2, we demonstrated the ability to fabricate microneedles using a new additive manufacturing technique called Continuous Liquid Interface Production (CLIP). This technique provides unlimited control over microneedle geometry, with prototyping speeds that are 400-1600X than traditional etching based techniques. Microneedles fabricated in Chapter 2 were composed of a model resin containing trimethylolpropane triacrylate (TMPTA) and 2.5wt%

diphenyl (2,4,6- trimethylbenzoyl) phosphine oxide (TPO) as a photoinitiator. This resin served as a positive control for chemistry throughout process development due to its previous use in stereolithography applications.<sup>9</sup> However, because TMPTA produces a non-degradable, tightly crosslinked hydrophobic network upon photopolymerization, it is not a suitable material for drug release applications. TMPTA also causes severe skin irritation upon contact,<sup>10</sup> and is therefore not a suitable material for a clinically translatable CLIP microneedle device. To take advantage of the potential to control drug release from microneedle devices, we endeavored to produce CLIP microneedles fabricated from biocompatible polymers designed to incorporate and control the release of therapeutics.

A number of different polymeric materials, both natural and synthetic, have been utilized for the incorporation and release of therapeutics for drug delivery applications. Release of the therapeutic is typically accomplished via one of three mechanisms- dissolution, degradation, or swelling of the matrix.<sup>7</sup> Appropriate dissolvable polymers are uncrosslinked, hydrophilic polymers that dissolve in aqueous environments. Some common examples of water-soluble natural and synthetic polymers used in drug delivery are polyvinylpyrrolidone (PVP), polyvinyl alcohol (PVA), lactose, and maltose, among others.<sup>11</sup> When uncrosslinked, These materials usually rapidly dissolve within the body, but dissolution rates can also be tailored by altering molecular weight and hydrophilicity of the polymer or the geometry of the device, depending upon the application.

Biodegradable polymers have components that chemically break down within the body. A variety of polymers have been used, including natural, synthetic, crosslinked, and uncrosslinked systems. In most cases, breakdown occurs via either hydrolysis (for synthetic systems) or enzymatic degradation (for natural systems) of the polymer backbone.<sup>12-13</sup> Therefore,

uncrosslinked systems typically undergo complete degradation, whereas crosslinked systems typically leave non-degradable crosslinks behind after degradation of the backbone.

Hydrolytically cleavable groups include esters, anhydrides, carbonates, amides, and urethanes, among others.<sup>12-13</sup> The most commonly utilized groups are poly( $\alpha$ -esters), such as polyglycolide, polylactides, polycaprolactones, and their copolymers.<sup>12-13</sup> Key advantages of such systems include their FDA approval and the ability to tune solubility and release rates by altering copolymer ratios. For example, poly(lactide-co-glycolide) (PLGA) copolymers degrade more quickly as the LA/GA ratio decreases because of the faster degradation rate of the polyglycolic acid (PGA); 85/15 blends of poly(lactide-co-glycolide) typically degrade over the course of 5-6 months, whereas 50/50 blends typically degrade over the course of 1-2 months.<sup>12-13</sup>

Enzymatically cleavable natural polymers including proteins (collagen, elastin, albumin) and polysaccharides (hyaluronic acid, chondroitin sulfate, chitosan, alginate) have also been utilized for drug delivery applications.<sup>12</sup> These natural polymers have some interesting bioactive/bioregenerative properties, but also tend to exhibit high patient to patient variability in degradation rates due to differences in endogenous enzyme levels.<sup>12</sup>

Lastly, non-degradable, crosslinked hydrophilic networks called “hydrogels” have been developed for pharmaceutical applications.<sup>14-16</sup> These hydrogels swell in aqueous environments to release therapeutics via diffusion through a crosslinked mesh.<sup>14-16</sup> Some commonly used hydrogels include crosslinked polyethylene glycol, polyvinylpyrrolidone (PVP), polyvinyl alcohol (PVA), polyacrylamide, polyacrylic acid, and hyaluronic acid, among others.<sup>14-16</sup> These materials provide opportunity to closely control release rates by altering the molecular weight between crosslinks (crosslink density), the hydrophilicity of the polymer chain, and electrostatic interactions between the cargo and the polymer backbone.<sup>14-16</sup> Stimulus-responsive hydrogel

systems have also been developed to control release in response to changes in temperature, pH, antibody binding, and glucose levels, among others.<sup>15</sup>

Given the range of biocompatible materials and pharmaceutical applications, there is no one system available that could be considered ideal for every case. The characteristics of the therapeutic (size, charge, solubility) and its desired release profile (rapid vs. sustained release) must be considered. Therefore, an ideal microneedle fabrication technique would allow for rapid optimization of microneedle composition for a given application. To this end, we aimed to use CLIP to fabricate microneedles from a wide variety of different biocompatible materials. More specifically, we aimed to show that CLIP could be used to fabricate biocompatible microneedles designed to control the release therapeutics via each of the three different release mechanisms- rapid dissolution, hydrolytic degradation, and swelling.

## **3.2 Results and Discussion**

### **3.2.1 Selection of Biocompatible Materials**

In selecting a biocompatible material suitable for use as a CLIP microneedle matrix, it was important to identify a low viscosity resin that would produce a strong microneedle after photopolymerization. Low viscosity resins are well suited for use with CLIP because they quickly flow into the build area as the build elevator moves upward throughout production. Low viscosity resins can be either a neat solution of liquid monomer/oligomer or a solid photoreactive monomer/oligomer dissolved in a liquid reactive or non-reactive diluent. For the purposes of this research, we chose to formulate solvent-free resins that do not contain any non-reactive diluents. Eliminating such a solvent from the system avoids 1) the formation of solvent-induced pores, which may decrease the strength of the microneedle, 2) chain transfer to solvent during the reaction 3) post processing steps required to remove solvent after microneedle fabrication and 4)



polymerize to form loosely crosslinked networks which release cargo more quickly, but are mechanically weaker. PEG550-dMa is among the highest molecular weight PEG-dMa that is still liquid at room temperature. We hypothesized that this low viscosity oligomer has a high enough molecular weight to allow cargo to escape over a reasonable period of time, but low enough molecular weight to form a strong microneedle capable of skin penetration. Methacrylate endgroups were chosen, as opposed to acrylates, due to their lower toxicity *in vivo*.<sup>17</sup>

To generate a microneedle designed for sustained release of hydrophobic cargos through degradation, a polycaprolactone triol was functionalized with methacrylic anhydride to form a polycaprolactone trimethacrylate (PCL1110-tMa) with a molecular weight of 1110 g/mol (Figure 4.2B). Although other polyesters may result in a stronger needle and/or allow for faster cargo release,<sup>12-13</sup> this material was chosen due to the commercial availability of the PCL triol, which allowed for functionalization with photoreactive endgroups.

The production of uncrosslinked, dissolvable microneedles using CLIP is more challenging. Because most uncrosslinked polymers are soluble in their own monomer, uncrosslinked CLIP parts typically dissolve inside the vat of monomer before part fabrication can be completed. Polyacrylic acid (PAA) provides a unique opportunity for use with CLIP because it belongs to a small class of polymers that are insoluble in their own monomer (due to the polar nature of the PAA, which makes it much more hydrophilic than the monomer).<sup>18</sup> This unique property enables the PAA polymer to precipitate out as it is formed in the vat of acrylic acid (AA) monomer to form a solid part. For this reason, AA was chosen as a monomer utilized to produce water-soluble polyacrylic acid microneedles.

All oligomers were mixed with 2.5wt% diphenyl(2,4,6-trimethylbenzoyl)phosphine oxide (TPO) as a photoinitiator.

### 3.2.2 Stereolithographic Working Curves

Chapters 2 underscores the critical importance of light intensity and build speed for the production of parts via CLIP. In Chapter 2, all light intensities and build speeds were determined empirically. Each new biocompatible resin used here will have its unique set of curing properties (polymerization rate, reaction volume, etc.). **Therefore, rather than empirically selecting new build parameters for each new biocompatible resin, we endeavored to develop a more efficient method of determining build parameters through use of working curves that have previously been used in stereolithography.**<sup>19-20</sup> Throughout this chapter, the terms “appropriate build parameters” is used to refer to light intensities and build speeds that produce dimensionally accurate parts.

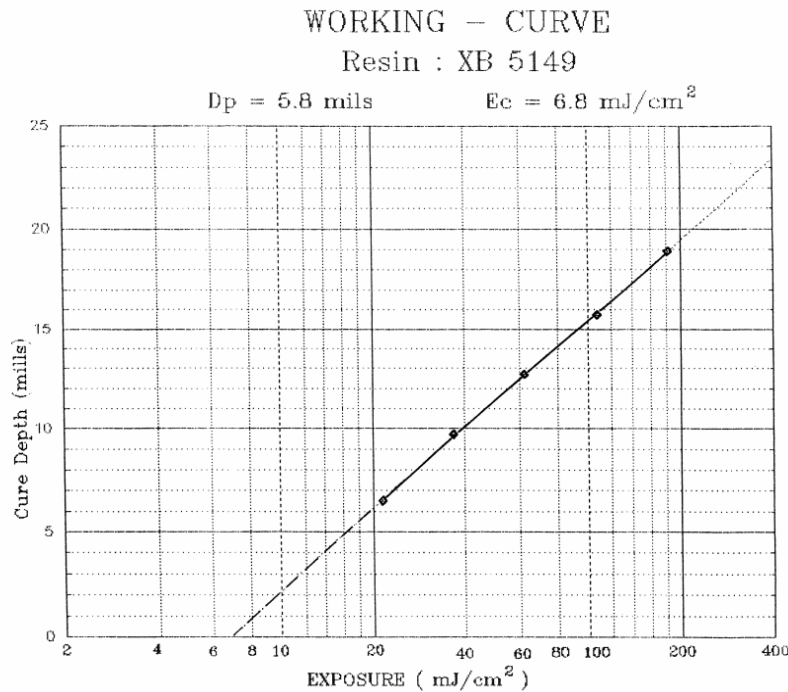


Figure 3.3 Sterolithographic working curve. Reproduced with permission from reference 20.

In the field of stereolithography, a calibration curve called a “working curve” has been utilized to determine the appropriate exposure time for the production of a part with a specific resin.<sup>19-20</sup> Exposure, in this case, is defined as the product of the light intensity given in mW/cm<sup>2</sup> with the exposure time given in seconds. Therefore, a part produced with 1mW/cm<sup>2</sup> of light with an exposure time of 2 seconds and a part produced with 2mW/cm<sup>2</sup> of light with an exposure time of 1 second both experience the same total light exposure. The working curve relates this applied light exposure per layer to resin cure heights. **The exposure that allows each layer to cure to the appropriate height (specified by the CAD file slice thickness) is used for part fabrication.** For example, a part that is 1cm in height could be sliced into one hundred layers, each measuring 100µm. Such a part would be exposed to a given intensity of light for the amount of time that enables the resin to cure to 100 µm tall. The working curve can be mathematically defined by Equation 3.1:

$$C_T = \frac{1}{\alpha} \ln\left(\frac{E}{E_c}\right) \quad (3.1)$$

where  $C_T$  is the cured thickness of the resin in µm,  $E$  and  $E_c$  are the actual and critical exposures, respectively, in units of mJ/cm<sup>2</sup>, and  $\alpha$  is the absorption coefficient of the resin in µm<sup>-1</sup>. A graph of a working curve, plotted on a log-linear scale, is given in Figure 3.3.

This working curve is fundamental to stereolithography and can be directly derived from the Beer-Lambert law, as described in the following section.

### 3.2.3 Derivation of the Working Curve from Beer-Lambert Law

The Beer-Lambert law, which describes the attenuation of a light source through an absorbant material, can be described by Equation 3.2:

$$I(z) = I_0 e^{-\alpha z} \quad (3.2)$$

where  $I$  is the intensity of the light source in power per unit area,  $\alpha$  is the absorption coefficient of the resin, and  $z$  is the depth of light penetration into the sample, in our case, a vat of resin.

Multiplying the equation by exposure time yields

$$It = I_0 t e^{-\alpha z} \quad (3.3)$$

Which is equivalent to

$$E = E_0 e^{-\alpha z} \quad (3.4)$$

In order for liquid resin to solidify to a particular depth ( $z_{ct}$ ), a critical exposure is required for cure. This is called the critical exposure ( $E_c$ )

$$E_c = E e^{-\alpha z_{ct}} \quad (3.5)$$

Solving for  $z_{ct}$  gives cured thickness as a function of the resin parameters  $\alpha$  and  $E_c$

$$z_{ct} = \frac{1}{\alpha} \ln\left(\frac{E}{E_c}\right) \quad (3.6)$$

which can be determined from the slope and intercept, respectively of the working curve.  $E_c$  can therefore be considered the minimum light exposure required to produce a solid structure.

### 3.2.4 Application of Working Curves to CLIP

Tumbleston et. al. investigated whether this working curve can be utilized to calculate appropriate light intensity and build speed for part fabrication via CLIP.<sup>3</sup> In order to generate a working curve, resin sitting on top of a glass wafer was exposed to a single frame of light. This frame was projected at different light intensities for different amounts of time (Figure 3.4A) using a CLIP device. The authors found that working curves could be generated to describe the relationship between exposure and cure height of the resin on the glass wafer. (Figure 3.4B). By

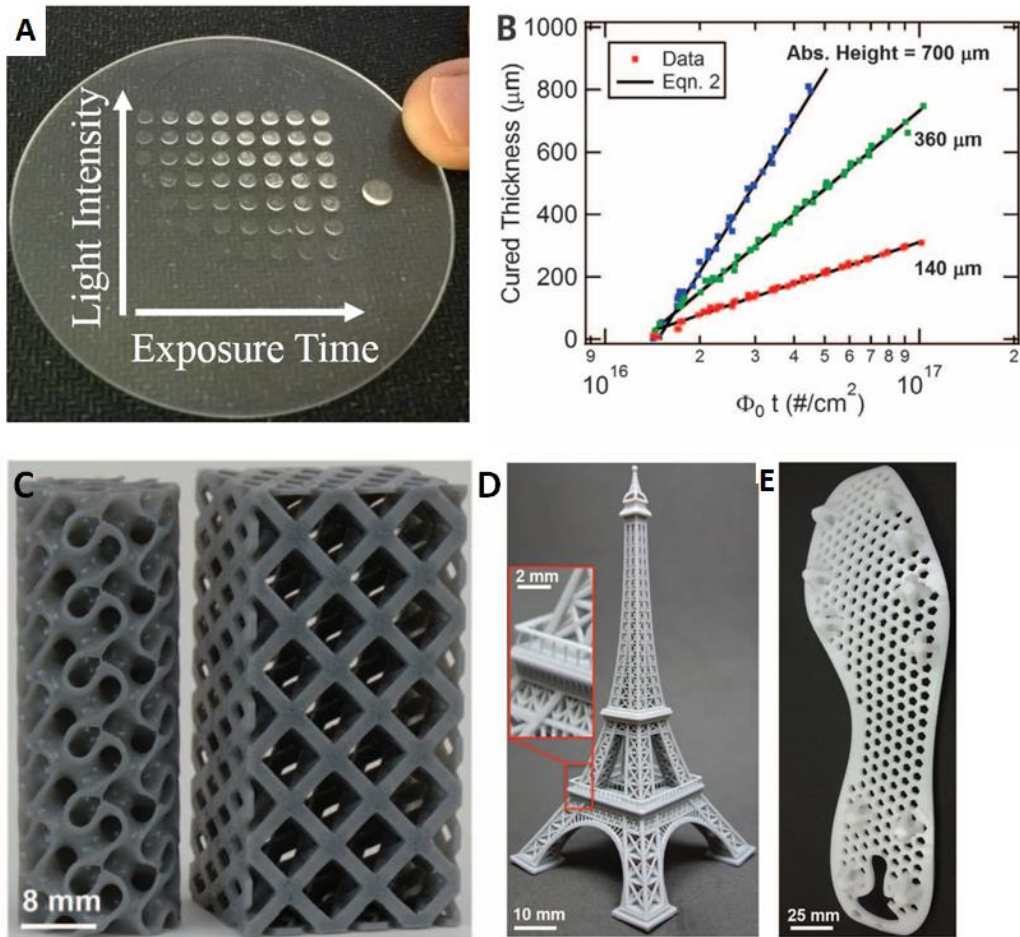


**Figure 3.4 CLIP working curves enable part production** A) Method for producing working curve. B) Working curve generated on a CLIP system. Figures are reproduced with permission from reference 3.

fitting this working curve to Equation 3.1, the absorbance of the resin,  $\alpha$ , and critical exposure,  $E_c$ , could be determined. Therefore, generation of working curves was possible using a CLIP device.

The application of working curves to CLIP is more complex than standard layer-by-layer based stereolithography systems because of the continuous movement of the build elevator. Nevertheless, the appropriate exposure per frame can be identified based on the rate of upward movement of the build elevator over time. For example, if the build elevator were to move upward at a rate of 100mm/hr through a 1mm slice, the exposure that cures the resin to 100  $\mu\text{m}$

thick within  $1/100^{\text{th}}$  of an hour would be selected for fabrication. These are not reasonable values, but are chosen for simplicity of explanation. This working curve method was used to produce a variety of different parts, including the gyroid, Eiffel tower, and shoe cleats in Figure 3.4C-E.

We then designed an experiment to determine whether this working curve based “calculator” could be used to calculate appropriate build parameters for small parts, such as microneedles. A test part was designed to have one “large” feature measuring 4mmx1mmx1mm (LxWxH) and several smaller microneedles measuring 1mm in height (Figure 3.5B). The width of these microneedles was 500 $\mu\text{m}$ , 333 $\mu\text{m}$ , 250 $\mu\text{m}$ , and 100 $\mu\text{m}$  moving from right to left along the test part. The large part served as a positive control for the utility of the working curve calculator for larger parts; the smaller microneedles were added to determine whether the calculator could be used for small parts. The optimal build speed for a given light intensity was identified using a TMPTA working curve developed by Carbon3D for TMPTA mixed with 2.5wt% TPO.

Figure 3.5A-C is an image of the test part printed with parameters identified using the working curve. All three parts were printed with equivalent exposures, but different combinations of light intensity and build speed. Although the height of the large rectangle and the microneedles are both 1mm in the CAD file, the microneedles are shorter than the rectangle for all fabricated parts. Quantification of the height of each object on each part is given in Figure 3.5E. The large 4mm wide rectangle was found to be within 5% of its intended height, confirming that the working curve based calculator does accurately identify build parameters for large parts. The percent reduction in height was also quantified for all microneedles (Figure 3.5E). As feature width decreases, the error in part height increases, suggesting that the

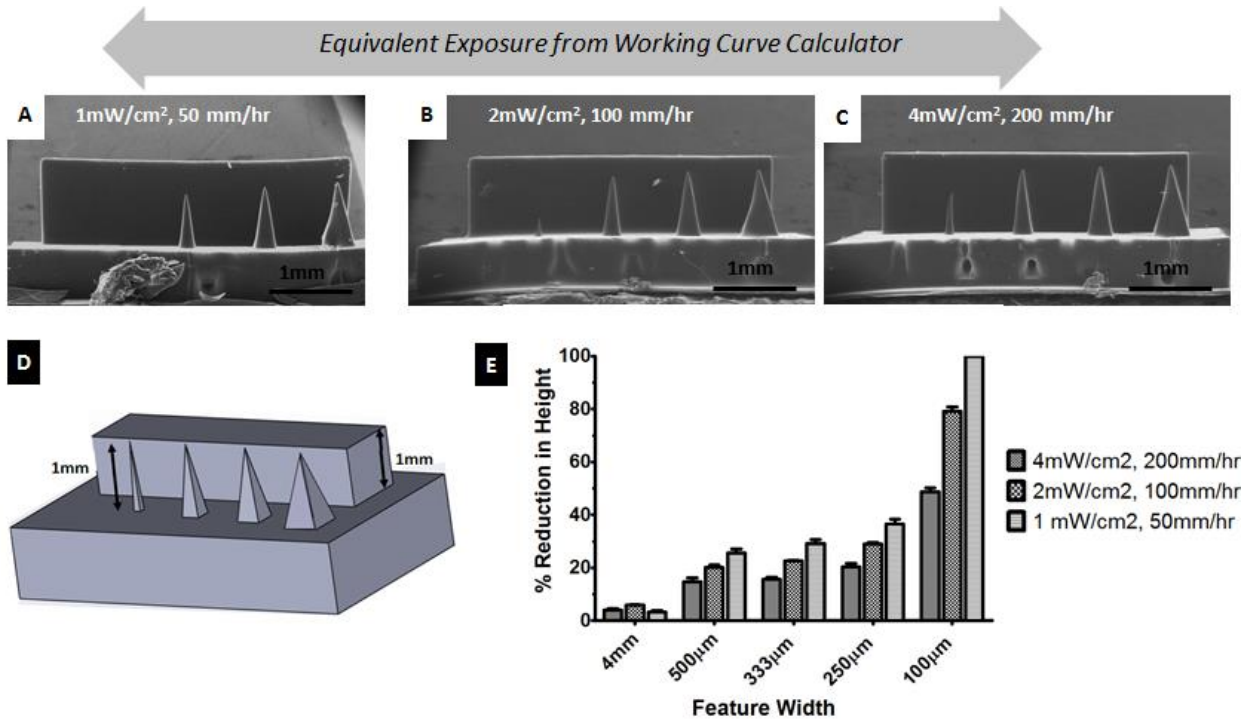


**Figure 3.5 Appropriate Build Parameters are Size Dependent on Small Scale.** TMPTA test parts fabricated with A) 1mW/cm<sup>2</sup> of light at 50mm/hr B) 2mW/cm<sup>2</sup> of light at 100mm/hr and C) 4mW/cm<sup>2</sup> of light at 200mm/hr. D) CAD file of the test part with 1mm tall microneedles with base widths ranging from 100µm to 500 µm and a large square measuring 4mmx1mmx1mm. E) Percent reduction (percent error) in height of all structures in A-C

calculator is not well suited for identifying appropriate build parameters for very small parts. We hypothesize that the difference in the height of small and large scale parts is due to differences in the quantity of light projected per unit area, caused by superposition of light distribution from neighboring pixels. This hypothesis is further investigated in Appendix B. Part width was found to be within 5% of the intended dimensions, regardless of part size (data not shown).

**The results demonstrate the working curve “calculator” could correctly identify appropriate build parameters for the fabrication of large parts. Microneedles, however, were shorter than the intended CAD file when fabricated with these build parameters. Therefore, appropriate build parameters are dependent on the size of the object on the small scale.** Appendix B presents a hypothesis to explain the difference in appropriate build parameters as a function of size.

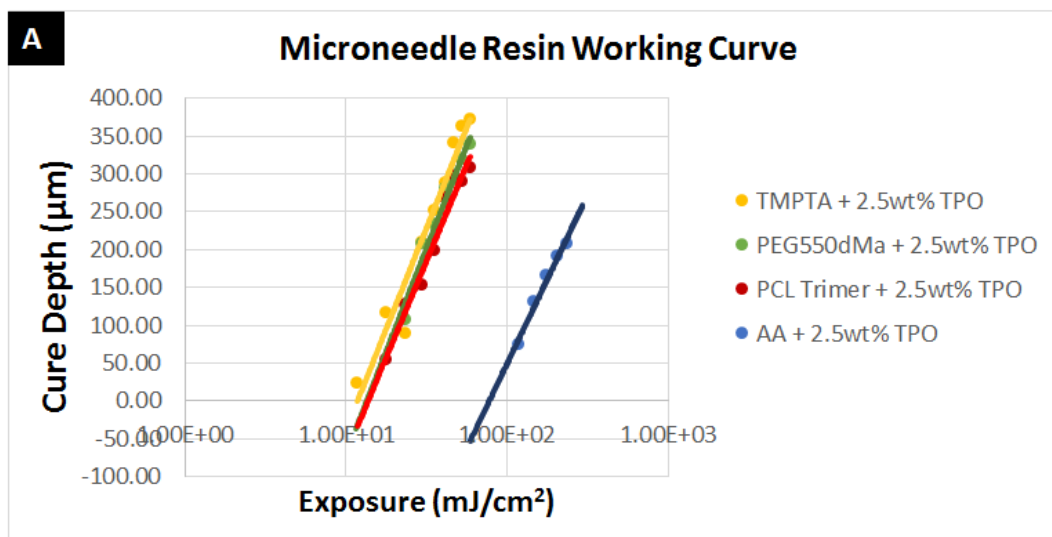
**We did, however, hypothesize that working curves could be utilized to mathematically convert build parameters that were empirically determined to be effective for the production of TMPTA microneedles to build parameters appropriate for the production of microneedles using new, biocompatible resins, as explained in the following section.**

### **3.2.5 Adaptation of Working Curves to Microneedle Fabrication**

In order to test this hypothesis, a working curve was established for TMPTA, PEG, PCL, and PAA. Methods were adapted from Tumbleston et. al.<sup>19</sup> A picture of the experimental setup used to produce the working curve is given in Figure 3.5A. Briefly, a dot of resin was placed on a cover slip on top of the printer window and exposed to a specified amount of light (Figure 3.5A), where exposure is defined as the product of light intensity (in mW/cm<sup>2</sup>) and exposure time (in seconds). The height of the resulting object was determined and plotted on a log-linear scale (Figure 3.6A), where the best fit line between individual data points is defined by the working curve equation

$$C_T = \frac{1}{\alpha} \ln\left(\frac{E}{E_c}\right) \quad (3.6)$$

where  $C_T$  is the thickness of a cured dot,  $\alpha$  is the absorption coefficient of the resin in units of  $\mu\text{m}^{-1}$ ,  $E$  is exposure of an individual frame (the product of light intensity and exposure time, given in  $\text{mJ}/\text{cm}^2$ ), and  $E_c$  is the critical exposure required to induce polymerization of the resin in units of  $\text{mJ}/\text{cm}^2$ . The absorption coefficient  $\alpha$  and critical exposure  $E_c$  of the resins (as reported in Figure 3.6B) could then be determined from the slope and x intercept of the best fit line, respectively.



**B**

Resin	Absorption Coefficient ( $\mu\text{m}^{-1}$ )	Critical Exposure ( $\text{mJ}/\text{cm}^2$ )
TMPTA + 2.5wt% TPO	0.0043	11.8
PEG550dMa + 2.5wt% TPO	0.0042	13.4
PCL tMa + 2.5wt% TPO	0.0045	13.7
AA + 2.5 wt% TPO	0.0052	77.3

**Figure 3.6 Stereolithographic Working Curve and Resin Properties.** A) The cure depth of microneedle resins as a function of applied dosage B) Absorption coefficient and critical exposure of microneedle resins determined from the working curves in figure A

The working curves for all four microneedle resins are shown in Figure 3.7. All resins have approximately equivalent slopes, indicating that they have an approximately equivalent absorbance. This equivalent absorbance is expected because all of the resins contain the same concentration of photoinitiator (2.5wt% TPO) and the absorbance of the oligomers at  $\lambda=365$  is negligible. PEG, PCL, and TMPTA resins have similar critical exposures, whereas the AA resin requires approximately six fold more light to solidify. The mechanism behind these trends in critical exposure is currently unconfirmed. Although one explanation may be differences in reaction rates, one would expect the AA monomer to react more quickly than methacrylated oligomer because of the increased reactivity of the acrylate relative to the methacrylate.<sup>21</sup>

**Table 3.1 Build parameters for biocompatible CLIP microneedles**

Resin	Build Speed (mm/hr)	Light Intensity (mW/cm <sup>2</sup> )
PEG550 + 2.5wt% TPO	25	1.2 mW/cm <sup>2</sup>
PCL + 2.5wt% TPO	25	1.5 mW/cm <sup>2</sup>
AA + 2.5wt% TPO	25	8.9 mW/cm <sup>2</sup>

Measuring reaction rates using photo-DSC would be a useful way to test this hypothesis.

Alternatively, the higher  $E_c$  of AA but may be related to the increased molecular weight of PEG550-dMa, PCL1110-tMa, and TMPTA as compared to AA, which would result in a greater increase in part volume per converted bond for these resins as compared to the AA. Differences in the functionality of the oligomer may also contribute to these trends.

Calculated critical exposures and absorption coefficients were used to convert empirically determined TMPTA microneedle build parameters to parameters used for fabricating microneedles with new resins. The appropriate exposure per frame was calculated by selecting the exposure that produces a cure thickness equivalent to TMPTA after exposure to a single frame, according to Equation 3.7 and Equation 3.8, below.

$$C_{T, TMPTA} = C_{T, ResinX} \quad (3.7)$$

$$1/\alpha_{TMPTA} \ln(E_{TMPTA} / E_{c, TMPTA}) = 1/\alpha_{ResinX} \ln(E_{ResinX} / E_{c, ResinX}) \quad (3.8)$$

During a continuous print, the applied exposure per frame (assuming constant slice thickness) is proportional to the applied light intensity divided by the build speed, given in mm/hr in the z direction, as shown in Equation 3.9

$$E_{applied} \propto \frac{\text{Light Intensity}}{\text{Build Speed}} \quad (3.9)$$

Because the absorption coefficients of microneedle resins are approximately equivalent (Figure 4.4), substituting into Equation 3.9 into Equation 3.8 yields

$$\frac{Intensity_{TMPTA}}{E_{c,TMPTA} \cdot Speed_{TMPTA}} = \frac{Intensity_{ResinX}}{E_{c,ResinX} \cdot Speed_{ResinX}} \quad (3.10)$$

A build speed of 25 mm/hr was selected for fabrication of biocompatible microneedles to minimize the potential for defects due to incomplete resin flow into the build area at higher build speeds. Therefore, the light intensity required for microneedle fabrication using an arbitrary Resin X could be calculated using Equation 3.11, below

$$Intensity_{ResinX} = \frac{Intensity_{TMPTA} \cdot E_{c,ResinX} \cdot Speed_{ResinX}}{Speed_{TMPTA} \cdot E_{c,TMPTA}} \quad (3.11)$$

Using Equation 11 and the critical exposures in Figure 3.6B, build parameters for the new resins could be calculated. These build parameters are given in Table 3.1.

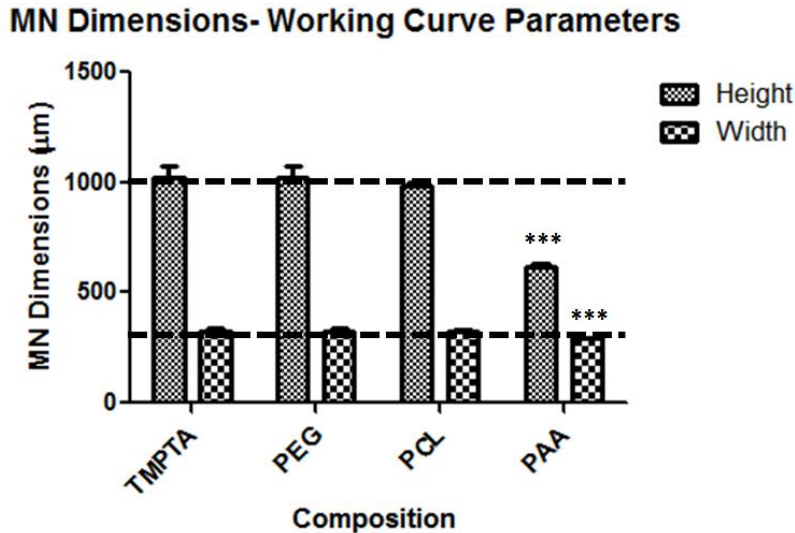


**Figure 3.7 Dimensions of Biocompatible MNs Produced Using Parameters from Working Curve.** Height and width of TMPTA, PEG, PCL, and PAA microneedles. Intended dimensions are marked with a dotted line. PAA microneedle height and width were determined to be significantly different from all other compositions at a  $p < 0.0001$  significance level. Data are presented as mean  $\pm$  SD

### 3.2.6 Production of Biocompatible CLIP Microneedles

Using the build parameters established in section 3.2.5 (Table 3.1) and a z scale factor of 1.175 (previously established for TMPTA microneedles in Chapter 2) biocompatible CLIP microneedles were fabricated. The dimensions of all microneedles produced using this technique were compared (Figure 3.7) to determine whether the working curve provided an effective method of producing equivalent parts from different resins. No statistically significant difference in dimensions of TMPTA, PEG, and PCL microneedles was found, but PAA microneedles truncated significantly relative to the other compositions (Figure 3.7) This may indicate that either 1) the working curve is not an effective method for selecting the correct build parameters for any material or 2) the working curve is only effective for selecting build parameters for crosslinked systems due to differences in the mechanism of formation of linear and crosslinked systems. This question will be revisited in Chapter 4 using a range of resins. To correct PAA

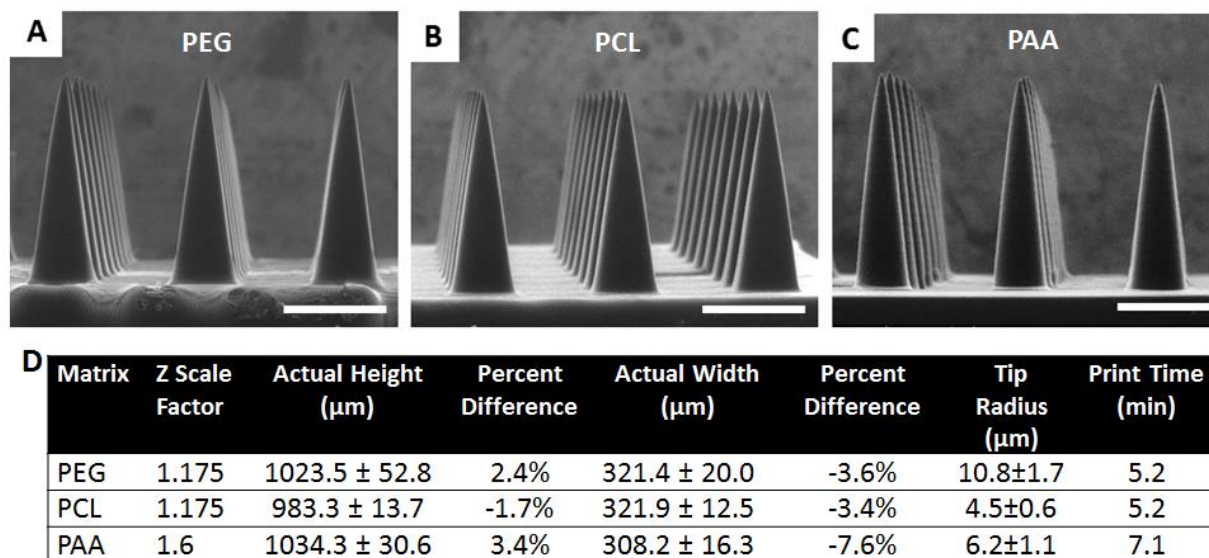


**Figure 3.8 Biocompatible microneedles.** ESEM images of A) Polyethylene glycol B) Polycaprolactone and C) Polyacrylic acid microneedles measuring approximately 1000 $\mu\text{m}$  in height and 333 $\mu\text{m}$  in width D) Dimensions, print times, and tip radii of biodegradable microneedles (n=9) shown in Figure 3. Scale bars measure 500 $\mu\text{m}$ . All data are represented as mean  $\pm$  SD

microneedle dimensions for use in this chapter, microneedles were re-scaled in the z direction (the z scale factor was increased to 1.6, resulting in a 1600 $\mu$ m tall CAD file), to enable production of the desired 1000 $\mu$ m tall microneedles, as shown in Figure 3.8.

Using this technique, fabrication of CLIP microneedles composed of PEG, PCL, and PAA was achieved (Figure 3.8A-C) and the structure of the CLIP microneedles was found to be consistent between resins. Microneedles measured approximately 1000 $\mu$ m in height with an aspect ratio (AR=height/width) of 3, with all microneedles measuring within  $\pm 10\%$  of their intended dimensions (Figure 3.8D). Tip radii for these biocompatible microneedles measure less than approximately 10 $\mu$ m, with fabrication times under 10 minutes per patch (Figure 3.8D).

### 3.2.7 Microneedle Skin Insertion Tests

In order to successfully deliver a cargo into the skin, CLIP microneedles must be capable of physically penetrating the stratum corneum. The ability of CLIP microneedles to puncture the skin was assessed using murine skin *ex vivo*. Microneedle penetration studies have been commonly performed *ex vivo*; a number of animal models have been used as a source for skin,

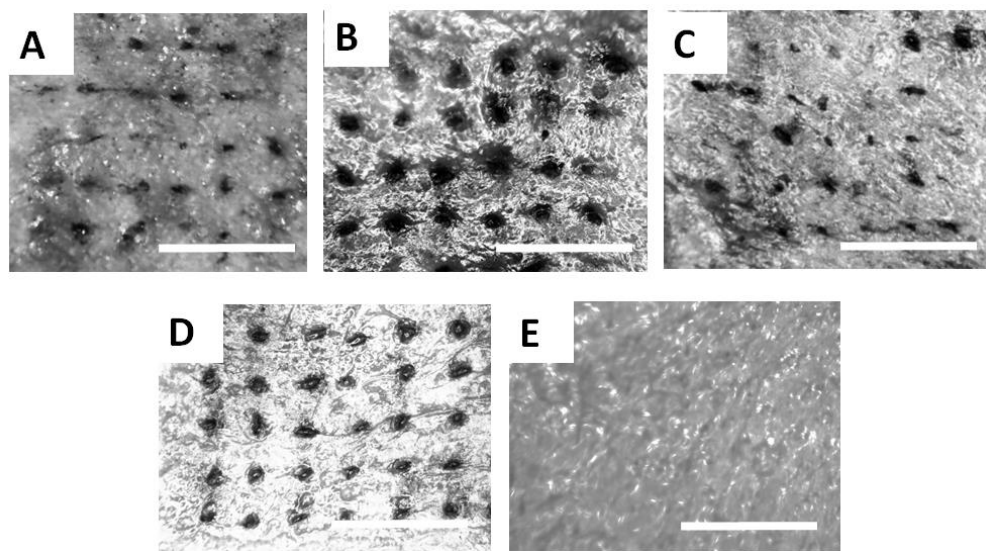


**Figure 3.9 Skin insertion tests.** Sites of skin penetration from CLIP Microneedle arrays made of A) PCL B) TMPTA C) PEG and D) PAA on murine skin can be visualized using a tissue marking dye. E) No insertion sites are visualized on a piece of control skin to which no microneedles were applied. Scale bars measure 1mm.

including nude mice, rats, and pigs. Murine skin is much thinner than human skin (murine skin is typically 300-500 $\mu$ m in thickness, whereas human skin varies widely in thickness, ranging from 600-3,000 $\mu$ m, depending on location).<sup>22-24</sup> Murine skin has also been shown to have vastly different mechanical properties than human skin.<sup>25</sup> Nevertheless, full thickness skin excised from nude mice was utilized for testing *ex-vivo* due to availability and continuity with potential pre-clinical *in vivo* studies. Further investigation of microneedle penetration using porcine skin, which is a better animal model, is performed in Chapter 4.

Microneedles of all four different compositions (TMPTA, PAA, PCL, and PEG) were applied to murine skin *ex vivo* by pressing firmly on the back of the microneedle patches with the thumb for 10 seconds. The microneedle patches were then removed and a green tissue marking dye that selectively marks sites of skin penetration was applied. All four microneedle compositions were observed to successfully breach murine skin (Figure 3.9A-D), whereas no sites of penetration were observed on untreated skin (Figure 3.9E). Some qualitative differences in the penetration efficacy of the four different microneedle compositions were observed. For example, the TMPTA and PAA microneedles appear to produce larger sites of penetration within the skin than the PCL and PEG microneedles, perhaps suggesting deeper penetration into the skin due to the superior mechanical properties of these compositions. Nevertheless, these results indicate that all four microneedle compositions exhibit sufficient strength to pierce murine skin. These materials may therefore be suitable for transdermal drug delivery in the form of CLIP microneedles.

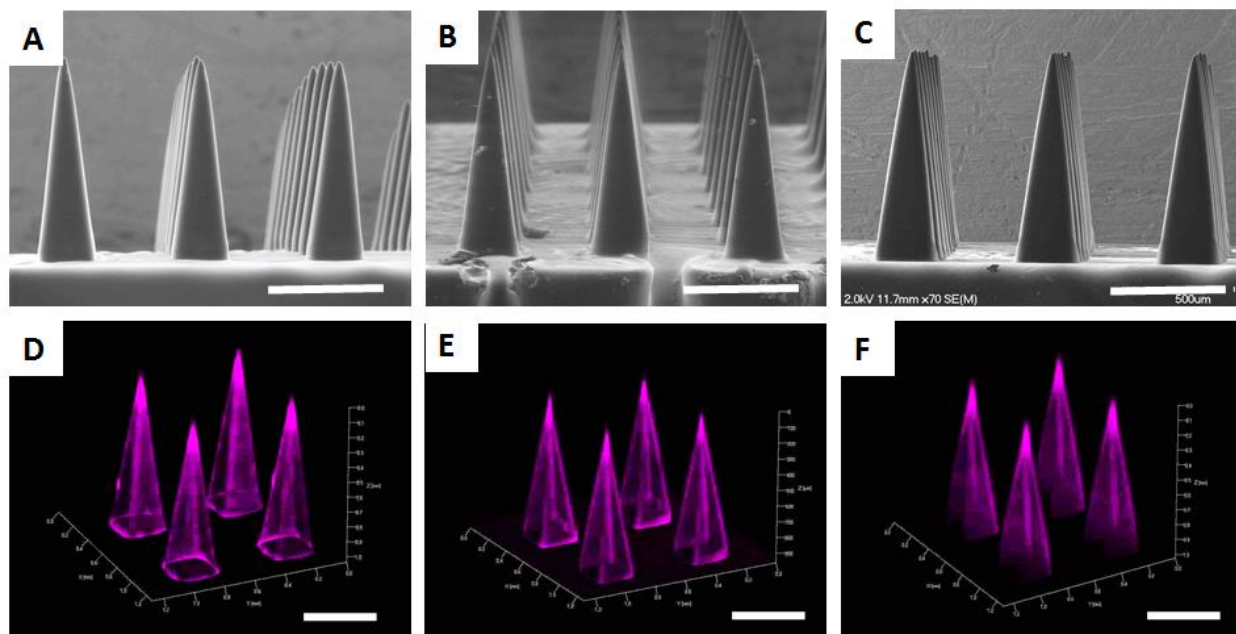


**Figure 3.10 Rhodamine loaded CLIP MNs.** Incorporation of rhodamine does not alter structure of A) PEG, B) PCL or C) PAA MNs characterized by ESEM. Rhodamine distributes throughout D) PEG, E) PCL, and F) PAA MNs needles visualized via confocal microscopy. The rhodamine channel is displayed in purple. Scale bars measure 500 $\mu$ m.

### 3.2.8 Loading and Release of Fluorescent Drug Surrogate

In order to determine whether CLIP microneedles can be utilized to encapsulate and release a therapeutic cargo, the fluorescent drug surrogate rhodamine was loaded into CLIP microneedles. Rhodamine was encapsulated by mixing 0.1wt% rhodamine into the photopolymerizable resin before fabricating the microneedle using the previously described methods. In order to demonstrate that cargo loading does not affect microneedle structure, microneedles were characterized by ESEM after cargo encapsulation (Figure 3.10 A-C). In order to assess cargo distribution within the microneedle matrix, rhodamine containing microneedles were also imaged via confocal microscopy (Figure 3.10 D-F). Results show that CLIP microneedles retain their structure after cargo incorporation. Rhodamine is uniformly distributed throughout the microneedle matrix.

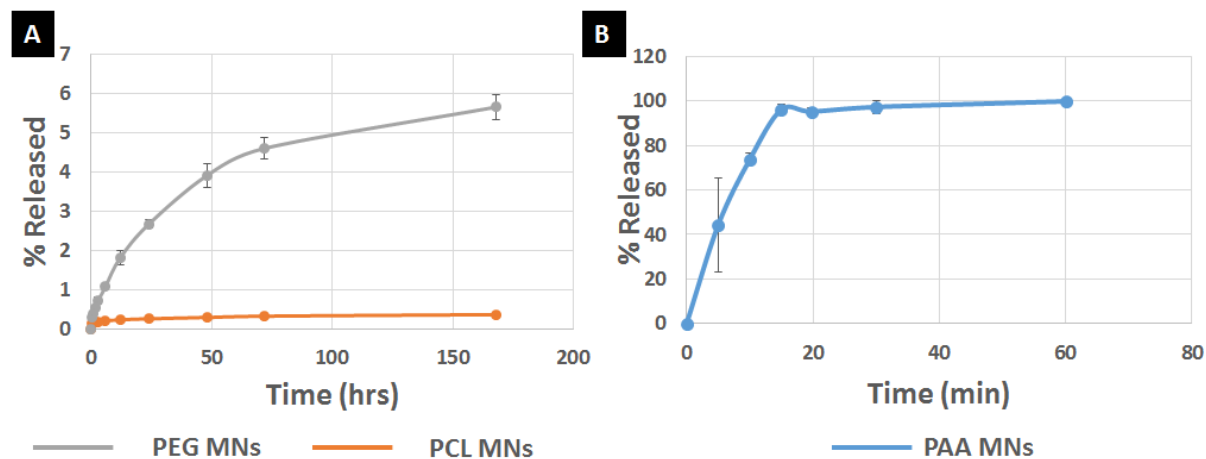


**Figure 3.11 Rhodamine release rates** Rates of rhodamine release from A) PEG, PCL and B) PAA MNs loaded with 0.1 wt% rhodamine

To assess drug release rates out of CLIP microneedles in solution, rhodamine containing microneedle arrays were submerged in 1mL of phosphate buffered saline (PBS). Rhodamine release was assessed via fluorescence over one week for PCL and PEG microneedles, and over the course of one hour for PAA microneedles. 500 $\mu$ L of solution was removed for quantification at each timepoint and replaced with an additional 500 $\mu$ L of PBS. Rhodamine release rates as a percentage of theoretical loading are reported in Figure 3.11. Both the PEG and PCL microneedles release rhodamine slowly. Over the course of one week, PCL microneedles release less than 1% of their cargo, whereas PEG microneedles release about 5.5% of cargo (Figure 3.11A). This slow, sustained release is expected due to the high crosslink density and slow degradation rates of PCL (typically on the order of months) and the highly crosslinked nature of the PEG matrix. The PAA microneedles, on the other hand, rapidly released all of their cargo by dissolution within 15 minutes. It is worth noting that release rates in aqueous media are likely to be more rapid than release rates in skin tissue (which is approximately 60-70% hydrated).<sup>26</sup> Nevertheless, release rates in solution provide a helpful mechanism for approximating release rates in skin. Together, these results indicate that CLIP microneedles can be utilized to tailor

drug release rates via appropriate matrix selection. Further consideration of the desired release rate and the properties of the desired cargo, such as solubility, charge, and size, would be necessary to select an optimal matrix for translational applications.

### 3.2.9 Dissolvable PAA Microneedles Release Cargo in Skin

Rapid release is ideal for applications being investigated within our laboratory, such as the delivery of insulin for diabetes treatment. Therefore, we continued to characterize cargo release from PAA microneedles both in solution and within murine skin *ex vivo*. In addition to rapidly releasing cargo, PAA microneedles should completely dissolve upon application, providing an opportunity to eliminate the production of sharp, biohazardous wastes. In order to confirm that PAA microneedles are completely dissolvable, rhodamine containing PAA microneedles on a PCL backing were imaged before and after submersion in aqueous media (Figure 3.12). Complete dissolution of the rhodamine containing PAA microneedles is observed within 15 minutes, leaving behind the water-insoluble PCL backing.

We then wanted to determine whether PAA microneedles are capable of delivering cargo to the skin. Rhodamine containing and blank PAA microneedles were administered to murine

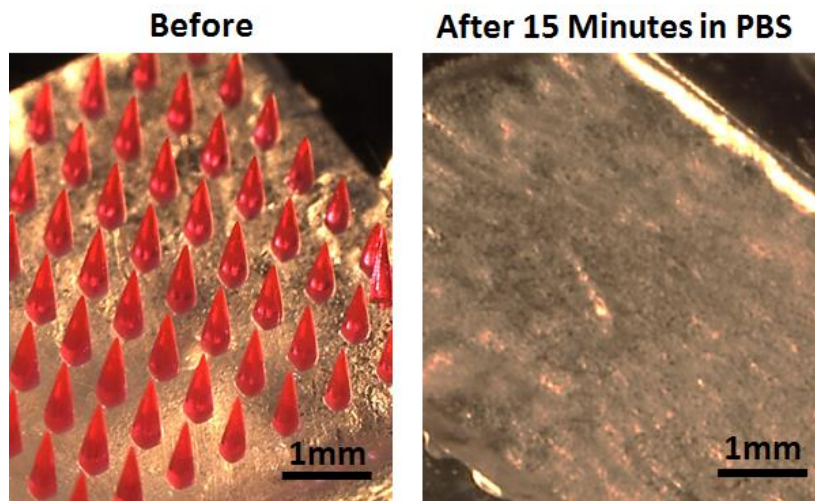
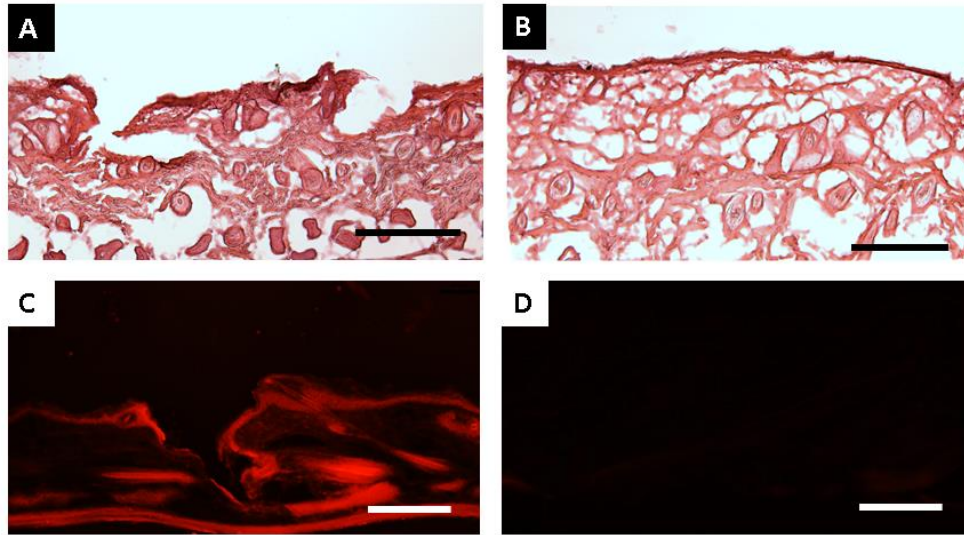


Figure 3.12 Dissolution of Rhodamine Containing PAA Microneedles



**Figure 3.13 Ex-vivo skin penetration and dye release.** H&E stained skin sections show A) epidermal breach upon application of PAA microneedles but B) no epidermal breach in untreated control. C) The application of rhodamine containing polyacrylic acid microneedles releases rhodamine into the skin. D) No fluorescence is visualized in sections to which no microneedles were applied. All scale bars measure 100 $\mu$ m.

skin *ex vivo* by applying a firm 10 second force of thumb to the back of the patch. Blank microneedles were removed after the 10 second application, but rhodamine containing microneedles were left in the skin for a period of 30 minutes to allow time for microneedle dissolution. Skin sections that came in contact with blank microneedles were then fixed, cryosectioned and stained with hematoxylin and eosin. Microneedle induced disruption of the stratum corneum can be observed in Figure 3.13A, whereas untreated skin sections remained intact (Figure 3.13B). Skin samples that came in contact with rhodamine containing PAA microneedles were then fixed, cryosectioned, and imaged with a fluorescence microscope. Rhodamine could be observed within the treated skin (Figure 3.13C), whereas no fluorescence could be observed in untreated sections (Figure 3.13D).

Together, these results indicate that CLIP can be utilized to produce completely water soluble microneedles that breach the stratum corneum to deliver a fluorescent drug surrogate into the skin.

### 3.2.10 Production and Skin Testing of Tip-Loaded Microneedles

The results in section 3.2.9 indicates that CLIP microneedles may be promising for transdermal drug delivery. However, microneedles have traditionally suffered from poor consistency of the dose delivered to the skin. A recent review of microneedle penetration depth into the skin showed that microneedles insert to anywhere between 10 and 80% of their total length.<sup>27</sup> For biocompatible microneedle configurations, this variability in penetration depth directly correlates to variability in delivered dose. This variability is a concern for a majority (52%) of health care providers, who agreed that they “would not be confident that [they] had delivered the correct dose of a drug when using microneedles” in a 2011 survey published by Birchall et. al.<sup>28</sup>

One approach that has been widely utilized in microneedle literature to combat dose inconsistency is concentrating the therapeutic in the tip of the microneedle.<sup>29-30</sup> Tip-loaded microneedles have been shown to deliver a higher portion of the intended dose than traditional

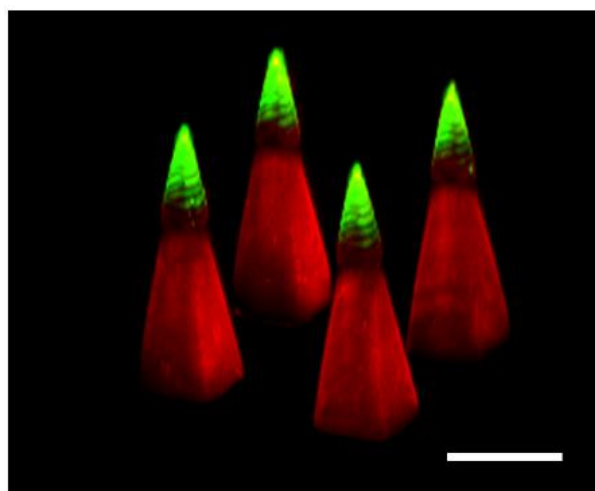


**Figure 3.14 Tip loaded CLIP microneedles.** The base of the microneedle is composed of PCL and rhodamine. The tip of the microneedle is composed of polyacrylic acid encapsulating fluorescein as a fluorescent drug surrogate. Scale bar measures 500 $\mu$ m.

needles;<sup>30</sup> they also compensate for patient-to-patient variability in depth of penetration.

Therefore, we aimed to produce tip-loaded CLIP microneedles.

Tip-loaded CLIP microneedles were fabricated with a PCL base and PAA tip. Fluorescein was selected as a drug surrogate incorporated into the PAA tip, rhodamine was incorporated into the PCL base to enable visualization of the base via confocal microscopy. Both resins contained 2.5 wt% TPO as a photoinitiator. Fabrication of tip-loaded microneedles was achieved by exchanging the resin in the middle of the production process. The microneedle base was first fabricated using the PCL resin before pausing the build. The support plate was then lifted above the PCL resin pool, which was removed and replaced with acrylic acid resin. The remainder of the microneedle tip was then fabricated using the AA resin.

A confocal micrograph of the tip-loaded microneedles is given in Figure 3.14. The rhodamine channel is displayed in red and the fluorescein channel is displayed in green; the overlay is displayed in yellow. These results demonstrate that it is possible to localize a desired cargo, in this case the fluorescent drug surrogate fluorescein, to the tip of a CLIP microneedle.

Importantly, this work also demonstrates the ability to combine rapid and sustained release of one or more therapeutic agents from a single microneedle device. Rapid release from the microneedle tip would be followed by sustained release from the base of the microneedle. A multitude of different applications could benefit from such a device. For example, a recent publication by DeMuth et. al. demonstrated that combining rapid and sustained release of soluble ovalbumin and poly I:C from microneedles for vaccine applications resulted in more T cell activation than rapid or sustained release alone.<sup>29</sup> Coordinated delivery of multiple

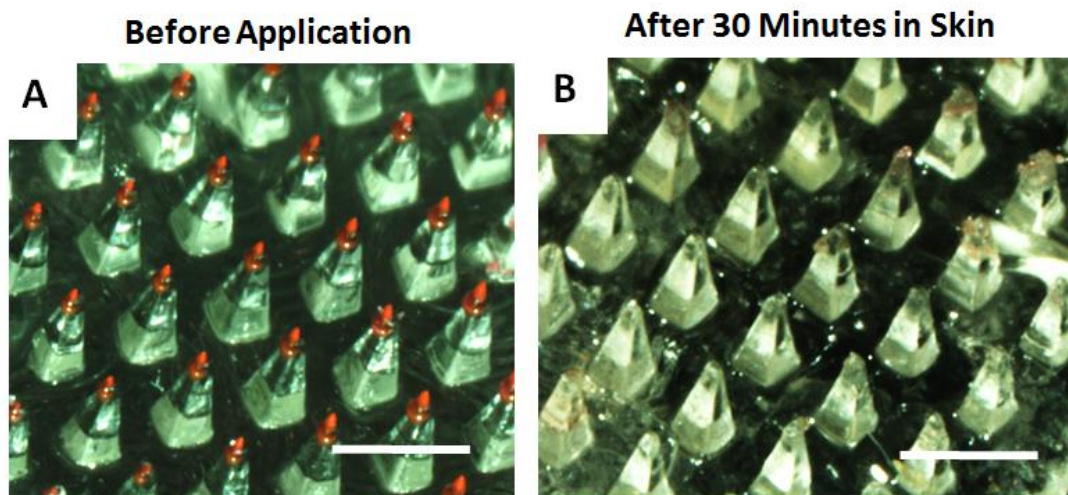


**Figure 3.15 Tip-loaded CLIP microneedles release entire payload in skin.** Scale bars measure 1mm. chemotherapies to also holds promise to combat tumor heterogeneity and drug resistance, while minimizing toxicity.<sup>31-32</sup>

In order to determine whether tip-loaded CLIP microneedles are capable of delivering their entire payload to skin, tip-loaded CLIP microneedles were applied to murine skin *ex-vivo* with 10 seconds of firm thumb pressure. In this case, microneedles containing a blank PCL base and rhodamine containing PAA tips were used to enable easy visualization of the red rhodamine tip. Microneedles were left in the skin for a period of 30 minutes prior to removal. As shown in Figure 3.15, the rhodamine containing PAA tips completely dissolve within the skin, leaving the water-insoluble PCL base behind.

### 3.2.11 Biocompatibility Testing

As mentioned previously, the materials used in this chapter are photopolymerizable derivatives of materials that are Generally Recognized as Safe (GRAS) by the United States Food and Drug Administration (FDA). GRAS materials have undergone extensive testing to show that they are safe for human use; they are commonly used as food additives and in medical devices. Adapting these GRAS materials for photopolymerization introduces additional

challenges that face all photopolymerized medical devices. These challenges include potential toxicity associated with 1) the photoinitiator, 2) any unreacted monomer/oligomer and 3) any non-degradable crosslinks created during photopolymerization, which need to be within a molecular weight range that is effectively cleared from the body.

Unreacted acrylates and methacrylates, in particular, have been associated with cytotoxicity induced by non-specific cell membrane disruption.<sup>31</sup> Nevertheless, methacrylate functionalized monomers and oligomers, particularly methyl methacrylate, have been widely utilized in biomedical applications as UV curable dental cements<sup>32</sup> and as bone cements used to affix joint replacements to native bone.<sup>33</sup> For these applications, minimizing the amount of unreacted monomer/oligomer is imperative to reducing side effects; reaction endproducts are biologically inert.

Establishing the biocompatibility of a medical device, such as a CLIP microneedle patch, is a complex and lengthy process guided by International Standard ISO-10993, “Biological Evaluation of Medical Devices Part 1: Evaluation and Testing”. Although verifying complete biocompatibility of CLIP microneedle devices is outside of the scope of this dissertation, this section describes some *in vitro* cytotoxicity studies designed to probe the biocompatibility of CLIP microneedle devices, with a particular focus on the role of unreacted monomer/oligomer on biocompatibility.

### **3.2.11.1 Cytotoxicity of CLIP Microneedle Arrays**

In order to test the biocompatibility of CLIP microneedles, a transwell cytotoxicity study was designed as shown in Figure 3.16A. One PEG, PCL, or PAA microneedle patch was placed inside of a cell culture insert (“transwell”) incubating with A549 human non-small cell lung

cancer cells in a 24 well plate. A549 cells were selected as a model cell line due to availability and easy handling. Cell viability was assessed after 24, 48, or 72 hr of incubation via MTT assay and compared to control cells incubated in the absence of a microneedle patch (Figure 3.16B). Cells incubated with either a PEG or a PCL microneedle patch showed a slight decrease in viability over the 72 hour time period, but viability remained greater than 80% for all timepoints, indicating that the PEG and PCL microneedles show promise for use as a biocompatible medical device. Longer term studies would need to be performed to analyze the toxicity of the degradation products. The PAA microneedles, on the other hand, show extreme toxicity, killing nearly all cells within 24 hours.

In order to further characterize the biocompatibility of PEG and PCL microneedles, the study was repeated using both A549 and human umbilical vein endothelial cells (HuVECs). Performing testing on both cancerous and healthy cell lines provides additional information to indicate how these microneedle devices may interact with cancerous and healthy cells within the body. Although the previous study (Figure 3.16) investigated the cytotoxicity of microneedle patches with a 1mm patch backing, the patch backing was reduced to  $\sim 100\mu\text{m}$  thick for this

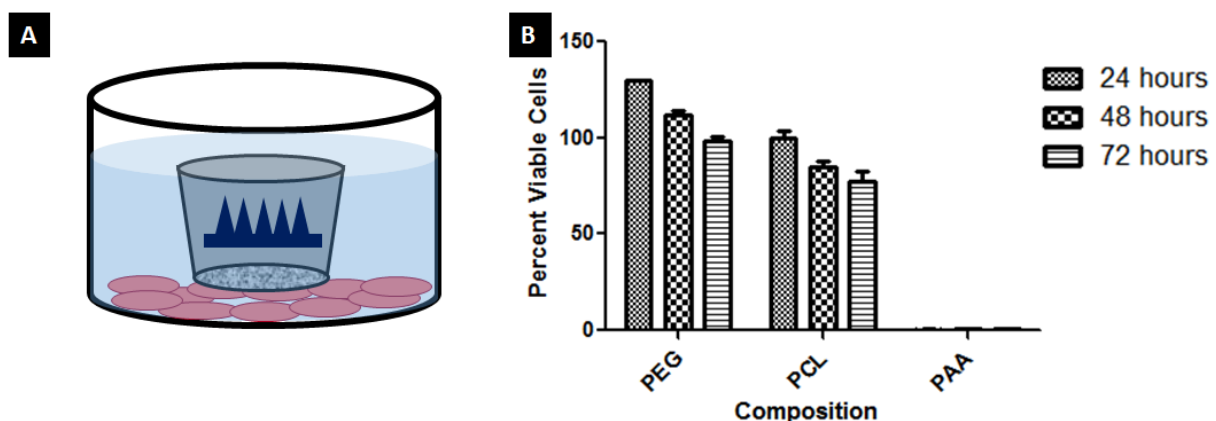


**Figure 3.16 Microneedle transwell study.** A) Diagram of experimental design, which shows the microneedle containing porous transwell incubating in a cell culture plate B) MTT Assay for A549 cells incubating with one PEG, PCL, or PAA microneedle patch over 24 to 72 hr

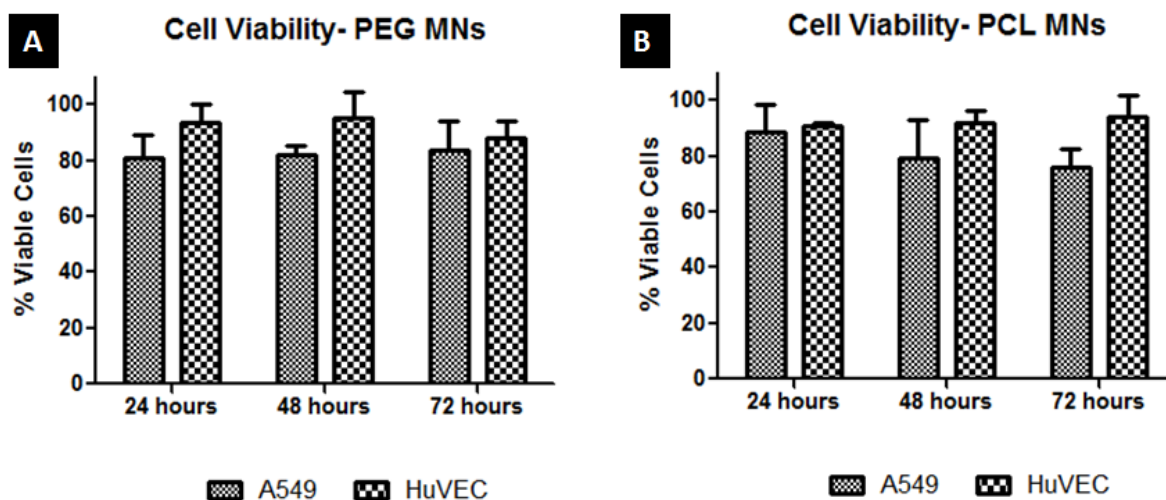


**Figure 3.17** Cell viability of A549 and HuVEC cells incubated with A) PEG and B) PCL MNs over 24, 48, and 72 h. Data are presented as mean±SD with n=3 wells per timepoint

study. This reduction in patch backing thickness provides a more accurate representation of an *in vivo* environment, where the patch backing is unlikely to significantly interact with cells within the body. Cell viability for HuVEC and A549 patches incubated with PEG and PCL microneedles over 24, 48, and 72 hr is shown in Figure 3.17. All cells were found to have approximately 80% viability or higher over all timepoints, indicating that these materials show promise for utilization as a biocompatible microneedle device.

The cytotoxicity of the PAA microneedles is further discussed in the remainder of this section, which seeks to understand the cause of PAA microneedle cytotoxicity through further characterization of the PEG, PCL, and PAA microneedle patches.

### 3.2.11.2 Resin Cytotoxicity

Differences in the biocompatibility of the three tested materials (PEG, PCL, PAA) may arise from one or more of several sources. These include potential differences in 1) the toxicity of the polymer, 2) the toxicity of the monomer/oligomer, 3) the quantity of unreacted monomer

/oligomer and/or initiator inside the microneedle, and 4) the rate of release of monomer/oligomer and/or photoinitiator out of the microneedle into cell culture medium. Experiments presented in this section aim to better understand the underlying cause of differences in microneedle toxicity between the compositions in an attempt to improve the biocompatibility of the PAA microneedles.

The toxicity of unreacted oligomers (PEG550-dMa, PCL1110-tMa, AA) was assessed by serially diluting oligomers into to cell culture medium, starting with 1 v/v% oligomer in culture medium. A549 and HuVEC cells were then incubated with the solution of cell culture medium and oligomer. Cell viability was assessed by 3-(4,5-dimethylthiazol-2-yl)-2,5-diphenyltetrazolium bromide (MTT) assay at 72 hr and compared to cells incubated with cell culture medium in the absence of oligomer (Figure 3.18). Although the HuVEC cells are more sensitive to oligomer than the A549 cells, both cell lines show that the AA monomer is more toxic than the PEG550-dMa and PCL1110-tMa oligomers. Higher toxicity of the AA monomer

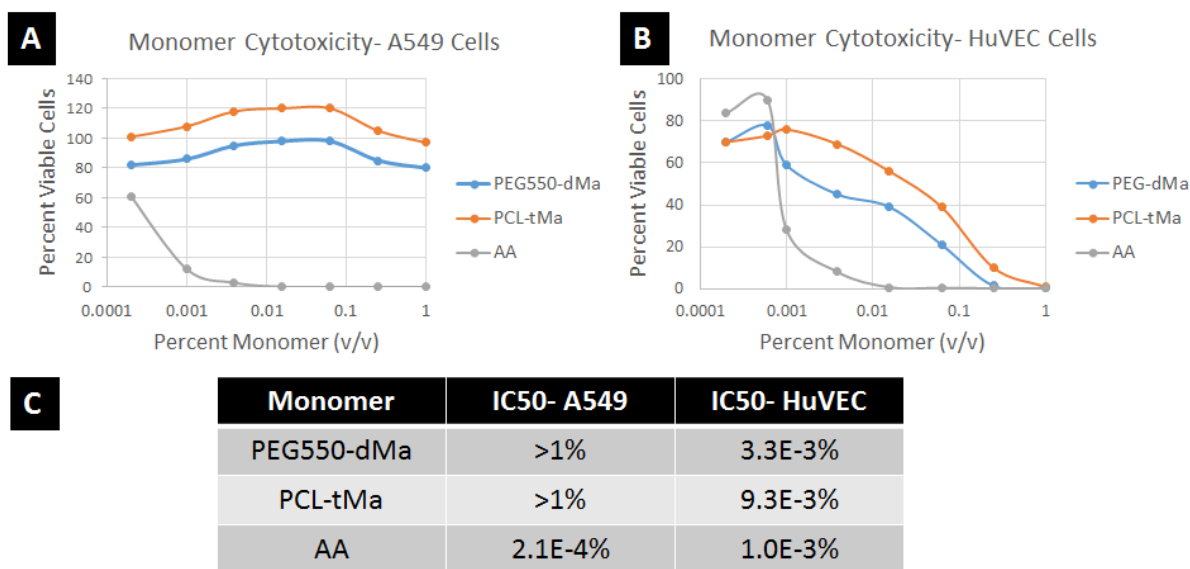


**Figure 3.18 Oligomer toxicity and IC50 values.** A) Toxicity of monomers on A549 cells B) Toxicity of monomers on HuVEC cells C) IC50 values of monomers on A549 and HuVEC cells. Concentrations are given as volume of monomer divided by total solution volume.

is expected because the reactive vinyl group is highly concentrated in this resin at one mole per 72g monomer. The reactive group is present at only one mole per 275g of the PEG550-dMa and one mole per 375g of the PCL1110-tMa by comparison. Therefore, the higher overall concentration of reactive groups in the AA resin is almost certainly one cause of the increase in toxicity of this resin relative to the others. Acrylate endgroups are also known to be more toxic than methacrylate endgroups,<sup>31</sup> which would also contribute to the high toxicity of the AA monomer. Therefore, this study suggests that differences in oligomer toxicity (caused by differences in both the concentration and reactivity of reactive groups) are a contributing factor to the increased toxicity of PAA microneedles relative to other microneedle formulations.

It is worth noting that the resins used for CLIP also contain photoinitiator that was not tested in these cytotoxicity studies due to poor solubility of TPO in cell culture medium. This poor solubility creates a turbid solution that interferes with the assay. For this reason, initiator toxicity is not investigated here, but is an important avenue for future investigation.

### **3.2.11.3 Characterization of Unreacted Fractions**

In order to further investigate whether residual monomer is the cause of microneedle toxicity, the final composition of CLIP microneedle patches was characterized. For PEG and PCL microneedles, the soluble fraction of the microneedles was measured by swelling microneedle patches in methanol to extract residual oligomer and then removing solvent under heat and vacuum. Microneedles were then left to equilibrate to ambient humidity overnight prior to weighing to determine percent weight lost during extraction. Figure 3.19A shows the soluble fraction of the PEG and PCL microneedles. The maximum total wt% soluble acrylate is also plotted, calculated by multiplying the soluble fraction by the fraction of each monomer (wt%) made up of methacrylate endgroups. Although this approach assumes that the entire soluble

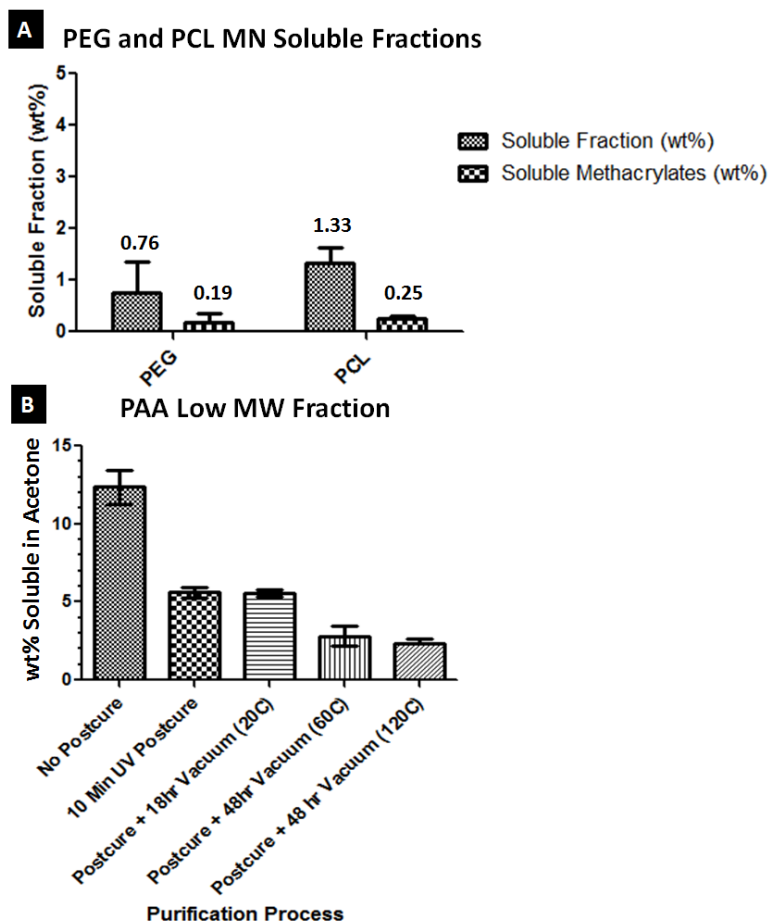


**Figure 3.19 Soluble and low molecular weight fraction of PEG, PCL, and PAA MNs**

fraction is monomer (which is unlikely), it presents a useful “worse case scenario” for the concentration of soluble acrylate. Both the PEG and PCL microneedles have low soluble fractions near 1wt%, with total weight percent soluble acrylate at or below 0.25wt%.

The soluble (“sol”) fraction, or the portion of a sample that is not reacted into a crosslinked network, is not an appropriate metric for an uncrosslinked polymer such as PAA. Water soluble materials like PAA are more typically dissolved and analyzed by aqueous gel permeation chromatography (GPC) to obtain a molecular weight distribution. Due to lack of an available aqueous GPC system, an alternate method was developed to estimate how much unreacted AA remained in the microneedle. Characterization was accomplished by soaking PAA

microneedle patches in acetone to extract AA monomer and low molecular weight oligomer from the patch; PAA is insoluble in acetone and is therefore not extracted. The acetone extract was then diluted in water and titrated to determine the concentration of acid. The “low molecular weight fraction” was calculated by taking the acid mass in the extract and dividing it by the total mass of the PAA microneedle patch (Figure 3.19B). In general, a large fraction (between 2wt% and 12wt%) of the PAA microneedle was found to be soluble in acetone. A portion of this extract may be toxic, unreacted AA monomer.

Several purification processes were investigated in an attempt to eliminate unreacted monomer from the PAA microneedle. These processes included postcuring the microneedles under a mercury lamp for 10 minutes to complete the reaction and heating the microneedles under vacuum to remove residual monomer (Figure 3.19B). These purification steps do reduce the low molecular weight fraction from approximately 12wt% to approximately 2wt% (Figure 3.20B), but do not completely eliminate the extractable fraction. One would expect the monomer

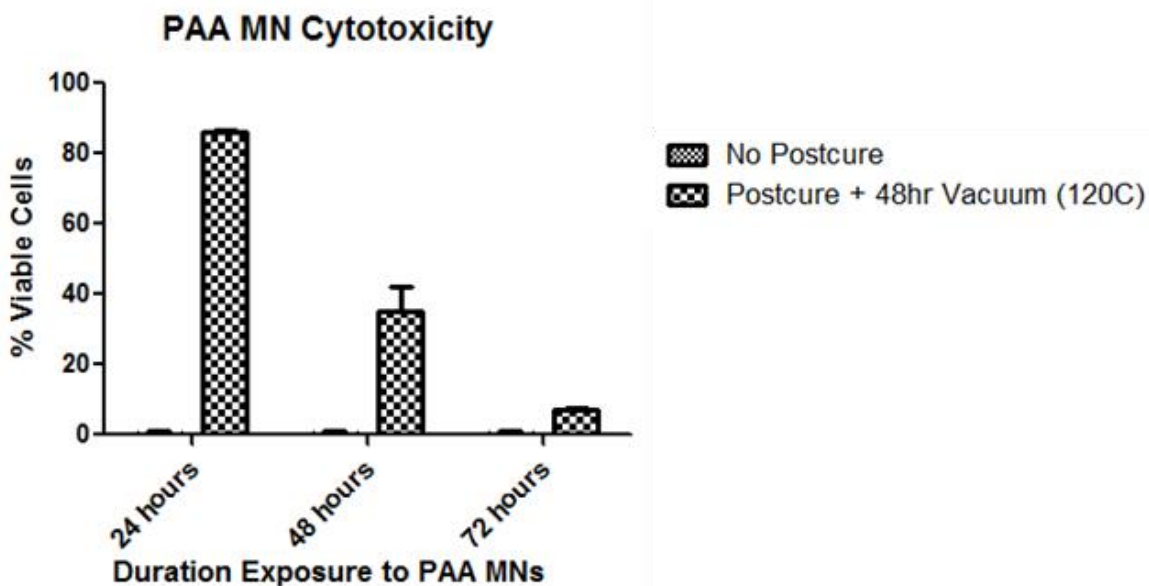


**Figure 3.20 Cytotoxicity of Purified and Unpurified PAA MNs.** Unpurified MNs were tested directly after printing plus a brief acetone wash. Purified MNs were tested after the brief acetone wash plus post cure plus 48 hours of heating at 120°C for 48 hr

to be completely removed after 48 hr of incubation under vacuum at 120°C due to the volatility of the AA monomer (its vapor pressure is 0.4 kPa at 20°C and boiling point is 141°C).

Therefore, we hypothesize that the remaining 2wt% is either dimer or low molecular weight oligomer, which may still be cytotoxic in cell culture.

In order to determine whether purification of the PAA removed a sufficient amount of monomer to enable cytocompatibility, the transwell experiment described in Figure 3.17A was repeated. Unpurified PAA microneedles and PAA microneedles that were postcured and heated to 120°C under vacuum were added to porous cell culture inserts and allowed to incubate with cells for 24, 48, or 72 hours. Figure 3.20 shows that the purification steps used to remove residual monomer do improve the cellular response to the PAA microneedles, but even the purified microneedles are still toxic after 72 hours.

We then decided to compare the calculated extractable for each of the three different microneedle compositions (PEG, PCL, PAA) to the IC50 values for monomer toxicity established in Figure 3.18 to determine whether unreacted monomer is the cause of toxicity. A

**Table 3.3 Comparison of extractable fractions and monomer IC50 values.** When complete release of the extractable fraction produces concentrations (row 1) that are higher than the IC50 value, the IC50 value is shown in red. When complete release of the extractable fraction produces concentrations (row 1) that are lower than the IC50 value, the IC50 value is shown in green.

	PEG	PCL	PAA
<b>Calculated v/v monomer released from MNs (Assuming Complete Release of Extractable Fraction)</b>	1.52E-2%	2.66E-2%	4.6E-2%
<b>IC50- A549 Cells (v/v)</b>	>1%	>1%	2.1E-4%
<b>IC50-HuVECs (v/v)</b>	3.3E-3%	9.3E-3%	1.0E-3%

conclusive determination of the concentration of unreacted monomer within each extractable fraction is not possible because it may contain low molecular weight oligomers as well as monomers. Nevertheless, if we assume that the entire extractable fraction is monomer, this fraction can then be converted to volume percent monomer in cell culture medium and compared to the monomer IC<sub>50</sub> values (Table 3.2). Calculations assume complete release of the extractable fraction into cell culture medium.

Interestingly, the cytotoxicity predicted by this calculation differs from the measured cytotoxicity (Figures 3.16 and 3.17). Complete release of the PAA extractable fraction would produce concentrations of monomer that are higher than the IC<sub>50</sub> value of AA on cells. Therefore, PAA microneedles are predicted to be cytotoxic on the basis of monomer concentrations alone, and were confirmed to be toxic in Figure 3.16. However, complete release of the soluble fraction from PEG or PCL microneedles should also be cytotoxic to HuVECs, despite their measured cytocompatibility. Therefore, we hypothesize that cytotoxicity results are also heavily influenced by the rate at which the soluble fraction is released into cell culture medium. Assessing PEG and PCL microneedle cytotoxicity at longer time points and/or *in vivo* toxicity studies are necessary to confirm that PEG and PCL microneedles have no adverse effects even after complete release of the soluble fraction.

### **3.3 Conclusions**

Herein, we report the fabrication of CLIP microneedles from three different materials (PEG, PCL, and PAA), which were designed to encapsulate and release therapeutic cargo via swelling, degradation, or dissolution, respectively. All microneedles effectively breached murine skin when applied with firm thumb pressure, indicating that these materials may be strong enough to be utilized as microneedle devices. All materials were loaded with the fluorescent

drug surrogate rhodamine, which released at different rates, ranging from complete release within 15 minutes to less than 1% release over 7 days, depending on microneedle composition. When tested on murine skin *ex vivo*, PAA microneedles demonstrate the ability to release rhodamine into skin. Excitingly, CLIP also enabled tip-loaded microneedles to be produced, which release all of the encapsulated cargo into the skin. Some initial studies were also performed to assess the biocompatibility of CLIP microneedle devices. PEG and PCL CLIP microneedles were nontoxic in cell culture, but PAA microneedles exhibited severe cytotoxicity.

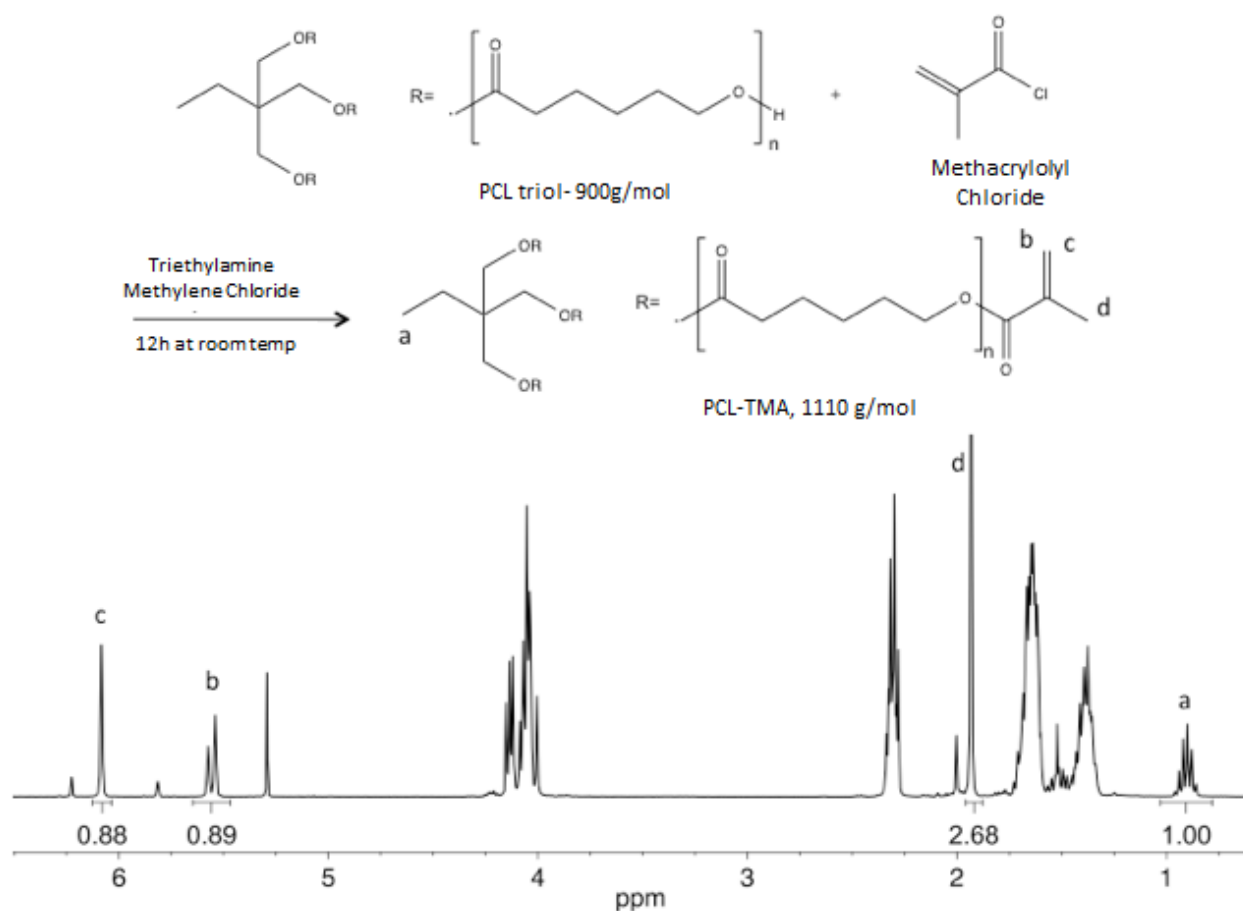


**Figure 3.21 Reaction scheme for PCL-trimethacrylate synthesis.** PCL was functionalized by reacting hydroxyl groups from a PCL-triol with methacryloyl chloride. <sup>1</sup>H NMR spectrum confirms methacrylate functionalization with peaks at 6.08 (c), 5.54 (b) and 1.93 ppm (d). Degree of functionalization was determined to be 89% by comparing the peak areas corresponding to the vinyl protons (c and b, 6.08 and 5.54 ppm) to the protons of the methyl group in the PCL backbone (a, 0.89 ppm).

The concentration and release rate of unreacted monomer are hypothesized to be primary drivers of the *in vitro* cytotoxicity. Future work will continue to investigate the biocompatibility of CLIP microneedle arrays in an attempt to develop a safe and efficacious CLIP microneedle device for transdermal drug delivery.

## **3.4 Experimental**

### **3.4.1 Synthesis of Polycaprolactone Trimethacrylate**

Polycaprolactone trimethacrylate (PCL-tMa) was synthesized from a commercially available poly- $\epsilon$ -caprolactone (PCL) triol (Sigma Aldrich) with an average molecular weight of 900g/mol (55.14 g, 61.3 mmol). The reaction scheme is given in Figure 3.21.

PCL triol was dried in a vacuum oven prior to use. A reaction flask was equipped with an addition funnel, sealed with rubber septa, and placed under magnetic stirring and N<sub>2</sub> flow. Distilled dichloromethane (DCM, 200mL, Fisher Scientific) and triethylamine (TEA, 275.9 mmol, Fisher Scientific) was added to a flask placed under magnetic stirring and N<sub>2</sub> flow in an ice bath. Methacryloyl chloride (MAcCl, 275.7 mmol, Sigma Aldrich) was added dropwise from the addition funnel over one hour and the reaction was allowed to proceed overnight. The byproduct TEA•HCl salt was filtered off and the filtrate was washed with sodium bicarbonate, dried over magnesium sulfate, and the DCM was removed by rotary evaporation. Confirmation of the final product was done by <sup>1</sup>H NMR (Figure 3.21).

### **3.4.2 Determination of Critical Exposure**

Methods for the determining critical exposure were adapted from Tumbleston et. al.<sup>19</sup> Briefly, 500 $\mu$ L of resin was placed on a cover slip on top of the printer window. Resin was exposed to a specified dosage of light ( $\lambda$ =365nm LED) in a circle pattern and residual, unreacted monomer was removed using an acetone wash. The height of polymerized circles was then

measured using a Mitutoyo Electronic Indicator (McMaster Carr). Resins utilized in this study were acrylic acid (Acros Organics, 99.5% purity), a poly- $\epsilon$ -caprolactone (PCL) trimethacrylate synthesized in house, and poly (ethylene glycol) dimethacrylate ( $M_n$  550, Sigma Aldrich) mixed with 2.5 wt% Diphenyl(2,4,6-trimethyl-benzoyl-)phosphine oxide (Sigma Aldrich) as a photoinitiator.

### **3.4.3 Fabrication of Biocompatible Microneedles**

To produce microneedles of different heights, CAD files of square pyramidal microneedles measuring 1000 $\mu$ m tall with an aspect ratio of 3 (aspect ratio= height/width) were generated using Solidworks 2014. All microneedles were spaced at one base width apart on a base measuring 6x6x1mm. CAD files were then sliced at 1 $\mu$ m slice thickness using the open source software Slic3r. Microneedles were then produced using a CLIP additive manufacturing system (Carbon 3D, Redwood City, CA) using polycaprolactone trimethacrylate (PCL1110-tMa), polyethylene glycol550 dimethacrylate (PEG550-dMa), or acrylic acid (AA), each mixed with 2.5wt% diphenyl(2,4,6-trimethylbenzoyl)phosphine oxide (Sigma Aldrich) (TPO) as a photoinitiator. PAA microneedles, PCL microneedles, and PEG microneedles were all printed at 25mm/hr, with 8.9, 1.5, and 1.2 mW/cm<sup>2</sup> of light( $\lambda$ =370nm LED), respectively. All needles were washed briefly with acetone and dried using compressed air. Microneedles were imaged using an environmental scanning electron microscope (FEI Quanta 200) in low vacuum mode.

Tip-loaded microneedles were fabricated from polycaprolactone trimethacrylate mixed with 0.05wt% rhodamine B base (Sigma Aldrich) and acrylic acid mixed with 0.05wt% fluorescein (Sigma Aldrich). Both resins contained 2.5wt% TPO as a photoinitiator. Slices 1 through 1700 were fabricated using PCL prior to lifting the build elevator, removing residual resin, and continuing to fabricate the remainder of the microneedle (slices 1701 through 2000)

using acrylic acid. Microneedles were post-cured under a mercury lamp for 10 min between compositions and after fabrication was complete.

#### **3.4.4 Microneedle Dissolution and Rhodamine Release Studies in Solution**

To model drug release profiles, all microneedle compositions were loaded with 0.1 wt% Rhodamine B Base (Acros Organics). All microneedles were fabricated on a blank base containing no rhodamine. The resin was then replaced with resin containing rhodamine prior to fabricating the microneedles using the build parameters given in Section 1.4.3. One microneedle patch was added to 1mL of phosphate buffered saline (PBS) in an Eppendorf tube (n=3 for each composition). The Eppendorf tubes were placed in a 37°C water bath. 0.5 mL of the supernatant was removed at each time point and replaced with an additional 0.5mL of PBS. Quantification of released rhodamine was performed by measuring fluorescence of the supernatant using a plate reader with excitation and emission of 544 and 590nm, respectively. Fluorescence was correlated to a standard curve to determine rhodamine mass released, then taken as a percent of theoretical rhodamine loading, calculated from microneedle volume and density.

To test for acrylic acid microneedle dissolution, one patch with a polycaprolactone base and polyacrylic acid microneedles containing 0.1 wt% rhodamine was submerged in 10mL PBS. The microneedle patch was imaged before and after dissolution using a Leica MZI6FA microscope in brightfield mode.

#### **3.4.5 Skin Penetration Studies**

Patches were tested on nude murine skin *ex vivo* with permission of the UNC Institutional Animal Care and Use Committee (IACUC). All samples were stored at -20°C until testing occurred. Prior to testing, skin was thawed briefly at room temperature and pinned over corkboard. CLIP microneedles were post-cured under a mercury lamp for 5 minutes to improve

mechanical strength prior to application. Microneedle patches were then applied to the skin with 10 seconds of thumb pressure before patch removal. A 50:50 mixture of Green tissue marking dye (Cancer Diagnostics) and isopropanol was then applied to the site for 3 minutes before being wiped away with water and isopropanol. Skin was imaged to visualize sites of microneedle insertion using brightfield macroscopy (Leica M420).

To further confirm skin penetration using histology, polyacrylic acid microneedles were applied to murine skin *ex vivo* with 10 seconds of thumb pressure before patch removal. Murine skin sections were then embedded in Tissue-Tec Optimum Temperature Cutting Medium (Sakura Finetek), bisected, and sectioned in 12 micron slices at -25°C (Leica Cryostat). Samples were H&E stained (Cryo-KIT, Cancer Diagnostics) and visualized using brightfield microscopy (Olympus BX61 Upright Brightfield Microscope).

To test for dye release via histology, polyacrylic acid microneedle patches containing 0.1wt% rhodamine B were applied to murine skin *ex vivo* and left to dissolve in the skin for 30 minutes. Samples were then briefly fixed in FROZEN-FIX (Cancer Diagnostics) for 10 seconds and visualized using fluorescence microscopy (Olympus BX61 Upright Fluorescence microscope).

To test for dye release from tip-loaded microneedles, tip-loaded microneedles were fabricated from blank polycaprolactone and a polyacrylic acid tip containing 0.1wt% rhodamine B base, as previously described. Microneedles were applied to murine skin *ex vivo* with gentle thumb pressure for a period of 10 seconds. Microneedles were then allowed to remain the the skin for a period of 30 minutes prior to imaging using a Leica MZ16FA macroscope in brightfield mode.

### **3.4.6 Characterization of Extractable Fractions**

PEG and PCL MN soluble fractions were determined by submerging three microneedle patches with 1mm backings in approximately 200mL of methanol (MeOH) over 24 hr. Microneedle patches were removed and heated to 100°C for 24 hr under vacuum. Microneedle patches were then removed from the vacuum and allowed to equilibrate to ambient humidity overnight prior to weighing to determine percent mass lost.

PAA extractable fraction was determined by submerging a single microneedle patch with a 1mm backing in acetone for 24 hours. The supernatant was then removed and diluted in deionized water. The concentration of acid within the supernatant was determined via standard acid-base titration.

### **3.4.7 Cytotoxicity of Photoreactive Monomer and Microneedle Arrays**

To assess monomer toxicity, cells were seeded in 200  $\mu$ L of media [RMPI 1640 Medium for A549; HuMEC for HuVEC] at a density of 5000 cells per  $\text{cm}^2$  into a 96-well microtiter plate. Cells were allowed to adhere for 24 hr and subsequently incubated with medium containing 1 to 0.0006% (v/v) monomer. After a 72 hr incubation period, all media were aspirated off cells. 100  $\mu$ L fresh medium was added back to cells, followed by the addition of 100  $\mu$ L CellTiter-Glo® Luminescent Cell Viability Assay reagent (Promega, Madison, WI). Plates were placed on a microplate shaker for 2 min, then incubated at r.t. for 10 min to stabilize luminescent signal. The luminescent signal was recorded on a Molecular Dynamics SpectraMax M5 plate reader. The viability of the cells was expressed as a percentage of the viability of cells grown in the absence of monomer.

To assess microneedle toxicity, cells were seeded in 1 mL of media at a density of 5000 cells per  $\text{cm}^2$  into a 24-well microtiter plate. Cells were allowed to adhere for 24 hr and

subsequently incubated with 2mL of culture medium and a cell culture insert containing a 3 $\mu$ m pore size. A microneedle patch was added to each well at 72 hr, 48 hr, or 24 hr timepoints. After a 72 hr incubation period, all media were aspirated off cells. 1 mL fresh medium was added back to cells followed by the addition of 100  $\mu$ L CellTiter-Glo<sup>®</sup> Luminescent Cell Viability Assay reagent (Promega, Madison, WI). Quantification was performed as previously described.

## REFERENCES

- (1) Donnelly, R. F.; Singh, T. R. R.; Morrow, D. I. J.; Woolfson, A. D. *Microneedle-mediated Transdermal and Intradermal Drug Delivery*; John Wiley & Sons, Ltd. 2012.
- (2) Prausnitz, M. R. *Adv Drug Deliv Rev.* **2004**, *56*, 581-587.
- (3) Donnelly, R. F.; Singh, T. R. R.; Garland, M. J.; Migalska, K.; Majithiya, R.; McCrudden, C. M.; Kole, P. L.; Mahmood, T. M. M.; McCarthy, H. O.; Woolfson, A. D. *Adv Funct Mater.* **2012**, *22*, 4879-4890.
- (4) Park, J. H.; Allen, M. G.; Prausnitz, M. R. *J Control Release.* **2005**, *104*, 51-66.
- (5) Lee, J. W.; Park, J. H.; Prausnitz, M. R. *Biomaterials.* **2008**, *29*, 2113-2124.
- (6) Escobar-Chávez, J. J.; Bonilla-Martínez, D.; Villegas-González, M. A.; Molina-Trinidad, E.; Casas-Alancaster, N.; Revilla-Vázquez, A. L. *J. Clin. Pharmacol.* **2011**, *51*, 964-977.
- (7) Ulrich, K. E.; Cannizzaro, S. M.; Shakesheff, K. M.; Langer, R. S. *Chem. Rev.* **1999**, *99*, 3181-3198.
- (8) Kutz, Meyer. *Standard Handbook of Biomedical Engineering and Design*; McGraw Hill Companies, Inc. 2003.
- (9) Jariwela A.S.; Ding, F.; Boddapati, A.; Breeveld, V.; Grover, M. A. *Rapid Prototyping Journal.* **2011**, *17*, 168-175.
- (10) Andrews, L. S.; Clary, J. J. *J Toxicol. Environ. Health.* **1986**, *19*, 149-164.
- (11) Kadajji, V. G.; Betageri, G. V. *Polymer.* **2011**, *3*, 1972-2009.
- (12) Nair, L. S.; Laurencin, C. T. *Prog. Polym. Sci.* **2007**, *32*, 762-798.
- (13) Pillai, O.; Panchagnula, R. *Curr Opin Chem Biol.* **2001**, *5*, 447-451.
- (14) Peppas, N. A.; Bures, P.; Leobandug, W.; Ichikawa, H. *Eur J Pharm Biopharm.* **2007**, *32*, 762-798.
- (15) Gupta, P.; Vermani, K.; Garg, S. *Drug Discov Today.* **2002**, *7*, 569-579.
- (16) Hoare, T. R.; Kohane, D. S. *Polymer.* **2008**, *49*, 1993-2007.
- (17) Tanii, H.; Hashimoto, K. *Toxicol Lett.* **1982**, *11*, 125-129.
- (18) Kricheldorf, Hans. *Handbook of Polymer Synthesis*; Marcel Dekker, Inc. 1991.
- (19) Tumbleston, J. R.; Ermoshkin, A.; Shirvanyants, D.; Ermoshkin, N.; Januszewicz, R.; Johnson, A. R.; Kelly, D.; Chen, K.; Pinschmidt, R.; Rolland, J. P.; Samulski, E. T.; DeSimone, J. M. *Science.* **2015**, *347*, 1349-1352.

- (20) Gibson, I.; Rosen, D. W.; Stucker, B. *Additive Manufacturing Technologies: Rapid Prototyping to Direct Digital Manufacturing*; Springer. 2010.
- (21) Degirmenci, I.; Avci, D.; Aviyente, V.; Van Cauter, T. K. V.; Van Speybroeck, V.; Waroquier, M. *Macromolecules*. **2007**, *40*, 9590-9602.
- (22) Godin, B.; Touitou, E. *Adv. Drug Deliv. Rev.* **2007**, *59*, 1152-1161.
- (23) Bartsova, L.; Bajgar, J. *Curr. Med. Chem.* **2012**, *19*, 4671-4677.
- (24) Kim, H. M.; Lim, Y. Y.; An, J. Kim, M. N.; Kim, B. J. *Int. J. Dermatol.* **2012**, *51*, 859-863.
- (25) Groves, R. *Quantifying the mechanical properties of skin in vivo and ex vivo to optimize microneedle device design*; ProQuest Dissertations Publishing. 2012.
- (26) Choi, J. W.; Kwon, S. H.; Huh, C. H.; Park, K. C.; Youn, S. W. *Skin Res. Tech.* **2013**, *19*, 349-355.
- (27) Romgens, A. M.; Bader, D. L.; Boustra, J. A.; Baaijens, F. P. T.; Oomens, C. W. J. *J Mech Behav Biomed Mater.* **2014**, *40*, 397-405.
- (28) Birchall, J. C.; Clemo, R.; Anstey, A.; John, D. N. *Pharm Res.* **2011**, *28*, 95-106.
- (29) Demuth, P. C.; Min, Y.; Irvine, D. J.; Hammond, P. T. *Adv Healthc Mater.* **2014**, *3*, 47-58.
- (30) Chu, L. Y.; Choi, S.; Prausnitz, M. R. *J Pharm Sci.* **2010**, *99*, 4228-4238.
- (31) Yoshii, E. *J Biomed Mater Res.* **1997**, *4*, 517-524.
- (32) Gosavi, S. S.; Gosavi, S. Y.; Alla, R. K. *Dent Res J.* **2010**, *7*, 82-87.
- (33) Vaisha, R.; Chauhan, M.; Vaish, A. *J Clin Orthop Trauma.* **2013**, *4*, 157-163.

## CHAPTER 4 MICRONEEDLE MECHANICAL PROPERTIES AND SKIN PENETRATION

### 4.1 Introduction

Microneedles have traditionally suffered from poorly controlled depth of penetration into the skin, which directly contributes to variability in delivered dose. A recent review of microneedle penetration depth showed that microneedles insert to anywhere between 10 and 80% of their total length.<sup>1</sup> This variability is a concern for a majority (52%) of health care providers, who agreed that they “would not be confident that [they] had delivered the correct dose of a drug when using microneedles” in a 2011 survey published by Birchall et. al.<sup>2</sup> Therefore, characterizing the factors that influence the depth and consistency of microneedle penetration is crucial to the advancement of microneedle technology.<sup>3</sup>

A multitude of different microneedle design parameters, including microneedle height,<sup>3-6</sup> shape,<sup>7-8</sup> aspect ratio,<sup>9-11</sup> tip radius,<sup>1, 11-12</sup> and composition,<sup>13</sup> are known to affect microneedle insertion to the skin. Chapter 2 and Chapter 3 demonstrate the unique ability of CLIP to systematically control such design variables in a high throughput fashion. Therefore, we hypothesized that CLIP would be an ideal tool for further investigation of microneedle insertion mechanics. Composition was selected as the first design variable to be studied (as opposed to size, shape, etc.) because 1) it began to affect preclinical microneedle development in our laboratory (Figure 5.2) and 2) composition is a contributing variable to any study investigating microneedle geometry. Therefore, the relationship between composition and insertion serves as

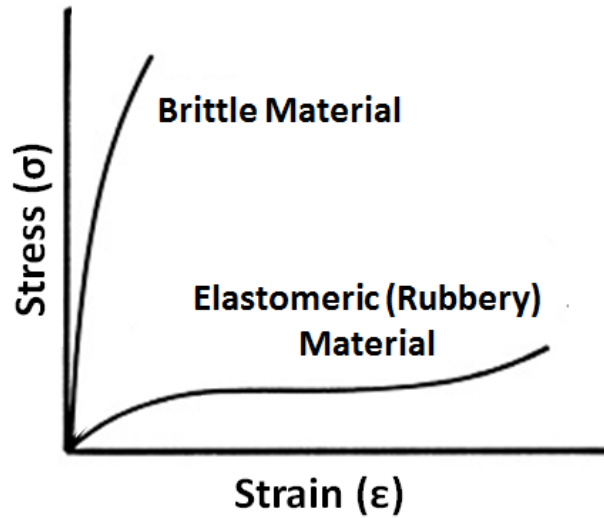


**Figure 4.1 Typical Stress-Strain Curve**

an important baseline that will inform future investigation of the role of CLIP microneedle geometry on insertion into the skin.

A variety of materials with different mechanical properties have been utilized for microneedle device manufacturing. The relationship between the stress and strain of these materials, either in tension or compression, provides interesting insight into material performance. A representative example of two types of stress strain curves is given in Figure 4.1. Materials can be classified as brittle materials, which fracture with minimal deformation, and elastomeric materials, which exhibit large deformations prior to material failure. Both types of materials have been utilized for the manufacture of microneedle arrays.

In order for a microneedle to successfully puncture the skin, the force required to insert the needle into the skin ( $F_{\text{insertion}}$ ) must be less than the force applied to the back of the microneedle array ( $F_{\text{applied}}$ ). In order to prevent breakage, the insertion force and the applied force need to be less than the fracture force ( $F_{\text{failure}}$ ), which is the force that causes the needle to fracture (Equation 4.1).

$$F_{insertion} < F_{applied} < F_{fracture} \quad (4.1)$$

Generally, microneedles can fail to insert into the skin via one of two different mechanisms, either 1) lack of penetration of an intact microneedle device or 2) fracture of the microneedle device. Device fracture is more likely for microneedles fabricated from brittle materials, such as silicon microneedles, which frequently fragment within the skin.<sup>14-15</sup> In this case, the applied force is greater than the fracture force ( $F_{applied} > F_{fracture}$ ), causing the device to break. Microneedles can also fail to puncture the skin because the applied force is too small (e.g.  $F_{applied} < F_{insertion}$ ). Tough, rubbery microneedles are more likely to fail to insert by this mechanism due to their tendency to absorb a large portion of the applied force through deformation. Therefore, although Equation 1 holds true regardless of material selected for device manufacture, the dominant factor in the equation is dictated by the mechanical properties of the chosen material.

The mechanical properties of a CLIP microneedle array can be controlled by deliberately altering the components of the photopolymerizable polymer network. This change in mechanical properties can be accomplished by either changing the chemical structure of the components, or, in our case, by changing the relative quantity of each component. In this chapter, we control the mechanical properties of PEG microneedles by changing the material's crosslink density, defined as the number of crosslinked monomer units per main chain. Varying ratios of polyethylene glycol 550 dimethacrylate (PEG550dMa) and ethylene glycol dimethacrylate (EGdMa) are utilized to produce microneedles with a range of mechanical properties. The ability of these microneedles to insert into the skin using a range of application forces is assessed with the ultimate goal of defining the microneedle mechanical characteristics necessary for the production of a successful microneedle device.

## 4.2 Results and Discussion

### 4.2.1 Skin Penetration of Biocompatible Microneedles on Murine Skin

Chapter 3 demonstrated that CLIP microneedles composed of four different materials (TMPTA, PEG, PCL, and PAA) were capable of piercing murine skin *ex vivo* when applied using firm thumb pressure. Murine skin, however, is a poor model for human skin because it is much thinner than human skin (murine skin is typically 300-500 $\mu\text{m}$  in thickness, whereas human skin varies widely in thickness, ranging from 600-3,000 $\mu\text{m}$ )<sup>16-17</sup> and is mechanically weaker than human skin.<sup>18</sup> Porcine skin is widely used for microneedle insertion testing in literature, and is considered to be a good model for human skin due to its similar thickness, mechanical properties, and permeability.<sup>18-21</sup> Therefore, we tested the previously fabricated microneedle compositions (TMPTA, PEG, PCL, PAA) for insertion into porcine skin *ex vivo*, applying the patches to skin using 10 seconds of firm thumb pressure (Figure 4.2). Results show that only TMPTA and PAA microneedles were capable of puncturing porcine skin. It is almost certain that PAA and TMPTA microneedles pierce porcine skin more effectively due to their superior mechanical properties as compared to PCL and PEG. PAA and TMPTA both have glass

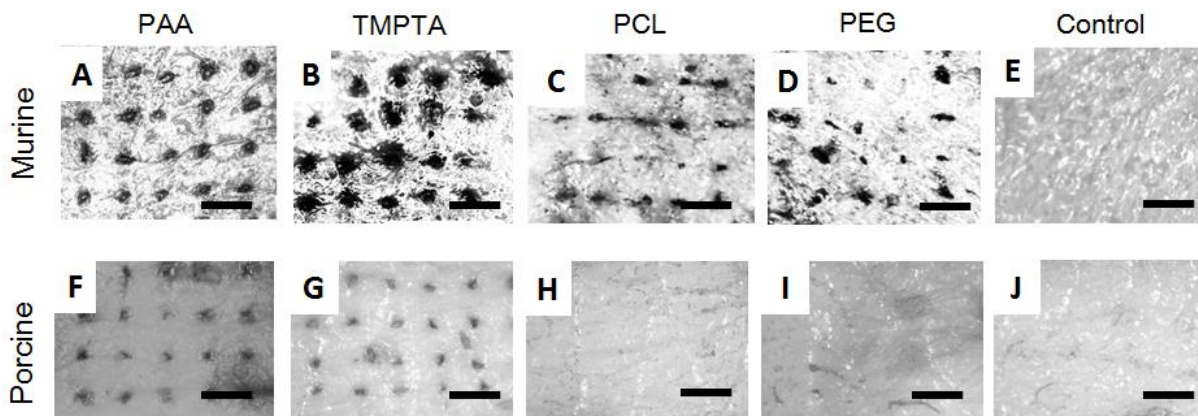


**Figure 4.2 Skin Penetration on Murine and Porcine Skin** A) PAA, B) TMPTA, C) PCL, and D) PEG CLIP microneedles effectively pierce murine skin, but the E) negative control shows no sites of penetration. F) PAA and G) TMPTA microneedles effectively pierce porcine skin, but H) PCL microneedles, I) PEG microneedles and J) the negative control show no sites of penetration. Scale bars measure 1mm.

transition temperatures ( $T_g$ ) above room temperature, whereas PCL and PEG have subzero glass transition temperatures. Therefore, PAA and TMPTA act as rigid, glassy materials at room temperature, whereas the PEG and PCL are elastomeric. This difference in the efficacy of insertion as a function of composition underscores the critical importance of microneedle composition in eliciting effective skin penetration. We therefore aimed to identify mechanical requirements necessary to enable microneedles to effectively insert into the skin.

#### 4.2.2 Fabrication of PEG Microneedles with Varying Crosslink Density

Increasing the crosslink density of a polymeric network decreases segmental motion, resulting in an increase in  $T_g$  and stiffness (Young's modulus,  $E$ ) and decreased elongation (strain,  $\epsilon$ ) at break.<sup>22-24</sup> In particular, increasing the crosslink density of (meth)acrylate functionalized PEG elastomers results a shift in mechanical behavior from that of a rubbery elastomeric material to that of a brittle plastic.<sup>25-26</sup> These changes in the mechanical properties of PEG hydrogels are due to a combination of decreased segmental motion of the PEG chains due to the crosslinks and the increase in the concentration of (meth)acrylate end groups as chain lengths shorten, which results in an increase in the mass of the alkyl backbone generated by photopolymerization relative to the mass of the PEG chain. The ability to alter the mechanical properties of the PEG hydrogel as a function of crosslink density provides an ideal model system

**Table 4.1 Composition of PEG Blends Utilized in Chapter 4**

<b>Resin Abbreviation</b>	<b>Wt% PEG550dMa</b>	<b>Wt% EGdMa</b>	<b>Wt% TPO</b>
PEG550dMa	97.5	0	2.5
PEG550dMa-EGdMa 75-25	73.125	24.375	2.5
PEG550dMa-EGdMa 67-33	65.325	32.175	2.5
PEG550dMa-EGdMa 59-41	57.525	39.975	2.5
PEG550dMa-EGdMa 50-50	48.75	48.75	2.5

to investigate how the mechanical properties of CLIP microneedles affect their skin penetration. Therefore, we aimed to fabricate CLIP microneedles from varying ratios of polyethylene glycol 550 dimethacrylate (PEG550-dMa) and ethylene glycol dimethacrylate (EG-dMa) (Table 4.1) All resins were mixed with 2.5wt% TPO as a photoinitiator.

It should be noted that PEG was selected as a model material because dimethacrylate functionalized PEG is commercially available in a number of different molecular weights. We do not, however, anticipate that PEG will be an ideal matrix for therapeutic applications because it has slow release rates (Figure 3.12.) even at crosslink densities that are too low to enable effective skin penetrations (Figure 5.2). Stronger materials will therefore be necessary for

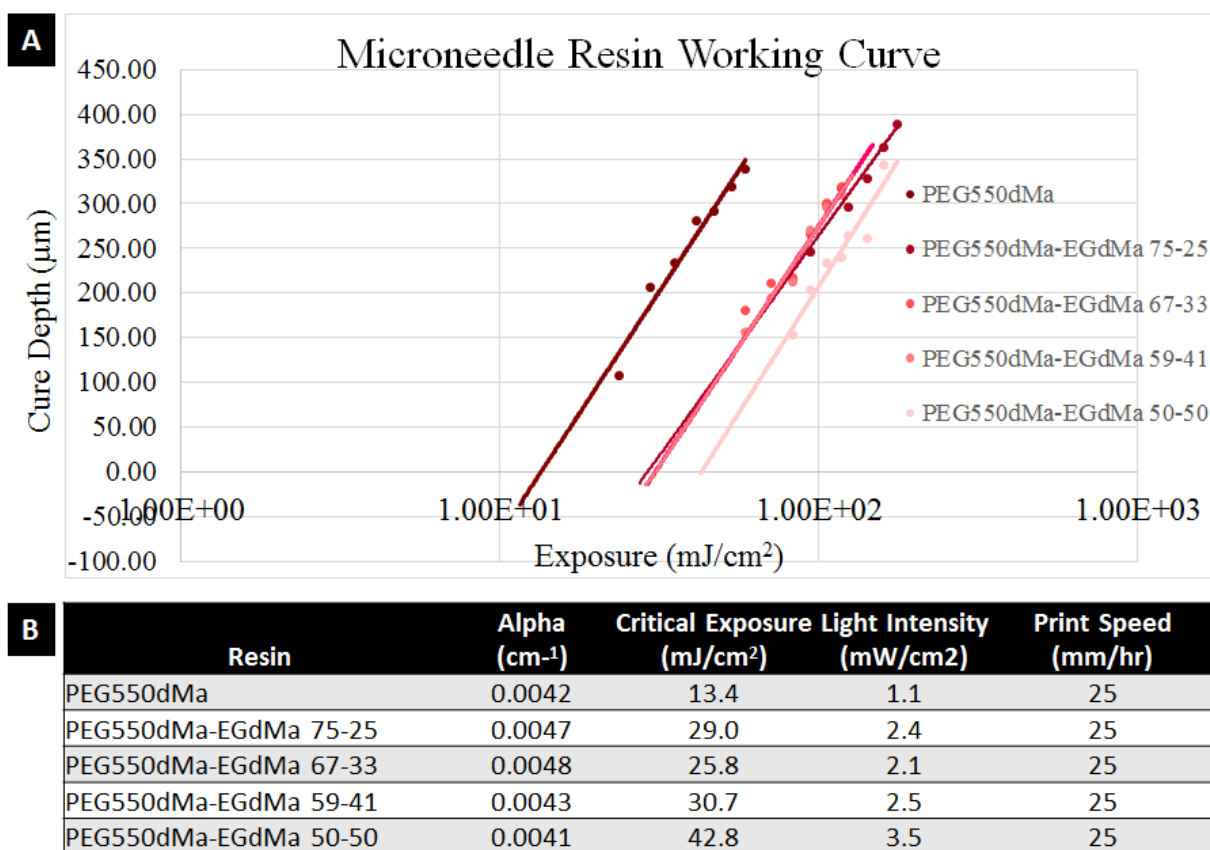


**Figure 4.3 Stereolithographic Working Curve and Resin Properties for PEG Blends.** A) The cure depth of microneedle resins as a function of applied dosage B) Absorption coefficient and critical exposure of microneedle resins determined from the working curves in figure A. The build parameters for each resin were calculated as described in Chapter 4 and are also listed.

translational applications. Nevertheless, dimethacrylate functionalized PEG provides an ideal model for this fundamental mechanics study.

Build parameters for microneedle fabrication using PEG blends were determined using the method presented in Chapter 3. This method compensates for differences in resin reactivity and reaction volume to identify the appropriate light intensity for the fabrication of microneedles using new resins. As in the previous chapter, all resins had approximately equivalent absorbance due to equal concentrations of the photoinitiator TPO. Microneedles were fabricated at 25mm/hr in order to ensure that resin was able to completely flow into the build area during the print. The working curve and resulting light intensity used for microneedle fabrication are given in Figure 4.4. Generally, increasing the wt% EG-dMa led to an increase in the critical exposure required for cure. Therefore, more light was required for fabrication of highly crosslinked microneedles.

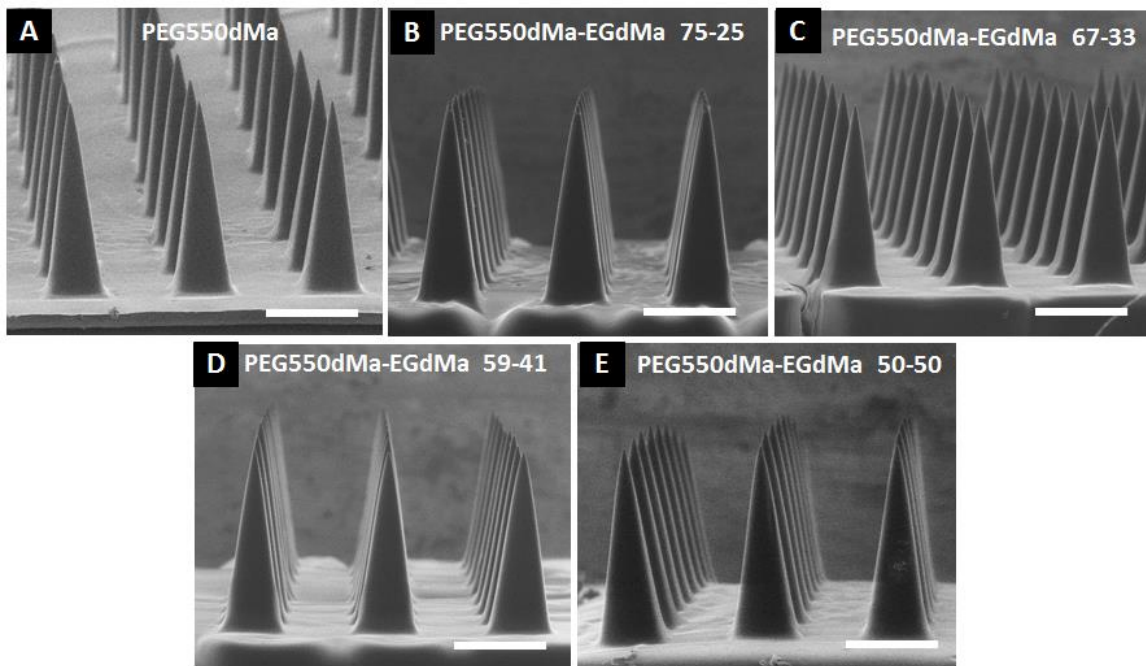


**Figure 4.4. CLIP Microneedles Fabricated from PEG Blends.** CLIP Microneedles are fabricated from A) Neat PEG550-dMa and B)50-50, C)67-33, D) 59-41, and E)50-50 ratios of PEG550-dMa to EG-dMa. All formulations are mixed with 2.5wt% TPO as a photoinitiator. Scale bars measure 500 $\mu$ m.

**Table 4.2 Dimensions of CLIP Microneedles Fabricated with PEG Blends.** Data are presented as mean  $\pm$ SD (n=9). No statistically significant difference in microneedle dimensions were found. Statistics were performed via one way ANOVA with Tukey’s honestly significantly different (HSD) post-test

Composition	Height ( $\mu\text{m}$ , n=9)	% Difference from Intended Height	Width ( $\mu\text{m}$ , n=9)	% Difference from Intended Width	Tip Radius ( $\mu\text{m}$ )
PEG550	988.67 $\pm$ 13.5	-1.1%	333.4 $\pm$ 10.0	0.0%	5.0 $\pm$ 0.4
PEG550-EG 75-25	1023.5 $\pm$ 13.6	2.4%	342.9 $\pm$ 13.7	2.9%	5.2 $\pm$ 0.8
PEG550-EG 67-33	990.9 $\pm$ 40.6	-0.9%	332.6 $\pm$ 13.5	-0.2%	4.9 $\pm$ 0.4
PEG550-EG 59-41	999.7 $\pm$ 37.0	0.0%	331.1 $\pm$ 13.5	-0.6%	5.1 $\pm$ 0.8
PEG550-EG 50-50	997.3 $\pm$ 23.3	-0.3%	334.0 $\pm$ 12.7	0.2%	5.0 $\pm$ 1.0

Microneedles were then fabricated using calculated build parameters on the CLIP7 additive manufacturing system. All PEG microneedles were found to have approximately equivalent structure, regardless of crosslinking density (Figure 4.4). Further analysis of microneedle dimensions demonstrated that all microneedle dimensions were found to be within 2.5% of the intended dimensions (Table 4.2). No statistically significant differences in the height, width, or tip radius of the microneedle arrays were found. Therefore, we can conclude that the working curve method of build parameter identification developed in Chapter 4 adequately calculates light intensity values that enable the production of dimensionally accurate CLIP microneedles. This result also underscores the “plug-and-play” nature of the CLIP microneedle fabrication process, which enables CLIP microneedles of virtually any composition to be fabricated with little to no lead time. We then proceeded to evaluate the mechanical properties of the PEG blends.

### 4.2.3 Mechanical Properties of PEG Blends

The mechanical properties of the photo-cured PEG blends were evaluated in compression according to ASTM Standard F451-08 “Standard Specification for Acrylic Bone Cement”. Compression testing (as opposed to testing in tension) was chosen to mimic microneedle application. Cylindrical test samples measuring 12mm in length and 6mm in diameter were

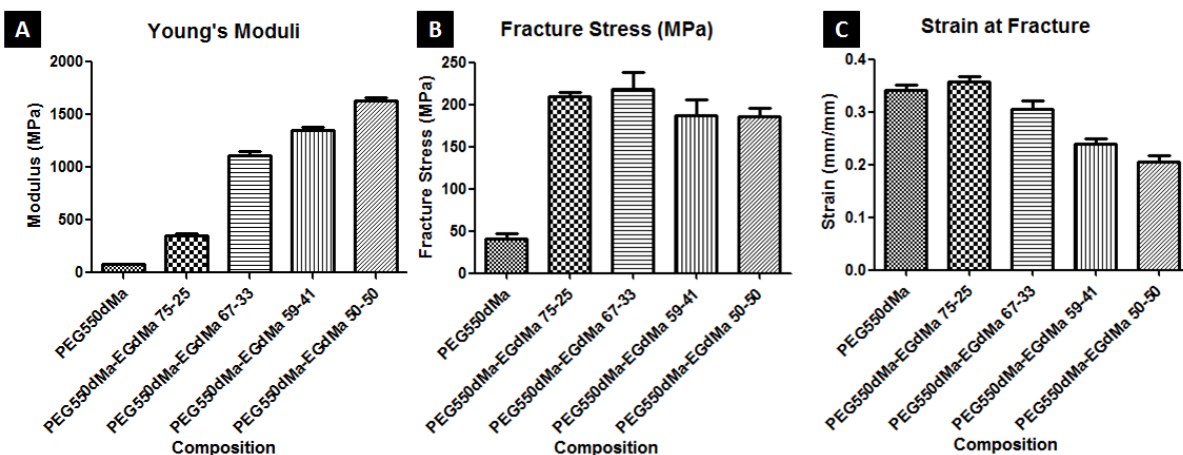


**Figure 4.5 Mechanical Properties of PEG Blends.** A) Young's moduli, B) Failure stress and C) Strain at failure for all PEG blends. Failure stress and strain at failure were determined using a zero slope method. Data are presented as mean  $\pm$ SD (n=3)

fabricated by CLIP using the same light intensity and build speeds used for microneedle fabrication (Figure 4.3). Test cylinders were post-cured for 10 minutes under UV light (equivalent to microneedle arrays) prior to mechanical testing. The mechanical properties identified by analysis of the stress-strain curves are given in Figure 4.5.

The mechanical properties of PEG blends follow expected trends. As crosslink density increases (i.e. as the weight percent EGdMa increases), the material becomes more stiff. Young's moduli range from approximately 80MPa for pure PEG550dMa to approximately 1.5 GPa for the PEG550dMa-EGdMa 50-50 blend. Fracture stress also increased as the crosslink density increased between the PEG550dMa and the PEG550dMa-EGdMa. Further increases in crosslink density have essentially no effect on fracture stress. Similar results have been previously published by Ortega et. al., who showed that increases in fracture stress of PEG based photopolymers as a function of crosslink density are more dramatic at low crosslink densities.<sup>27</sup> The strain at failure decreases as crosslink density increases, as expected, due to the increased rigidity of the crosslinked networks. Therefore, we successfully produced photo-cured PEG

blends with a range of mechanical properties that can be utilized to assess how material properties affect microneedle insertion.

Ideally, the mechanical properties of CLIP microneedles would be measured directly rather than using a macroscopic test cylinder to determine mechanical properties. However, measuring the mechanical properties of a microneedle is challenging because of the changing cross sectional area of a microneedle (which makes it difficult to accurately determine stress) and the small dimensions of the structure. Therefore, the gel fraction and solvent uptake of test cylinders and microneedle patches were compared to confirm that they are composed of equivalent materials (Figure 4.6). Small differences in gel fraction and solvent uptake of the cylindrical test sample and the microneedle patch were found. In general, the gel fraction of the microneedle patches was less than that of the cylindrical test samples. The solvent uptake of the microneedle patches was greater than that of the cylindrical test samples. These results suggest that the crosslink density of the microneedle patches may be slightly less than the crosslink density of the test cylinder. The shape of the structures may also play a role. Nevertheless,

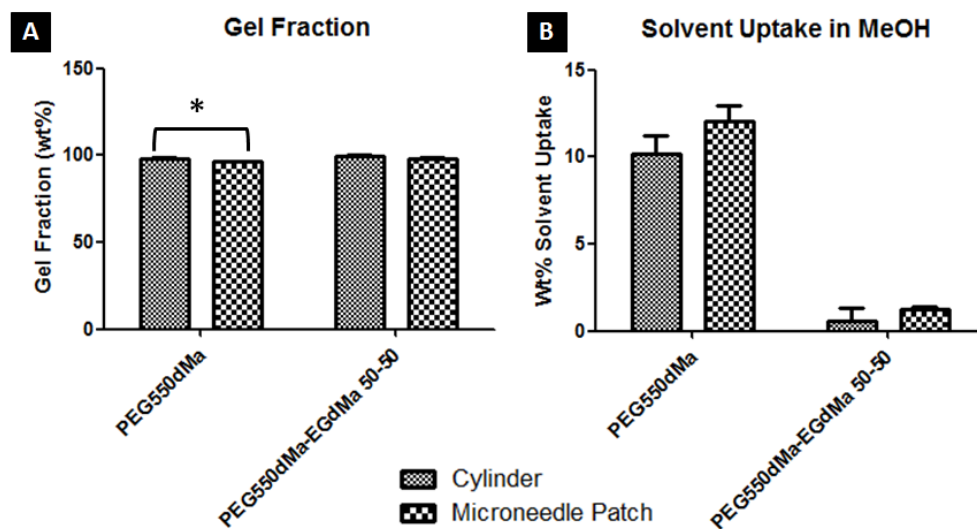


**Figure 4.6 Gel Fraction and Solvent Uptake of PEG Networks.** Cylindrical test samples and microneedle patches were found to have similar A) gel fractions and B) solvent uptakes. Data are presented as mean  $\pm$  SD (n=3).

differences in solvent uptake between shapes are much less than the differences between compositions. Therefore, we assume that the test cylinders and microneedle patches are composed of relatively equivalent materials throughout the remainder of this chapter.

#### 4.2.4 Quantification of Microneedle Insertion Forces

The force used to apply a microneedle device ( $F_{\text{application}}$ ) is an important variable affecting the efficacy of insertion. In microneedle literature, investigators frequently apply microneedles to the skin by pressing firmly on the back of the patch with their thumb. Bearing in mind that the vast majority of microneedles in preclinical literature are applied using “force of thumb”, we aimed to quantify “force of thumb” for ten different people in order to determine 1) a relevant range of applications forces for studies where microneedles are inserted using a more quantitative application force and 2) to determine how much variability in “force of thumb” exists among potential microneedle users. It may be necessary to develop a simple microneedle applicator to improve the consistency of insertion between users in a clinical setting; the studies presented here will provide information regarding user to user variability to determine whether an applicator is necessary.

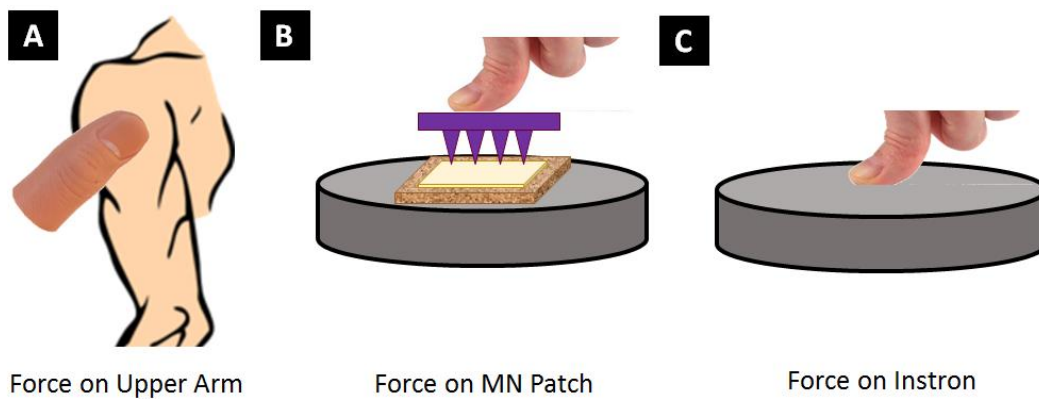


**Figure 4.7 Study Design for Quantifying Force of Thumb**

Ten study participants were recruited, ranging in age from 21 to 70 years old. Each participant was asked to apply three equal forces of five second duration (Figure 4.7). First, each participant used their thumb to press against their upper arm to identify a comfortable force for application of a microneedle array (Figure 4.7A). Each participant was then asked to use the same force to apply pressure to the back of a microneedle array. This microneedle array was resting on full-thickness porcine skin sitting on a piece of corkboard. The entire assembly was placed on top of an Instron compression plate connected to a load cell used to measure the application force (Figure 4.7B). Lastly, each participant applied the force directly to the Instron

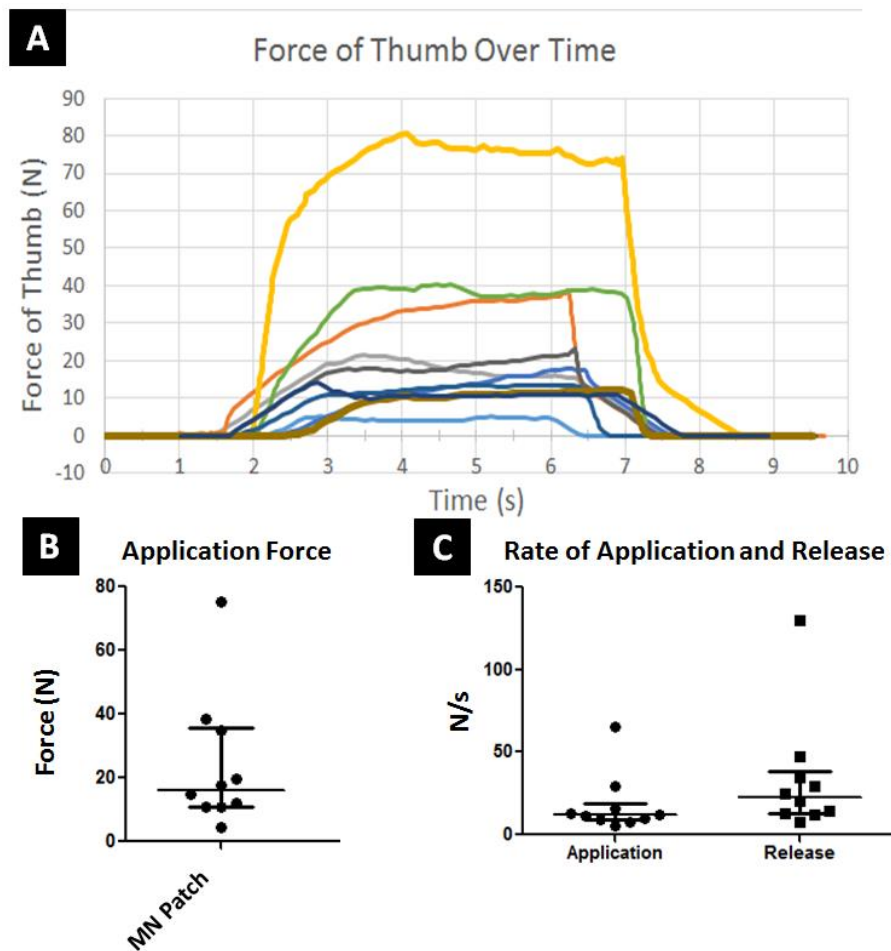


**Figure 4.8. Quantification of Force of Thumb.** A) Force vs. time curves for ten participants applying microneedle patches to porcine skin B) Quantification of the force applied by each of ten participants directly to the microneedle patch and to the compression plates. These forces correspond to the diagram in Figure 5.7 B and C, respectively C) Rate at which the force is applied and released from the microneedle patch for each of the ten participants

compression plate. This final force acted as a control intended to determine whether the microneedle array/corkboard assembly would absorb enough energy to alter the force experienced by the load cell. No significant difference in applied force was found with and without the corkboard (data not shown). Therefore, the results were taken from force B (Figure 4.7), where participants applied force directly to the microneedle patch. The force of thumb was taken by averaging the force applied during the 5 second plateau in force; force values during application and release were ignored in this quantification.

Figure 4.8 shows that a large amount of variability in applied force was observed between participants. Force of thumb ranged from 4N to 80N, with an average application force of approximately 25N (Figure 4.8B). The rate of application and release of this force ranged from 5 to 130 N/s, with an average of approximately 25 N/s. These values fall within the same range as forces reported in a similar study by Larraneta et. al.<sup>21</sup> Therefore, we decided to investigate microneedle insertion using controlled application forces of 6N, 12.5N, 25N, and 75N applied and released at 25 N/s. These forces fall within the range of forces that can be applied via thumb pressure and may therefore provide a comfortable range of application forces for patients in a clinical setting.

#### **4.2.5 Percent Insertion as a Function of Composition and Applied Force**

We then aimed to investigate how microneedle composition and applied force affect microneedle insertion into the skin. Microneedles composed of all PEG blends (Figure 4.4, Table 4.2) were applied to porcine skin *ex vivo* using a controlled application force of 6N, 12.5N, 25N, or 75N. Force was applied using an Instron Universal Testing Station with application and release rates of 25N/s. To determine whether microneedles fracture during/prior to insertion, all microneedles were imaged after application. No evidence of microneedle fracture was found for

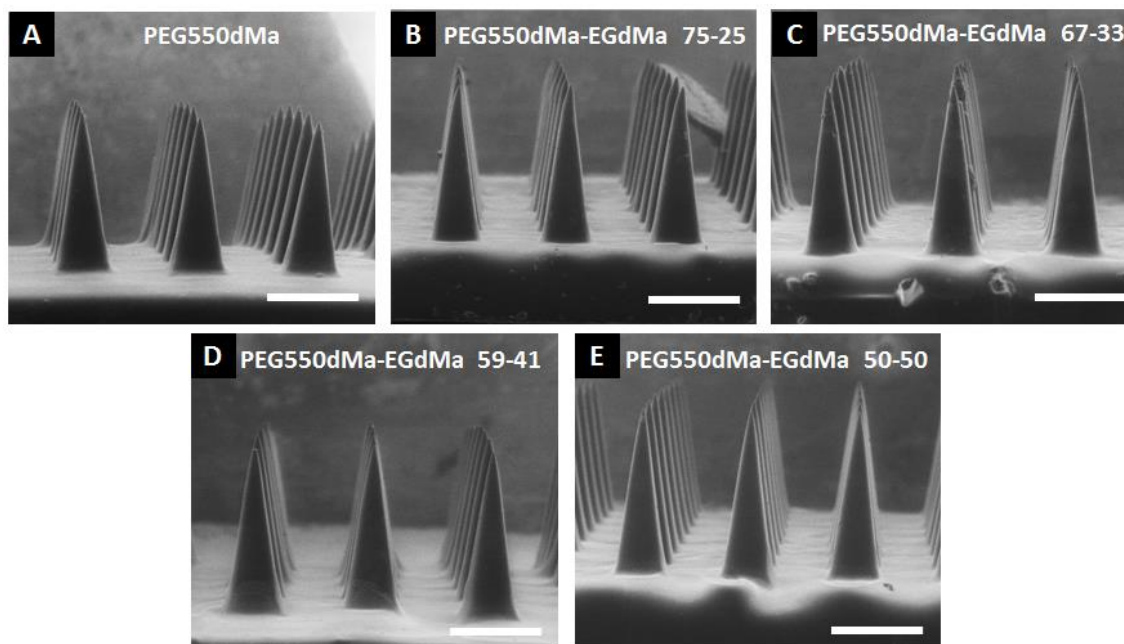


**Figure 4.9 PEG Microneedle Arrays After Application with 75N Force.** Microneedles composed of A) PEG550dMa, B) PEG550dMa-EGdMa 75-25, C) PEG550dMa-EGdMa 67-33, D) PEG550dMa-EGdMa 59-41, E) PEGdMa-EGdMa 50-50, and F) PEG550dMa-EGdMa 75-25 remain intact after application. Scale bars measure 500µm.

any of the compositions at any applied force; an image of intact microneedles after application to skin with 75N of force is shown in Figure 4.9. Based on this data, we can conclude that the microneedles that fail to insert into the skin because the force required to insert the array into the skin ( $F_{insertion}$ ) is greater than the applied force ( $F_{applied}$ ), not due to microneedle fracture.

After microneedle application to porcine skin, sites of insertion were marked with tissue marking dye, as shown in Figure 4.10. The percentage of microneedles that insert into the skin was calculated by counting the number of insertion sites and dividing by the total number of microneedles within the array. Figure 4.10 provides an example of a microneedle array that does not penetrate the skin (Figure 4.10A), an array that partially punctures the skin (Figure 4.10B) and an array that completely punctures the skin (Figure 4.10C).

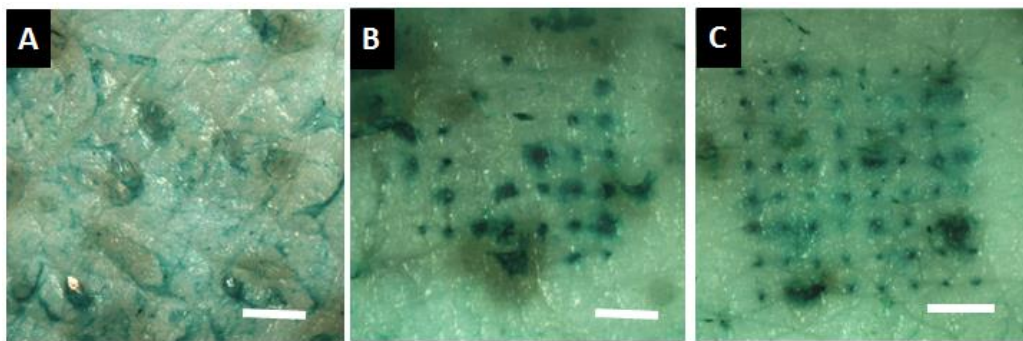


**Figure 4.10 Assessment of Percent Insertion Using Tissue Marking Dye.** Some microneedles arrays A) do not insert into the skin, B) partially insert into the skin or C) completely insert into the skin. Percent penetration is taken by dividing the number of penetration sites visualized by the total number of microneedles in an array (64 microneedles). Scale bars measure 1mm.

Using this technique, the percent of needles within an array that insert into the skin with a given application force was calculated for six replicates of all five compositions (Figure 4.11).

With a 6N application force (equivalent to 93.75 mN/microneedle), none of the tested compositions successfully punctured murine skin (Figure 4.11A), but insertion was material dependent at higher application forces. Therefore, data is also graphed according to microneedle composition for additional clarity (Figure 4.12). For this study, when 90% or more of the microneedles in an array (marked by the dotted line) puncture the skin's surface, the array is considered to effectively insert. When less than 90% of needles in the array insert into the skin, the insertion is considered ineffective.

Microneedles made of PEG550dMa did not insert into the skin, even with up to 75N of applied force (Figure 4.12A). Microneedles made of PEG550dMa-EGdMa 75-25 also exhibited poor insertion into the skin (Figure 4.12B). Although some of the needles in a given array do puncture the skin surface, less than 90% of the total number of needles in an array punctured in all cases. Substantial variability in the percentage of needles that insert is also present between applications, even though an automated device was used for application. Because neither of these

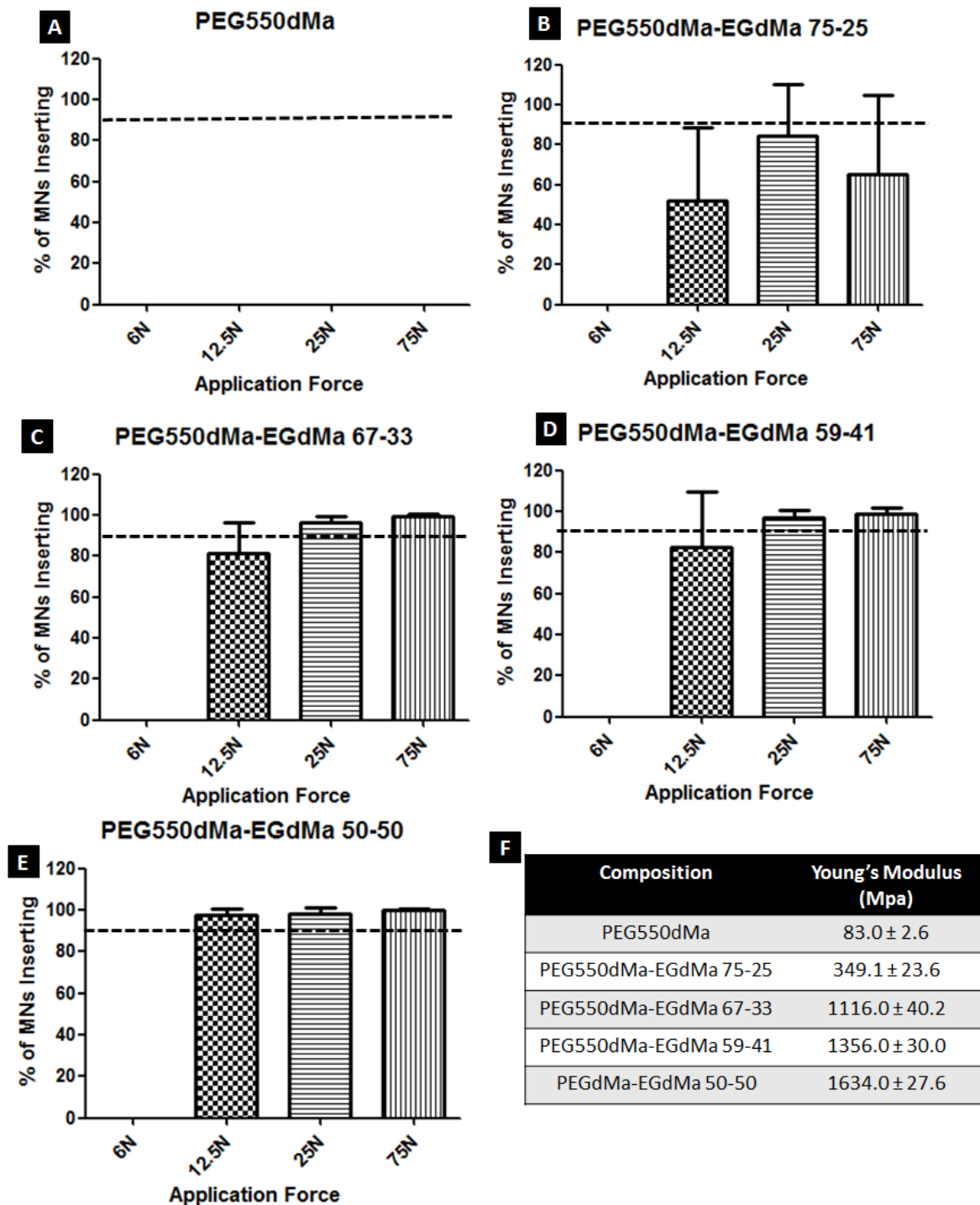


**Figure 4.11 Percent of needles that puncture skin as a function of composition.** Arrays of 64 microneedles composed of A) PEG550dMa, B) PEG550dMa-EGdMa 75-25, C) PEG550dMa-EGdMa 67-33 D) PEG550dMa-EGdMa 59-41 and E) PEG550dMa-EGdMa 50-50 microneedles were applied to full thickness porcine skin ex vivo using 6N, 12.5N, 25N, and 75N of force. The percentage of needles in an array that punctured skin is given. F) Young's moduli for microneedle compositions in A)-E). Data are graphed as mean ± SD (n=6)

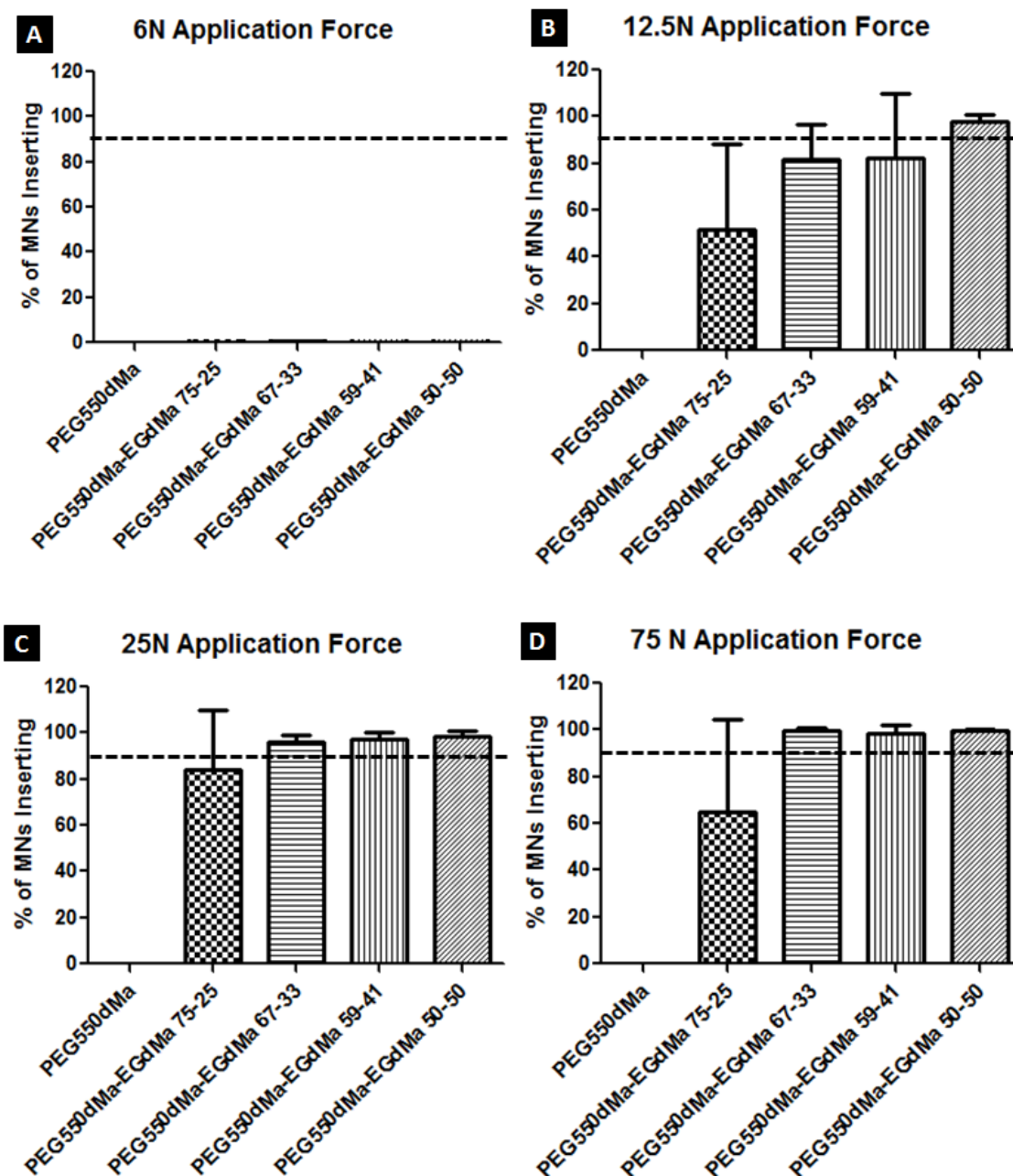


**Figure 4.12 Percent of needles that puncture skin as a function of insertion force.** Arrays of 64 microneedles composed of a variety of PEG blends were applied to porcine skin ex vivo with A) 6N, B) 12.5N, C) 25N, or D) 75N of force. Data is presented as mean  $\pm$ SD (n=6) of the percent of microneedles inserting into skin, calculated by dividing the number of insertion sites by the total number of microneedles in the array. The dotted line represents 90% of microneedles inserting into the skin.

compositions fractured during application (Figure 4.9A-B), future studies could investigate whether forces that are greater than 75N would enable these microneedles to effectively insert into the skin. At some point, further increases in applied force may become uncomfortable for the patient; therefore, establishing a maximum tolerable force would be essential to such investigations.

Microneedles composed of stiffer materials (PEG550dMa-EGdMa 67-33, PEG550dMa-EGdMa 59-41, and PEG550dMa-EGdMa 50-50) effectively punctured porcine skin *ex vivo* within the tested range of application forces. While the stiffest microneedles (composed of PEG550dMa-EGdMa 59-41 and PEG550dMa-EGdMa 50-50) effectively punctured the skin when a force of 25N or greater was applied, microneedles composed of PEG550dMa-EGdMa 50-50 required only 12.5N of force to insert into the skin. Therefore, a tradeoff between stiffness and the minimum required application force exists.

As stated previously, none of the tested microneedle compositions fractured prior to insertion. Therefore, the elastic modulus of the microneedle matrix played a more important role in microneedle insertion than fracture strength for the tested microneedle arrays. Further, this data demonstrates that the force required to insert a microneedle array decreases as the stiffness of the material increases. Although producing very stiff microneedle arrays is a straightforward method for ensuring effective insertion, some desirable properties of a microneedle matrix decrease the elastic modulus. For example, in crosslinked networks, the rate of diffusion of a therapeutic out of the matrix typically decreases as crosslink density and stiffness increase. Some therapeutics may also plasticize the polymer matrix, causing the material's stiffness to decrease as the total therapeutic volume increases. Therefore, increasing the amount of the therapeutic or its rate of release would correspond to a decrease in stiffness. For these reasons, a

comprehensive understanding of the required mechanical properties will continue to aid microneedle design for specific therapeutic applications.

This data also suggests that for effective microneedle application via force of thumb, a modulus of approximately 1GPa or greater is recommended. This is of the same order of magnitude as results reported by Lee et. al.<sup>13</sup> Throughout this study, other microneedle design variables, including tip radius and the number of needles per array, were held constant. Such variables would indubitably alter the required modulus. For example, the ability of a microneedle to insert into the skin has been previously shown to be determined by the applied force per microneedle, not the total force applied to the array.<sup>28</sup> Therefore, decreasing the number of microneedles in an array would increase the force applied to each needle; such an approach may lower the minimum modulus required. This hypothesis could be easily tested by altering the number of needles per array using the CLIP platform. Although decreasing the total number of microneedles in the array decreases the total volume available for drug loading, the tiered microneedles presented in Chapter 2 could potentially be used to decrease mechanical requirements by decreasing the number of microneedles inserting into the skin at a given moment in time, while maintaining high drug loading capacity on an array.

Further, Davis et. al. demonstrated that the force required to insert a microneedle into the skin depends on needle sharpness, quantified by the tip radius of the array.<sup>12</sup> Microneedle insertion force was found to increase linearly with the surface area of the microneedle tip (i.e. tip radius squared). Therefore, this recommended modulus is also likely to be specific to microneedles that have a tip radius at or near 5 $\mu$ m.

#### 4.2.6 Depth of Penetration vs. Force

The insertion data presented in the previous section was obtained by using tissue marking dye to mark sites of penetration. Therefore, this data provides useful information about how many needles puncture the stratum corneum, but it does not provide any indication of each needle's depth of penetration into the skin. Traditionally, assessing penetration depth requires the skin to be frozen and sectioned, which may alter the structure and dimensions of the tissue due to dehydration and extensive mechanical manipulation.<sup>3</sup> Optical coherence tomography (OCT), a noninvasive imaging technique that is considered an optical equivalent to ultrasound, has been used by Donnelly<sup>3</sup> and others<sup>29-30</sup> to assess microneedle penetration depth in skin. This technique, which has been used to image up to 2mm deep into tissue,<sup>31</sup> allows microneedle penetration depth to be accurately measured without manipulating the structure of the skin.

Here, we use optical coherence tomography to assess the depth of penetration of microneedle arrays as a function of composition and applied force. Microneedle arrays were applied to full thickness porcine skin *ex vivo* using an Instron Universal Testing Station, as previously described. Microneedle compositions and applied forces were down-selected from Figures 5.11 and 5.12 by to select force-composition combinations that allowed >90% of the microneedles within the array to puncture the skin surface. Other compositions were not tested because the tissue marking dye experiments already indicated that they do not effectively penetrate skin.

Microneedles were then imaged using OCT by pointing the laser through the back of the microneedle array (Figure 5.13A) while it was embedded in porcine skin. Data was collected in two different channels, a co-polarized signal (HH, where input and output polarization was equal, which contrasts optically isotropic light scatterers) and a cross-polarized signal (HV,

where input and output polarization were orthogonal, which contrasts optically anisotropic material). Initial OCT images in the HH signal (Figure 5.13B) showed that the microneedle backing and the surface of the skin could be visualized. The surface of the skin was visible in white due to the strongly scattering nature of the skin tissue. The edges of the microneedle backing could likewise be visualized in white. The microneedles themselves, however, were not strongly scattering, but appeared as dark voids in the skin. The tips of the microneedles could not be visualized within the tissue (Figure 5.13B).

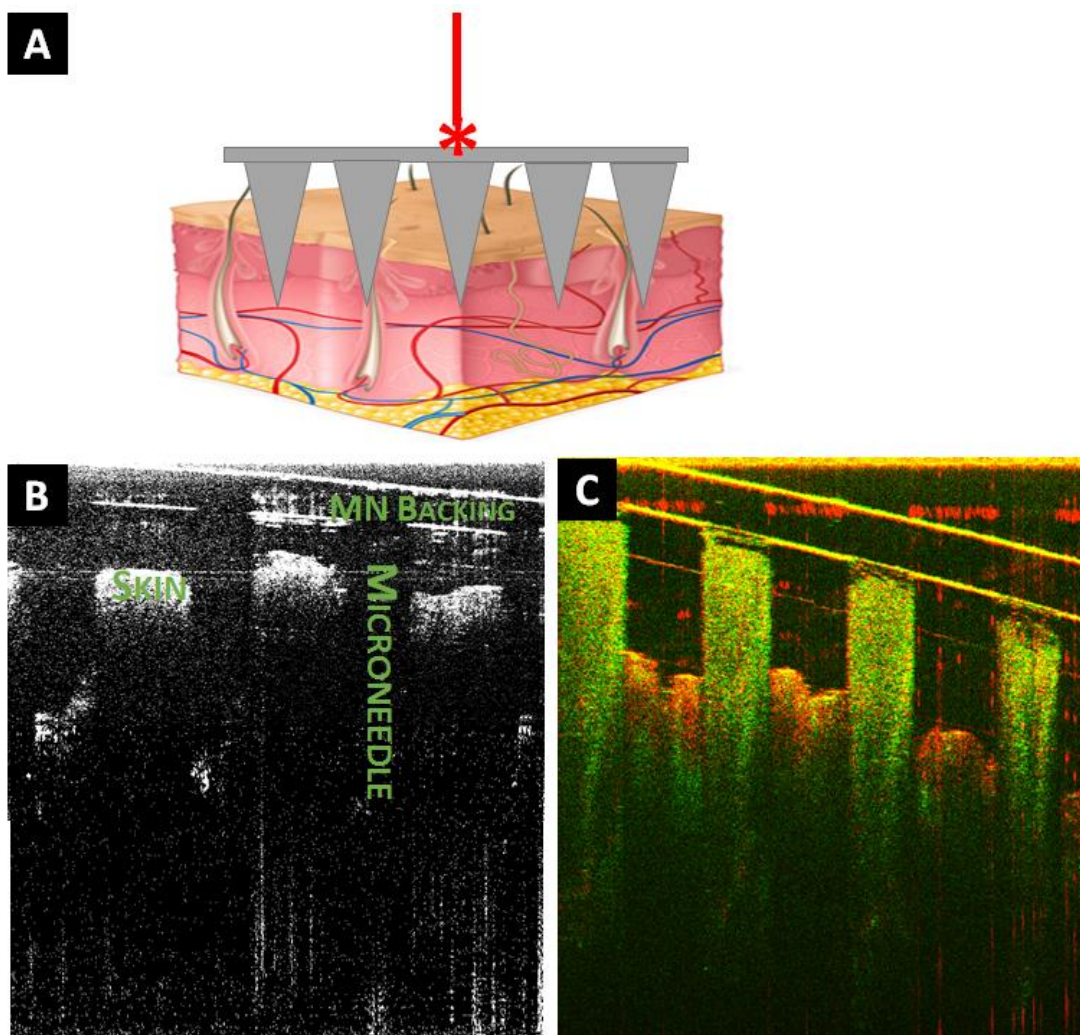
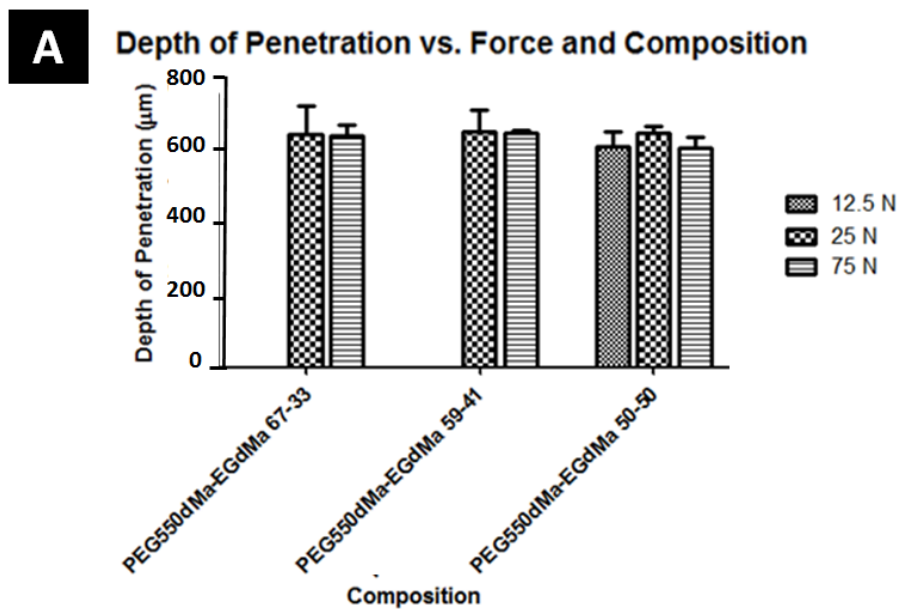


**Figure 4.13 OCT Experimental Setup and Images.** A) Images were obtained by pointing the laser through the backing of the applied microneedle patch into skin. B) HH image of blank microneedle array in porcine skin. C) HV-HH overlay of microneedle array containing GNRs

In an attempt to improve the image such that the entire length of the microneedle could be visualized, 2wt% 84x22nm gold nanorods (GNRs) were incorporated into microneedle devices by mixing GNRs with the photoreactive resin prior to fabrication. GNRs were not incorporated into the patch backing. Because these GNRs have a plasmon resonance of 800nm, they were strongly scattering, producing a distinct contrast in the HV output of the OCT system,<sup>37</sup> allowing for clear visualization of the needle. The HH and HV outputs were stacked, where HH is in red and HV is in green, to produce the image of GNR containing microneedles shown in Figure 5.13C. The microneedles in this image show up strongly in green due to the cross-polarized signal from the GNRs. Figure 5.13C confirms that the voids seen in Figure 5.13B are indeed due to microneedles penetrating into the skin. Unfortunately, the microneedle tip could still not be clearly visualized. Therefore, the penetration depth of the microneedle was determined by subtracting the distance between the MN backing and the skin surface from the total microneedle length (measured by ESEM). Although these GNRs were useful to validate the measurement technique, they were not included in the tested samples because the GNRs may alter the mechanical properties of the materials under investigation.

The measured depth of penetration as a function of composition and applied force is given in Figure 4.14. All microneedles penetrate to approximately 650 $\mu$ m deep into the porcine skin, regardless of the material properties of the array and the application force used to administer the array. The variation in penetration depth between arrays ranged from 4.8 $\mu$ m up to approximately 40  $\mu$ m for most conditions. The variability between arrays was found to be similar to the variability in microneedle insertion within a single array (data not shown). Much of the variability within a single array appeared to be due to the undulating surface topology of the skin



**B**

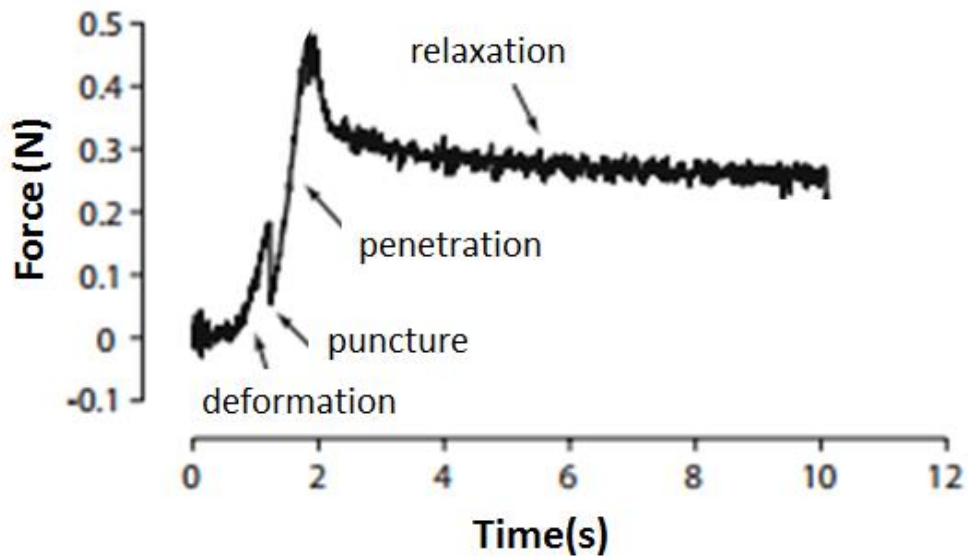
Composition	MN Height	Penetration Depth 12.5N Force	Penetration Depth 25N Force	Penetration Depth 75 N Force
PEG550dMa-EGdMa 67-33	931.4 $\pm$ 40.6	651.3 $\pm$ 40.2	648.0 $\pm$ 15.5	648.0 $\pm$ 15.5
PEG550dMa-EGdMa 59-41	939.7 $\pm$ 37.0	658.0 $\pm$ 31.5	655.0 $\pm$ 4.8	655.0 $\pm$ 4.8
PEG550dMa-EGdMa 50-50	906.1 $\pm$ 23.4	625.0 $\pm$ 20.7	643.7 $\pm$ 10.3	622.6 $\pm$ 15.9

Figure 4.14 Depth of Penetration of PEG Blends. A) Depth of penetration of microneedle arrays as determined by OCT. B) The same data is given numerically. Data are presented as mean $\pm$ SD between arrays (n=3 arrays), where the average penetration depth for each array is rather than actual variability in needle penetration. Therefore, skin penetration was determined to be very consistent using this method of application.

This pilot study seems to indicate that once microneedles penetrate the outer layer of the skin, they insert to the same depth, regardless of composition and insertion force. This study, however, contradicts an existing report by Donnelly et. al. showing that microneedle penetration depth increases with increases in application force for 600 $\mu\text{m}$  tall microneedles composed of a mixture of methylvinylether and maleic anhydride (PMVE/MA) applied with 0.48 to 1.82N of force per microneedle.<sup>3</sup> Forces of 0.09 to 1.17N per microneedle are tested here, for comparison.

No studies investigating depth of penetration as a function of material properties have been published, to our knowledge.

A multitude of different theoretical models, ranging from simple to complex, have been applied to needle insertion into soft tissues. The development and evaluation of such a model is outside the scope of this dissertation, but the framework used to develop previous models may be useful to interpreting the results presented here. Models proposed by Mavash and Dupont,<sup>32</sup> Akamura,<sup>33</sup> and Azar and Hayward<sup>34</sup> describe needle insertion into soft tissues in four steps: 1) deformation, 2) puncture, 3) penetration, and 4) relaxation (Figure 4.15). Deformation spans the period of time over which the needle compresses the tissue until the pressure on the tissue is equal to its yield stress. Puncture is the moment where the tissue ruptures to produce a crack. Penetration spans the period of time over which the tissue is displaced to propagate the crack and allow the microneedle to continue to move further into the tissue. Relaxation occurs when the application force is removed, allowing the tissue to recoil due to its natural elasticity. This tissue



**Figure 4.15** Process of microneedle penetration into the skin. Adapted from reference 34.

recoil has been shown to decrease the penetration of an individual microneedle by approximately 34% after relaxation, as reported by Romgens et. al.<sup>1</sup>

This framework suggests that increasing the application force should result in an increase in the maximum penetration depth by providing more energy to displace the native tissue during the penetration phase. However, the role of tissue recoil on our measurements is currently unknown. Some OCT measurements were taken up to an hour after microneedle insertion; therefore, the relaxation/dehydration of the tissue over time may have masked differences in penetration depth. A time course study investigating the depth of penetration throughout insertion may be useful to determine whether the tissue's elasticity plays a significant role in microneedle penetration depth. Insertion testing of the arrowhead microneedles fabricated in Chapter 2 may also provide more information about the role of tissue recoil on microneedle depth of penetration and may potentially increase total insertion depths. Nevertheless, taking depth of penetration measurements after recoil, as we did in this experiment, is a clinically relevant scenario that informs microneedle design.

It is conceivable that microneedle stiffness has little effect on depth of penetration. The stiffness of skin tissue in compression has been shown to be on the order of 2 kPa,<sup>35</sup> but measurements also vary widely, according to age, environmental conditions, testing methods, and the anatomical location on the body, etc. Nevertheless, because the microneedles utilized here have much higher elastic moduli (and are therefore much stiffer) than skin, the microneedles may not deform substantially after the initial puncture. Further experiments are necessary to conclusively determine whether force and composition affect microneedle penetration depth.

### 4.3 Conclusion

Here, we fabricate microneedle arrays from a variety of polyethylene glycol (PEG) blends with different mechanical properties. The moduli, strain at break, and failure stress of these materials are characterized. Moduli range from approximately 83 MPa to nearly 2 GPa. Strain at break and failure stress range from 0.05 to 0.4 and from 50MPa to 200MPa, respectively. The ability of these microneedles to penetrate porcine skin *ex vivo* when applied with a range of forces was assessed using tissue marking dye. Insertion efficacy was found to be dependent on both modulus and applied force. Stiffer microneedles effectively inserted into the skin at lower application forces, whereas higher forces were required to insert more rubbery materials. Depth of penetration was quantified as a function of applied force and material properties using Optical Coherence Tomography (OCT). Future work will investigate how altering microneedle shape influences skin penetration to identify optimal microneedle designs.

### 4.4 Experimental

#### 4.4.1 Identification of PEG Microneedle Build Parameters

Methods for the determining critical exposure were adapted from Tumbleston et. al.<sup>36</sup> Briefly, 500 $\mu$ L of resin was placed on a cover slip on top of the printer window. Resin was exposed to a specified dosage of light ( $\lambda=365$ nm LED) in a circle pattern and residual, unreacted monomer was removed using an acetone wash. The height of polymerized circles was then measured using a Mitutoyo Electronic Indicator (McMaster Carr). Resins utilized in this study were blends of ethylene glycol dimethacrylate and polyethylene glycol dimethacrylate ( $M_n$  550, Sigma Aldrich) mixed with 2.5 wt% Diphenyl(2,4,6-trimethyl-benzoyl-)phosphine oxide (Sigma Aldrich) as a photoinitiator. Specific ratios of each component are given in Table 4.1. The light intensity utilized for microneedle fabrication was then calculated as described in Section 4.2.2.

#### **4.4.2 Fabrication of PEG Microneedles**

To produce microneedles of different heights, CAD files of square pyramidal microneedles measuring 1000 $\mu$ m tall with an aspect ratio of 3 (aspect ratio= height/width) were generated using Solidworks 2014. All microneedles were spaced at one base width apart on a base measuring 6x6x1mm. CAD files were then sliced at 1 $\mu$ m slice thickness using the open source software Slic3r. Microneedles were then produced using the CLIP7 additive manufacturing system (Carbon 3D, Redwood City, CA) using blends of PEG550-dMa, EG-dMa, and TPO with compositions provided in Table 5.1. PEG550dMa, PEG550dMa-EGdMa 75-25, PEG550dMa-EGdMa 67-33, PEG550dMa-EGdMa 59-41, and PEG550dMa-EGdMa 50-50 microneedles were produced at 25mm/hr with 1.1, 2.4, 2.1, 2.5, and 3.5mW/cm<sup>2</sup> of UV light ( $\lambda=370$ ). All needles were washed briefly with acetone and dried using compressed air. All microneedles were post-cured for 10 minutes under a mercury lamp. Microneedles were imaged using an environmental scanning electron microscope (FEI Quanta 200) in low vacuum mode.

#### **4.4.3 Mechanical Testing of PEG Blends**

Test cylinders were fabricated by drawing a circle measuring 6mm in diameter directly into the .LUA script using the addcircle function. This circle was projected continuously as the build elevator moved upwards a distance of 12mm to produce a cylindrical test part. All test cylinders were produced using the E20 CLIP additive manufacturing system (Carbon3D, Redwood City, CA) using light intensities specified in Section 4.4.2. All parts were postcured for 10 minutes under a mercury lamp.

Test cylinder stress-strain curves were obtained using an Instron 5566 Universal Testing Machine. Compression was applied at a rate of 1mm/s with a 1N preload until part failure. The instrument was equipped with a 10kN load cell. The Young's modulus, strain at fracture, and

stress at fracture were automatically calculated using Bluehill3 Software, where fracture was automatically identified using a zero slope method.

#### **4.4.4 Gel Fraction and Solvent Uptake**

The gel fraction and solvent uptake of PEG550dMa cylinders, PEG550dMa microneedles, PEG550dMa-EGdMa 50-50 cylinders, and PEG550dMa-EGdMa 50-50 microneedles were determined as follows. Three microneedle patches with 1mm backings and one cylindrical test part were each weighed ( $W_i$ ) and then submerged in separate amber bottles containing approximately 200mL of methanol (MeOH) over 24 hr. After this extraction of the soluble fraction, parts were then removed from the methanol, dried using a Kimwipe, and weighed again ( $W_s$ ) to determine solvent uptake. Solvent uptake was calculated by taking  $(W_s - W_i)/W_i$ . Parts were then heated to 100°C for 24 hr under vacuum to remove residual methanol, removed from vacuum to equilibrate to ambient humidity overnight and then weighed again ( $W_d$ ) to determine weight percent mass lost. Gel fraction was calculated by taking  $(W_d/W_i)$ .

#### **4.4.5 Quantification of Force of Thumb**

Ten study participants were recruited, ranging in age from 21 to 70 years old. Each participant was asked to apply three equal forces of five second duration. First, each participant used their thumb to press against their upper arm using a force that they deemed acceptable for insertion of a microneedle array. They were then asked to use the same force to apply pressure to the back of a microneedle array resting on top of a sample of full-thickness porcine skin on top of a corkboard. This entire assembly was placed on top of an Instron 5566 Universal Testing Machine compression plate connected to a 500N load cell used to measure the application force. Lastly, each participant applied the force directly to the Instron compression plate. All data was collected using Bluehill3 Software.

#### **4.4.6 Skin Insertion Tests**

For Figure 5.1, PEG550dMa, PCL, and PAA microneedles were applied to murine and porcine skin by applying firm thumb pressure to the back of the patch for 10 seconds. Murine skin excised from nude mice with permission of the UNC Institutional Animal Care and Use Committee (IACUC). Full thickness porcine skin was purchased from Stellen Medical.

To assess microneedle application using a controlled force, microneedle patches were placed needle side down on a section of full thickness porcine skin resting on corkboard. An Instron 5566 Universal Testing Machine equipped with a 100N load cell was utilized to apply controlled forces by bringing the instron compression plates into contact with the microneedle array prior to force application. Forces of 6N, 12.5N, 25N, and 75N were applied for 5 seconds; force was applied and released at a rate of 25 N/s. The transducer gain was set at 0.0025 to enable load control.

#### **4.4.7 Optical Coherence Tomography (OCT)**

Images were acquired using a custom built, ultra-high resolution, polarization-sensitive, spectral-domain optical coherence tomography system, as previously described.<sup>39</sup> Briefly, the OCT system was comprised of a Michelson interferometer with a Titanium:Sapphire laser (Griffin, KMLabs, Inc.) source ( $\lambda=800\text{nm}$ ,  $\Delta\lambda=120\text{nm}$ ). Polarization sensitivity was obtained by isolating horizontally polarized light at the input of the interferometer. A quarter-wave plate in the reference arm was used to obtain equal portions of horizontal and vertically polarized light. The reference and sample beams were recombined and split into two outputs using a polarizing beam splitter, resulting in a co-polarized signal (HH, where input and output polarization was equal to contrast optically isotropic light scatteres) and a cross-polarized signal (HV, where input and output polarization were orthogonal to contrast optically anisotropic light

scatterers). The resolution of the system, in air, was  $3\mu\text{m} \times 10\mu\text{m}$  (axial ( $z$ ) vs. transverse ( $x$ )). Images were acquired using a line-scan camera (Piranha, Dalsa Inc.) at a rate of 10 kHz with  $70\ \mu\text{s}$  exposure time.

Three-dimensional scans were obtained for each sample. For each 2D B-mode image ( $x,z$ ), 1000 A-lines were collected as the imaging beam was scanned laterally over 5mm, resulting in  $\Delta x=5\mu\text{m}$ . A total of 500 images were collected, scanned transversely ( $y$ ) over 5mm, resulting in a spacing of  $\Delta y=10\mu\text{m}$ . Since PS-SD-OCT collects images in the frequency domain, images were post processed to obtain intensity images, using a dispersion compensation algorithm,<sup>39</sup> and re-contrasted using histogram stretching for visualization. Final 3D images were  $5x5x2.08\text{mm}$  (in air), collected into  $1000x500x1024$  pixels ( $x, y, z$ ). Quantification was performed according to Equation 4.2

$$d_{z,object} = n_{pixels,z\ object} \cdot \frac{h_{image,air}}{n_{pixels,z\ image}} \cdot N \quad (4.2)$$

where  $d_{z,object}$  is the distance,  $n_{pixels,object}$  is the number of pixels comprising the object in the  $z$  direction,  $h_{image,air}$  is the total length of the image in air,  $n_{pixels,z\ image}$  is the total number of pixels along the  $z$  axis of the collected image, and  $N$  is the refractive index of the measured object. The distance between the patch backing and the surface of the skin was then subtracted from the total microneedle length to obtain depth of penetration.

Samples doped with GNRs ( $84x22\text{nm}$ ), fabricated as previously described,<sup>40</sup> were used as a contrast agent to compare with images of needles containing no GNRs. Since the plasmon resonance of these rods was  $800\text{nm}$ , the rods were strongly scattering in the HV output of the PS-SD-OCT system, allowing for clear visualization of the needle. This allowed for validation of the markers used in measuring needle penetration depths in samples not containing GNRs.

## REFERENCES

- (1) Romgens, A. M.; Bader, D. L.; Boustra, J. A.; Baaijens, F. P. T.; Oomens, C. W. J. *J Mech Behav Biomed Mater.* **2014**, *40*, 397-405.
- (2) Birchall, J. C.; Clemo, R.; Anstey, A.; John, D. N. *Pharm Res.* **2011**, *28*, 95-106.
- (3) Donnelly, R. F.; Garland, M. J.; Morrow, D. I.; Migalska, K.; Singh, T. R.; Majithiya, R.; Woolfson, A. D. *J Control Release.* **2010**, *147*, 333-341.
- (4) Badran, M. M.; Kuntsche, J.; Fahr, A. *Eur J Pharm Sci.* **2009**, *36*, 511-523.
- (5) Verbaan, F. J.; Bal, S. M.; van den Berg, D. J.; Dijksman, J.A.; van Kecke, M.; Verpoorten, H.; van den Berg, A.; Lutge, R.; Bouwstra, J. A. *J Control Release.* **2008**, *128*, 80-88.
- (6) Yan, G.; Warner, K. S.; Zhang, J.; Sharma, S.; Gale, B. K. *Int J Pharm.* **2010**, *391*, 7-12.
- (7) Chu, L. Y.; Choi, S.; Prausnitz, M. R. *J Pharm Sci.* **2010**, *99*, 4228-4238.
- (8) Chua, B.; Desai, S.; Tierney, M. J.; Tamada, J. A.; Jina, A. N. *Sens Act A Phys.* **2013**, *373-381*.
- (9) Park, J. H.; Allen, M. G.; Prausnitz, M. R. *J Control Release.* **2005**, *104*, 51-66.
- (10) Park, J. H.; Prausnitz, M. R. *J Korean Phys Soc.* **2010**, *56*, 1223-1227.
- (11) Ji, J.; Tay, F. E. H.; Miao, J.; Iliescu, C. *J Micromech Microeng.* **2006**, *16*, 958.
- (12) Davis, S. P.; Landis, B. J.; Adams, Z. H.; Allen, M. G.; Prausnitz, M. R. *J Biomech.* **2004**, *37*, 1155-1163.
- (13) Lee, J. W.; Park, J. H.; Prausnitz, M. R. *Biomaterials.* **2008**, *29*, 2113-2124.
- (14) O'Mahony, C. *Biomed Microdevices.* **2014**, *16*, 333-334.
- (15) Khanna, P.; Luongo, K.; Strom, J. A.; Bhansali, S. *Microsyst Technol.* **2010**, *16*, 973-978.
- (16) Godin, B.; Touitou, E. *Adv. Drug Deliv. Rev.* **2007**, *59*, 1152-1161.
- (17) Bartsova, L.; Bajgar, J. *Curr. Med. Chem.* **2012**, *19*, 4671-4677.
- (18) Kim, H. M.; Lim, Y. Y.; An, J. Kim, M. N.; Kim, B. J. *Int. J. Dermatol.* **2012**, *51*, 859-863.

- (19) Groves, R. *Quantifying the mechanical properties of skin in vivo and ex vivo to optimize microneedle device design*; ProQuest Dissertations Publishing. 2012.
- (20) Qvist, M. H.; Hoek, U.; Kreilgaard, B.; Madsen, F.; Frokjaer, S. *Eur J Pharm Sci.* **2000**, *11*, 59-68.
- (21) Larraneta, E.; Moore, J.; Vicente-Perez, E. M.; Gonzalez-Vazquez, P.; Lutton, R.; Woolfson, D. A.; Donnelly, R. F. *Int J Pharm.* **2014**, *472*, 65-73.
- (22) Park, J. H.; Choi, S. O.; Seo, S.; Choy, Y. B.; Prausnitz, M. R. *Eur J Pharm Biopharm.* **2010**, *76*, 282-289.
- (23) Stutz, H.; Illers, K. H.; Mertes, J. *J Polym Sci B Polymer Phys.* **1990**, *28*, 1483-1498.
- (24) Iza, M.; Stoianovici, G.; Viora, L.; Grossiord, J. L.; Couarraze, G. *J Control Release.* **1998**, *52*, 41-51.
- (25) Wong, R. S.; Ashton, M.; Dodou, K. *Pharmaceutics.* **2015**, *7*, 305-319.
- (26) Scott, R. A.; Peppas, N. A. *Biomaterials.* **1999**, *20*, 1371-1380.
- (27) Ortega, A. M.; Kasprzak, S. E.; Yakacki, C. M.; Diani, J.; Greenburg, A. R.; Gall, K. *J Appl Polym Sci.* **2008**, *110*, 1559-1572.
- (28) Olatunji, O.; Das, D. B.; Garland, M. J.; Belaid, L.; Donnelly, R. F. *J Pharm Sci.* **2013**, *102*, 1209-1021.
- (29) Enfield, J.; O'Connell, M. L.; Lawlor, K.; Jonathan, E.; O'Mahony, C.; Leahy, M. *J Biomed Opt.* **2010**, *15*, 046001.
- (30) Rattanapak, T.; Birchall, J.; Young, K.; Ishij, M.; Meglinski, I.; Rades, T.; Hook, S. *J Control Release.* **2013**, *172*, 894-903.
- (31) Huang, D.; Swanson, E. A.; Lin, C. P.; Schuman, J. S.; Stinson, W. G.; Chang, W.; Hee, M. R.; Flotte, T.; Gregory, K.; Puljafito, C. A.; Fujimoto, J. G. *Science.* **1991**, *254*, 1178-1181.
- (32) Mahvash, M.; Dupont, P. *IEEE Trans Biomed Eng.* **2010**, *57*, 934-943.
- (33) Okamura, A. M., Simone, C., O'Leary, M. D. *IEEE Transactions on Biomedical Engineering.* **2004**, *10*, 1707-1716.
- (34) Azar, T.; Hayward, V. *Estimation of the Fracture Toughness of Soft Tissue from Needle Insertion*. Springer, 2008.

- (35) Bader, D. L.; Bowker, P. *Biomaterials*. **1983**, *4*, 305-308.
- (36) Tumbleston, J. R.; Ermoshkin, A.; Shirvanyants, D.; Ermoshkin, N.; Januszewicz, R.; Johnson, A. R.; Kelly, D.; Chen, K.; Pinschmidt, R.; Rolland, J. P.; Samulski, E. T.; DeSimone, J. M. *Science*. **2015**, *347*, 1349-1352.
- (37) Oldenburg, A. L.; Chhetri, R. K.; Cooper, J. M.; Wu, W. C.; Troester, M. A.; Tracy, J. B. *Opt Lett*. **2013**, *38*, 2923-2926.
- (38) Chhetri, R. K.; Kozek, K. A.; Johnston-Peck, A. C.; Tracy, J. B.; Oldenburg, A. L. *Phys Rev E*. **2011**, *83*, 040903.
- (39) Oldenburg, A. L., Chhetri, R. K. *Proceedings of SPIE*. **2011**, 7889, 78891V-78891V-6.
- (40) Kozek, K. A.; Kozek, W. C., Wu, C.; Mishra, S. R.; Tracy, J. B. *Chem Mater*. **2013**, *25*, 4537-4544.

## CHAPTER 5 CONCLUSIONS AND FUTURE DIRECTIONS

### 5.1 Continuous Liquid Interface Production on the Micron Scale

The work presented herein is the first report of Continuous Liquid Interface Production of parts measuring less than 1mm in height. CLIP enables fabrication of micron-scale features that cannot be generated using traditional silicon and/or micromolding based processes, such as the undercut arrowhead microneedles presented in this dissertation. While not demonstrated here, the fabrication of even more complex structures, such as hollow or porous features, is also feasible using this technique. In addition, CLIP enables easy “plug-and-play” of material composition on the micron-scale, as demonstrated by the nine different microneedle compositions used in this dissertation. Such simultaneous control over shape and material properties is unprecedented in micro-manufacturing.

Most traditional micro-manufacturing techniques require extensive expertise. Years of training are typically required to gain a working understanding of the benefits, process optimization, and limitations of various micro-manufacturing techniques (photolithography, wet and dry etching, machine milling, chemical vapor deposition, etc.). The expense of required equipment can be cost-prohibitive, especially in academic environments. Therefore, equipment is therefore usually located in centralized facilities, limiting access to this important technology. The CLIP process presented here, on the other hand, is undergoing development to become a push-button technique that produces desired structures on demand with little to no training. While traditional etching based techniques are accomplished at 60-300 $\mu\text{m/hr}$  in the z direction,<sup>1</sup>

the structures produced here are fabricated at rates of up to 100mm/hr. Therefore, prototyping micron-scale structures using CLIP is approximately 400-1600X faster per part than traditional micromanufacturing techniques, in addition to the dramatically reduced lead times. Therefore, with advantages in control over geometry, material flexibility, and speed, CLIP is poised to challenge existing microfabrication techniques and enable rapid production of micron-scale features for a number of different industries. Such capacity provides access to far-reaching and previously unimaginable opportunities in research and in product development.

Many of the fundamental studies presented here lay a critical foundation for the future of small-scale production of parts via Continuous Liquid Interface Production. Particularly, we establish the dominant role that light distributions play in the fabrication of small parts through the following observations:

- The optical system used to focus light on the window plays a dominant role in part quality on the small scale
- Light intensity affects part dimensions as much as the dimensions of the input CAD file
- A proposed model based on assuming each pixel's light projection can be represented as a Gaussian light distribution qualitatively predicts the shape of the cure of a single frame

In addition to establishing the importance of light intensity distributions, we also demonstrated that a technique called antialiasing is necessary to produce smooth parts on a small scale. The introduction of grayscale smooths the sharp transitions between individual pixel projections from the DLP chip. Here, antialiasing is utilized to smooth stair-stepping on the 10 $\mu$ m size scale, but printers with larger pixel sizes are likely to produce surface stair-stepping at size scales that are equivalent to their projected pixel size. For example, a CLIP system with a

100 $\mu\text{m}$  pixel size would produce parts with 100  $\mu\text{m}$  wide stair-stepping along the surface, rather than the 10  $\mu\text{m}$  wide stair steps seen here (for a printer with a  $\sim 10\mu\text{m}$  projected pixel). Therefore, antialiasing is also an important consideration for production of both macroscopic and microscopic objects.

The ability to continue to produce smaller and smaller objects via Continuous Liquid Interface Production will rely on further improvements in system optics. The dominant role of the light distribution (as opposed to the CAD file) suggests a need to expand the use of modeling to identify build parameters capable of producing dimensionally accurate parts in order to improve efficiency, accessibility and ease of use of this technology for production on the small scale. Although the model proposed here has been utilized to qualitatively predict the geometry resulting from exposure to a single frame, further model development may enable the exact dimensions of micron-scale three dimensional CLIP parts to be accurately predicted.

## **5.2 Continuous Liquid Interface Production of Materials for Release of Therapeutics**

The work presented herein also represents the first use of CLIP for biological applications, and, in particular, the first attempt at generating biocompatible materials for drug release using CLIP. CLIP microneedles were fabricated from resins containing acrylic acid, methacrylate functionalized polyethylene glycols (PEGs), and methacrylate functionalized polycaprolactone (PCL) mixed with the photoinitiator diphenyl(2,4,6-trimethyl-benzoyl-) phosphine oxide (TPO). Upon photopolymerization, these resins react to form water soluble polyacrylic acid (PAA) microneedles, swellable PEG hydrogel microneedles, and a hydrolytically degradable PCL based microneedle. The ability to rapidly adjust microneedle composition using CLIP demonstrates that it is a “plug-and-play” approach to producing microneedles with differing mechanisms of drug release. The fluorescent drug surrogate

rhodamine was homogeneously incorporated into all patches. Release rates of rhodamine from microneedle patches were found to vary from complete release within 15 minutes (for dissolvable polyacrylic acid microneedles) to less than 1% release over one week (for PCL microneedles) in aqueous solution. Therefore, the release rate of an encapsulated therapeutic from a CLIP microneedle can be tailored to specific applications through careful selection of the microneedle matrix. The wide range of matrix solubilities utilized here, from a very hydrophilic PAA to hydrophobic PCL suggests that therapeutics of a range of different solubilities could be encapsulated into CLIP microneedles.

Although the microneedles fabricated in this dissertation are strong proof of concept that CLIP can be used to directly manufacture microneedle arrays, further effort is necessary to identify an appropriate matrix for translational applications. All three microneedle compositions (PEG550dMa, PCL, PAA) effectively pierced murine skin, but both the PEG550dMa and PCL microneedles failed to penetrate porcine skin. Because human skin is more similar to porcine skin than murine skin, we anticipate that the PEG550dMa and PCL microneedles would also fail to puncture human skin. For this reason, PEG550dMa and PCL microneedles are not recommended for ongoing investigations. Other polyesters, such as PLA or PLGA may be more ideal, due to their improved mechanical properties and faster release rates. More densely crosslinked PEG microneedles did enable penetration of porcine skin (Chapter 5), but these highly crosslinked PEG microneedles reduced rhodamine release rates in solution to fractions of a percent over one week (data not shown). Complete drug release from such highly crosslinked materials would likely occur over the course of years; such slow release rates are not ideal for the vast majority of applications. For this reason, even highly crosslinked PEG microneedles are not suitable materials for translational applications.

The PAA microneedles exhibited a clinically relevant release profile, completely releasing cargo through dissolution within 15 minutes. The dissolvable nature of this matrix would make it easy to apply and would not require the patient to wear the patch over an extended period of time. Furthermore, a dissolving microneedle would eliminate sharp, biohazardous waste during patch application and potentially reduce disease transmission caused by needle reuse. Unfortunately, PAA microneedles were cytotoxic to both A549 human non-small cell lung cancer cells and human umbilical vein cells (HuVECs) in cell culture, which suggests that they may produce undesirable side effects *in vivo*. Therefore, the development of strong, quick releasing, and biocompatible materials is important to the advancement of CLIP microneedle technology, as discussed in the following sections.

### **5.3 Development of Biocompatible CLIP Matrices**

#### **5.3.1 Biocompatibility of (Meth)acrylate Based Chemistry**

All materials used for CLIP must be photopolymerizable. Photopolymerization has been previously used for biomedical applications due to its inherent benefits, including rapid cure rates, low temperature operation, the ability to spatially and temporally control polymerization and the potential to perform polymerization *in vivo*.<sup>2</sup> Clinically, photopolymerization is common in dental restoration.<sup>3-4</sup> Photoreactive monomers are also used in acrylic bone cements during orthopedic surgery, although they are typically reacted via thermal or redox initiation mechanisms.<sup>5-7</sup> Contact lenses are also fabricated by photopolymerization.<sup>8</sup> Such applications utilize dimethacrylate based resins, which are typically composed of a combination of photoreactive oligomers, pre-reacted polymers, and filler materials designed to improve mechanical properties and reduce shrinkage. The structures of some commonly used oligomers are given in Figure 6.1. These include 2,2-bis[4-(2-hydroxy-3-

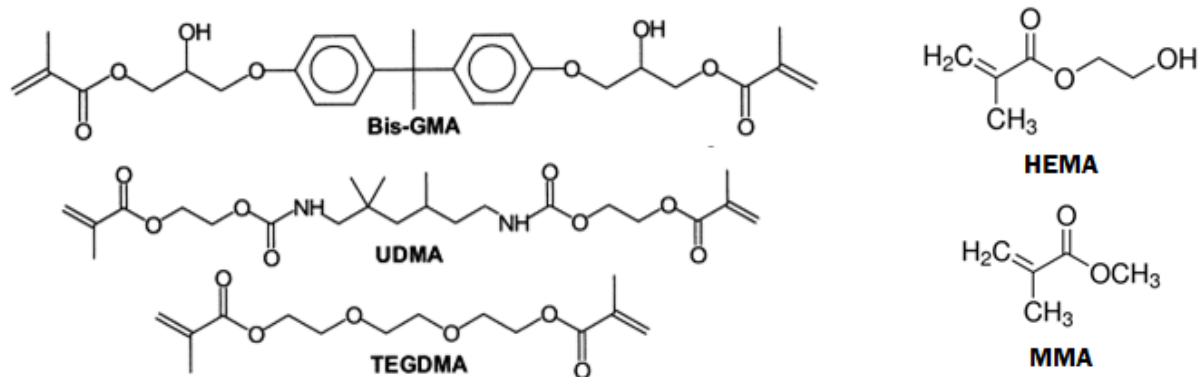


**Figure 5.1** Methacrylate monomers and oligomers used commercially methacryloyloxypropyl)phenyl]propane (Bis-GMA), 1,6-bis-[2-methacryloyloxyethoxycarbonylamino]-2,4,4-trimethyl hexane (UDMA), and triethyleneglycol dimethacrylate (TEGDMA), hydroxyethyl methacrylate (HEMA) and methyl methacrylate (MMA).<sup>4,7</sup> **Together, these clinical applications demonstrate that dimethacrylate based photopolymerization is safe for use in clinical settings.** Accordingly, our highly crosslinked PEG and PCL microneedles (which were produced with dimethacrylate based resins) had no adverse effects on cells over 72 hours.

Nevertheless, residual, unreacted (meth)acrylates are known to induce toxicity.<sup>7,9-10</sup> This toxicity is generally attributed to the reactivity of the acrylate double bond toward Michael Addition reactions with amino- or thiol-groups of proteins or DNA.<sup>11</sup> Meth(acrylates) are also known skin irritants, possibly due to the effects of acrylic or methacrylic acids formed by ester hydrolysis of these compounds.<sup>7</sup> In some cases, unreacted meth(acrylates) have also been found to be carcinogenic.<sup>7</sup> **Importantly, (meth)acrylate based materials used in clinical applications are designed to limit exposure to unreacted (meth)acrylate through high extents of reaction conversion and high crosslink density to ensure device safety..**

Further characterization of unreacted (meth) acrylate within CLIP microneedle devices is essential to future development. Although current clinical applications of photochemistry limit free (meth)acrylate toxicity through high bond conversion, immobilization of remaining free (meth)acrylates through dense crosslinking is also essential to their biocompatibility.<sup>12</sup> Therefore, the development of biocompatible CLIP materials that enable rapid drug release, but limit release of unreacted oligomer may be challenging. **Elimination of any and all unreacted (meth)acrylate from the final product is essential to the future development of CLIP microneedles.** This could be accomplished by 1) further optimization of resin formulations and fabrication conditions to complete reaction conversion and 2) utilizing higher molecular weight oligomers to reduce the concentration of reactive endgroups. It is important to note that high molecular weight oligomers typically increase viscosity, which can result in a decrease in reaction conversion.<sup>3</sup> Balancing these tradeoffs will be important in future studies. Previous work with high molecular weight, low viscosity branched polymers could be of interest.<sup>13</sup> The high functionality of these materials also tether most of the unreacted groups into the matrix, which should reduce leachable (meth)acrylate concentrations. The effect of pendant unreacted groups on biocompatibility would need to be evaluated.

Alternatively, additional post-fabrication steps could be used to purify unreacted materials out of the needle. Washing the part or applying heat or vacuum to remove residual monomer/oligomer could be feasible approaches to producing a biocompatible device. Although PAA microneedles were demonstrated to be cytotoxic in this dissertation, we still believe that this may be a promising material for further consideration. Additional optimization of the reaction conditions and purification steps may reduce the toxicity of PAA microneedle devices.

Importantly, such post-fabrication purification steps have a risk of accidentally removing or damaging the therapeutic of interest during processing. Therefore, incorporating therapeutics into microneedles after fabrication and purification may be of interest. Coating the microneedle with the therapeutic or chemically conjugating the therapeutic to the matrix after fabrication may be viable approaches to producing toxin-free microneedle devices with active therapeutics.

### **5.3.2 Alternatives to Meth(acrylate) Based Chemistry**

Some alternative radical photopolymerization chemistries have been developed to circumvent toxicity issues associated with (meth)acrylates. One common example is thiol-ene chemistry, which has been extensively investigated by Anseth, Bowman, and Hoyle.<sup>14</sup> Unlike methacrylate mediated radical photopolymerization, thiol-ene reactions take place via a step-growth mechanism, which reduces radical lifetimes.<sup>14-15</sup> This reaction mechanism has been utilized to encapsulate bioactive cargos, such as cells, proteins, and enzymes with little loss of activity.<sup>15</sup> Unfortunately, because this reaction is not susceptible to oxygen-induced inhibition<sup>14</sup> it is incompatible with CLIP.

An interesting alternative chemistry, which may be suitable for use with CLIP, is radical photopolymerization with vinyl esters.<sup>16-17</sup> The decrease in reactivity of the vinyl ester, as compared to the acrylate, decreases cytotoxicity by one to two orders of magnitude<sup>17</sup>. Vinyl esters have typically been associated with slower reaction rates, so polymerization kinetics would need to be carefully considered.<sup>16</sup>

### **5.3.3 Role of Photoinitiators**

Although the role of photoinitiator cytotoxicity is understudied throughout this work, the role of the photoinitiator in the biocompatibility of the final part is an important consideration. Several studies have been performed to assess the role of photoinitiators on cytotoxicity for

applications in cell encapsulation within photopolymerizable scaffolds.<sup>18-20</sup> For these applications, many photoinitiators have been associated with increases in the concentration of intracellular reactive oxygen species, which induce cell death.<sup>18</sup> Some photoinitiators, such as Irgacure 2959 and camphorquinone (CQ), have been shown to have minimal cytotoxicity in these applications.<sup>18</sup>

The use of photo initiators for the production of CLIP microneedles differs from such applications because no active radicals are placed in direct contact with cell populations during fabrication. In fact, the initiators react with monomers/oligomers to start the polymer chain, and are therefore chemically conjugated to the matrix. For this reason, the toxicity of leachable, unreacted photoinitiator is more relevant to CLIP microneedles than the toxicity of free radicals generated during initiation. Although photoinitiators are somewhat toxic in cell culture, the toxicity of native photoinitiator is much less than that of active free radicals.<sup>18</sup> High molecular weight initiators may be less likely to be released from the matrix.<sup>21-22</sup> The investigation of self-initiating monomers and/or initiation by natural products<sup>24</sup> may also be of interest, but may require different wavelengths of light for effective initiation.

#### **5.3.4 Characterization of Products and Degradation Products**

Further characterization of the nature of CLIP products is necessary. For PAA microneedles, characterization of the molecular weight distribution of the formed PAA will be essential to verify that dissolution products are of a molecular weight that is safe for clinical use. Similarly, further characterization of the degradation products of crosslinked CLIP materials will be necessary. Determining the molecular weight of the non-degradable alkyl backbone during photopolymerization and verifying its clearance from the body are critical to ensuring device safety.

## **5.4 Incorporation of Therapeutic Cargo**

As described in Chapter 1, microneedles have been used to deliver a wide variety of therapeutic agents, including small molecules, proteins, nucleic acids, and nanoparticles. Applications include delivery of vaccines, insulin, NSAIDs, chemotherapy and hormone delivery, among others. Microneedles are most useful, however, for the delivery of therapeutics which are not effectively delivered orally, such as proteins, nucleic acids, and large or hydrophobic compounds. Acrylate reactivity with proteins and nucleic acids may prevent these compounds from being encapsulated without damage.<sup>15</sup> A number of protein protection techniques have been investigated to ameliorate these issues.<sup>26</sup> Some of these protein protection techniques may be of interest, but the vast majority do not completely recover protein activity. Ultimately, encapsulating the therapeutic after microneedle fabrication via coating or chemical conjugation may be a better approach to maintaining the activity of biotherapeutics. CLIP microneedle technology is strongly suited for the delivery of large and/or hydrophobic small molecules, nanoparticles and microparticles, which are less susceptible to damage than biologic drugs.

## **5.5 Microneedle Mechanics**

The ability to use CLIP to rapidly alter microneedle composition was harnessed to investigate how a microneedle's composition affects its ability to insert into the skin. Polyethylene glycol (PEG) based microneedles with varying crosslinking density were fabricated. Young's modulus and stress at fracture increased from approximately 80MPa to approximately 1600MPa with increasing crosslink density, whereas strain at break decreased with increasing crosslink density. The ability of microneedles to insert into the skin was found to depend on both the application force and the properties of the material used for device

manufacture. None of the tested compositions were found to fracture during insertion, suggesting that microneedle stiffness plays a more important role in skin penetration than fracture strength for these materials. A minimum Young's modulus of approximately 1100 MPa is recommended for insertion of the tested microneedle array with reasonable application forces. This stiffness requirement is likely to vary with microneedle design parameters, such as shape, tip radius and the number of needles per array. The CLIP microneedle platform is ideal for investigating how such design parameters affect insertion.

A pilot study demonstrated that depth of penetration was independent of both applied force and composition. Theoretical considerations cast doubt on this experiment. Additional experiments with undercut (arrowhead) CLIP microneedles could be performed to determine whether the elasticity of the skin pushes microneedles back out, masking differences in penetration depth.

All evaluation was performed using porcine skin *ex vivo*. Further investigation with human subjects is necessary to evaluate how well *ex vivo* results correlate to clinical studies and to account for potential differences in the mechanical properties of human and porcine skin.

## **5.6 CLIP Microneedles for the Advancement of Transdermal Drug Delivery**

This work demonstrates that Continuous Liquid Interface Production is a powerful tool for advancing microneedle technology. The unparalleled, rapid control over microneedle geometry achievable by this technique provides a unique opportunity to answer previously inaccessible research questions related to the role of microneedle geometry in therapeutic efficacy. Proof of concept for one step fabrication of CLIP microneedles containing a therapeutic agent is demonstrated, where the fluorescent drug surrogate rhodamine is encapsulated into the

microneedle through mixing with a photopolymerizable matrix used for needle fabrication. Further investigation of this one step fabrication approach may enable direct fabrication of biocompatible, commercial microneedle products. Alternatively, CLIP could easily be utilized as an approach to fabricating microneedle master templates, which could be utilized for subsequent micromolding. Such an approach would enable the improved geometrical control of CLIP to be combined with the proven biocompatibility of established micromolding processes previously utilized for microneedle fabrication.

## REFERENCES

- (1) Jansen, H. V.; de Boer, M. J.; Legtenberg, R.; Elswenspoek, M. *J Micromech Microeng.* **1995**, *5*, 115-120.
- (2) Elisseef, J.; Anseth, K.; Sims, D.; McIntosh, W.; Randolph, M.; Langer, R. *Proc Natl Acad Sci USA.* **1999**, *96*, 3104-3107.
- (3) Cramer, N. B.; Stansbury, J. W.; Bowman, C. N. *Crit Rev Oral Biol Med.* **2011**, *90*, 402-416.
- (4) Moszner, N.; Salz, U. *Prog Polym Sci.* **2001**, *26*, 535-576.
- (5) Lewis, G. *J Biomed Mater Res B Appl Biomater.* **2007**, 301-319.
- (6) Magnan, B.; Bondi, M.; Maluta, T.; Smaila, E.; Schirru, L.; Dall'Oca, C. *Musculoskelet Surg.* **2013**, 93-100.
- (7) Leggat, P. A., Smith, D. R.; Kedjarune, U. *Arch Environ Occup Health.* **2009**, *64*, 207-212.
- (8) Nicolson, P. C.; Vogt, J. *Biomaterials.* **2001**, *22*, 3273-3283.
- (9) Qreim, H.; Ahlers, A. J.; Bias, R.; Broecker, B.; Hollander, H.; Gelbke, H.; Jacob, S. H.; Klimisch, H. J.; Manglesdorf, A. I.; Mayr, W.; Schong, N.; Stropp, G.; Stahnecker, P.; Vogel, E.; Weber, C.; Ziegler-Skylakakis, K.; Bayer, E. *Chemosphere.* **1995**, *31*, 2637-2659.
- (10) Yoshii, E. *J Biomed Mater Res.* **1997**, *4*, 517-524.
- (11) Husar, B.; Heller, C.; Schwentenwein, M.; Mautner, A.; Varga, F.; Koch, T.; Stampfl, J.; Liska, R. *J. Polym. Sci. Part A: Polym Chem.* **2009**, *49*, 4927-4934.
- (12) Spahl, W.; Budzikiewicz, H.; Geurtsen, W. *J Dent.* **1998**, *26*, 137-145.
- (13) Wan, Q.; Rumpf, D.; Schrickler, S. R.; Mariotti, A.; Culbertson, B. M. *Biomacromolecules.* **2001**, *2*, 217-222.
- (14) Hoyle, C. E.; Bowman, C. N. *Angew Chem Int Ed.* **2010**, *49*, 1540-1573.
- (15) McCall, J. D.; Anseth, K. S. *Biomacromolecules.* **2012**, *13*, 2410-2417.
- (16) Mautner, A.; Qin, X.; Wutzel, H.; Ligon, S. C.; Kapeller, B.; Moser, D.; Russmueller, G.; Stampfl, J.; Liska, R. *J Poly Sci Part A: Polym Chem.* **2012**, *51*, 203-212.

- (17) Husar, B.; Heller, C.; Schwentenwein, M.; Mautner, A.; Varga, F.; Koch, T.; Stampfl, J.; Liska, R. *J Poly Sci Part A Polym Chem.* **2011**, *49*, 4927-4934.
- (18) Bryant, S. J.; Nuttelman, C. R.; Anseth, K. S. *J Biomater Sci Polymer Edn.* **2000**, *1*, 439-457.
- (19) Williams, C. G.; Malik, A. N.; Kim, T. K.; Manson, P. N.; Elisseeff, J. H. *Biomaterials.* **2005**, *26*, 1211-1218.
- (20) Hanks, C. T.; Strawn, S. E.; Wataha, J. C.; Craig, R. G. *J Dent Res.* **1991**, *70*, 1450.
- (21) Aparico, J. L. *Packaging Tech Sci.* **2015**, *28*, 181-203.
- (22) Allen, N. S. *J Photochem Photobiol A Chem.* **1996**, *100*, 101-107.
- (23) Jonsson, E. S.; Lee, T. Y.; Viswanathan, K.; Hoyle, C. E.; Roper, T. M.; Guymon, C. A.; Nason, C.; Khudvakov, I. V. *Prog Organic Coatings.* **2003**, *52*, 63-72.
- (24) Bertolotti, S. G.; Previtali, C. M.; Rufs, A. M. *Macromolecules.* **1999**, *32*, 2920-2924.
- (25) Jonsson, E. S.; Lee, T. Y.; Viswanathan, K.; Hoyle, C. E.; Roper, T. M.; Guymon, C.A.; Nason, C.; Khudyakov, I. V. *Prog Organic Coatings.* **2005**, *52*, 63-72.
- (26) Lin, C. C.; Sawicki, S. M.; Metters, A. T. *Biomacromolecules.* **2008**, *9*, 75-83.

## APPENDIX A CONTINUOUS LUA SCRIPT

```
model= "C:\\Users\\eipi\\desktop\\Microneedles\\1000_AR3.svg"
- Provides .SVG file of the part to be generated
speed=25
--Defines build speed in z direction in mm/hr, which affects rate of upward movement of
the build elevator and the rate at which the frames are displayed
fill=82
--Light intensity value between 0( black) and 255 (white)
n_begin=1
--Sets the first slice to be projected
n_end=loadslices(model)
■ Loads the model's slices and sets the last slice to be projected
z_begin=0.025
-- Sets the height of the build elevator (in mm) when the first slice projects

for n=1,n_end, 1 do
fillmask(fill,n-1)
end
--Sets the light intensity of every slice
moveto(2, 20000)
moveto(0.15, 1000)
moveto(z_begin,200)
-- Lowers the build elevator before the print begins
showframe(-1)
relay(true)
-- Turns the light source on
for n= n_begin, n_end-1, 1 do
z= sliceheight(n)+ z_begin
showframe(n-1)
moveto(z, speed)
print(string.format("Layer: %d / %d. Height: %.3f mm.\n", n, n_end, z))
end
--moves the build elevator up as each slice projects
relay(false)
--turns the light off
moveto(70, 20000)
-- Moves the build elevator back to the start position
```

## APPENDIX B MODELING OF SMALL SCALE CLIP PARTS

Throughout Chapters 2 and 3, we showed that small objects tend to truncate in the z direction relative to the input CAD file, whereas the dimensions of large CLIP parts are accurate to the CAD file (Table 2.2, Figure 3.6). **Here, we hypothesize that differences in the production of large and small parts are due to differences in the amount of light projected per unit area for small and large objects.**

In order to test this hypothesis, we calculated cure depth as a function of feature size after resin was exposed to a single frame of light. The cure depth equation (also called the “working curve”) derived in Chapter 3

$$C_T = \frac{1}{\alpha} \ln\left(\frac{E}{E_c}\right)$$

is a function of the resin specific coefficients  $E_c$ , which is the critical light exposure (in  $\text{mJ}/\text{cm}^2$ ) required to induce cure of the resin and  $\alpha$ , which is the absorption coefficient of the resin as well as light exposure. **Therefore, if cure depth decreases as a function of feature size, this also suggests that the light exposure decreases with feature size because exposure is the only independent variable in the equation.** Light intensity was not directly measured due to the difficulty of performing light intensity measurements with micron-scale spatial resolution.

The experimental setup is given in Figure B.1. A drop of trimethylolpropane triacrylate (TMPTA) mixed with 2.5 wt% diphenyl (2,4,6-trimethylbenzoyl) phosphine oxide (TPO) initiator was placed on top of a glass coverslip sitting on the CLIP7 printer window. The resin was exposed to a single frame of light made up of a series of squares ranging in size from  $40 \times 40$  pixels ( $392.1 \mu\text{m} \times 392.1 \mu\text{m}$ ) to  $1 \times 1$  pixel ( $9.803 \mu\text{m} \times 9.803 \mu\text{m}$ ). Illumination was performed

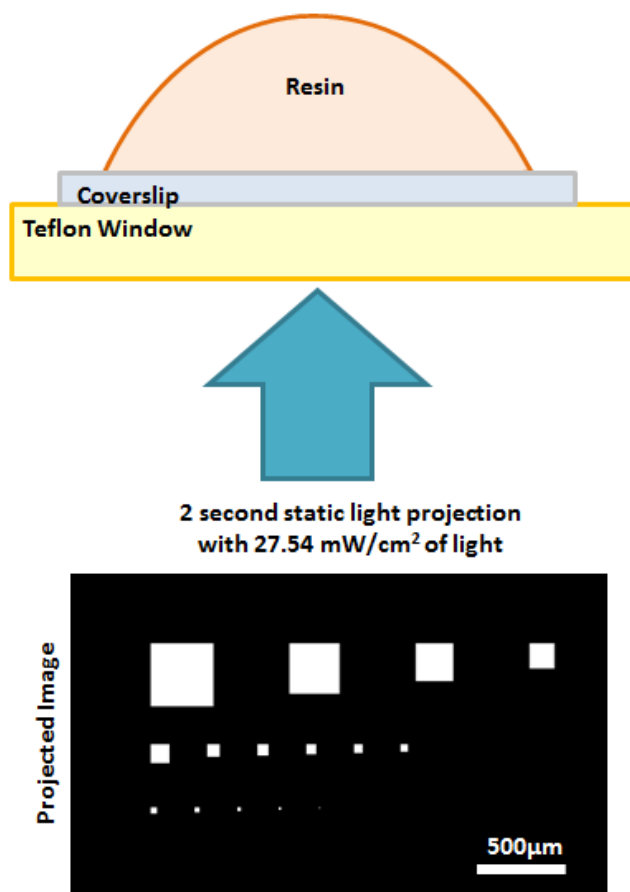
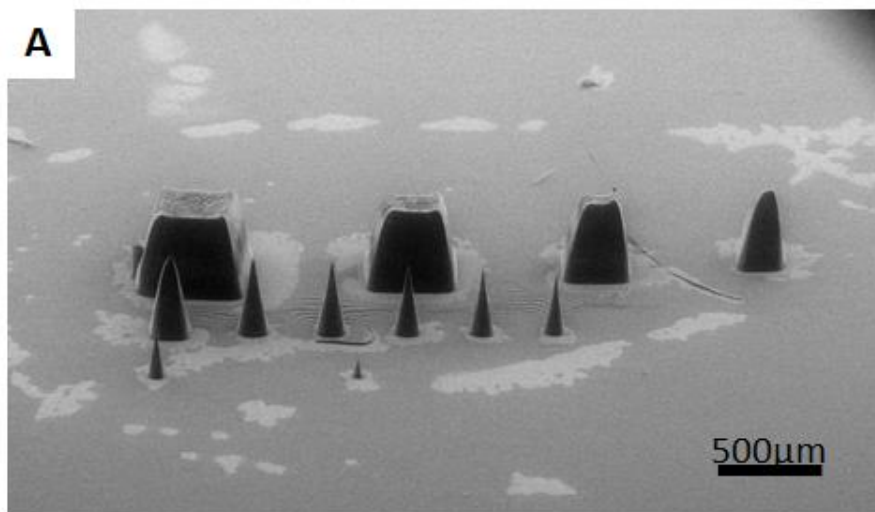


**Figure B.1 Experimental setup for testing cure depth as a function of feature size**

with Windows GDI+ to eliminate any affect that grayscale may have on cure dosage. Residual unreacted resin was then washed off of the coverslip with acetone and the cover slip was left to air dry over the course of one hour. An image of the cured objects on the glass slide and their measured heights are given in Figure B.2. A few important observations were made. First, as the width of the feature decreases, the cure depth also decreases. **This observation supports the hypothesis that exposure decreases with feature size.** Second, the shape of the cured object changes as the feature size becomes smaller. The larger square projections, such as the 40x40 pixel square to the back left of Figure B.1, produce cured objects that are approximately square (back left of Figure B.2A). The smaller cured objects, such as the object resulting from the projection of a 2x2 pixel square at the front right of Figure B.2A are more conical in shape.



**B**

Number of Pixels	Projected Feature Size	Height
40x40	392.1 $\mu$ m x 392.1 $\mu$ m	295 $\mu$ m
30x30	294.0 $\mu$ m x 294.0 $\mu$ m	285 $\mu$ m
15x15	147.0 $\mu$ m x 147.0 $\mu$ m	291 $\mu$ m
10x10	98.0 $\mu$ m x 98.0 $\mu$ m	272 $\mu$ m
8x8	78.4 $\mu$ m x 78.4 $\mu$ m	260 $\mu$ m
6x6	58.8 $\mu$ m x 58.8 $\mu$ m	238 $\mu$ m
4x4	39.2 $\mu$ m x 39.2 $\mu$ m	163 $\mu$ m
3x3	29.4 $\mu$ m x 29.4 $\mu$ m	109 $\mu$ m
2x2	19.6 $\mu$ m x 19.6 $\mu$ m	44 $\mu$ m

**Figure B.2 Cure depth as a function of feature size.** A) Cured objects resulting from experiment described in Figure B.1 B) The heights of each cured object.

Therefore, this experiment suggests that both the shape and the intensity of the light distribution change with decreasing feature size. Note that some of the cured objects were accidentally removed from the coverslip during washing. Therefore, absent features are not indicative of lack of curing for this experiment.

### B.1 Pixel Blending

Similar effects have been observed and are well documented for other DLP based light projection systems in literature and are known to be caused by blending of light distributions from neighboring pixels.<sup>1-3</sup> Ideally, the light coming of each square micromirror (“pixel”) would

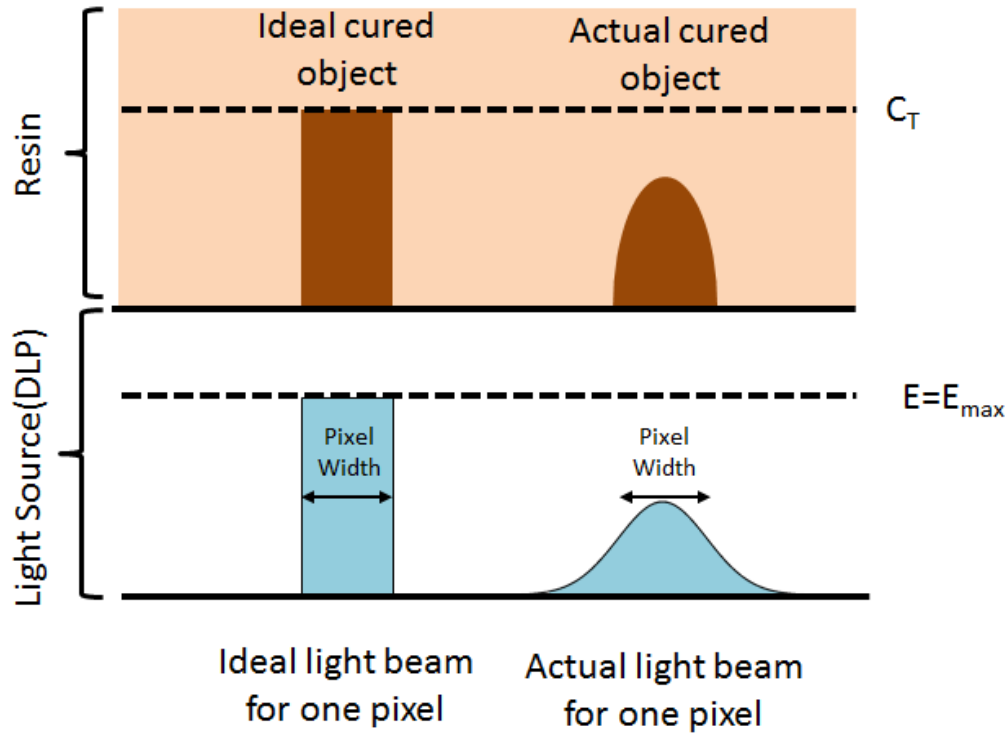


**Figure B.3 Ideal versus actual light distributions and their resulting cured objects.** Figure adapted from 3.

be a perfect step function, where the maximum exposure (which is the exposure specified by the user) would be projected inside the pixel, and no light would be projected outside that pixel.

However, in actuality, this light actually exists as a distribution inside and outside of the pixel due to a number of factors, including diffraction, imperfect focus, and aberrations, which were thoroughly discussed in the introduction to Chapter 2 (Figure B.3).<sup>3</sup> The overlap between

neighboring pixels, which is sometimes referred to as “pixel blending”, is subject to superposition. Therefore, the projected light intensity per unit area increases as the number of neighboring pixels increases for small feature sizes (Figure B.4). When the number of neighboring pixels increases (e.g. as pixel size increases), the shape of each individual light distribution also becomes less apparent because the light distributions add together to create a light distribution that more closely resembles the idealized step function (Figure B.4).

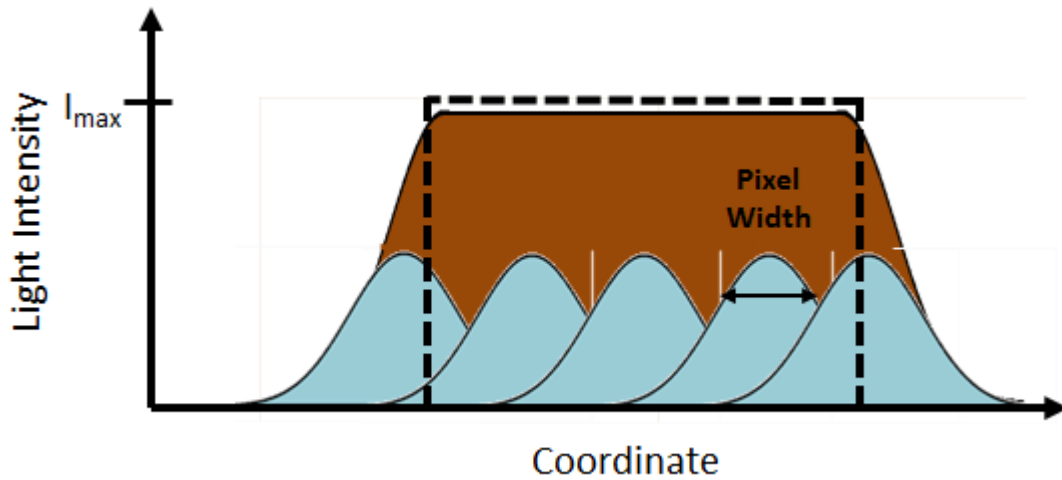


**Figure B.4 Representative light distribution of five neighboring pixels.** The additive effect of neighboring pixels increases light intensity and results in a better approximation of an ideal light distribution, marked with a dotted line

## B.2 Application of Sun et. al. Model to CLIP

Sun et. al. recently published a model for the light intensity distribution reflecting off of a DLP chip. This model assumes that the light distribution reflecting off of an individual micromirror can be represented using a Gaussian function, where the light intensity is defined by Equation B.1

$$I(r) = I_0 e^{-\left(\frac{r}{\omega_0}\right)^2} \quad (1)$$

where  $I_0$  is the maximum light intensity reflecting off of an infinite number of neighboring pixels,  $r$  is the distance from the center of the distribution, and  $\omega_0$  is the radius of the Gaussian distribution. **We aimed to apply the model developed by Sun et. al.<sup>1</sup> to the CLIP7 additive manufacturing system in order to 1) confirm that the decrease in cure depth as a function of feature size can reasonably be attributed to reduced “pixel blending” due to a reduction in the number of neighboring (or near-neighboring) pixels and 2) determine whether the CLIP7 system can be adequately modeled by assuming that the light distribution from a**

**single pixel is approximately a Gaussian function.** We know that the output light intensity distribution can be represented by the convolution of the light entering the optical system and the impulse response of the system. Therefore, if the impulse response is wide relative to the size of each input light pixel for a non-ideal system, this Gaussian function may be a good approximation for the system output. However, if the impulse response is small relative to the size of each input light pixel (for a more ideal optical system), the system output may more closely resemble a square step function than a Gaussian distribution.

Taking the Gaussian function (Equation B.1)

$$I(r) = I_0 e^{-\left(\frac{r}{\omega_0}\right)^2} \quad (\text{B.1})$$

and using the Pythagorean theorem to solve for  $r$ , the light intensity at a coordinate  $(x,y)$  resulting from the projection of a single micromirror centered at coordinate  $(i,j)$  is given by

$$I(x, y) = I_0 e^{-\left(\frac{\sqrt{(x-i)^2+(y-j)^2}}{\omega_0}\right)^2} = I_0 e^{-\frac{(x-i)^2+(y-j)^2}{\omega_0^2}} \quad (\text{B.2})$$

The total light intensity at  $x,y$  is a sum of all Gaussian distributions, such that

$$I(x, y) = \iint_{-w_x}^{w_x} \iint_{-w_y}^{w_y} I_0 e^{-\frac{(x-i)^2+(y-j)^2}{\omega_0^2}} dj di \quad (\text{B.3})$$

where  $w_x$  and  $w_y$  are one half of the width and length of a rectangular projection. Integrating this equation gives

$$I(x, y) = \frac{I_{max}}{4} \left[ \text{erf}\left(\frac{w_x+x}{\omega_0}\right) + \text{erf}\left(\frac{w_x-x}{\omega_0}\right) \right] \left[ \text{erf}\left(\frac{w_y+y}{\omega_0}\right) + \text{erf}\left(\frac{w_y-y}{\omega_0}\right) \right] \quad (\text{B.4})$$

which is the light intensity at a given point on the  $x,y$  plane.

In order to determine  $w_0$ , the radius of the Gaussian distribution used in the model, we use relationship between the maximum light intensity projecting from an infinite number of

neighboring pixels  $I_{max}$  and the light maximum intensity  $I_{actual}$  projecting from a square of width  $W$ . For a square of width  $W$  centered at the origin, the maximum light intensity will be found at  $x=0, y=0$ . Therefore, Equation B.4 can be written as

$$I(x, y) = \frac{I_{max}}{4} \left[ \operatorname{erf}\left(\frac{w_x}{w_0}\right) + \operatorname{erf}\left(\frac{w_x}{w_0}\right) \right] \left[ \operatorname{erf}\left(\frac{w_y}{w_0}\right) + \operatorname{erf}\left(\frac{w_y}{w_0}\right) \right] \quad (\text{B.5})$$

for a square projection,  $w_x = w_y = \frac{W}{2}$ . Therefore,

$$I(x, y) = \frac{I_{max}}{4} \left[ 2 \operatorname{erf}\left(\frac{W}{2w_0}\right) \right] \left[ 2 \operatorname{erf}\left(\frac{W}{2w_0}\right) \right] \quad (\text{B.6})$$

$$\frac{I}{I_{max}}(W) = \left[ \operatorname{erf}\left(\frac{W}{2w_0}\right) \right]^2 \quad (\text{B.7})$$

The relationship between  $I$  and  $I_{max}$  as a function of feature width is then calculated using the cure heights given in Figure B.2B by rearranging the working curve equation. Starting with the working curve, Equation B.8

$$C_T = \frac{1}{\alpha} \ln\left(\frac{E}{E_c}\right) \quad (\text{B.8})$$

We solve for exposure

$$E = E_c e^{\alpha C_T} \quad (\text{B.9})$$

and then divide by the maximum exposure, which occurs at  $C_{T, max}$  to obtain

$$\frac{E}{E_{max}} = \frac{e^{\alpha C_T}}{e^{\alpha C_{T, max}}} \quad (10)$$

Given that exposure is the product of light intensity and exposure time  $t$ ,

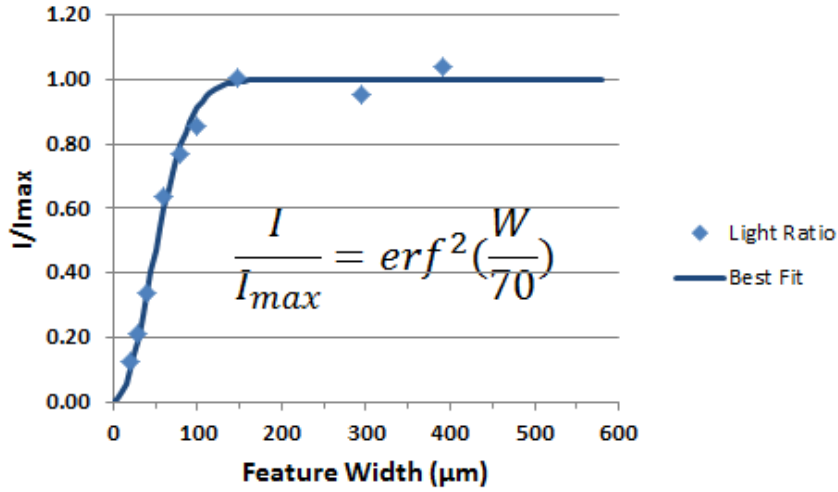


**Figure B.5 Relationship between feature width and projected light intensity normalized by the maximum light intensity**

$$\frac{It}{I_{max}t} = \frac{e^{\alpha C_T}}{e^{\alpha C_{T,max}}} \quad (B.11)$$

which simplifies to

$$\frac{I}{I_{max}} = \frac{e^{\alpha C_T}}{e^{\alpha C_{T,max}}} \quad (B.12)$$

Using values for  $C_T$  and  $C_{T,max}$  from Figure B.2 and the absorption coefficient alpha for TMPTA + 2.5 wt% DPO calculated in Chapter 3 yields the relationship shown in Figure B.5. As expected, the light intensity decreases as feature size decreases. Decreases in light intensity as a function of feature size begin to become relevant for parts that are less than 100μm wide at any location on that part. Much more experimentation should be performed to verify this conclusion by measuring cure depth at a wide range of light intensities and exposure times. Fitting the curve defined by Equation 5 to the data suggests that  $w_0$ , the radius of the Gaussian light distribution, measures 35μm. Therefore, this model suggests that light from a single ~10 μm pixel spreads

over approximately seven pixels. Direct measurement of light intensity distributions is necessary to verify this conclusion.

### B.2.1 Predicted Light Intensity Distributions

Having identified an appropriate radius for the model of the Gaussian light distributions, light distributions could be calculated for any point (x,y) along the build plane using equation B.4, which is reprinted below for clarity.

$$I(x, y) = \frac{I_{max}}{4} \left[ \operatorname{erf} \left( \frac{w_x + x}{w_0} \right) + \operatorname{erf} \left( \frac{w_x - x}{w_0} \right) \right] \left[ \operatorname{erf} \left( \frac{w_y + y}{w_0} \right) + \operatorname{erf} \left( \frac{w_y - y}{w_0} \right) \right] \quad (\text{B.13})$$

An image of the calculated light distributions as a function of feature size is given in Figure B.6. As expected, the light intensity distributions at larger feature sizes, such as the 40x40 pixel projection shown in Figure B.6A, fall closer to the ideal step function than light intensity distributions for smaller feature sizes. Additionally, this theoretical model predicts decreases in the maximum light intensity output per unit area from approximately 25mW/cm<sup>2</sup> for the large 40x40 pixel object, down to less than 5mW/cm<sup>2</sup> for the 3x3pixel object. These modeled light intensity distributions need to be validated through direct quantification of the projected light. Nevertheless, this theoretical framework supports the hypothesis that projected light intensity decreases with feature size on the micron scale in this system.

In order to begin to investigate whether this model can be validated using experimental results, the profile of the cured object that should result from these light intensity distributions was calculated. Again, the working curve equation,

$$C_T(x, y) = \frac{1}{\alpha} \ln \left( \frac{I(x,y)t}{E_c} \right) \quad (\text{B.14})$$

was used to establish cure thickness profiles using the calculated light intensity distributions in Figure B.6.  $E_c$  and  $\alpha$  were taken from the working curve for TMPTA+2.5wt%TPO in Chapter 3. Exposure time was 2 seconds, as described for the experiment outlined in Figure B.1. The modeled cure thicknesses are given in Figures B.7-B.10. In order to compare this calculation to experimental cure profiles, the experiment described in Figure B.1 was repeated using TMPTA+2.5wt% TPO mixed with 0.1wt% rhodamine. The resulting cured objects (analogous to those shown in Figure B.2) were imaged via confocal microscopy and are shown in Figures B.7-B.10. Although no quantitative assessment was performed, the modeled and experimental structures are qualitatively similar, indicating that a single-pixel based approach may more accurately describe CLIP fabrication on the micron-scale than traditional working curves.

Altogether, these results support the hypothesis that part deviations from the input CAD file may be due to the limited spatial bandwidth of the imaging system. A model by Sun et. al., which calculates light distributions, and the resulting cured object based on Gaussian light distributions was investigated for potential application to CLIP. The modeled cured objects appear qualitatively similar to the actual objects (Figure B.7), suggesting that this may be a useful model for predicting how build parameters (light intensity and build speed) and resin properties (critical exposure, absorbance) dictate the size and shape of an object produced using CLIP on the micron-scale. While these single pixel based effects have little bearing on the working curve “calculator” used to identify parameters for the production of large objects, more investigation of pixel level effects will be important to understand CLIP of parts on the micron scale.

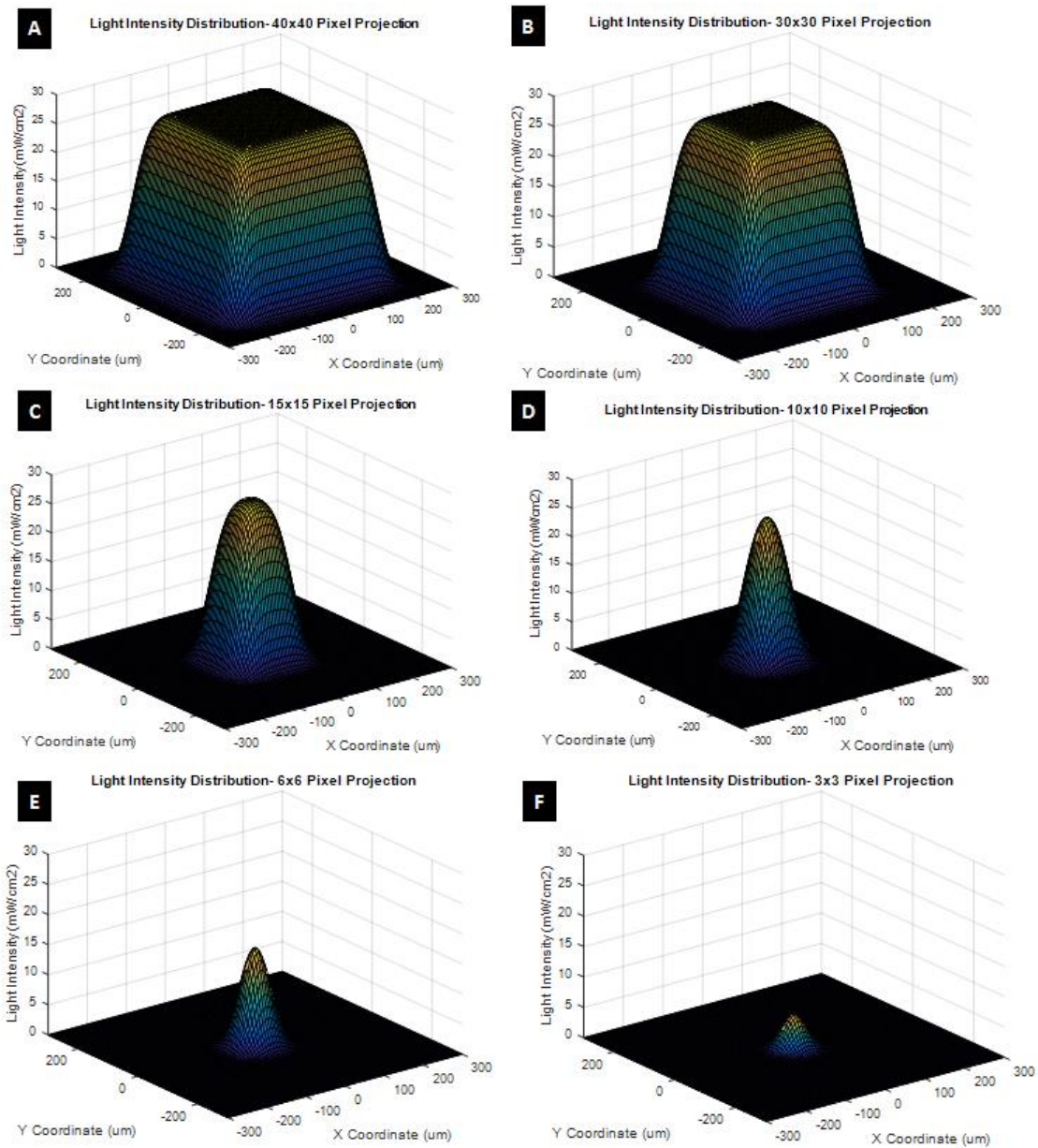


**Figure B.6 Modeled light intensity distributions as a function of feature size.** Light intensity distributions were modeled as described in Sun et.al for projections measuring A) 40x40 pixels, B) 30x30pixels, C) 15x15pixels, D) 10x10pixels, E) 6x6 pixels and F) 3x3 pixels. Theoretical modeling indicates that light intensity decreases with feature size for this system.

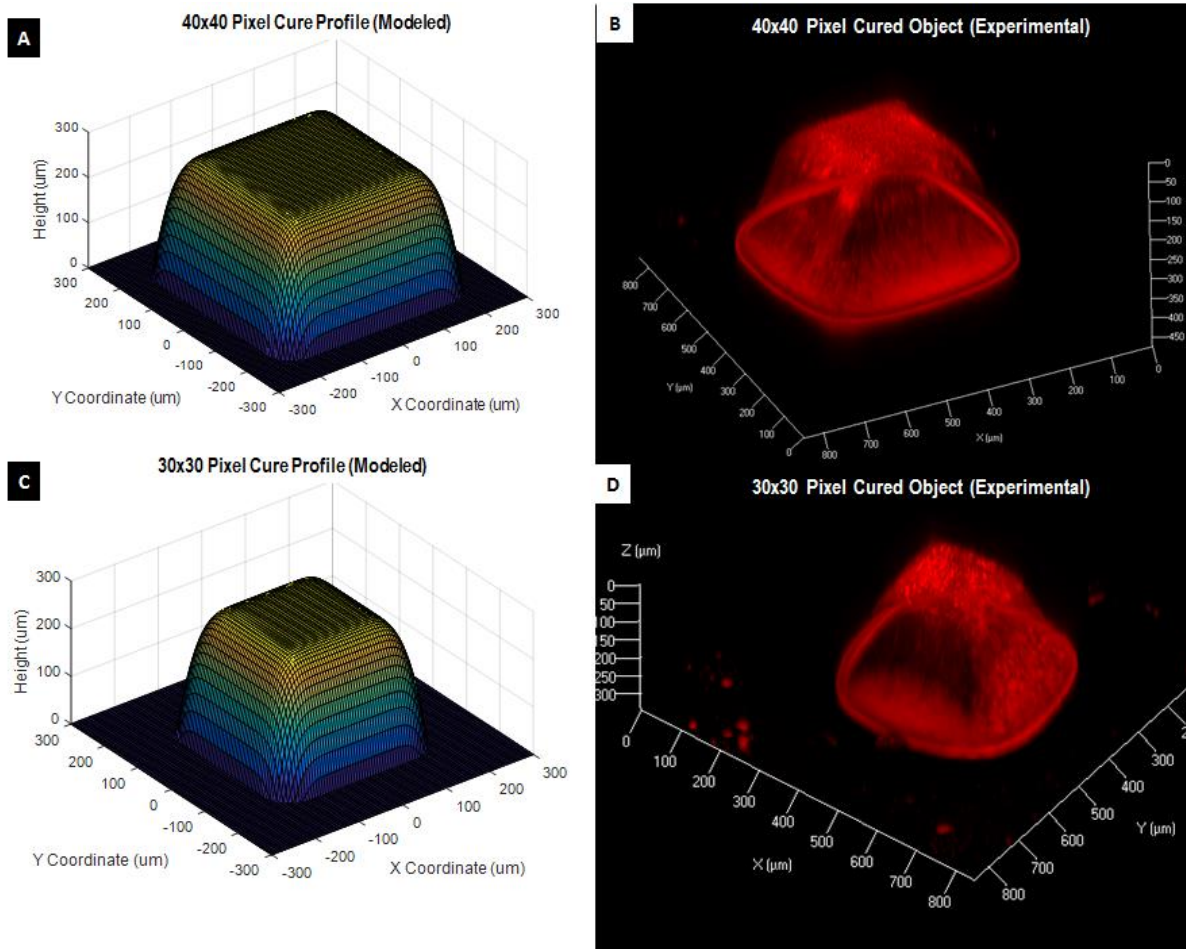


**Figure B.7** Modeled and experimental cure profiles of TMPTA exposed to a single frame of UV light measuring 40x40pixels (A-B) or 30x30pixels(C-D)

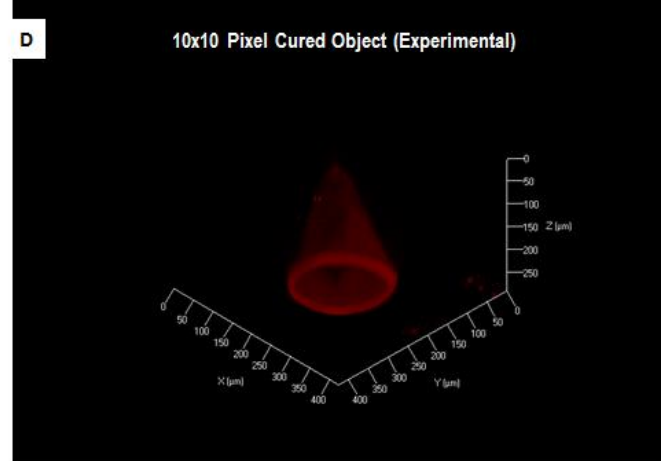
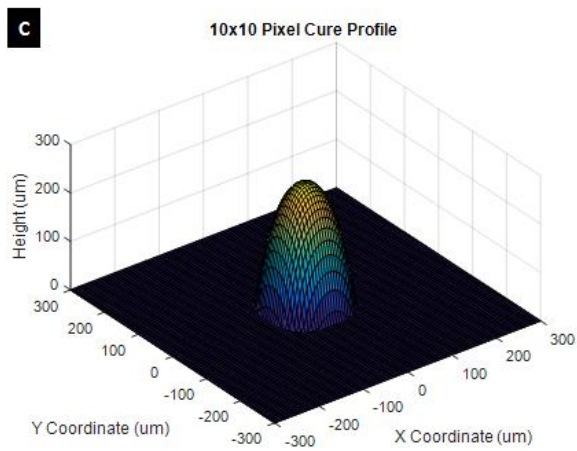
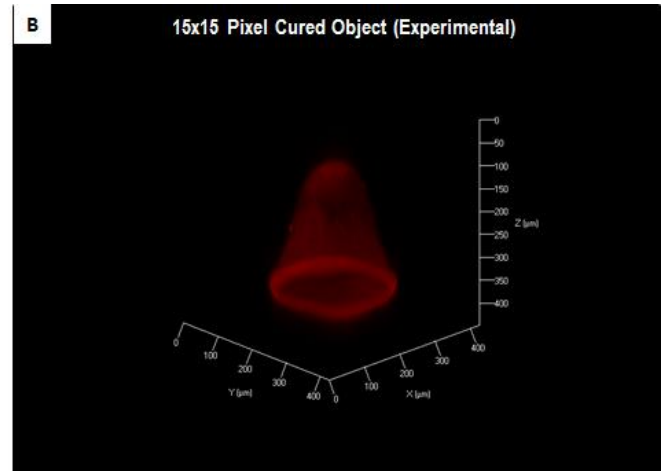
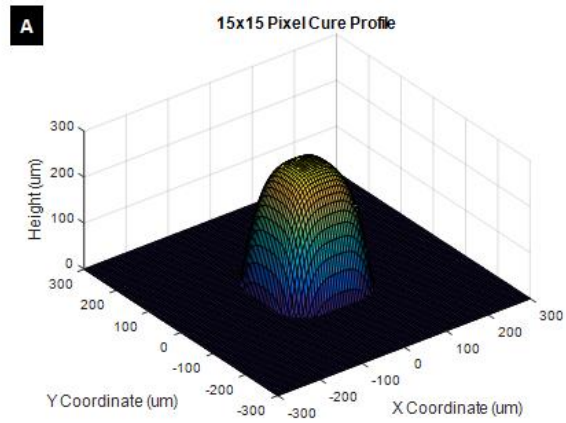


**Figure B.9** Modeled and experimental cure profiles of TMPTA exposed to a single frame of UV light measuring 15x15pixels (A-B) or 10x10pixels(C-D)

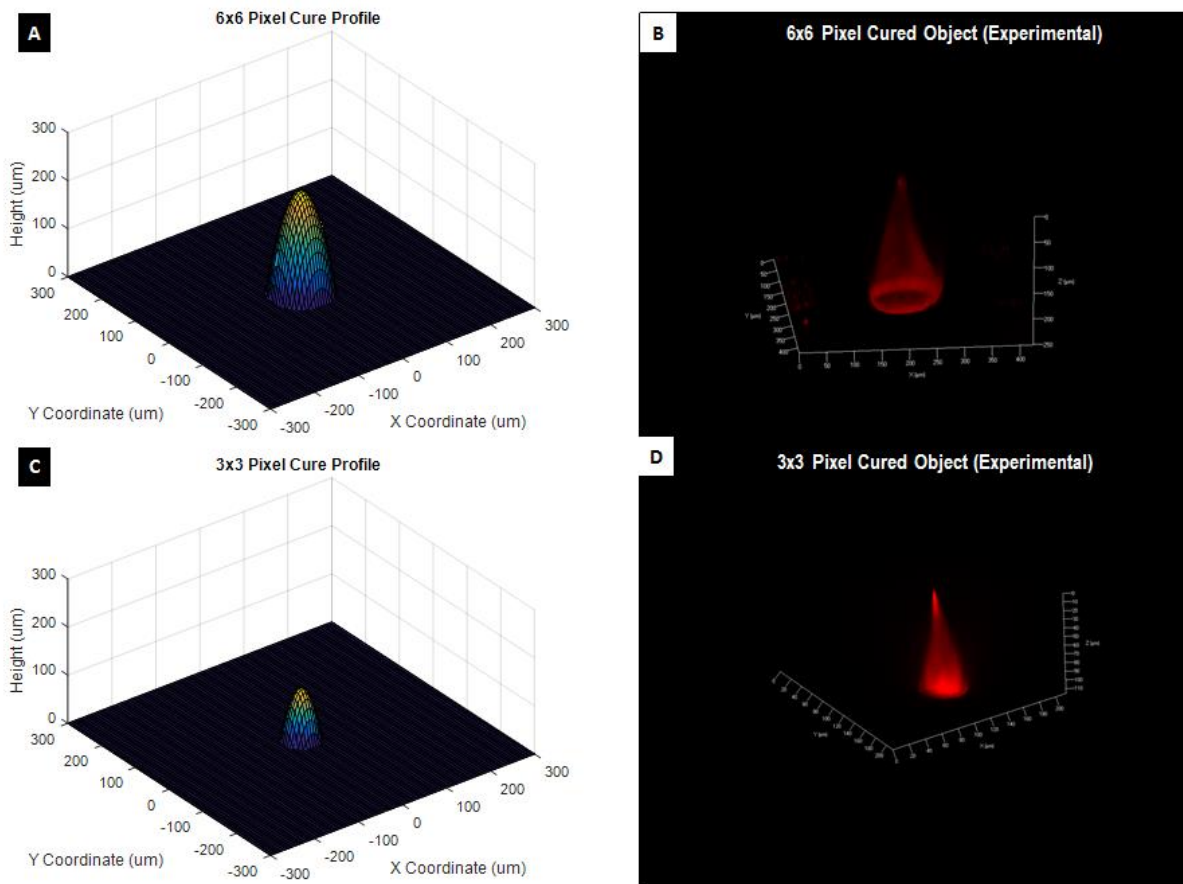


**Figure B.10 Modeled and experimental cure profiles of TMPTA exposed to a single frame of UV light measuring 6x6pixels (A-B) or 3x3 pixels(C-D)**

## REFERENCES

- (1) Sun, C.; Fang, N.; Wu, D. M.; Zhang, X. *Sens Actuators A*. **2005**, *121*, 113-120.
- (2) Zhou, C.; Chen, Y.; Waltz, R. *J Manufact Sci Eng*. **2009**, *131*, 061004.
- (3) Zhou, C.; Yong, C. *Proceedings of NAMRI/SME*. **2011**, *39*, 107-118.